Si Waveguide Technology for High Performance Millimeter-Wave/Terahertz Integrated Systems

by

Nazy Ranjkesh

A thesis
presented to the University of Waterloo
in fulfillment of the
thesis requirement for the degree of
Doctor of Philosophy
in
Electrical and Computer Engineering

Waterloo, Ontario, Canada, 2015

AUTHOR'S DECLARATION

I hereby declare that I am the sole author of this thesis. This is a true copy of the thesis, including any required final revisions, as accepted by my examiners.

I understand that my thesis may be made electronically available to the public.

Abstract

The terahertz (THz) spectrum (0.3 – 3 THz) offers new opportunities to a wide range of emerging applications which demand high-quality THz sources, detectors, amplifiers, and integrated circuits. On-chip integration of planar transmission line passive components degrades their performance due to the conduction loss. Therefore, a hybrid integrated technology in which all of the high-quality passive components are implemented using a suitable off-chip planar integrated technology and the active devices are placed on-chip, has become the most promising approach.

In this thesis, a low-cost and low-loss silicon-on-glass (SOG) integrated circuit technology is proposed for THz/millimeter-wave (mmW) applications. Highly-resistive intrinsic silicon (Si) is selected as the main guiding region due to its high transparency at mmW/THz frequency ranges and the maturity of Si-devices fabrication. In the proposed technology, all of the passive components and waveguide connections are made of highly-resistive Si on a glass substrate. The proposed technique leads to a high-precision and low-cost fabrication process, wherein the alignment between the sub-structures is automatically achieved during the fabrication process. This is performed by photolithography and dry etching of the entire integrated passive circuit layout through the Si layer of the SOG wafer. The SOG dielectric ridge waveguide, as the basic component of the SOG integrated circuit, is theoretically and experimentally investigated. A test setup is designed to measure propagation characteristics of the proposed SOG waveguide. Measured dispersion diagrams of the SOG dielectric waveguides show average attenuation constants of 0.63 dB/cm, 0.28 dB/cm, and 0.53 dB/cm over the frequency ranges of 55 – 65 GHz, 90 – 110 GHz, and 140 – 170 GHz, respectively.

Extending the SOG platform toward the THz range is achieved by new SOG waveguide structures wherein the glass substrates below the Si channels are etched to reduce the effect of greater glass material loss at higher frequencies (i.e., > 200 GHz). To fabricate these structures, the glass substrate is etched in hydrophilic acid before bonding to the Si. Four new SOG configurations, called the *suspended* SOG, *corrugated* SOG, *rib* SOG, and *U*-SOG waveguides are proposed with their respective fabrication techniques for the THz range of frequencies. In the suspended SOG waveguide, a periodic configuration of Si beams supports the Si guiding channel over the etched grove on the glass substrate. Measurements of two suspended SOG waveguides show low attenuation constants of 0.031 dB/λ_0 and 0.042 dB/λ_0 (on average) over the frequency ranges of 350 - 500 GHz and 400 - 500 GHz, respectively. It is theoretically demonstrated that the rib SOG and U-SOG waveguides are promising candidates for

THz high-density and low-loss integrated circuits. Rib SOG waveguide and U-SOG waveguide test devices are designed over the frequency bands of 0.8 – 0.9 THz and 0.9 – 1.1 THz. The proposed SOG waveguide technology can easily be extended to several THz with no limitations.

A new mmW low-loss dielectric phase shifter integrated in the corrugated SOG platform is designed, fabricated, and measured. Phase shifts of 111 ° and 129 ° at frequencies of 85 GHz and 100 GHz, with maximum insertion losses of 0.65 dB and 2.5 dB, are achieved during measurements of the proposed phase shifter. Millimeter-wave integrated SOG tapered antennas are developed and implemented. The idea of a suspended SOG tapered antenna is demonstrated to enhance the radiation efficiency and the gain of the SOG tapered antenna over 110 – 130 GHz. The suspended SOG tapered antenna, which can function under two orthogonal mode excitations, shows measured efficiencies of higher than 90 % for the two vertical polarizations.

Acknowledgments

I would like to thank my supervisors Prof. Safieddin Safavi-Naeini and Prof. Mohamed Basha for their insightful guidance and support during my PhD studies. Especially I would like to thank Prof. Safieddin Safavi-Naeini for his encouragement, knowledge, and giving me great freedom to try and explore my ideas. My sincere thanks to Dr. Chattopadhyay from JPL (Jet Propulsion Laboratory, Nasa) for accepting to be my external examiner. I also would like to thank my thesis committee, Prof. Strickland, Prof. Chaudhuri, and Prof. Saini for their suggestions and comments on my thesis.

I express my thanks to Brian Goddard, Rodello Salandanan, Dr. Anita Fadavi, Dr. Reza Khorasaninejad, Dr. Nathan Nelson-Fitzpatrick, and Richard Barber for sharing their experience and expertise in clean room fabrication.

I also would like to thank all of my colleagues at Centre for Intelligent Antenna and Radio Systems (CIARS), specially Dr. Gigoyan and Dr. Rafi for sharing their experience with me. This work is funded by the Natural Sciences and Engineering Research Council of Canada (NSERC) and Blackberry (formerly Research In Motion).

Last but not least, I would like to express my heartfelt appreciations to my parents, sisters, and lovely nephews for their love and support.

Dedication

This thesis is dedicated to my parents who have always been there for me.

Contents

List of figures:

List of tables:

List of abbreviations:

AUT (Antenna Under Test)

BLT (Barium Lanthanide Tetratitanates)

CIARS (Centre for Intelligent Antenna and Radio Systems)

CPW (Coplanar Waveguide)

DRIE (Deep Reactive Ion Etching)

5G (fifth generation mobile networks)

HFSS (High Frequency Structure Simulator)

HF (Hydrofluoric Acid)

IC (Integrated Circuit)

KOH (Potassium Hydroxide)

LTCC (Low Temperature Co-fired Ceramic)

mmW (millimeter-wave)

MEMS (Micro-Electromechanical System)

PCB (Printed Circuit Board)

PEC (Perfect Electric Conductor)

PML (Perfect Matched Layer)

RIE (Reactive Ion Etching)

Si (Silicon)

SOG (Silicon-On-Glass)

SIW (Substrate Integrated Waveguide)

SIIG (Substrate Integrated Image Guide)

SOI (Silicon-On-Insulator)

SEM (Scanning Electron Microscope)

SLL (Side-Lobe Level)

THz (Terahertz)

UV (Ultraviolet)

Chapter 1 Introduction

1.1 Motivation

The terahertz (THz) spectrum refers to electromagnetic radiation whose frequency spans from 0.3 THz to 3 THz. The millimeter-wave (30-300 GHz; mmW) and THz frequency ranges offer new opportunities for a wide variety of emerging applications in high-speed communications, high-resolution imaging, molecular spectroscopy, security imaging, medical imaging, and for various novel sensors with unique capabilities [1-15].

Terahertz and mmW frequencies are attractive for communication systems due to their large bandwidth and high rate of data transfer capacities. However, due to the high atmospheric loss, these radiations cannot be used for long-distance wireless communication; instead, applications in ultra-fast short-range wireless systems are under development [2-8].

Radiation at THz frequencies penetrates nonpolar and nonmetallic materials such as paper, plastic, clothes, wood, and ceramics. This property makes them applicable for security scanning for the detection of concealed objects [9-11]. The low photon energy of THz radiation is not harmful to tissues, as opposed to *X-ray* radiation, and specific bandwidths of THz radiation can penetrate tissues which have a low water content to a depth of several millimeters and reflect the energy back. Different polar molecules absorb specific THz frequencies, and can be characterized and recognized by observing their absorption and refractive index spectra using THz spectroscopy. For example, in biochemistry, different tissues such as fat, muscle, healthy, or cancerous, can be recognized based on their absorption spectra. The short wavelength of THz radiation is very advantageous for high resolution imaging. This property, along with the spectral signatures of materials and biological tissues in the THz region, offer the possibility to combine spectral identification and spatial imaging. Numerous THz applications in body imaging, cancerous tissue recognition, burn injury characterization, and tooth decay identification are under development [12- 18].

Realization of the abovementioned applications demands high-performance technology platforms and devices such as sources, detectors, amplifiers, and integrated circuits. Due to the lack of appropriate technology, the THz band has been known as the THz gap for long time. During the past few decades, great progress has been made in shrinking the THz gap. However, more research and development efforts are needed to actually realize THz applications.

Low-loss and low-cost THz integrated-circuit technology is essential for realizing a vast number of the promising applications of this band in high-speed communication, security imaging, medical imaging, and molecular spectroscopy. Terahertz semiconductor amplifiers are under development and devices with operation frequencies of $f_{max} \sim 1$ THz and $f_T > 500$ GHz have been realized [19- 22]. These on-chip active devices are conventionally integrated using metallic on-chip interconnects which have planar and compact geometries; these properties make them compatible to the chip manufacturing process. However, the on-chip integration of planar transmission line passive components suffers from excessive conductor loss due to the field singularities at the conductor edges, and the decreasing skin depth with higher frequencies [23-25]. Furthermore, they consume a large portion of the chip area and consequently increase the manufacturing costs.

One existing approach to alleviating the on-chip loss problem is the implementation of passive components off-chip. These passive components are then integrated with the on-chip active devices in a hybrid configuration. In this technology, the connection to the chip is achieved by a transition between the on-chip and off-chip planar transmission lines using a compatible passive elements technology. One current approach for the realization of mmW/THz hybrid integrated circuits uses the miniaturized metallic rectangular waveguides in planar form. The main issue with planar metallic waveguides is their fabrication complexity at mmW/THz frequencies.

In this research, the focus is on the development of a new silicon (Si)-based technology platform for mmW/THz hybrid integrated circuits. Current state-of-the-art mmW planar dielectric waveguides cannot provide low-loss platforms for high-density integrated circuits as the frequency increases toward the THz range. Furthermore, their implementation at high frequencies fails due to the lack of high-precision and automated fabrication techniques. Based on this fact, the main goal of this research is to develop a low-loss and high-density integrated-circuit technology which is compatible with a low-cost and high-precision fabrication technique and which eliminates the requirement for any manual alignment of the substructures.

The frequency range of interest in this thesis falls between 50 GHz and 1.1 THz. It is worth mentioning that the proposed SOG waveguide technology can easily be extended to several THz with no limitation. However, the proof-of-concept prototypes are fabricated between 50 GHz to 1.1 THz merely because of test instrument limitations. As the basic components of the passive integrated circuits, high-resistivity Si waveguides are designed and fabricated on glass substrates. In order to maintain the low-loss characteristics of the silicon-on-glass (SOG) dielectric waveguides over the THz range, where the

material loss in the Pyrex glass increases, novel SOG waveguide structures with etched grooves on the glass substrates below the Si guiding channels are proposed and developed. The low attenuation constants of the proposed SOG waveguides are theoretically and experimentally demonstrated over different mmW and THz frequency ranges up to 1.1 THz.

1.2 Thesis Overview

Chapter 2 reviews the state-of-the-art mmW/THz hybrid integrated-circuit techniques. Different mmW/THz planar metallic waveguide and dielectric waveguide structures are studied and compared to each other in terms of their loss characteristics, fabrication simplicity, and potential extension to higher THz frequencies.

In Chapter 3, an SOG platform is proposed for mmW high-density integrated circuits up to 200 GHz. Forming the basic component of an SOG integrated circuit, SOG dielectric waveguides are designed and fabricated. Si-confined modes in the SOG ridge dielectric waveguides are defined and their cutoff conditions and frequencies are studied. A test setup is designed for measuring the attenuation constant of the SOG waveguide. The low-loss performance of the SOG waveguides is theoretically and experimentally confirmed up to 170 GHz. The high performance of the SOG platform is compared with that of state-of-the-art techniques in terms of fabrication simplicity and attenuation constant.

Chapter 4 investigates the extension of the SOG platform to higher frequencies above 200 GHz from different standpoints of fabrication feasibility and dielectric material properties. It is shown that the SOG fabrication technique, which provides sub-micron dimensional accuracy, can be easily extended to THz frequencies. However, the increasing Pyrex glass material loss as the frequency rises degrades the SOG waveguide's performance above 200 GHz. The problem of greater glass material loss at higher frequencies is overcome by new configurations, where the glass substrates below the Si guiding channels are etched. Two new SOG waveguide structures, called the *suspended* SOG and *corrugated* SOG waveguides, are introduced. The new waveguide structures are designed, fabricated, and tested. The low attenuation constant of the suspended SOG waveguide is experimentally and theoretically demonstrated over the frequency range of 350–500 GHz.

Chapter 5 discusses the drawbacks of the suspended SOG waveguide for THz high-density integrated circuits. To overcome these drawbacks, and to attain a high-performance waveguide at higher frequencies ~ 1.1 THz, two novel dielectric waveguide structures called the *rib SOG* waveguide and *U-SOG* waveguide are proposed along with their respective fabrication techniques. Full-wave

simulations are conducted to study the effect of different parameters on the performances of these two novel waveguides. Rib SOG and U-SOG waveguides are designed for fabrication and measurement over the frequency ranges of 0.8–0.9 THz and 0.9–1.1 THz. The fabrication of the U-SOG waveguide is underway.

Chapter 6 discusses mmW integrated passive components implemented in the proposed SOG platform. Two new mmW fully-dielectric phase shifters are proposed and implemented in the SOG platform and their low-loss characteristics are compared with those of state-of-the-art techniques. SOG tapered antennas are designed, fabricated, and tested over the frequency ranges of 50–75 GHz and 110–130 GHz. The idea of etching the glass substrate below the Si tapered antenna is demonstrated in order to achieve a better antenna performance in terms of gain and efficiency.

Chapter 7 summarizes the achievements of this research and provides directions for possible future research work.

Chapter 2 Terahertz and Millimeter-Wave Integrated Circuits: A Technology Overview

The richness of terahertz (THz) radiation has become a strong motivator for the realization of high performance THz systems. During the last two decades, optical and microwave technologies have made great progress in closing the THz gap. In terms of millimeter-wave (mmW) and THz hybrid/integrated circuits, the state-of-the-art technologies and fabrication techniques can be categorized into two main approaches:

- Miniaturization of conventional microwave metallic rectangular waveguides in planar form.
- Planar dielectric waveguides inspired by optical integrated circuits and guided-wave structures.

In this Chapter, the existing mmW and THz integrated waveguide technologies are discussed in some detail.

2.1 Metallic Rectangular Waveguides for Millimeter-Wave and Terahertz Integrated Circuits

Metallic rectangular waveguides are widely used in the microwave range of frequencies due to their low insertion loss. However, these waveguides suffer from difficulty with integration due to their non-planar form. To overcome this issue, researchers have focused on finding planar realizations of these waveguides. A planar realization of the rectangular waveguide, with the potential to be integrated with active devices in a hybrid configuration, was reported in [26]. In their structure, called the substrate integrated waveguide (SIW), two rows of periodic metallic vias in a double-sided substrate play the roles of the metallic sidewalls of the rectangular waveguide (Fig. 2.1) [26- 32]. However, it is not practicable to realize low-loss mmW/THz integrated circuits based on the SIW approach due to the difficulty of fabricating the miniature metallic vias with high precision. In SIW, optimal field confinement is determined by the proper design of the periodic metallic vias dimensions; these requirements will soon extend beyond the capacity of current technologies as frequency increases. The highest reported operation frequencies for SIW systems are 94 GHz and 140 GHz, for antenna array structures fabricated on printed circuit boards (PCB) [30], and low temperature co-fired ceramic (LTCC) technologies [31, 32], respectively. The highest frequency at which a measured attenuation constant was reported for the SIW structure was 27-81 GHz [29]. Measurements of this structure, which was fabricated on an RT/Duriod 5880 substrate, showed an insertion loss of 0.31 dB/cm at mid-band.

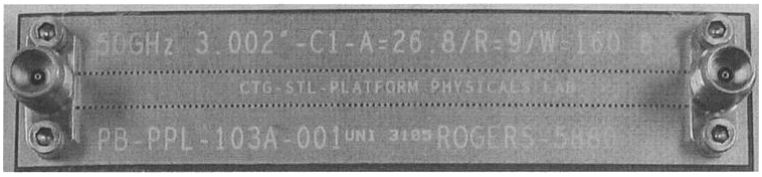

Fig. 2.1 SIW structure.

The main drawback in the realization of planar miniaturized metallic waveguides at high mmW/THz frequencies, where finer dimensions and higher dimensional accuracies are needed, is their complex and difficult fabrication. Therefore, in [33- 48] micromachining techniques were involved to deal with these difficulties. In [33- 41], the waveguide channels were formed in a planar substrate first and then metal-coated using the sputtering technique. To form the waveguide channel, three different techniques have been reported. These techniques are: *i*) ultraviolet (UV) exposure of an SU-8 photoresist layer [33], *ii*) wet etching of a silicon (Si) substrate [34, 35], and *iii*) deep reactive ion etching (DRIE) of Si [36- 41].

The first method, UV exposure of SU-8 photoresist [33], was demonstrated up to 325 GHz and waveguides with operating frequencies over 110-170 GHz, 140-220 GHz, and 220-325 GHz were tested with insertion losses of 0.5 - 0.8 dB/λ, 0.6 - 1 dB/λ, and 1.1 - 1.6 dB/λ, respectively. In [34], two Si wafers were etched in potassium hydroxide (KOH) to form the two half-waveguide channels. The fabricated waveguide was actually a stack of four bonded Si layers which formed the waveguide top face, two half-waveguide channels, and the bottom supporting slab, respectively. The measured insertion loss of this structure was 0.04 dB/λ at 100 GHz. A critical aspect of the fabrication of split-waveguide circuits is the challenging high-precision alignment required between the two waveguide halves.

Using the DRIE process to form the guiding channel was reported in [36- 41]. This technique is capable of providing vertical sidewalls with less surface roughness than the other two techniques which create sloping profiles with poor sidewall quality. The technique was used to construct a metallic rectangular waveguide in the form of a two-layer stack [37]. The whole waveguide channel was made by DRIE halfway through one Si wafer, while the other Si wafer formed the waveguide top face. These two wafers were bonded after gold metallization. A measured attenuation constant of 0.15 dB/mm at 600 GHz was reported for this waveguide, which was designed for operation over 500-750 GHz [37]. Using the same technique, a measured average attenuation constant of 0.068 dB/mm was reported over 350-

460 GHz by [36]. Three important factors that contributed to the reported attenuations were the conductor loss, surface roughness, and imperfect metal coverage [37]. A 385 GHz metallic waveguide band-pass filter based on DRIE of Si was reported in [38]. The lowest measured band-pass insertion loss for this filter was 2.7 dB. The measured 3 dB bandwidth was 15 GHz, while the filter was designed for a 10 GHz bandwidth.

The techniques reported in [33- 41] require a large number of steps for construction and a high degree of fabrication complexity; a significant challenge at mmW/THz frequencies. Of particular difficulty in the abovementioned fabrication processes, is the bonding between the two plated wafers to form the waveguide. This is a critical fabrication step where any discontinuity, or misalignment in the case of the split-waveguide, would significantly increase the waveguide attenuation and degrade its performance. In [33- 41], during fabrication the waveguide corners needed to be inspected for continuity and smoothness at the bonding site between the two wafers. In order to ensure complete metal coverage over the entire vertical waveguide boundaries, the waveguide channels were metallized using combinations of sputtering and electroplating. In [40], Si compression pins were used to improve the alignment accuracy in split-waveguide circuits.

The challenge of the difficult and costly fabrication of mmW/THz metallic rectangular waveguides becomes even more problematic when the demand arises for integration with active devices. Furthermore, very often it is not possible to make all of the required passive components in the same waveguide technology. For active integration, a transition structure implemented on an *E*-plane membrane centered inside the waveguide was designed to couple the TE_{10} waveguide mode to the coplanar waveguide (CPW) mode in [37, 41]. The entire fabricated structure was a three-dimensional assembly of four individually fabricated Si and membrane wafers which were bonded to each other; precise alignment between the bonded layers is crucial for stack structures [37]. In [42], an array of glass lens antennas arranged on a Si substrate was reported. The antenna array was excited with metallic rectangular waveguides which were coupled to the antennas through etched holes within the Si substrate. The reported 500-600 GHz test prototype was a three dimensional arrangement of glass antennas on top a Si substrate coupled with Si-micromachined metallic waveguides [42].

A different fabrication approach for integrated rectangular waveguides was reported in [43- 45]. The measured attenuation constant of the 3 THz test structure was 0.12 dB/λ [43]. The fabrication process of this waveguide began with a Si substrate whose top face was covered with metal. This metal layer acted as the bottom metallic face of the waveguide. Other metallic walls were realized by electroplating

a photoresist mold, which was coating the waveguide bottom metal face. The main disadvantage of this technique is the additional loss due to the periodic configuration of access holes laid on the deposited top metallic wall of the waveguide (Fig. 2.2(b)). These holes were used to remove the photoresist from the waveguide interior after electroplating the sidewalls [43].

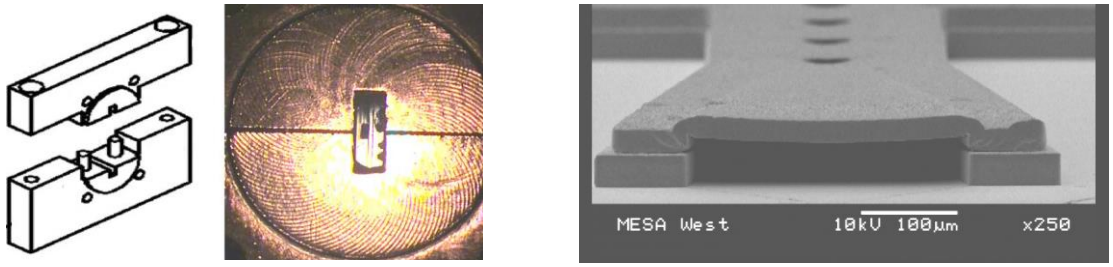

(a) (b)

Fig. 2.2 a) Si-micromachined metallic waveguide made of two half-waveguide channels [38] and b) fabricated metallic waveguide with access holes on the top metallic wall [44].

In [46, 47], a Si-filled metallic waveguide with a trapezoidal cross section was reported. The fabrication process was based on the KOH wet etching of a high-resistivity Si wafer which was glued on a glass substrate with two intermediate deposited metal layers. Aluminum was sputtered onto the surfaces of the structure to form the top and side metallic walls. This waveguide was tested over 77-110 GHz where an average insertion loss of 0.2 dB/mm was obtained. To provide better geometrical accuracy, [48] reported a Si-filled metallic waveguide with rectangular cross section formed using DRIE through a high-resistivity Si wafer. However, the metallization of the vertical sidewalls was a technological challenge. The measured attenuations for an 80-110 GHz test structure fabricated using this technique were 0.125 dB/mm and 0.121 dB/mm at frequencies of 100 GHz and 105 GHz, respectively.

2.2 Planar Dielectric Waveguides for Millimeter-Wave and Terahertz Integrated Circuits

Dielectric waveguides are commonly used in optical integrated circuits. Researchers began several decades ago to investigate dielectric waveguides for mmW integrated circuits [49- 54]. Alumina was the material most commonly used to fabricate the guiding channels in insulated image guides, which were then thermally bonded to the ground plane using a low-permittivity insulating film [52]. Insertion of the melt-processable insulating film solved the problem of mechanical mounting of the guiding

channel on the ground plane. The insulating film also reduced the waveguide attenuation due to the conduction loss and surface roughness at the ground plane. The very high precision alignment required by the manual assembly of the complex structures is the main drawback to realizing mmW/THz integrated circuits based on this technique. In 1991, ridge dielectric waveguide structures with alternating low and high permittivity layers were designed and fabricated for operation over 0.1-0.3 THz and 0.3-2 THz frequency ranges [55, 56]. The fabrication of these waveguides, which were optimized for field confinement within the low-permittivity regions, was based on etching of multilayered wafers.

The idea of using dielectric waveguides for mmW/THz integrated circuits did not continue in the 1990s, and no measurement results for the fabricated structures were reported until 2003, when mmW rectangular rod waveguides were reported [57, 58]. Based on the introduced structure, an array of antennas made of sapphire was designed, fabricated, and measured [57]. In [58], transitions from rectangular rod waveguides made of polyethylene into micro-strip and slot lines were designed and tested. The antenna array and transition structures are shown in Fig. 2.3. Theoretically, dielectric rod waveguides would eliminate the effects of conduction loss, as opposed to image guides. However, no mechanical supports were introduced for these waveguide structures to make them practically appropriate for implementing mmW/THz integrated circuits.

(a) (b)

Fig. 2.3 a) An array of antennas made of dielectric rod waveguides [57] and b) transitions from rectangular rod waveguides into micro-strip and slot lines [58].

To facilitate assembly of the complex structures required by the conventional insulating image guide topology [52], a substrate integrated image guide (SIIG) was introduced in 2005 [59]. In the SIIG

structure, as shown in Fig. 2.4(a), the guiding channel of the image guide is surrounded by a lattice of periodic air holes inside the guiding substrate to create regions with low effective permittivity. The perforated substrate is then bonded to the ground plane using a low-permittivity insulating film [59-65]. A transition from the coplanar waveguide to the SIIG on an alumina substrate (ε_r = 9.8 and tanδ = 0.002) was designed, fabricated, and tested over the frequency range of 80-110 GHz [60]. An array of metallic-strip antennas fed by SIIG on a 381 μm thick alumina substrate was presented at 94 GHz [61]. A tapered dielectric antenna fed by SIIG fabricated on alumina substrate was also reported at 94 GHz [62]. In all of the reported SIIG structures, polyethylene (ε_r~2.3) was used as the insulating film material. High-resistivity Si (ε_r = 11.7 and tanδ = 0.0007) wafers with a thickness of 525 μm were used to fabricate the SIIGs over the frequency range of 65-110 GHz [59]. A measured attenuation constant 0.25 dB/cm was reported at the single frequency of 72 GHz based on comparison loss measurements of two lengths of this waveguide.

Although the insulating film in the SIIG structure reduced the conduction loss to some extent, this waveguide still suffered from additional losses due to the finite conductivity and surface roughness at the ground plane. To reduce the field concentration close to the ground plane, an SIIG supported on small copper strips, which formed a thick gap between the waveguide slab and the ground plane, was reported [64, 65]. A measured attenuation constant of 0.7 dB/cm at 90 GHz was reported for a fabricated alumina test structure operating in the higher order E_x^{11} mode (electric field parallel to the ground plane) [64].

The design and simulation of complex perforated structures requires significant memory and computational time. The wave guiding principle utilized in the perforated SIIG is based on the variation in the effective permittivity created by a lattice of air holes (Fig. 2.4(a)). This technique suffers from additional scattering loss due to the periodic holes. To realize a quasi-homogeneous effective permittivity in the perforation zone, and to prevent the occurrence of stop-band in the operation frequency band, the lattice dimensions should be chosen to be smaller than a fraction of the guided wavelength. Therefore, the perforation of the dielectric slab is a crucial fabrication step; for high-performance waveguides a complex and high-precision perforation method is needed. In order to create a high refractive index contrast between the guiding channel and the perforated zone, a large portion of the substrate material should be removed by perforation at the expense of reducing the mechanical stability. Furthermore, high-density integration using this method is quite difficult due to the

requirement of several rows of holes to be made between two dielectric guiding regions to minimize coupling and leakage.

(a) (b)

Fig. 2.4 Perforated SIIG structure [59] and b) fabricated LTCC-based SIIG leaky-wave antenna [67].

To overcome the issues consequent to the insertion of air holes in the perforated SIIG configuration, an SIIG implemented in LTCC technology was reported [66- 68]. The LTCC-based SIIG offers better fabrication reliability and more efficient simulation time as compared to the perforated SIIG [66]. However, the insulating film in the LTCC-based SIIG structure, which was realized with a single ceramic layer that had dielectric characteristics similar to those of the guiding channel, was unable to reduce the field concentration close to the ground plane as opposed to the perforated structure. An LTCC-based SIIG with dielectric characteristics (ε_r = 5.9 and tanδ = 0.002) was fabricated and tested over 57-67 GHz. Comparison loss measurements of two lengths of this waveguide at 62 GHz showed an attenuation constant of 0.29 dB/cm. Fig. 2.4(b) shows a fabricated leaky-wave antenna on LTCC-based SIIG waveguide platform.

A high-resistivity Si rod dielectric waveguide fabricated using photolithography and DRIE of a Si wafer, was presented recently and waveguides with operation frequencies over 90-140 GHz and 140-220 GHz were designed, fabricated, and measured [69]. In the measurement setup, supporting beams were added to the structure and then the fabricated structure was manually mounted in a groove on a metallic slab to support the waveguide (Fig. 2.5(a)).

In [70, 71], a resonator and switch based on photonic crystal structures were designed and fabricated on high-resistivity Si wafers. As shown in Fig. 2.5(b), the photonic crystal Si slabs were held manually

in the air during the measurements. However, to develop an integrated circuit technology, a supporting slab would be needed. The requirement for a supporting slab becomes more important as the operation moves to higher frequencies and the Si substrate becomes thinner and consequently more fragile.

(a) (b)

Fig. 2.5 a) Test setup of the high-resistivity Si rod dielectric waveguide [69] and b) test setup of the photonic crystal resonator devices mounted between two metallic ports [71].

Using dielectric waveguides for mmW/THz integrated circuits offers several advantages over using metallic waveguides. As the frequency increases the skin depth decreases by a factor of $1/\sqrt{f}$ and, consequently, the conduction loss increases dramatically. In addition, the metallic waveguide performance is degraded by surface roughness of the conducting boundaries. Dielectric waveguide attenuation is primarily determined by the dielectric material loss. Finding a highly transparent material enables the dielectric waveguide to operate with lower loss compared to a rectangular metallic waveguide. It is fortunate that some dielectric materials, such as highly resistive Si, high-resistivity gallium arsenide, and sapphire, have low-loss characteristics over the mmW/THz frequency ranges. Furthermore, dielectric waveguide structures are in a planar form; highly appropriate for implementing integrated circuits.

Despite the advances in developing dielectric-waveguide-based mmW/THz integrated circuits, more research needs to be performed to realize a technology platform which addresses the practical requirements of emerging mmW/THz systems. To this end, in addition to a highly transparent dielectric guiding medium, the other crucial steps include identifying a low-loss supporting substrate, developing a low-cost and feasible fabrication process, and specifying a high-precision implementation with minimal requirements for manual mounting, alignment, and assembly of the sub-structures in an

integrated circuit. Finally, the sought for technology platform should support high-density integration and particularly integration with active devices.

2.3 Planar Goubau Line

Beyond the two main approaches mentioned above, the potential applications of the planar Goubau line for mmW and THz integrated circuits was investigated in [72- 74]. The Goubau line, which consists of a single metallic circular line coated with dielectric material, was first introduced in 1960 by Goubau [75]. In the planar structure, a rectangular metallic strip, mounted on a dielectric substrate, plays the role of the metallic circular line in a conventional Goubau line. Researchers in [73] fabricated and tested back-to-back transitions from coplanar waveguides to planar Goubau lines designed on a quartz substrate with metallic strips made from silver, gold and titanium-gold. The test results for 1.5 mm lengths of these lines at 300 GHz showed insertion losses of 2.8 dB, 3.6 dB, and 3.8 dB, respectively [73]. The main issue with the reported structures is the challenging fabrication of the squared metallic strips. To simplify the fabrication, and to make it compatible with current fabrication techniques, the square metallic strip can be thinned to less than 20 μm. Nevertheless, this will increase the waveguide attenuation and causes strong deviations of the electromagnetic field distribution from that of the conventional Goubau line.

Chapter 3 Silicon-on-Glass Dielectric Waveguide for Mmillimeter-Wave Integrated Circuit

3.1 Introduction

Realization of millimeter-wave (mmW) high-resolution imagers, high-speed communication systems, and a wide variety of attractive mmW applications, depend on the availability of cost-effective technology platforms for high-quality integrated circuits. Low-loss and high-performance mmW integrated circuits require low-loss waveguide structures with minimal dispersion.

Dielectric waveguides are promising candidates for mmW and terahertz (THz) hybrid integrated circuits due to their intrinsic planar form. The waveguide attenuation is dominantly determined by the material loss of the dielectric medium which forms the guiding channel. Extensive research has been conducted to characterize different dielectric materials over the THz range [76- 85]. Based on these studies, dielectrics such as polymer (the polyethylene family), germanium (Ge), gallium arsenide (GaAs), sapphire, quartz, and high-resistivity silicon (Si) have low absorption in THz. Many potential applications of these dielectrics for THz wave-guiding have been demonstrated [49- 71, 86- 88]. Regarding planar dielectric waveguides for mmW/THz, however, despite the achievements of the past two decades, some practical aspects have remained unaddressed. More research is required to realize novel dielectric waveguide structures which satisfy the following requirements:

- Low-loss supporting substrate
- High-precision, uniform, and low-cost fabrication technique
- Minimal need to manually assemble or align the sub-structures
- High-density integration and particularly ease of integration with active devices

In this Chapter, a low-loss silicon-on-glass (SOG) dielectric *ridge* waveguide is introduced for mmW integrated circuits. The proposed SOG technology is a promising solution to the aforementioned challenges. In the SOG dielectric waveguide structure, the guiding channel is made of high-resistivity Si and the glass plays the role of the *thick* cladding substrate. A high-precision and uniform fabrication technique which is fully compatible with the currently developed techniques for Si-device fabrication, is developed for the proposed waveguide structure. The fabrication technique eliminates the need for the excessively difficult and costly alignment of the sub-structures used in the conventional insulated

image guide [52]. The proposed SOG technique can serve as a platform for various types of mmW complex passive components and integrated circuits.

3.2 Material Characterization

Physical mechanisms determining the absorption characteristics of materials in the THz range are different from those in optics and microwaves. Consequently, some materials commonly used in the optical and microwave ranges of frequencies show high absorption at THz frequencies. However, there are remarkably transparent dielectric materials in the THz range [1].

A high dielectric constant in the main guiding region of the waveguide is highly advantageous as it provides strong field confinement within the waveguide, which consequently enhances the possibility of higher density circuit implementation. Among high dielectric constant materials commonly used for waveguide fabrication, intrinsic Si, sapphire, intrinsic Ge, alumina, and high-resistivity GaAs have been recognized for their low absorption at mmW/THz frequencies. Time-domain THz spectroscopy has been used to measure different materials' absorption coefficients and refractive indices in THz [76-85]. The reported measurment results based on this technique are summarized in Tables 3.1, 2. These studies show that crystalline high-resistivity Si is surprisingly transparent up to and beyond 3 THz [1, 81- 83].

Crystalline Si, whose electrical and mechanical properties have been extensively studied and reported, is the most important material in the THz spectrum. High-purity, float-zone crystalline Si is the most transparent and also the least dispersive medium at mmW/THz frequencies [1, 80- 83]. While early measurements of intrinsic Si had shown higher THz absorptions, recent experiments have concluded that previously reported absorption rates were dominated by free carriers due to residual impurities and are not the properties of intrinsic Si. Measurements of high-resistivity Si samples show that absorption is mainly due to free carriers and is dominantly controlled by carrier concentration. *High-purity* Si, produced by the float-zone crystal growth, has a remarkably low carrier concentration and consequently high resistivity. Measurements for float-zone, *high-resistivity* Si ($\rho > 10$ KΩ.cm), show a power absorption coefficient of less than 0.025 cm^{-1} up to 2 THz and less than 0.15 cm^{-1} up to 4 THz. These measurements demonstrate a remarkably constant refractive index of $n = 3.4175$ with small changes of 0.0001 over the entire 0.5-4.5 THz band [1, 81- 83].

High-purity float-zone Si wafers are available at low-cost. Furthermore, Si-device fabrication is a well-developed technology and numerous fabrication techniques are available for Si-devices [89- 92]. In this

research, Si wafers with high-resistivity ranging from 10 KΩ.cm to 20 KΩ.cm are used to implement the main guiding region.

Table. 3.1. Reported Measured Loss Characteristics of Dielectrics (data from [1, 78- 83]).

Dielectric material	Loss characteristic (unit)	Measured value	frequency
high-resistivity GaAs (ρ = 10 MΩ.cm)	power absorption coefficient (α, cm^{-1})	α = 0.2 / 0.4	0.25 / 0.5 THz
intrinsic Ge	power absorption coefficient (α, cm^{-1})	α > 0.5	0.2 – 2 THz
o-Sapphire	power absorption coefficient (α, cm^{-1})	α = 0.1 / 1	0.5 / 1 THz
e-Sapphire	power absorption coefficient (α, cm^{-1})	α = 0.1 / 1.1	0.5 / 1 THz
high-resistivity Si (ρ > 10 KΩ.cm)	power absorption coefficient (α, cm^{-1})	α < 0.025 / α < 0.15	0.1 - 2 / 0.1 - 4 THz
Alumina	loss tangent, tanδ	0.004 / 0.02	1 / 3 THz
	power absorption coefficient (α, cm^{-1})	254 / 3870	1 / 3 THz

Table. 3.2. Reported Measured Dielectric Constants (data from [1, 78- 83]).

Dielectric material	refractive index (n) / dielectric constant (ε_r)	frequency
high-resistivity GaAs	n = 3.59 - 3.61	0.3 - 2 THz
intrinsic Ge	n = 3.992 - 4.004	0.3 - 2 THz
o-Sapphire	n = 3.066 - 3.083	0.3 - 2 THz
e-Sapphire	n = 3.414 - 3.437	0.3 - 2 THz
high-resistivity Si	n = 3.41745 - 3.41755	0.5 - 4.5 THz
Alumina	n = 3.04 - 3.08	0.5 - 3 THz

State-of-the-art planar dielectric waveguide structures for mmW/THz are basically supported by metal ground planes [52, 59- 68]. These structures suffer from excessive attenuation due to the conduction loss and problems consequent to the manual alignment of sub-structures in integrated circuits. To overcome these challenges, in this research, a low-permittivity and low-loss dielectric substrate with the potential of bonding to Si is suggested. Different glass materials are studied for this purpose; among them, Pyrex 7740 is selected as the glass substrate of choice.

The THz absorption coefficient and refractive index spectra for different types of glasses have been derived using THz time domain spectroscopy [84, 85]. These glasses include amorphous silica, polycrystalline quartz, Pyrex, and different types of Schott glass such as BK7, B270, and NZK7. These

studies show higher refractive indices for these glasses in THz as compared to those seen in optics. Silica and quartz, which are actually two different compounds of silicon-dioxide with different fabrication processes, have fairly similar absorption and dispersion characteristics in the THz range. These two glasses have an almost constant refractive index of $n = 1.95$ in THz range and a power absorption coefficient which is less than 1.3 cm^{-1} up to 0.5 THz, reaching ~ 2.7 cm^{-1} at 1 THz. Pyrex's refractive index, which is $n = 2.1$, is almost constant with small variations of ± 0.05 over the THz range. Material loss in Pyrex is low up to about 200 GHz but increases rapidly above 200 GHz, reaching 7 cm^{-1} at 0.5 THz [85]. The Schott glasses investigated have higher absorptions than Pyrex, silica, and quartz [84, 85].

A comparison among the mentioned glass materials confirmed remarkably low THz absorptions for silica/quartz [85]. However, fabrication of the SOG waveguide using silica and quartz is much more challenging and, ultimately, quite costly. The main difficulty is the high complexity of the Si-quartz/silica bonding process which requires plasma assisted bonding techniques [93- 95].

The main difficulty in Si – quartz direct bonding is due to the difference in the thermal expansion coefficients of the two materials; quartz has a thermal expansion coefficient of 14.5 - 16.9 × 10^{-6}, while that of Si is 4.9 × 10^{-6} at 300 °C [93]. For high bonding strength, high temperature annealing is required. However, due to the large thermal expansion coefficient difference, the bonded wafers will break unless one of the wafers is thinned to a submicron thickness. Si – quartz direct bonding is performed through multiple time-consuming steps of low-temperature initial bonding, long-time storage at a constant temperature, and multi-temperature consecutive annealing with low temperature ramping rates (1 °C /min). This multi-step bonding process is performed over several days [94]. In order to achieve low-temperature and quicker Si - quartz direct bonding, oxygen plasma surface activation techniques has been used [95]. Oxygen plasma-assisted treatment increases the initial bonding strength by providing a highly hydrophilic and contamination-free contact surface due to the bombardment of energetic ions [95]. By using the plasma-assisted bonding technique, better bonding energies at lower bonding and annealing temperatures can be attained and the bonding time can be decreased to several hours (~ 10 hours) [95]. However, even with the plasma activation technique the bonding strength of Si - quartz is still lower than that of bonded Si – Pyrex wafers. Furthermore, plasma-assisted bonding needs to be performed in special advanced equipment which is not accessed in most laboratories.

Thin films of silica can be grown on Si surface via thermal oxidation methods. This is the method used to form thin layers of silicon-dioxide in silicon-on-insulator (SOI) technology, a well-developed

technology for optical integrated circuits and microchips. At optical wavelengths, the oxide layer is thick enough to act as a low-permittivity cladding layer. However, in the mmW/THz ranges a thin oxide layer is not sufficient due to the much longer wavelengths. Therefore, the main issue is that the growth of a large thickness of oxide film on the Si surface, required as a cladding layer at mmW/THz frequencies, becomes quite challenging.

Pyrex glass is a widely used substrate material in Si-based micro-electromechanical systems (MEMS) technology due to its attractive features and compatibility with Si for fabrication [96- 98]. The other desirable properties include optical transparency and electrical isolation. Pyrex's thermal expansion coefficient (2.9×10^{-6} / °C) is almost the same as that of Si (2.6×10^{-6} / °C) [96]. The other important advantage is that Pyrex is appropriate for bonding to Si via anodic bonding without using any intermediate adhesive. Si – Pyrex anodic bonding is a quick process (< 1 hour) and provides a strong connection between the two wafers [99- 103]. Pyrex and Si can be bonded permanently and hermitically through applying high voltage and temperature during the anodic bonding process. The sodium and oxygen ions in the Pyrex substrate become mobile under the high temperature (300 – 500 ℃). These mobile ions move toward the Si interface and form strong molecular Si-O bonds between the two wafers [99].

For the proposed SOG waveguide structure, considering mmW/THz transmission properties and fabrication feasibility, Pyrex is selected as the glass substrate. Up to 200 GHz, Pyrex substrate meets all the requirements in terms of transmission properties and fabrication simplicity.

3.3 Silicon-on-Glass Dielectric Waveguide Structure

The proposed SOG dielectric waveguide, as shown in Fig. 3.1, consists of a high-resistivity Si rectangular channel that forms the main guiding region of the waveguide. In order to support the Si guiding channel and to realize an integrated waveguide structure, the Si is attached to a low-loss and low-permittivity dielectric substrate. The large contrast between Si and Pyrex results in strong field confinement within the Si channel.

Si-based optical integrated circuits using SOI is a matured technology. At optical wavelengths, the oxide layer is thick enough to act as a low-permittivity cladding layer. In [105], an optical SOG dielectric waveguide based on Pyrex glass was reported for the purpose of realizing future waveguides with preprocessed claddings or ultrathin nano-sized Si waveguides. However, in mmW/THz frequency

ranges, due to the much longer wavelengths, a thin oxide layer cannot work as cladding and a thick glass substrate is needed to realize an effective cladding layer.

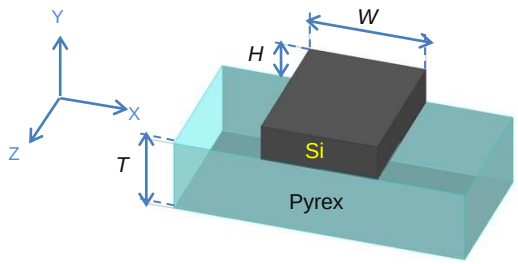

Fig. 3.1 Structure of the SOG dielectric waveguide made of the SOG wafer [104].

In the proposed SOG structure, a large thickness of Pyrex substrate makes it superior over other mmW dielectric waveguide structures which were basically supported on the metallic ground plane [52, 59-68]. In those structures, although the low-permittivity bonding insulator reduced the conduction and surface-roughness loss due to the ground plane to some extent, metallic loss still made a significant contribution to the total transmission loss. As the frequency increases, the skin depth decreases by a factor of $1/\sqrt{f}$ and metallic loss affects the guide performance more drastically.

The high permittivity of Si leads to strong field confinement inside the guiding channel. This large index contrast is essential to maintain low scattering (radiation) loss at the bends, to minimize the coupling between adjacent waveguides, and to support single-mode operation by an appropriate choice of the guiding channel dimensions. These properties make SOG technology appropriate for high-density integrated circuits. As a result, SOG provides a large index-contrast medium with minimal attenuation for mmW/THz signal propagation.

3.4 Computational Simulations and Studies

Modal analysis of the proposed SOG dielectric waveguide is conducted in high frequency structure simulator (HFSS). In all the simulated structures in this Chapter, the high-resistivity Si has a relative permittivity of $\varepsilon_r = 11.7$ and an equivalent conductivity of $\sigma = 0.01$ S/m. Pyrex's relative permittivity is $\varepsilon_r = 4.41$ while its loss characteristics vary with frequency.

From measured data collected via THz time domain spectroscopy [84], the equivalent conductivity of Pyrex is estimated as 0.02, 0.0987, 0.2508, and 0.4861 S/m at frequencies of 50 GHz, 100 GHz, 150 GHz, and 200 GHz, respectively. To extract Pyrex's equivalent conductivity from the measured absorption coefficient [85], the expression $\sigma = \alpha n / Z_0$, in which n, σ, α, and Z_0 are respectively the refractive index, the equivalent conductivity, the measured power absorption coefficient, and the air characteristic impedance, is used.

3.4.1 Modal Analysis

Fig. 3. 2 shows dispersion diagrams for the first four propagating modes of the SOG dielectric waveguide with dimensions W = 1.6 mm and H = 0.5 mm (Fig. 3.1). These modes are called E_x^{11}, E_y^{11}, E_x^{21}, and E_y^{21}, in which the superscripts indicate the numbers of cycles of variations along the x- and y-directions, respectively [106- 108].

Figs. 3.2 (a-b) respectively show the normalized phase constant (β/k_0), which is also referred to as the "effective refractive index" (n_{eff}), and the attenuation constant (dB/mm) diagrams for these modes. These four modes have cutoffs at frequencies of 56 GHz, 78 GHz, 92 GHz, and 105 GHz, respectively. The attenuation constant plots show that the loss is quite low even at high frequencies above 100 GHz. The attenuation constant of E_x^{11} mode decreases from 0.022 dB/mm at 60 GHz to 0.012 dB/mm at 120 GHz. This decrease is a result of better field confinement inside the Si channel as the frequency increases.

Studies of modal field distributions show that for the E_x (E_x^{nm}) modes, the transverse dominant component of the electric field is in the x-direction, while the other transverse component of the electric field is negligible everywhere except at the corners of the guiding channel. For the E_y (E_y^{nm}) modes, the transverse dominant component of the electric field is in the y-direction. The designation of the modes as E_x^{nm} and E_y^{nm} originates from the aforementioned facts.

Figs.3.3, 4 show the distributions of the electromagnetic field components of E_x^{11} and E_y^{11} modes at 110 GHz, for the SOG waveguide studied in Fig. 3.2. Fig. 3.5 shows the distributions of the dominant transverse electric field components of E_x^{21} and E_y^{21} modes at 110 GHz

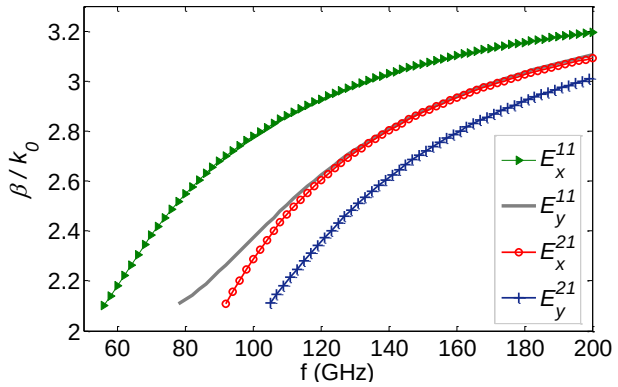

(a)

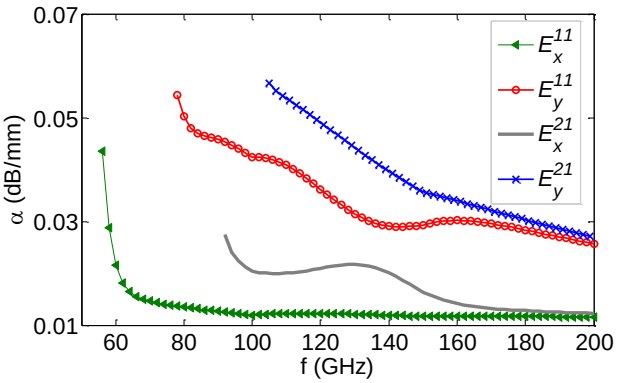

(b)

Fig. 3.2 Propagation constant of the SOG waveguide, (a) normalized dispersion (β/k_0) and (b) attenuation constant (dB/mm) [104].

For the abovementioned modes, the electromagnetic field components are oscillating inside the Si guiding channel and exponentially decaying in the outer region. The single mode operation extends over 56-78 GHz. Over the single-mode operation bandwidth, only the E_x^{11} mode has its energy confined inside the Si guiding channel while higher order modes are below the cutoff.

In the proposed SOG waveguide, depending on the Si channel dimensions, either the E_x^{11} or the E_y^{11} mode will be dominant. When W is greater than H, E_x^{11} will be the dominant mode, while a choice of W smaller than H makes the E_y^{11} mode dominant. In this thesis, only SOG waveguides with dominant E_x^{11} modes are studied; SOG dielectric waveguides with dominant E_y^{11} modes are studied in [109].

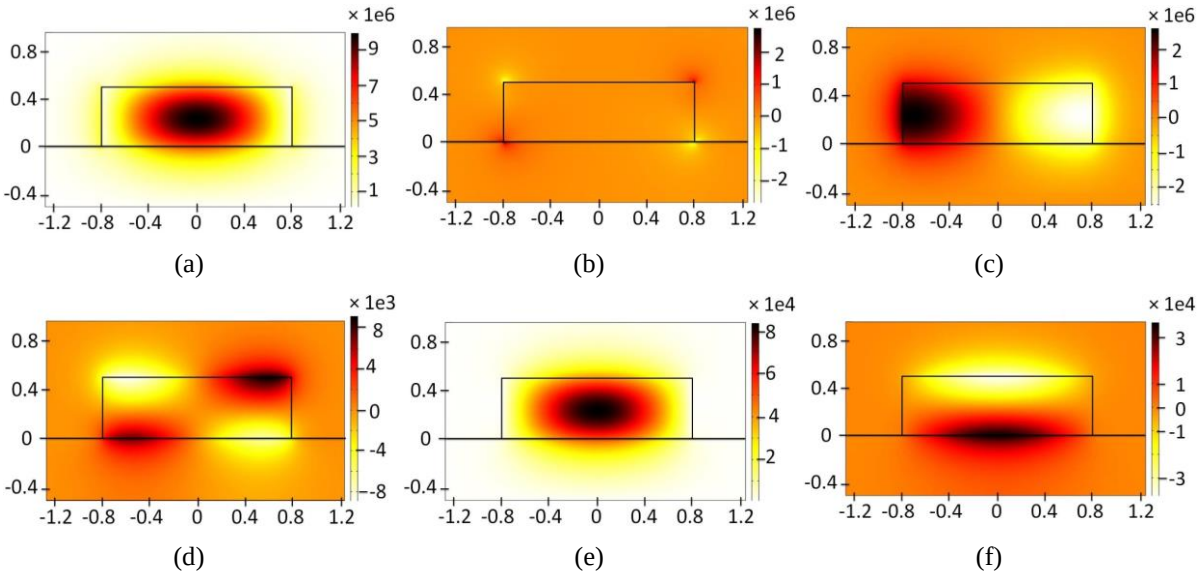

Fig. 3.3 Distribution of the electromagnetic field components of the E_x^{11} mode at 110 GHz: (a) E_x component, (b) E_y component, (c) E_z component, (d) H_x component, (e) H_y component, and (f) H_z component.

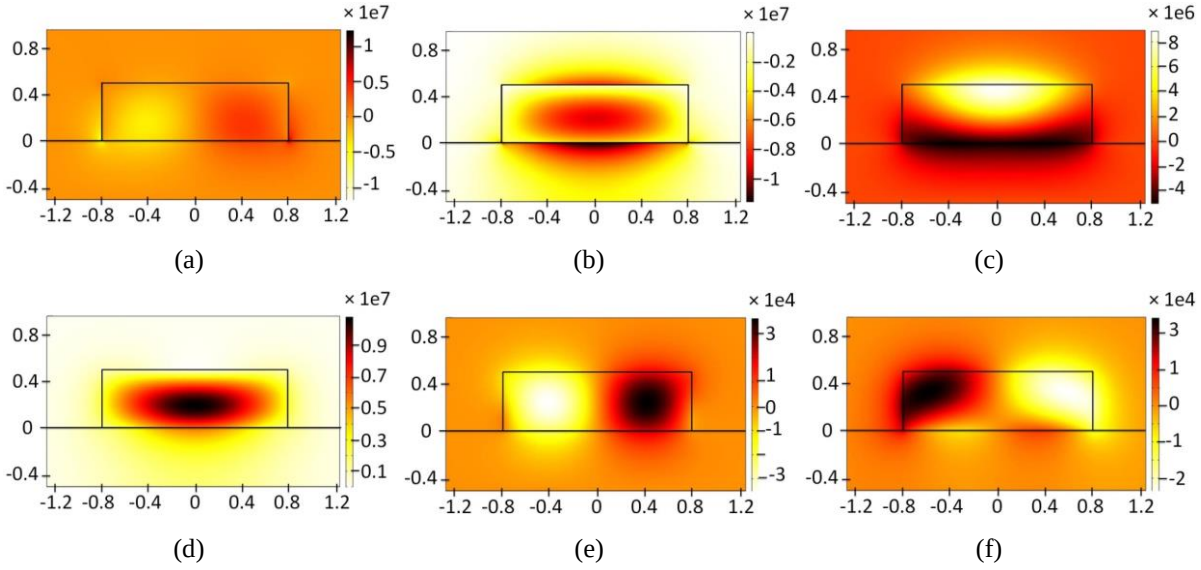

Fig. 3.4 Distribution of the electromagnetic field components of the E_y^{11} mode at 110 GHz: (a) E_x component, (b) E_y component, (c) E_z component, (d) H_x component, (e) H_y component, and (f) H_z component.

Fig. 3.5 Dominant transverse electric field component distribution at 110 GHz: (a) E_x of E_x^{21} mode and (b) E_y of E_y^{21} mode [104].

In the HFSS simulations, the Pyrex and air regions are truncated by PML (perfect matched layer) boundaries at appropriate distances from the guiding channel to model two cladding half-spaces. However, in reality the Pyrex substrate has finite dimensions. In the fabricated SOG test structures, the thickness of the Pyrex substrate is T = 0.5 mm and the waveguides are supported on test setups made of aluminum (Fig. 3.16).

To study the effect of the metal plane of the measurement setup on the propagation characteristics of the SOG waveguide, modal analysis simulations are conducted for two different structures: *I*) SOG waveguide on a Pyrex half-space, and *II*) SOG waveguide on a grounded finite-thickness Pyrex substrate. In these two structures, the guiding channel dimensions are W = 1.6 mm and H = 0.5 mm. In the second structure, the Pyrex substrate has a thickness of T = 0.5 mm and it is supported on a metal plane made of aluminum with a conductivity of $\sigma = 3.744\times10^7$ S/m. Fig. 3. 6 shows the propagation constants of the first four modes of these two structures for comparison.

In the first structure, where the Si channel is supported on a Pyrex half-space, the E_x^{11}, E_y^{11}, E_x^{21}, and E_y^{21} modes start at the frequencies of 56, 78, 92, and 105 GHz, respectively. However, in the second structure, the modes with oscillating (non-evanescent) field inside the glass substrate are also supported due to the total reflection at the glass-metal interface. As a result, the four modes mentioned for the first structure are also supported by the second structure, but with different cutoff frequencies of 42, 28, 52, and 60 GHz, respectively. It is interesting to note that similar modes are supported if the glass-metal interface is replaced by a glass-air interface. These modes have properties similar to those of the *cladding modes* in optical fibers [110].

The large index contrast between the Si channel and the surrounding media results in a strong field confinement inside the Si channel. This effect, along with the considerable thickness of the Pyrex

substrate, minimizes the effect of the metal plane on the propagation characteristics of the Si-confined modes. For a Si-confined mode, a large portion of the power propagates through the Si channel and only a small part goes through the substrate, the field amplitude being vanishingly small at the glass-metal interface.

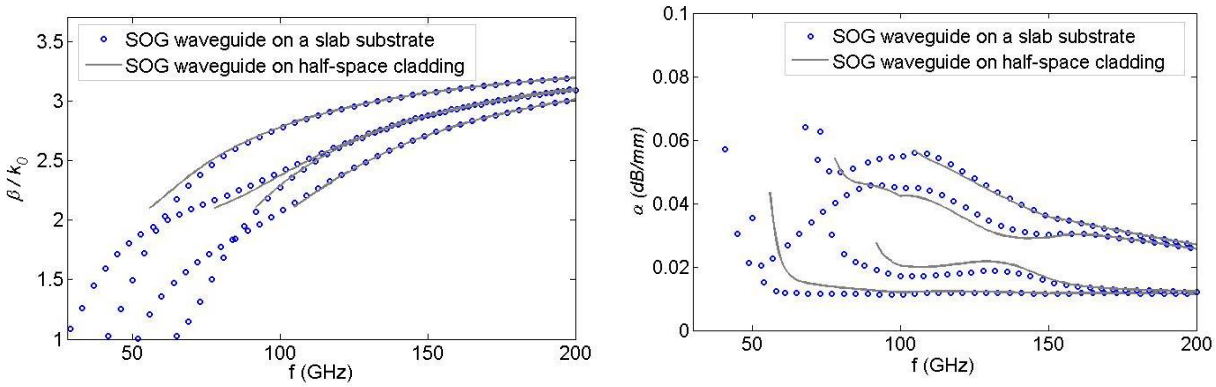

(a) (b)

Fig. 3.6 Propagation constants of two SOG structures: (a) normalized dispersion (β/k_0) and (b) attenuation constant (dB/mm) [104].

As the frequency increases above the cutoff frequencies of the Si-confined modes, the modal confinement inside the Si increases and the modal dispersion diagrams of the SOG waveguide on the finite-thickness Pyrex substrate approach those of the SOG waveguide on the Pyrex half-space. This property can be clearly observed in Fig. 3.6. However, higher order modes are supported in the actual SOG waveguide test structures. Additional attention should be applied during the test setup design to make sure undesired higher order modes are not excited.

It is worth mentioning that the ground plane below the glass substrate (Fig. 3.16) in the fabricated test structures is part of the measurement setup. For a number of applications under consideration, the proposed structure in packaged form does not need a ground plane. Non-metallic packaging for the proposed applications is under development.

3.4.2 Parametric Studies

To gain a deeper understanding of the SOG waveguide behavior and effect of different parameters on the dispersion characteristics, a modal analysis of SOG waveguides with different dimensions is performed in HFSS. Fig. 3.7 shows the dominant E_x^{11} mode cutoff frequencies for different height and width values of the Si channel in the SOG waveguide. As expected, by decreasing the Si-channel dimensions, the SOG waveguide operation bandwidth is shifted to higher frequencies. The cutoff frequencies are defined as the lowest frequencies where the field components are still exponentially decaying inside the Pyrex substrate. Above the cutoff frequency, the modal field is confined within the Si guiding channel.

Fig. 3.8 shows the attenuation constants of the SOG waveguides studied in Fig. 3.7, over their dominant E_x^{11} operation bandwidths. As shown in these figures, for a certain value of H, the attenuation constants of the SOG waveguides decrease by increasing W.

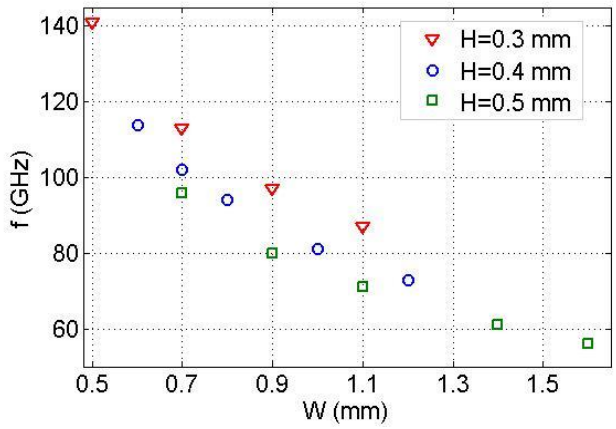

Fig. 3.7 Cutoff frequencies of the E_x^{11} dominant modes of the SOG waveguides [104].

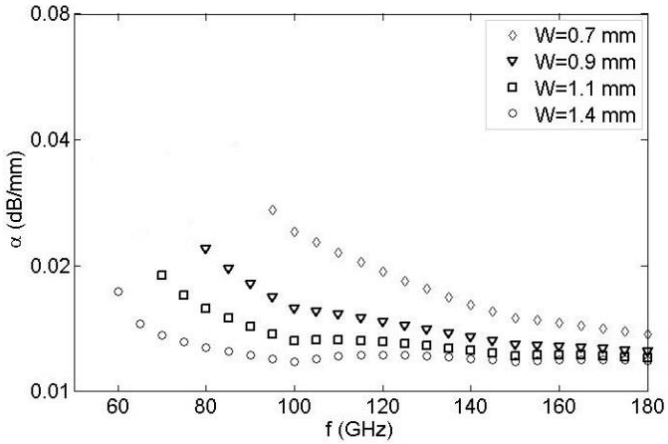

(a)

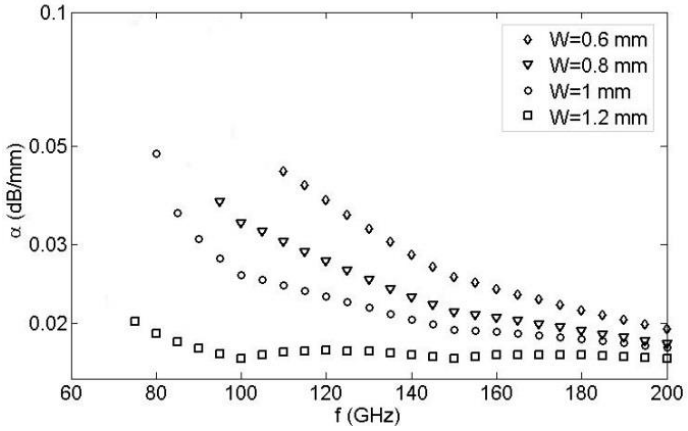

(b)

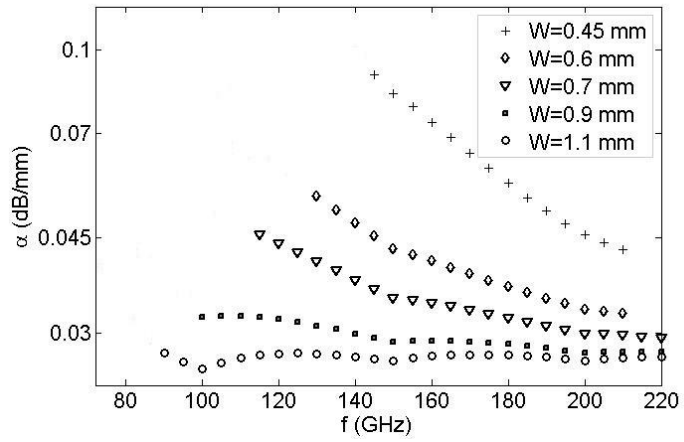

(c)

Fig. 3.8 Attenuation constants of the SOG waveguides E_x^{11} modes over their operation bandwidths for different values of W when: (a) H = 500 μm, (b) H = 400 μm, and (c) H = 300 μm [104].

3.5 Fabrication Technique

The main advantage of the proposed SOG technology, other than the low-loss materials used, is its high-precision which comes from photolithography process and deep reactive ion etching (DRIE) of Si. The fabrication method is a simple one-mask process, making it economically attractive. Furthermore, the fabrication technique provides wafer-scale batch fabrication, thus reducing the cost per component. The fabrication technique is discussed in this Section.

3.5.1 Process Flow

The entire process flow is shown in Fig. 3.9. The process starts with Pyrex 7740 and high-resistivity Si wafers. First, the surfaces of the wafers are cleaned to remove any organic residues and particles before the anodic bonding. The two wafers are cleaned using the Piranha process (H_2SO_4 / H_2O_2 4:1) at room temperature for 15 min. The SOG wafer is formed via anodic bonding between the Pyrex and Si wafers at a temperature of 450 °C and a bond voltage of 1000 volts. Anodic bonding provides a strong connection between the two wafers [99- 103].

The Si surface is coated with a thick photoresist (*AZ P4620*) using a spinner. The photoresist is spread for 10 seconds at a speed of 500 RPM, followed by a spin of 25 seconds at a speed of 2000 RPM. This results in uniform coverage of the photoresist with a thickness of ~ 11 μm. The photoresist is baked for 90 seconds on a hotplate at a temperature of 115 °C. This layer is then patterned via optical lithography to form a thick photoresist mask for dry etching of the Si layer. During this step, the photoresist coating is exposed to ultraviolet radiation (UV), which is passed through a glass-chrome mask. The pattern is projected on the photoresist and the exposed parts are removed via development in AZ 400K.

The selectivity of the etching process with respect to the masking photoresist is above 70. This high selectivity is appropriate to mask the guiding channel during a deep etching through the Si layer. Finally, DRIE utilizing a Bosch process (2 μm/min), will define the Si guiding channel. The remaining photoresist mask is removed in acetone. The fabricated wafer is then diced to test each individual component/circuit.

The Pyrex-Si bonding characteristics are highly desirable for eliminating the need for difficult and hugely time-consuming manual mounting and assembling of Si sub-structures on the glass substrate. Unlike previously reported integrated circuit techniques based on insulated image guides [52], in this case the Si wafer is first bonded to the Pyrex wafer and then high-permittivity passive components are made out of high-resistivity Si via DRIE through the Si layer. The entire integrated circuit pattern is

projected on the etching mask via the photolithography process. During the DRIE process, these Si components are masked against the plasma attack and supported on the glass substrate which, at the same time, acts as an etch stop.

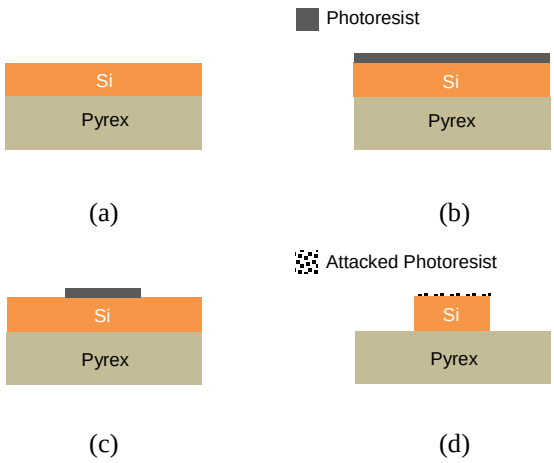

Fig. 3.9 Fabrication process of the SOG dielectric waveguide: (a) bonding Si to Pyrex, (b) coating photoresist on the Si surface, (c) optical lithography to form the mask, and (d) DRIE of the Si [104].

A unique advantage of the SOG technology developed here is that the manual and time-consuming alignment of the complex structures used in conventional image line fabrication [52], is replaced by a high-precision and uniform photolithography process. The designed prototype on the glass mask, including the arrangement of different fabricated structures as well as the alignment of the complex structures, is projected on the photoresist by a high-precision and uniform optical lithography process. The proposed SOG technology, which relies on the matured current Si-based fabrication techniques, provides ease of integration, high precision, and uniformity at low-cost. A wide variety of mmW integrated passive components are being developed in the proposed SOG platform via DRIE of the Si layer [109, 111- 114].

3.5.2 Fabrication Precision

The fabrication technique, developed in this technology, provides high-precision at low-cost. Scanning electron microscope (SEM) and microscopic images of the fabricated samples, shown in Figs. 3.11, 13, are analyzed to evaluate the dimensional accuracy and sidewall roughness.

Photolithography is a highly precise process capable of creating extremely small features down to a fraction of micron with exact control over the sizes and patterns. Fig. 3.10 shows the microscopic images of the thick photoresist mask on the Si surface. This mask is prepared for the fabrication of an SOG waveguide with W = 0.9 mm and the SOG tapered antenna. Figs. 3.10(a, b) show the measured width of the waveguide and the tip of the tapered section on the patterned mask, respectively. Fig. 3.10(c) shows the periodic beams connected to the SOG tapered antenna (presented in Chapter 6). As shown in these figures, the photoresist masks are patterned with high dimensional accuracy.

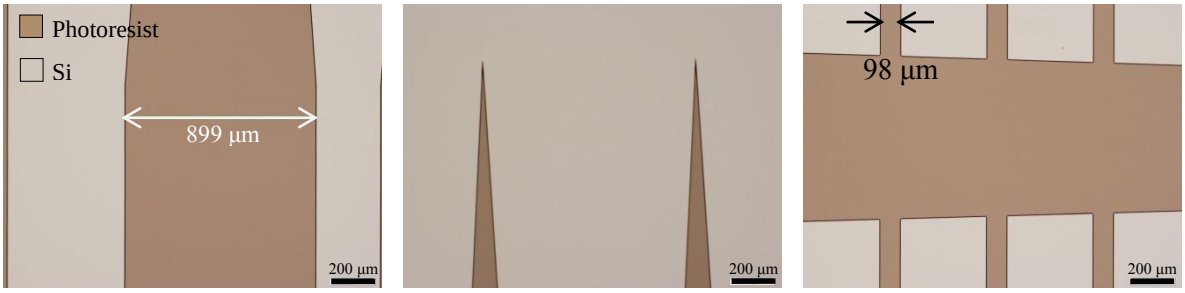

(a) (b) (c)

Fig. 3.10 Microscopic images of the patterned thick photoresist mask: a) beginning of the tapered section for an SOG waveguide with W = 900 µm, b) tip of the tapered section, and c) periodic beams with a designed width of 100 µm.

DRIE is a highly anisotropic etching process which can create closely vertical sidewalls with deep penetration and high aspect-ratios [115]. Fig. 3.11(a) shows the microscopic image of the top-view of the fabricated SOG waveguide with W = 0.7 mm. The measured width of this sample is 702 µm. Fig. 3. 11(b) shows the microscopic top-view image of the tips of the SOG waveguide tapered sections. As shown in this figure, the tapered tips are formed with high precision. Figs. 3.11(c- e) show SEM images of the SOG waveguides and tapered sections along with an SEM image of the etched sidewall of the sample. As shown in this figure, the etched sidewall has a roughness of around ~ 120 nm, which is quite small when compared to the dimensions of the fabricated sample.

As mentioned, the DRIE technique is capable of creating vertical etched walls. However, different physical phenomena affect the quality of the etched sidewalls during the process. One important factor affecting the fabrication accuracy is the notching effect. This effect is a phenomenon of through-etching of a Si layer supported on an insulating substrate (glass in this case) [116, 117]. This effect, which refers to the dependency of the etching rate on the aspect ratio, is a major problem with those etching

patterns which combine narrow and wide trenches. Under these conditions, ions passing to the insulating substrate through wider etched cavity electrically charge the insulating film increasing its potential. Consequently, successive ions are deflected by the induced potential toward the sidewalls of the Si cavity and start etching the sidewalls at the bottom of the Si structure, destroying the anisotropic nature of DRIE. This effect is shown in Fig. 3.12.

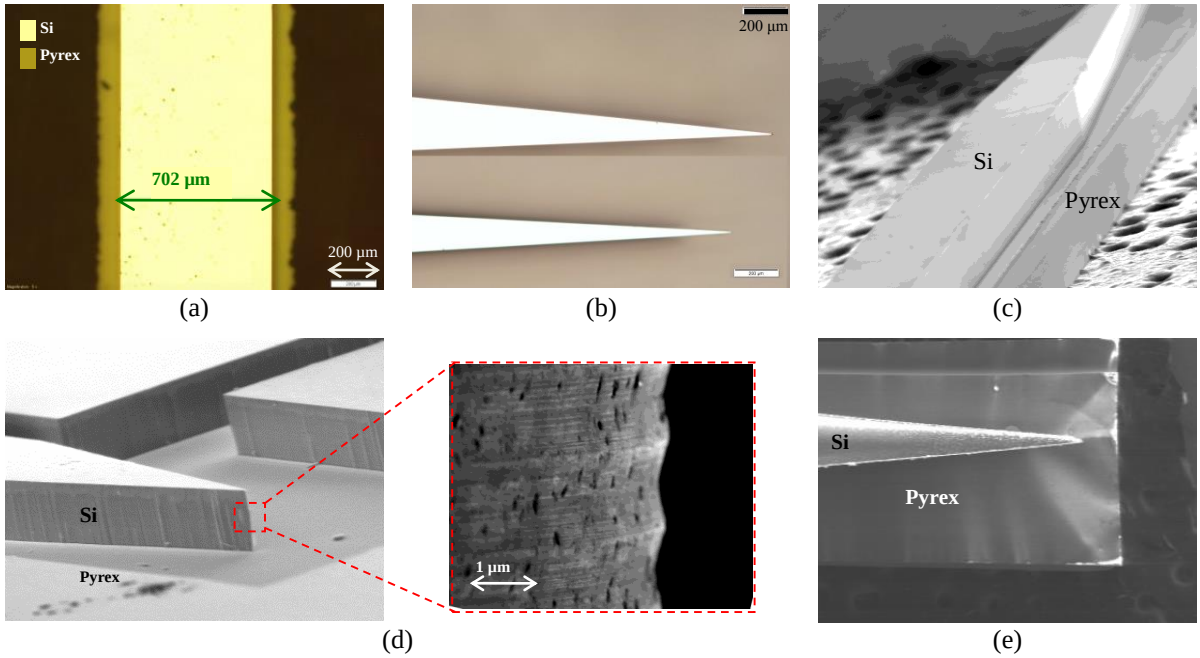

Fig. 3.11 Fabricated samples: (a) microscopic image of the top-view of the waveguide, (b) microscopic images of the etched SOG waveguides showing the Si tapered sections tips, c) SEM image of the SOG waveguide, d) SEM image of the etched SOG components showing the sidewalls and sidewall roughness, and (e) SEM image of the top-view of the tapered section [104].

In the proposed SOG waveguide structure, the etched patterns have dimensions in the same order of magnitude. In this case, as long as over-etching is prohibited, the notching effect should not be a major problem. The other difference is related to the electrical characteristics of the Si wafers used in this technology as compared to those of the Si wafers used in MEMS technology. The high-resistivity Si used in this research is a good insulator which changes the accumulation of charges during the etching process. To study the notching effect on the etching characteristics of the high-resistivity Si in the proposed SOG dielectric waveguide structure, SEM and microscopic images of fabricated samples,

shown in Fig. 3.13, are analyzed to evaluate the quality of the etched sidewalls and the etched angles with respect to the vertical case.

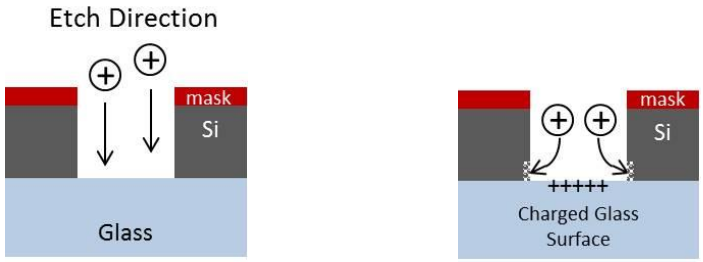

Fig. 3.12 Mechanism of the SOG notch effect (as depicted in SOG MEMS technology using low-resistivity Si).

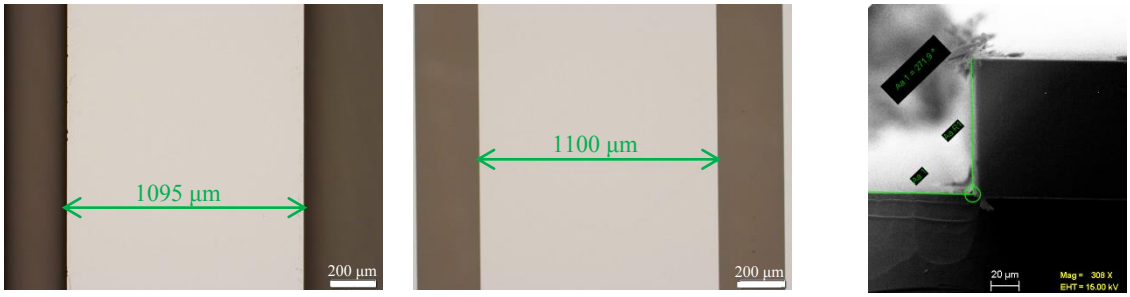

(a) (b) (c)

Fig. 3.13 Fabricated sample: (a, b) microscopic image of the SOG waveguide with W = 1100 µm, (a) top-view (Si side) and (b) bottom-view (glass side), c) SEM image of the etched sidewall measuring the etched sidewall angle.

Fig. 3.13(a, b) shows the microscopic images of the fabricated SOG waveguides with W = 1100 µm and H = 400 µm. These figures show the measured widths of the Si guiding channel from the top (Si side) and bottom (glass side), respectively. As shown in these images, the difference is quite small at ~ 5 µm, which with considering a height of 400 µm etching, shows an angle of ~ 89 ° for the etched sidewalls. Fig. 3.13(c) shows the SEM image of the etched Si sidewall supported on the Pyrex substrate. The measured angle of the Si sidewall is 90°.

3.5.3 Fabrication Error Tolerances

To study the effect of the sidewall roughness on the propagation characteristics of the SOG waveguide, modal analysis has been performed for the waveguide dimensions W = 0.7 mm and H = 0.5 mm. The

Groisse model in HFSS, with a 200 nm surface roughness on the Si channel sidewalls, is used in this study. A comparison between the attenuation constants for two different cases of the waveguides with smooth sidewalls, and with sidewalls having a 200 nm roughness, shows that the increase in the waveguide attenuation due to the surface roughness, over 140 - 170 GHz is negligible. As mentioned previously, the etched sidewalls are very close to 90 ° and high dimensional accuracies are provided by the fabrication technique.

3.6 Coupling Characteristics

In the proposed SOG technology, the modal confinement inside the Si guiding channel is strong due to the high permittivity of the Si guiding channel as compared to that of the surrounding media. This is a huge advantage as it reduces the radiation loss at the bends and reduces the coupling of the adjacent waveguides. Several SOG bend structures and a power divider with dominant E_y^{11} mode operation were designed over W band (140 - 220 GHz) in [109].

To study the coupling, the modal characteristics of two adjacent Si guiding channels, as shown in Fig. 3.14, are studied and compared with those of a single Si guiding channel; both structures are supported on glass substrates. The Si channels' dimensions are H = 500 μm and W = 1.6 mm. The normalized phase constants of the two *even* and *odd* modes of the two coupling channels, and that of the dominant E_x^{11} mode of the single channel, are shown in Fig. 3.15 for different values of the distance between the two coupled Si guiding channels (d_c).

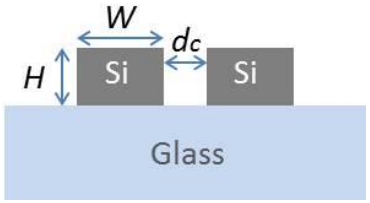

Fig. 3.14 Coupled SOG waveguides [104].

As shown in this figure, the phase constants of the three modes are close to each other and become even closer by increasing the coupling distance. At coupling distances greater than $d_c > 800$ μm, the differences among the three graphs are negligible. This confirms the weak coupling between the two adjacent waveguides at these distances.

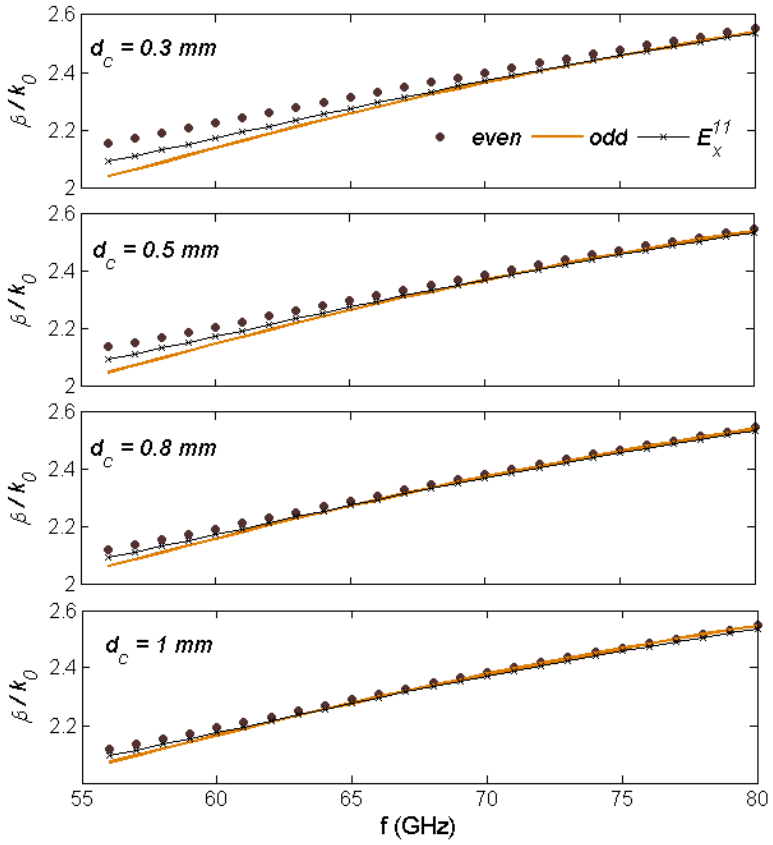

Fig. 3.15 Normalized phase constants of even and odd modes of two adjacent Si channels at a distance of d_c and dominant E_x^{11} mode of a single Si channel with the same dimensions [104].

3.7 Experimental Verification

To experimentally verify the performance of the proposed SOG dielectric waveguide, a number of test devices are designed, fabricated, and measured. The measurements are performed using a PNA-X made by Keysight (former Agilent) Technologies Inc., with standard rectangular waveguide ports.

3.7.1 Measurement Setup Design

A test setup, consisting of an aluminum case with rectangular waveguide sections connected to the ports of the network analyzer, is developed. The test setup, as shown in Fig. 3.16, includes transitions from standard rectangular waveguides to the proposed dielectric waveguide, using tapered sections of the Si channel inside the rectangular waveguide sections.

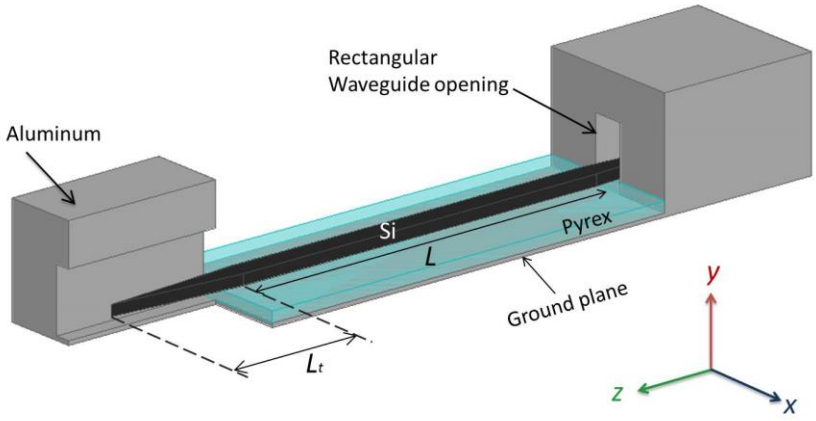

Fig. 3.16 Test structure [104].

As shown in Fig. 3.16, to excite the dominant E_x^{11} mode, rectangular waveguides are rotated by 90 °. The dominant TE_z^{01} mode in the rectangular waveguide has sinusoidal variation along the *y*-direction and no variation along the *x*-direction. Maximum coupling occurs when the Si guiding channel is centered inside the rectangular waveguide. This can be achieved either by adjusting the level of the ground plane below the SOG dielectric waveguide or with an appropriate choice of thickness for the Pyrex substrate below the Si. To gradually confine the field inside the Si, the Si guiding channel is tapered inside the rectangular waveguides in the *x*-direction.

The state-of-the-art mmW dielectric waveguide structures are mostly image guides for which the guiding channels were simply tapered inside the metallic waveguide while the metallic wall of the rectangular waveguide worked as the ground plane [59]. In [118], transitions from layered ridge dielectric waveguides to rectangular metallic waveguides are discussed. In their reported structure all dielectric layers were tapered inside the metallic waveguide. In this thesis, to improve the transmission characteristics of the transition from the rectangular waveguide to the SOG dielectric waveguide, the idea of etching parts of the Pyrex substrate below the Si tapered sections is proposed and implemented. Hydrofluoric acid (HF, 49 %) wet etching with a chromium/gold (50/1000 nm) mask is used to etch the Pyrex wafer before bonding to Si. The details of the fabrication are provided in Chapter 4.

Fig. 3.17 shows part of the fabricated SOG wafer before dicing. As shown in this figure, parts of the Pyrex substrate below the tapered sections are etched up to a height of 100 µm. The wafer is then diced and is ready for testing each individual waveguide. The paths along which the wafer is diced in *x*- and *z*- directions are shown with dashed lines. Dicing along the *x*-direction is performed from the Pyrex

side to an appropriate height so that the etched parts of the Pyrex substrate are totally removed from below the tapered sections.

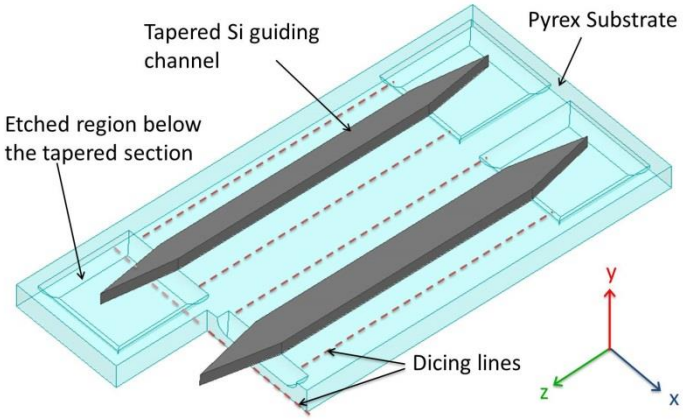

Fig. 3.17 Fabricated SOG substrate before dicing [104].

Simulations are conducted in HFSS to show the effects of removing the Pyrex substrate on the coupling characteristics of the transition. The (back-to-back) transition from the standard WR10 waveguide to the SOG waveguide and back again to the rectangular waveguide, as illustrated in Fig. 3.16, is simulated for four different structures: Structure *A*, Structure *B*, Structure *C*, and Structure *D*. In all of the structures, the SOG waveguide has dimensions $W = 1.1$ mm and $H = 0.5$ mm. The length of the SOG waveguide between the two tapered sections is $L = 19$ mm and the tapered sections are $L_t = 6.3$ mm long each. In Structures *A* and *B*, as illustrated in Fig. 3.18(a), Pyrex is removed from below the tapered sections and $T = 1$ mm and $T = 0.5$ mm, respectively. In Structures *C* and *D*, as illustrated in Fig. 3.18 (b), the Pyrex substrate is not etched and $T = 1$ mm and $T = 0.5$ mm, respectively.

As the simulated plots in Fig. 3.19 show, etching the Pyrex substrate decreases the insertion loss of the transition significantly. Structures *A*, *B*, *C*, and *D* show average insertion losses of 0.71 dB, 0.82 dB, 5.93 dB, and 4.44 dB, respectively, over the entire 90 - 110 GHz band. In Structure *A*, a choice of $T = 1$ mm adjusts the Si channel centered inside the rectangular waveguide and improves the coupling behavior of the transition to a greater extent than Structure *B*. As the frequency increases, the proposed modifications have more significant effects on improving the coupling characteristics of the transition. An investigation of $|S_{11}|$ shows that etching the Pyrex makes a significant improvement in the return

loss as well. While the return loss in Structure *C* reaches 8.8 dB, in Structure *A* it is always better than 25 dB.

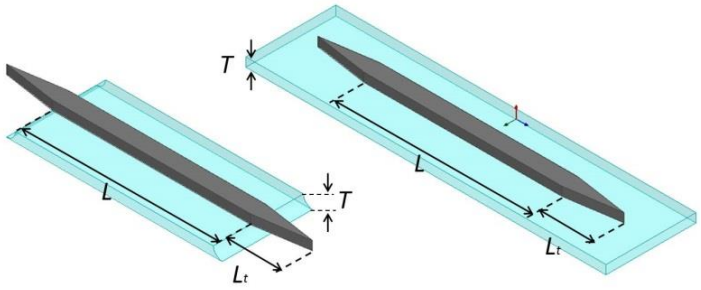

(a) (b)

Fig. 3.18 SOG tapered waveguides: (a) Structures *A* and *B* and (b) Structures *C* and *D* [104].

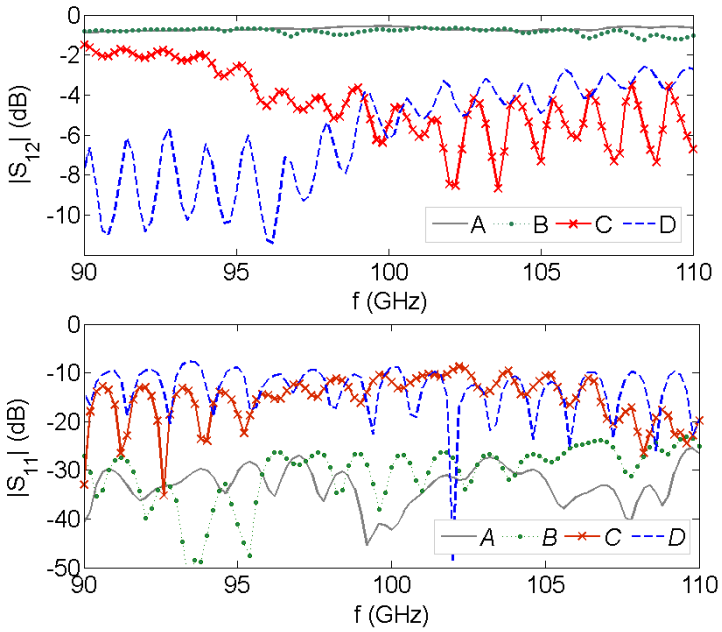

Fig. 3.19 Simulated scattering parameters of the back-to-back transitions from WR10s to the SOG waveguides for four different transition structures [104].

Fig. 3.20 shows the magnitude of the electric field at 100 GHz for a specific time instant on the *y*-*z* plane bisecting the transitions in Structures *A* and *C*. This figure shows the tapered sections and 4.5 mm lengths of the SOG waveguides. In Figs. 3.20(a - b), cross sections *a* show the tapered sections'

beginnings where they connect to the waveguides. As these images show, the field close to the tapered section in Structure *A* is more confined than that of Structure *C*.

The maximum field in the middle of WR10 efficiently couples to the Si guiding channel as the beginning of the tapered section is approached without any disturbance due to the Pyrex. Fig. 3.20(c) shows the field in Structure *A*, over different cross sections indicated with dotted lines in Fig. 3.20(b). These images, from right to left, show the field over cross sections passing through the tip of the tapered section, the middle of the tapered section, the rectangular waveguide opening, and at a distance of 4.5 mm along the waveguide section, respectively.

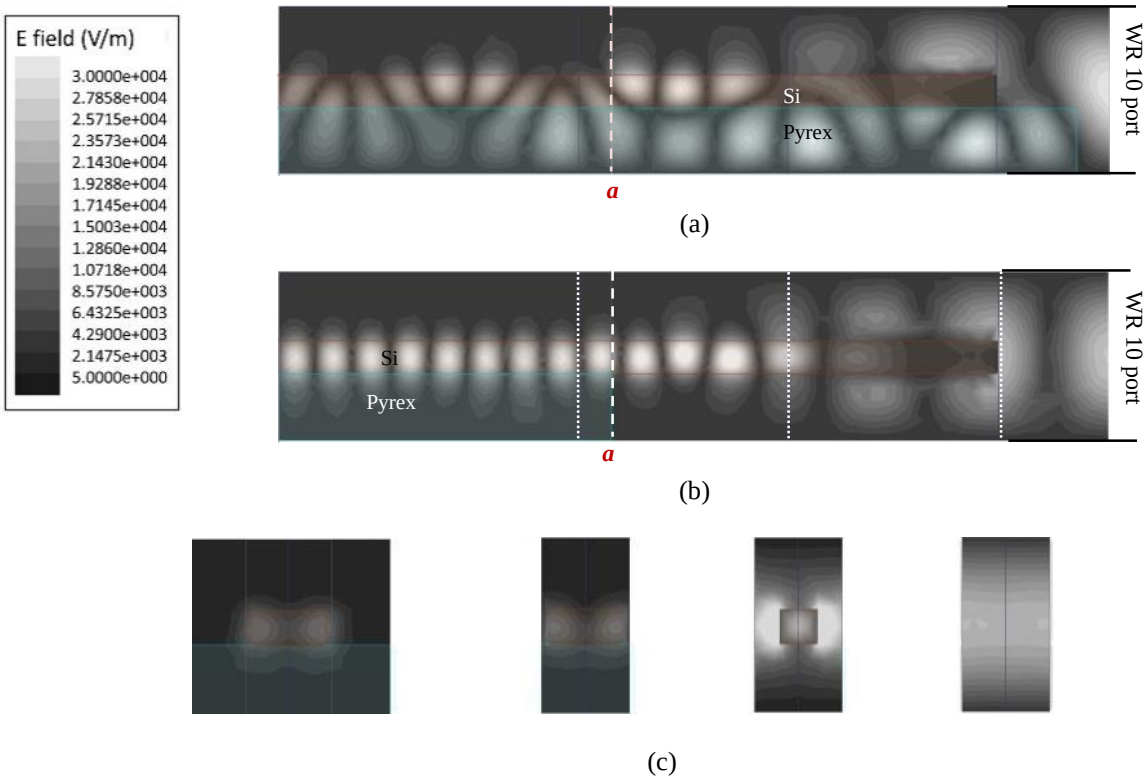

Fig. 3.20 (a, b) Field distribution on the *y*-*z* plane bisecting the tapered section and SOG waveguide: (a) in Structure *C*, (b) in Structure *A*, (c) field distribution at different cross sections of Structure *A* indicated with dotted lines [104].

To make sure higher order modes are not excited by the transition, half of the test structure shown in Fig. 3.16, is simulated in HFSS. The resultant generalized scattering parameters show that the coupling to the higher order modes is negligible and below - 20 dB.

3.7.2 Measurement Results

Three SOG waveguides with dimensions of $T = 0.5$ mm, $H = 0.5$ mm, and widths of $W = 1.6$ mm, $W = 1.1$ mm, and $W = 0.7$ mm, are tested over frequency ranges of 55 - 65 GHz, 90 - 110 GHz, and 140 - 170 GHz, respectively. In order to obtain the dominant mode dispersion characteristics from the measurement results, two different lengths of the mentioned SOG waveguides are fabricated and characterized. The fabricated waveguides are shown in Fig. 3.21. Figs. 3.22-24 show the simulation and measurement results of the (back-to-back) transitions from the standard rectangular waveguides to the fabricated SOG waveguides.

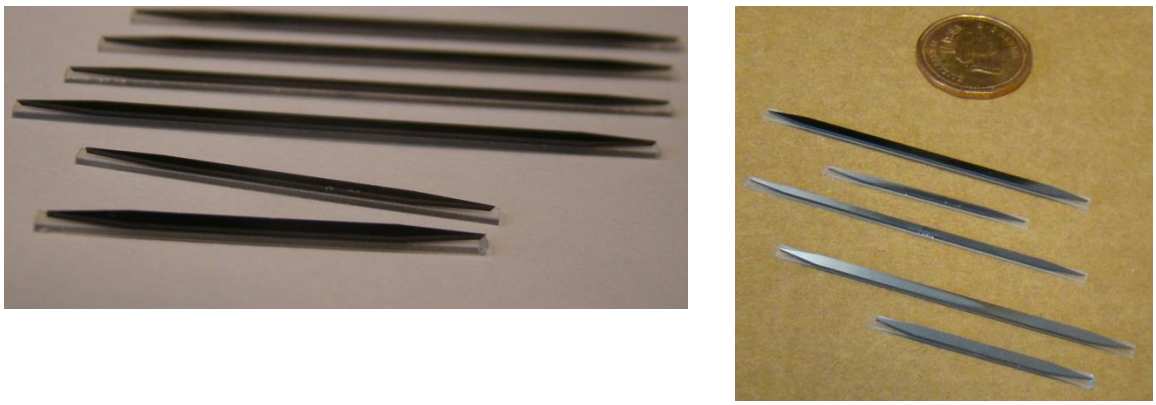

Fig. 3.21 Fabricated SOG waveguides with $W = 1.6$ mm.

Fig. 3.22 shows the scattering parameters of the back-to-back transition from WR15 to the SOG waveguide with $W = 1.6$ mm, for a length of $L = 18.2$ mm of the SOG waveguide between the two transitions, over 55 - 65 GHz. As mentioned earlier, etching the Pyrex below the tapered sections improves the coupling characteristics of the transition significantly as the frequency increases above 80 GHz. The effect is insignificant at lower frequencies. In the case of the waveguide structures with $W = 1.6$ mm, the Pyrex substrates extend below the tapered sections and are cut uniformly along the structures with widths slightly smaller than the width of the WR15 (Fig. 3.21). As shown in Fig. 3.22, the measured return loss is better than 16 dB over the entire band and the insertion loss varies between 1.8 dB and 2.8 dB. The HFSS simulated insertion loss is less than 1.1 dB. The main source of the small disagreement between the simulated and measured scattering parameters is the error in aligning the

SOG waveguide tapered sections inside the rectangular waveguides. The effect of this misalignment is discussed in the following Section. Misalignment between the rectangular waveguide sections of the test setup and those of the network analyzer, as well as the surface roughness of the rectangular waveguide sections of the test setup, also contribute to the disagreement between the results. The other source of discrepancies between the results is the power leakage at the discontinuities of the connections between the metallic ports of the PNA-X and those of the test setup.

The measured results for a length of 38.2 mm of the same waveguide show an average difference of 1.18 dB between the insertion losses of the two waveguides over the entire 55 - 65 GHz band. An average attenuation constant of 0.59 dB/cm is estimated from the aforementioned difference. In the fabricated structures with $W = 1.1$ mm and $W = 0.7$ mm, the Pyrex substrate is 1 cm wide and is removed from below the tapered sections. Fig. 3.23 shows the results for the SOG waveguide with $W = 1.1$ mm excited with WR10 ports. Measurement results show an insertion loss varying between 1.90 dB and 2.61 dB for a length of $L = 19$ mm, and between 1.67 dB and 2.42 dB for a length of $L = 9$ mm. As shown in Fig. 3.23, the difference between the two measured insertion losses for the two different lengths is quite small. The average difference between the two results over the entire band is only 0.27 dB. A small average attenuation constant of 0.27 dB/cm is estimated from this difference.

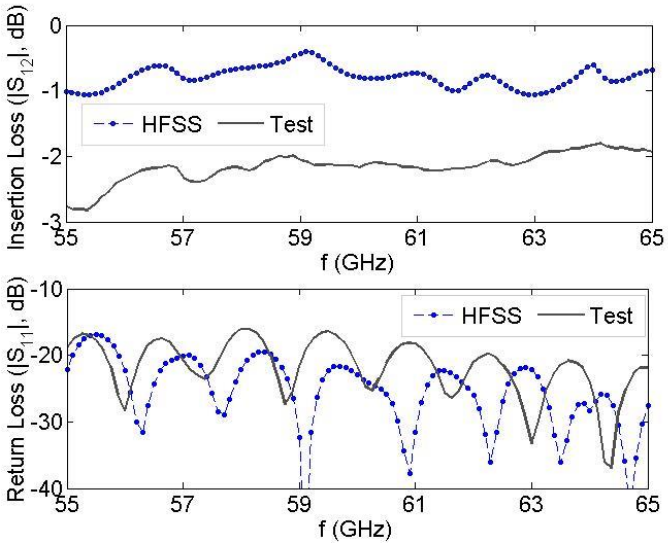

Fig. 3.22 Simulated and measured scattering parameters of the back-to-back transition from WR15 to the SOG waveguide with $W = 1.6$ mm [104].

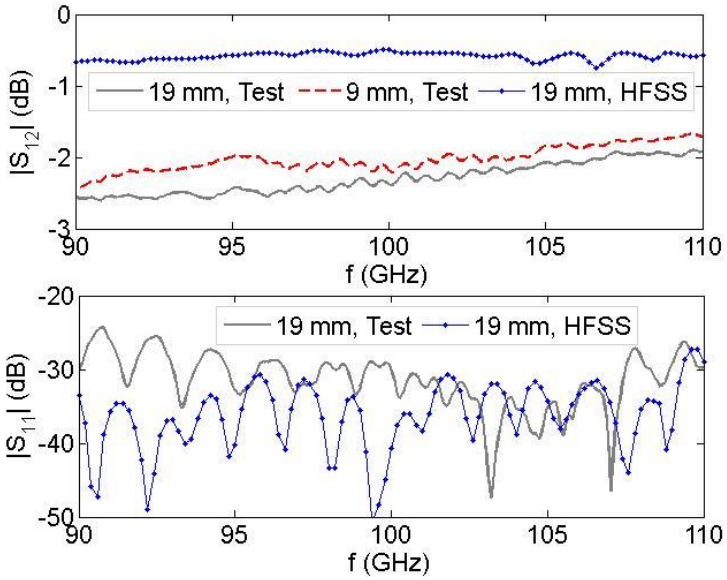

Fig. 3.23 Simulated and measured scattering parameters of the back-to-back transition from WR10 to the SOG waveguide with W = 1.1 mm [104].

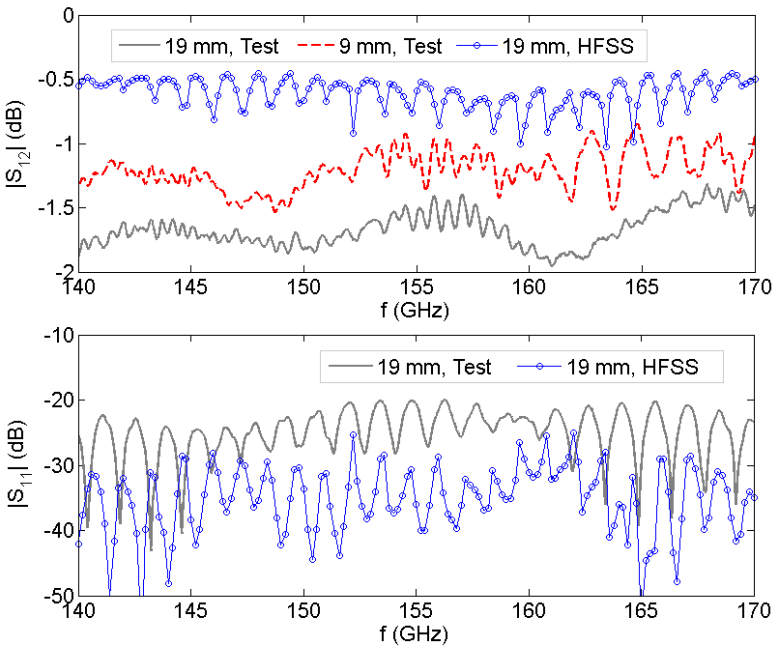

Fig. 3.24 Simulated and measured scattering parameters of the back-to-back transition from WR6 to the SOG waveguide with W = 0.7 mm [104].

Two SOG waveguides with $W = 0.7$ mm in two different lengths were measured using WR6 ports. The measured scattering parameters, represented in Fig. 3.24, show that the insertion loss varies between 1.32 dB and1.95 dB for $L = 19$ mm, and between 0.85 dB and 1.54 dB for $L = 9$ mm. For these structures, the average difference between the two measured insertion losses is quite small and equal to 0.46 dB over the frequency range of 140 - 170 GHz. The main sources of the discrepancies between the simulated results and measured data are the lateral, axial, and angular misalignments of these SOG waveguide structures inside the test setups.

3.7.3 Study of the Misalignment Effect

As shown in Fig. 3.21, in the SOG waveguides with $W = 1.6$ mm, the Pyrex substrates extend below the tapered sections with a width smaller than that of the metallic waveguide ports. The misalignment can be related to the SOG waveguide structure being slightly shifted along the *z*-axis from a centered position. The other source of error is possibly the fact that the Pyrex substrate is not uniformly attached to the ground plane. Three typical cases of misalignment are studied in Fig. 3.25. This figure shows the scattering parameters of the back-to-back transitions from the rectangular waveguide to the SOG waveguide with a length of $L = 18.2$ mm between the two transitions for the misalignment cases mentioned in Table 3.3, compared with the aligned case.

Table. 3.3. Misalignment cases studies in Figs. 3.25-27.

$W = 1.6$ mm, studied in Fig. 3.25	
Misaligned 1	Displacement of 500 μm along the *z*-axis
Misaligned 2	The waveguide is not parallel to the ground plane by 3 °
Misaligned 3	The waveguide is not parallel to the ground plane by 3 ° and is shifted by 800 μm along the *z*-axis
$W = 1.1$ mm, studied in Fig. 3.26	
Misaligned 1	Displacement of 800 μm along the *z*-direction
Misaligned 2	Displacement of 100 μm along the *x*-direction
$W = 0.7$ mm, studied in Fig. 3.27	
Misaligned 1	Displacement of 80 μm along the *x*-direction
Misaligned 2	Displacement of 200 μm along the *z*-direction
Misaligned 3	0.5 ° angular misalignment with respect to the *z*-axis

As shown in this figure, for the SOG waveguide with W = 1.6 mm, a lack of parallelism with the ground plane is the main source of the deviations of the scattering parameters of the misaligned waveguides from those of the aligned waveguide. Simulations demonstrate that an axial misalignment of 0.8 mm along the z-axis, combined with a lack of parallelism between the Pyrex substrate and the ground plane by an angle of 3 °, increases the insertion loss by 0.9 dB on average over the entire band.

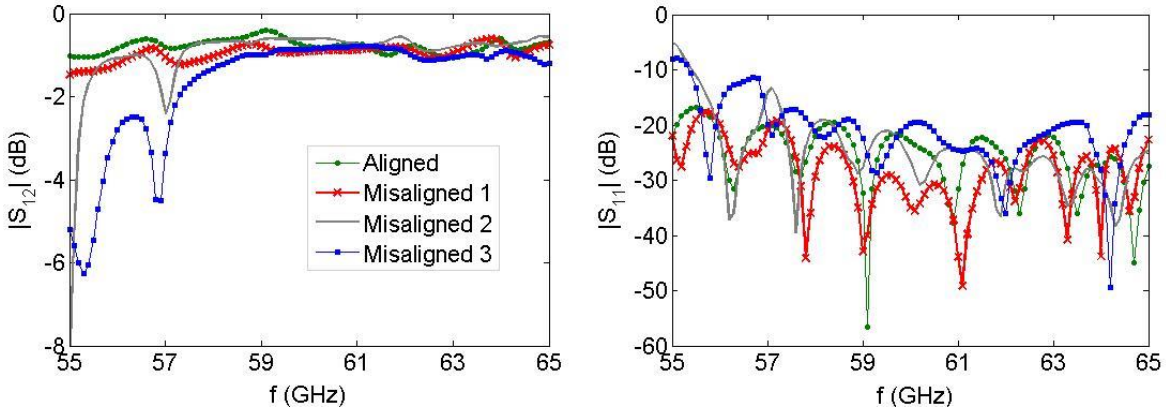

Fig. 3.25 Scattering parameters for the SOG waveguide test structure with W = 1.6 mm and L = 18.2 mm when the SOG waveguide is misaligned inside the test setup.

The simulation results for two typical misalignment cases for a length of L = 19 mm of the SOG waveguide with W = 1.1 mm are shown in Fig. 3.26. The studied misaligned cases are summarized in Table 3.3. Simulations confirm that a displacement of 80 µm along the x-axis for the SOG waveguide with W = 1.1 mm, increases the insertion loss by an average of 0.25 dB over the entire band. A misalignment of 200 µm along the z-axis degrades the insertion loss by 0.2 dB on average.

The simulation results for three typical misalignment cases for a length of L = 19 mm of the SOG waveguide with W = 0.7 mm are shown in Fig. 3.27. The studied misaligned cases are summarized in Table 3.3. According to the simulations, a displacement of 80 µm along the x-axis for the SOG waveguide with W = 0.7 mm increases the insertion loss by an average of 0.25 dB over the entire band. A misalignment of 200 µm along the z-axis degrades the insertion loss by 0.2 dB on average and an angular misalignment of 0.5 ° with respect to the z-axis increases the average insertion loss by 1.2 dB over 140 - 170 GHz.

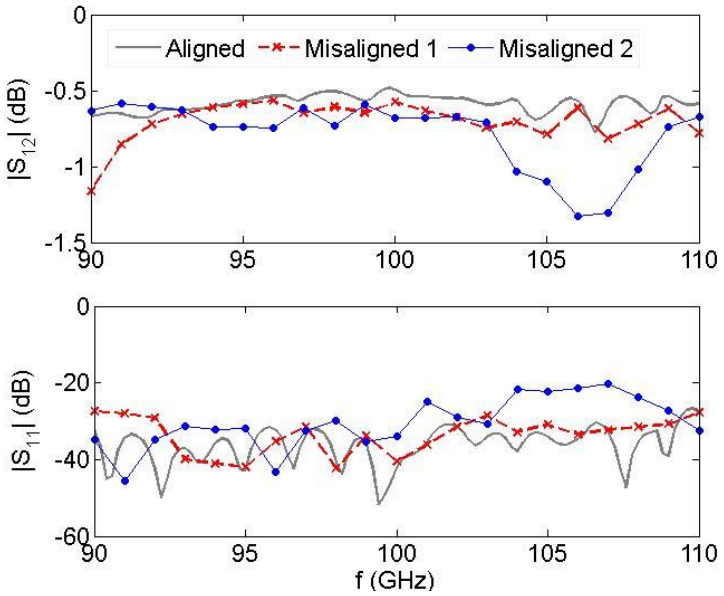

Fig. 3.26 Scattering parameters for the SOG waveguide test structure with W = 1.1 mm and L = 19 mm when the SOG waveguide is misaligned inside the test structure.

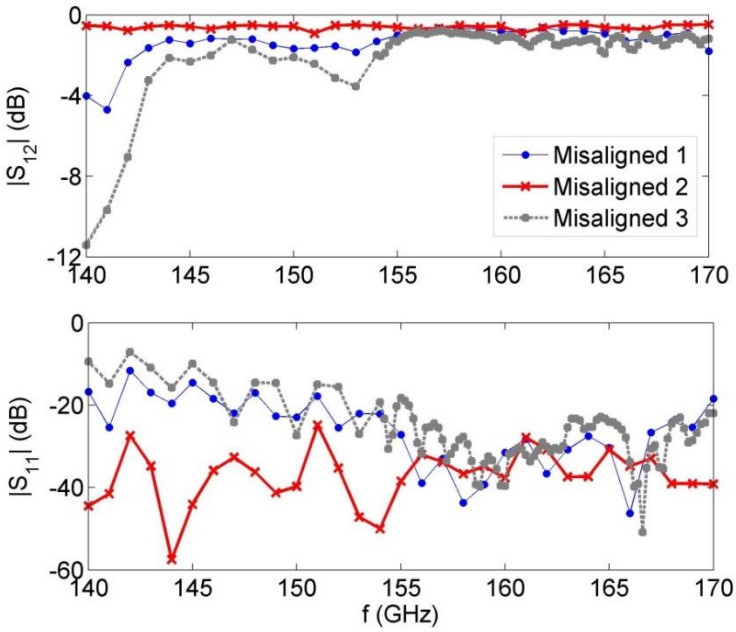

Fig. 3.27 Scattering parameters for the SOG waveguide test structure with W = 0.7 mm and L = 19 mm when the SOG waveguide is misaligned inside the test structure.

It is worth mentioning that the misalignment of the SOG waveguide tapered sections inside the rectangular waveguide ports is mainly due to the fact that the test instrument has rectangular waveguide ports. The ultimate objective of the proposed technology is to integrate the entire system, including the coupling to the active devices and antenna on one substrate without any rectangular waveguide interconnections.

3.7.4 Extracting the Propagation Constant

The de-embedding method described in [119] is used to obtain the dispersion diagrams from the measured data. Using this method, the attenuation constant of the SOG waveguide is determined from measurements of two different lengths of the waveguide. This helps to de-embed the effects of mismatch and higher-order modes excitation at the feed point discontinuity. The de-embedded parts include the rectangular waveguide ports and tapered sections as well as the waveguide sections, which contain higher order modes.

Suppose T_1 and T_2 are the transmission matrices of the two measured setups, then:

$$T_i = T_x \, T_{Li} \, T_y \text{ (i = 1 and 2)} \tag{3.1}$$

where the de-embedded sections have transmission matrices T_x and T_y, and T_{Li} is the transmission matrix of the length L_i of the single-mode waveguide section between the two de-embedded sections, defined as:

$$T_{Li} = \begin{bmatrix} e^{-\gamma L_i} & 0 \\ 0 & e^{+\gamma L_i} \end{bmatrix} \tag{3.2}$$

in which $\gamma = j\beta + \alpha$ is the waveguide dominant mode propagation constant. Multiplying T_2 by the inverse of T_1, the following equation is derived:

$$T_2 \, T_1^{-1} = T_x \, T_{L21} \, T_x^{-1} \tag{3.3}$$

in which:

$$T_{L21} = \begin{bmatrix} e^{-\gamma (L_2 - L_1)} & 0 \\ 0 & e^{+\gamma (L_2 - L_1)} \end{bmatrix} \tag{3.4}$$

Matrices $T_2 \times T_1^{-1}$ and T_{L21} have equal eigenvalues from which the waveguide complex propagation constant is derived. Fig. 3.28 shows the propagation constant of the proposed dielectric waveguide, derived from the measured results and compared with full-wave simulations.

Fig. 3.28(a) shows the attenuation constant and the normalized phase constant of the SOG waveguide with $W = 1.6$ mm. There is excellent agreement between the simulated and measured dispersion plots with a maximum deviation of 0.015 in the normalized phase constant at 65 GHz. For this waveguide, the simulated attenuation constant is less than 0.02 dB/mm over the entire band of 55 - 65 GHz and the measured attenuation constant varies between 0.05 dB/mm and 0.084 dB/mm with an average of 0.063 dB/mm.

Fig. 3.28(b) shows the attenuation constant extracted from the measurements of the SOG waveguides with $W = 1.1$ mm compared with the simulation results. For this waveguide, the maximum simulated attenuation constant is 0.022 dB/mm over the entire band of 90 - 110 GHz. The measured attenuation constant varies between 0.005 dB/mm and 0.048 dB/mm with an average of 0.028 dB/mm which is in excellent agreement with the simulation.

As shown in Fig. 3.28(c), for the SOG waveguide with $W = 0.7$ mm, the extracted attenuation constant from the measurements has a minimum and maximum of 0.018 dB/mm and 0.181 dB/mm, respectively, with an average of 0.053 dB/mm over 140 - 170 GHz. The simulated attenuation constant is always less than 0.016 dB/mm over 140 - 170 GHz.

In Fig. 3.28, the attenuation constants derived from the measurements exhibit some ripple. Further study shows that the ripple originates from the constructive and destructive interference of reflections from transitions between the rectangular waveguides and the SOG waveguides. In an ideal case, the applied de-embedding method would de-embed the effects of these transitions. However, the method does not completely compensate for the partial mismatch due to the transitions. This occurs as the main assumption in this method is that transitions are the same for waveguide structures with two different lengths [119]. Due to the misalignment, this condition is not completely satisfied in reality.

Theoretically, there is no reason for the waveguide attenuation to be higher over 55 - 65 GHz and 140 - 170 GHz than that over 90 - 110 GHz. Since the proposed SOG waveguide has low attenuation, the differences between the insertion losses of the two waveguide structures having two different lengths are within the network analyzer's error range. The calibration error causes ripples of around 0.2 dB in the S_{12} measurement of the two ports directly connected ("through connection" of the two ports) after calibration. As a result, the waveguide attenuation constant derived from the measurements is very sensitive to the network analyzer's error. This is the main source of discrepancies between the attenuation constants derived from simulations and measurements. Overall, the analysis supports the claim that the calibration error, and the error due to misalignment, are the main sources of the small

discrepancies between the attenuation constants derived from the full-wave simulations and the measurements.

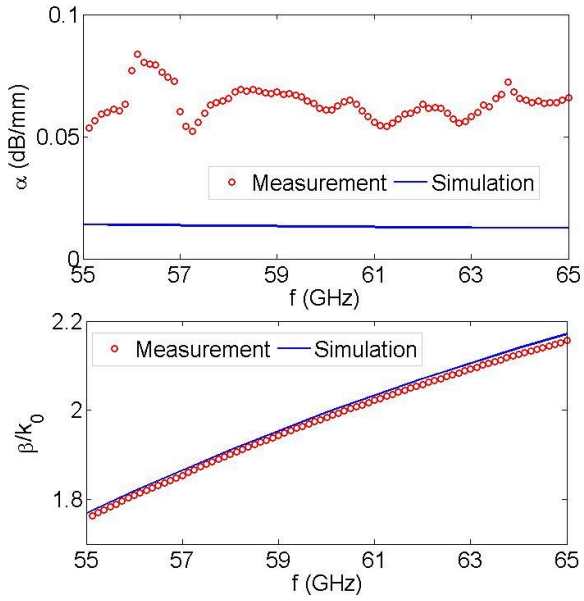

(a)

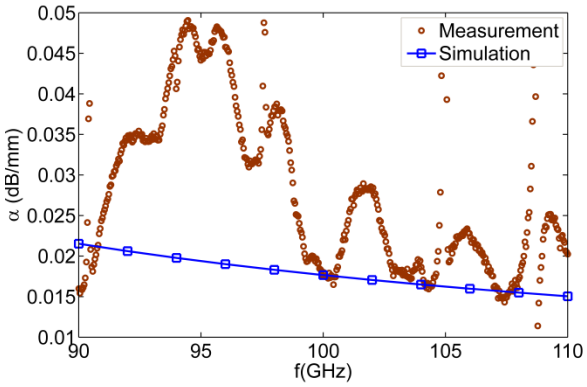

(b)

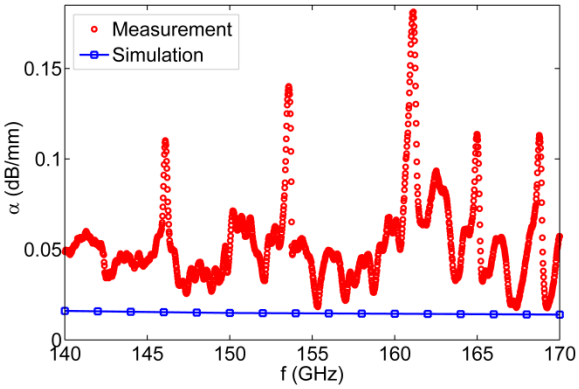

(c)

Fig. 3.28 Simulated and extracted measured propagation constants of the SOG waveguides: (a) attenuation constant and normalized phase constant (β/k_0) of the SOG structure with W = 1.6 mm, (b) attenuation constant of the SOG structure with W = 1.1 mm, and (c) attenuation constant of the SOG structure with W = 0.7 mm.

In order to extract the modal attenuation constant from the measured scattering parameters of the two lengths of the waveguide, the main condition is the single mode operation. However, in the case of the fabricated SOG waveguides with W = 1.1 and 0.7 mm, as the simulation results of the modal analysis plotted in Figs. 3.29,30 show, the waveguides are not measured over their single mode operation bandwidths. The main reason these waveguides are not designed for single-mode operation, is the limitation in the number of different thicknesses of the Si wafers used in this research. In order to satisfy single mode operation conditions over frequency ranges of 90 - 110 GHz and 140 - 170 GHz, the required Si wafers should have thicknesses of $H \sim 400$ μm and ~ 300 μm, respectively. However, to demonstrate the SOG waveguide low insertion loss performance at higher frequencies up to 170 GHz using readily available wafers, the single-mode operation condition is neglected in these experiments.

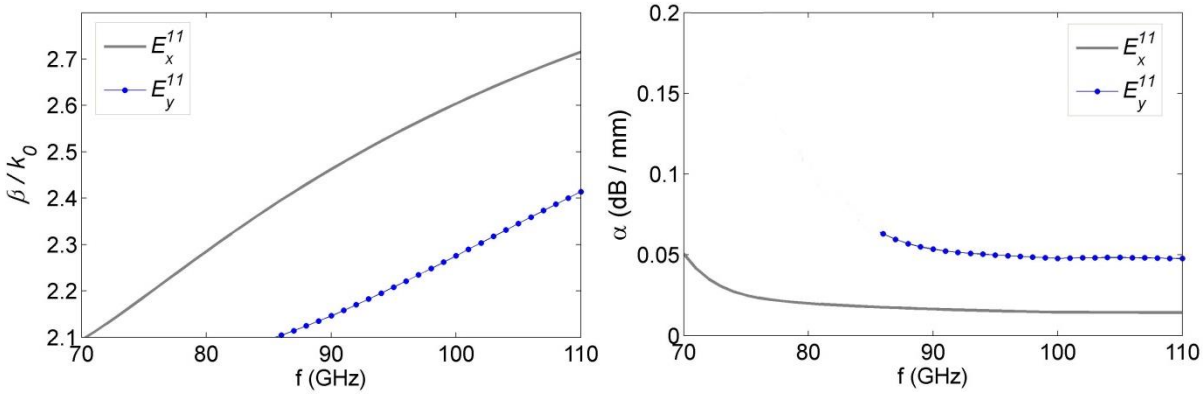

Fig. 3.29 Propagation constants of the SOG waveguide, (a) normalized dispersions (β/k_0) and (b) attenuation constants (dB/mm).

It is interesting that although the SOG waveguides are not designed for single-mode operation over the measured bandwidths, the higher order modes are not excited in the designed test setup structures. Since x-polarization is used to excite the SOG waveguide, the E_y modes are not excited in the SOG waveguides. Due to the polarization of TE_z^{01} of the rectangular waveguide with even symmetry, the higher order E_x^{12} mode is not excited either. To confirm the fact that higher order modes are not excited in the SOG waveguides under test, half of the test setup structure shown in Fig. 3.16 is simulated in HFSS. The simulated generalized scattering parameters are evaluated in the middle of the SOG

waveguide for the dominant mode and the higher order modes. Based on these simulations, the coupling to the higher order modes is found to be below -40 dB. Even for the misalignment cases studied in Figs. 3.25-27 , the coupling to the higher order modes is below -20 dB.

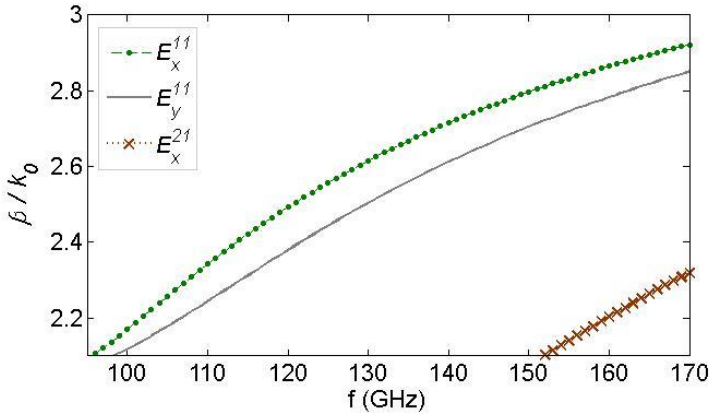

(a)

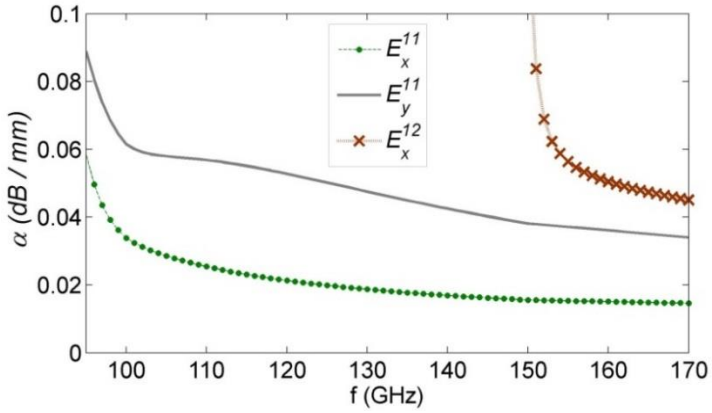

(b)

Fig. 3.30 Propagation constants of the SOG waveguide, (a) normalized dispersions (β/k_0) and (b) attenuation constants (dB/mm).

3.8 Concluding Remarks and Discussion

A new high-performance SOG dielectric waveguide has been presented. The proposed concept can potentially serve as a platform for hybrid mmW integrated circuits. The fabrication process of the proposed structure is quite cost-effective and compatible with currently developed Si-based fabrication

techniques. SOG is a promising candidate for mmW/THz high-density integrated circuits which do not require manual mounting and assembling of sub-structures. The proposed SOG technology platform has the following advantages when compared to state-of-the-art techniques reported in the literature:

- The high-resistivity Si (ρ = 10 KΩ - 20 KΩ), used in the proposed SOG technology structure, is almost non-dispersive over the mmW and THz frequency ranges and has a very low attenuation constant. The existence of a thick Pyrex substrate that eliminates the effect of the lossy ground plane below the substrate, particularly at higher mmW frequencies. Computational modal analysis and simulations confirm that the waveguide has a very low attenuation at higher mmW frequencies. The loss characteristics, extracted from the measured results, show average attenuation constants of 0.63 dB/cm, 0.28 dB/cm, and 0.53 dB/cm over the frequency ranges of 55 - 65 GHz, 90 - 110 GHz, and 140 - 170 GHz, respectively. Table 3.4 compares the loss characteristics of the proposed SOG ridge dielectric waveguide with state-of-the-art techniques. This table confirms the low-loss characteristics of the proposed SOG waveguide as compared to the existing integrated mmW waveguides reported in the literature.

Table. 3.4. Performance Comparison.

Structure	Attenuation Constant (α)		Frequency
	α (dB/cm)	α (dB/λ)	
Substrate integrated waveguide (SIW) [29]	0.31	0.17	54 GHz
Metallic waveguide [33]		0.5 - 0.8	110 - 170 GHz
Metallic waveguide [33]		0.6 - 1	140 - 220 GHz
Metallic waveguide [34]	0.013	0.04	100 GHz
Si filled metallic waveguide [46]	0.2 (average)		77-110 GHz
Si filled metallic waveguide [48]	0.125 / 0.121	0.038 / 0.035	100 / 105 GHz
Perforated image guide [59]	0.25	0.104	72 GHz
Perforated image guide [64]	0.7	0.23	90 GHz
LTCC-based image guide []	0.29	0.14	62 GHz
SOG waveguide	0.63 (average)	0.32 (average)	55 - 65 GHz
SOG waveguide	0.28 (average)	0.086 (average)	90 - 110 GHz
SOG waveguide	0.53 (average)	0.102 (average)	140 - 170 GHz

- The high permittivity of Si, as compared to that of its surrounding media in the SOG structure, leads to strong field confinement inside the Si. This large index contrast is essential to maintain low scattering (radiation) loss at the bends and to minimize the coupling between adjacent waveguides. These properties make SOG technology appropriate for mmW/THz high-density integrated circuits.

- In the proposed SOG technology, the alignment between the sub-structures in the integrated circuit is automatically achieved during the fabrication process due to the fact that the entire circuit is developed during a single-mask process without any manual intervention. This is one of the most significant advantages of the proposed technique compared to the conventional methods. Whereas in the conventional insulator image guide, the components are cut from the dielectric slab and then manually bonded to the ground plane using a low-permittivity insulating film. In the proposed SOG technique, since the bonding between the Si and Pyrex is performed before the DRIE of Si, there is no need to manually assemble or align the sub-structures in an integrated circuit.

  To further clarify this, consider the following example. Suppose an integrated circuit, as shown in Fig. 3.31 (composed of two coupled resonators and one power divider), is made using the dielectric waveguide technologies reported in [52, 59] and the SOG technology from this research. Using the technique in [52], first the components are cut from the high-permittivity dielectric slab, and then the components are attached to the metallic ground plane using a low-permittivity plastic film. The main problem with this technique is the precise alignment of the coupled resonators at certain distances from the dielectric waveguides, as shown in Fig. 3.31(a). As the frequency rises, the required dimensions become smaller and the alignment becomes excessively difficult and costly.

  Synthesized dielectric image guides based on the perforation of the dielectric substrate was reported to alleviate the alignment issue at the cost of complexity [59]. Using this technique, the low-permittivity medium surrounding the dielectric waveguide channels and the resonators is realized by a lattice of periodic air holes in the high-permittivity dielectric slab. This perforated slab is then bonded to the ground plane using a low-permittivity insulating film as shown in Fig. 3.31(b). The Si slab perforation is a major fabrication step in this technique.

  Fig. 3.32 shows the SOG technology developed in this research. In the proposed SOG technology, first the high-permittivity Si layer is bonded to the Pyrex wafer. Then, using the

photolithography technique, the entire circuit pattern is imaged on the coated thick photoresist. Next, the pattern is etched by DRIE through the Si layer using the photoresist mask. The Pyrex substrate provides a strong mechanical support for the Si components attached to it.

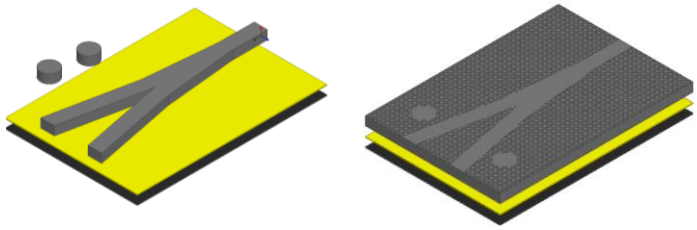

(a) (b)

Fig. 3.31 Planar dielectric waveguide techniques reported in the literature: a) insulated image guide in [52] and b) perforated image guide in [59] (figures are from [113]).

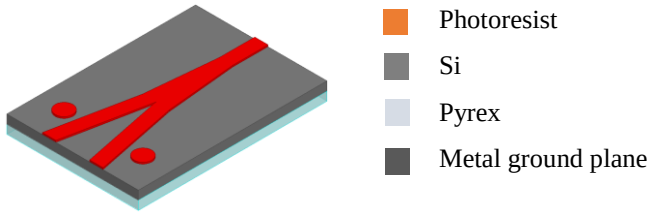

(a)

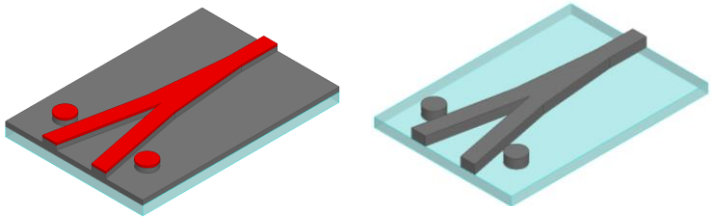

(b) (c)

Fig. 3.32 SOG technology platform: a) photolithography to pattern the mask for the DRIE, b) structure during the DRIE, and c) fabricated circuit after the DRIE through the Si [113].

- The SOG technology offers a much more convenient and low-cost fabrication technique as compared to other techniques such as mmW metallic waveguides. It is worth mentioning that etching the Pyrex substrate below the tapered sections is a part of the measurement setup design due to the fact that the test instrument has rectangular waveguide ports. The ultimate objective

is to integrate the entire system including the coupling to the active devices and antenna on one substrate. For SOG circuits operating under the E_x^{11} mode, which have better confinement inside the Si, at operation frequencies below 200 GHz, the fabrication process consists of only three standard and well-established steps of anodic bonding, optical lithography, and DRIE of Si.

- Optical lithography and DRIE are high-precision techniques. A significant advantage of DRIE is the ability to create closely spaced vertical sidewalls. The surface roughness over the etched sidewalls is quite negligible as compared to the wavelength. The effect of this amount of surface roughness (~ 120 nm) on the waveguide propagation characteristics is insignificant.

Chapter 4 Silicon-on-Glass Dielectric Waveguide for Sub-Terahertz Applications

4.1 Introduction

In Chapter 3, a silicon-on-glass (SOG) platform consisting of a high-resistivity silicon (Si) wafer bonded on a glass substrate was proposed, developed, and demonstrated for millimeter-wave (mmW) integrated circuits. In SOG technology, all integrated passive components and waveguide connections are made out of high-resistivity Si via deep reactive-ion etching (DRIE) through the Si layer. Pyrex 7740 was selected as the glass substrate material due to its appropriate transmission properties at mmW range and its compatibility with Si fabrication. SOG ridge dielectric waveguides for mmW were tested up to 170 GHz and their low-loss transmission characteristics were demonstrated. This Chapter investigates extending the SOG platform into sub-mmW/sub-terahertz (THz) frequency ranges.

Measurements have shown that highly-resistive Si is a very low-dispersion and low-loss medium for THz wave propagation. However, as the frequency increases the material loss in Pyrex, and thereby the waveguide attenuation, starts to increase rapidly. The problem of high material loss in the Pyrex substrate is overcome by the fabrication process proposed in this Chapter. In the proposed process, parts of the Pyrex substrate below the Si guiding channel are etched. Two SOG structures are proposed in this Chapter. These two structures, which are respectively called the s*uspended SOG waveguide* and the *corrugated SOG waveguide*, are described in details in this Chapter. To investigate the new concepts, simulation and measurement results are also provided.

4.2 Limitations of Silicon-on-Glass Waveguide for Terahertz Applications

In this Section, extending the SOG platform operation into higher THz frequencies is investigated; its limitations and advantages are studied. In SOG technology, all integrated passive components and waveguide connections are made out of high-resistivity Si via DRIE through the Si layer. During the DRIE process, these Si components are masked against the plasma attack and supported on the glass substrate. Optical lithography is used to pattern the etching mask. From the fabrication point of view, there is no limitation on extending the operation frequency of the proposed SOG technology into higher THz frequencies. SOG fabrication technique is an attractive candidate for making THz waveguides and components due to its high-precision which provides sub-micron dimensional accuracy. Photolithography is a highly precise process which can create fine patterns down to less than 1 μm

feature size. DRIE is a highly anisotropic etching process with the significant advantage of creating vertical sidewalls with high aspect ratios. Scanning electron microscope (SEM) images of the fabricated samples, presented in Chapter 3, confirm that the etched sidewalls are quite smooth.

Terahertz absorption coefficient and refractive index spectra for different types of materials were obtained through THz time domain spectroscopy [76- 85]. Previous research has shown that highly-resistive intrinsic Si is a very low-dispersion and low-loss medium for THz wave propagation [1, 81]. Fig. 4.1 shows the reported measured power absorption coefficient for high-purity, float-zone crystalline Si with high resistivity (ρ > 10 KΩ .cm) [81]. The measurements for high-resistivity Si show a power absorption coefficient of less than 0.025 cm^{-1} up to 2 THz, and less than 0.15 cm^{-1} up to 4 THz. The measured power absorption coefficient of high-resistivity Si reaches 0.01 cm^{-1} at 1 THz. This amount of material loss is equivalent to a conductivity of 0.009 S/m at 1 THz. The equivalent conductivity of the high-resistivity Si can be obtained from the measured power absorption coefficient, using the expression $\sigma = \alpha n / Z_0$, in which n, σ, α, and Z_0 are respectively the Si refractive index, the measured Si power absorption coefficient, and the air characteristic impedance.

Up to 200 GHz, Pyrex substrate meets all the requirements in terms of transmission properties and fabrication simplicity. However, above 200 GHz, Pyrex material loss increases rapidly (e.g., Pyrex equivalent conductivity reaches 4 S/m at 500 GHz). This amount of material loss significantly increases the SOG waveguide attenuation and results in a deterioration of its high-performance.

Fig. 4.2(a) shows the measured absorption coefficient of different glass materials, including Pyrex, in the THz range from [84]. The composition of Pyrex is: SiO_2 81 %, B_2O_3 13 %, Na_2O 4 %, Al_2O_3 2 % [120]. Fig. 4.2(b) shows the equivalent-conductivity of Pyrex derived from experimental data up to 1.2 THz. To extract the Pyrex equivalent conductivity from the measured power absorption coefficient, the expression $\sigma = \alpha n / Z_0$ is used.

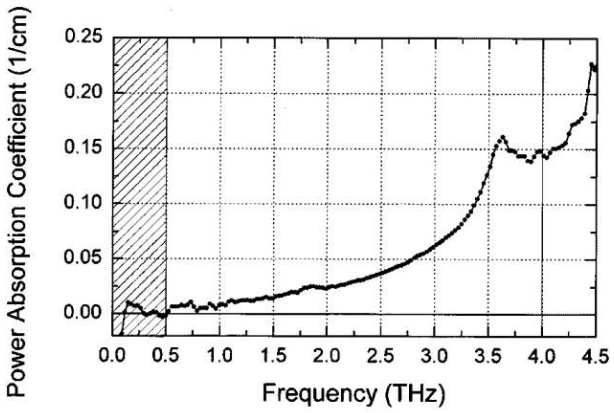

Fig. 4.1 Measured upper limit of the power absorption coefficient of high-resistivity intrinsic Si [81].

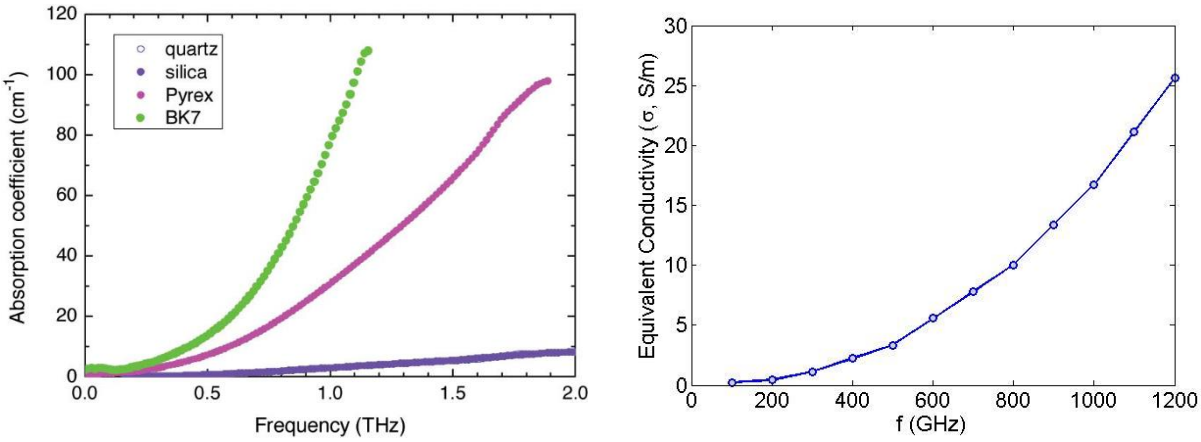

(a) (b)

Fig. 4.2 Pyrex 7740 material loss characteristics: (a) measured power absorption coefficients of different glass materials [84] and (b) Pyrex equivalent conductivity in THz [121].

4.3 Terahertz Silicon-on-Glass Waveguide Structures

In order to reduce the waveguide attenuation due to the glass substrate at higher frequencies above 200 GHz, new SOG dielectric waveguide structures are proposed. In the proposed structures, part of the Pyrex substrate below the Si guiding channel is etched to reduce the effect of the glass material loss.

Full-wave simulations are performed to study the effect of etching the Pyrex on the transmission characteristics of the Si guiding channel. In order to accomplish this, modal analysis of the SOG structure cross sections *A* and *B*, shown in Fig. 4.3, are performed in high frequency structure simulator

(HFSS). The waveguide dimensions are selected as W = 310 µm, H = 100 µm, T = 500 µm, and in the structure with cross section B, a = 100 µm and b = 3 mm.

Hydrofluoric acid (HF; 49 %) wet etching is used to etch the Pyrex. The wet etching of Pyrex is a fully isotropic etching process. As shown in Fig. 4.3(b), in the etched structure the Pyrex has rounded sidewalls which reflect the isotropic property of the HF wet etching. In reality the sidewalls are not ideally round due to the mask break-down which occurs during the etching process [122]. However, due to the minimal interaction of the guided modal fields with the Pyrex substrate, the shapes of the Pyrex etched sidewalls do not affect the waveguide's performance.

Reported measured power absorption coefficients of high-resistivity Si, shown in Fig. 4.1, show that the absorption is quite low up to 500 GHz, reaching 0.01 cm^{-1} (σ_{eqv} = 0.009 S/m) at 1 THz. In all of the simulations reported in this Chapter, Si is considered to have a conductivity of σ = 0.01 S/m and a relative permittivity of ε_r = 11.7 (11.68). Pyrex's relative permittivity is assumed to be ε_r = 4.41 [84], while its equivalent conductivity is plotted in Fig. 4.2. Fig. 4.4 shows the propagation constants of the dominant E_x^{11} modes of the SOG waveguide structures with cross sections A and B.

As shown in Fig. 4.4, etching the Pyrex below the guiding channel reduces the waveguide attenuation constant significantly and shifts its dispersion diagram (β/k_0) downward. At 500 GHz, the two structures with cross sections A and B have attenuation constants of 0.301 dB/mm and 0.007 dB/mm, respectively.

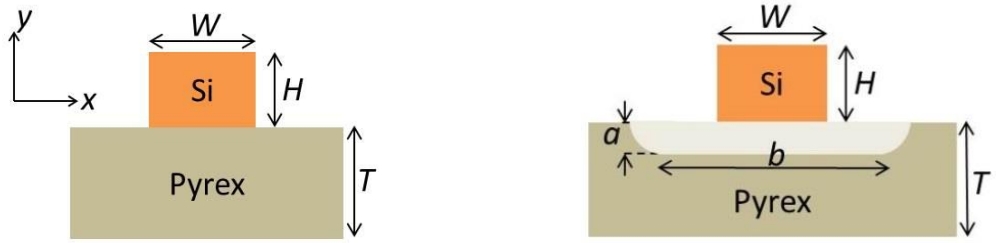

(a) (b)

Fig. 4.3 Cross sections of the simulated SOG structures: (a) cross section A and (b) cross section B [121].

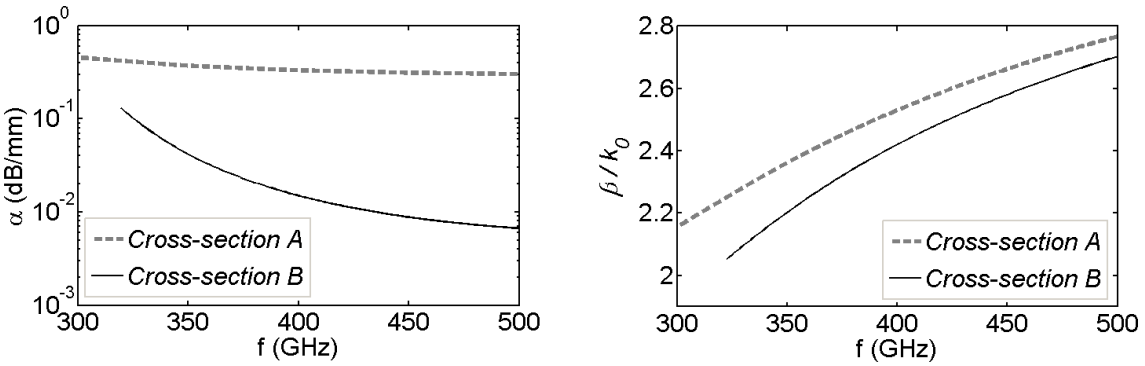

(a) (b)

Fig. 4.4 Propagation constants of the SOG structures with cross sections *A* and *B*: (a) attenuation constant (α) and (b) normalized phase constant (β/k_0) [121].

To support the Si guiding channel over the etched region of the Pyrex substrate, two novel SOG waveguide structures are proposed. In the first structure, the guiding channel is supported from both sides by means of two Si supporting blocks which connect to the Si guiding channel via a periodic configuration of Si beams. This new configuration of the SOG waveguide is called a *suspended SOG waveguide*, and is shown in Fig. 4.5.

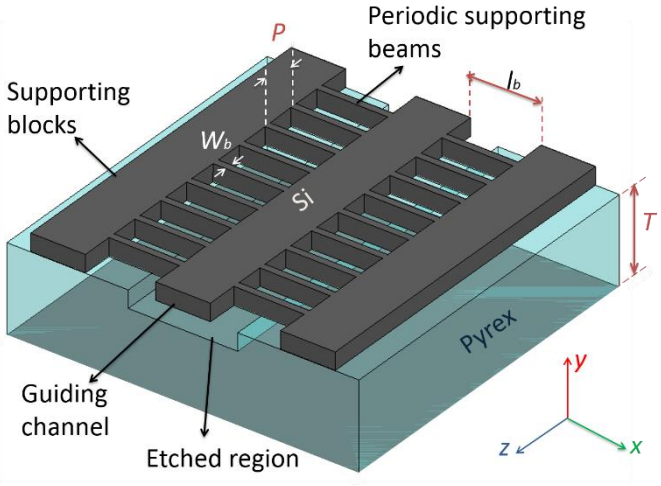

Fig. 4.5 Suspended SOG waveguide structure.

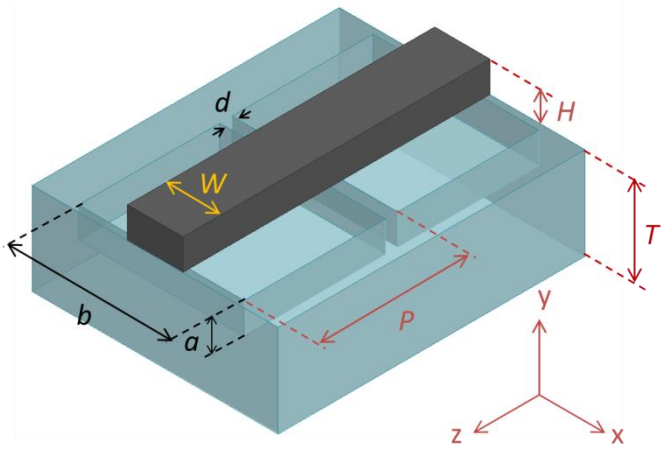

Fig. 4.6 Structure of the corrugated SOG waveguide [114].

In the second proposed SOG platform, called a *corrugated SOG waveguide*, part of the glass substrate below the high-quality Si guiding channel is etched in a periodic pattern. The structure of the corrugated SOG waveguide is shown in Fig. 4.6.

4.4 Fabrication Technique

The fabrication process of the new SOG structures is quite simple and essentially consists of the same steps as the ones described in the mmW SOG platform described in Chapter 3. The fabrication is a two-mask process. The first mask defines the etched regions on the Pyrex surface and the second mask defines the etched regions within the Si layer. In this technique, the guiding channel along with its supporting parts (in the suspended SOG waveguide structure) are made by DRIE through the Si layer of the SOG platform. A thick photoresist (*AZ P4620*), patterned via optical lithography, is used as a mask for the DRIE step of the Si. This process is performed after anodic bonding of the Si wafer on an etched Pyrex surface. HF wet etching with a chromium/gold (Cr/Au; 100 nm / 1 μm) mask is used to etch the Pyrex. The process flow is shown in Fig. 4.7 and described in detail below. The process flow for the fabrication of the corrugated SOG waveguide is the same as that of the suspended SOG waveguide.

The process begins with a Pyrex 7740 wafer with a thickness of 500 μm and a diameter of 4 inch. The Pyrex wafer is cleaned using the Piranha process (H_2SO_4 / H_2O_2 4:1) at room temperature for 15 min. The surface of the wafer is coated by sputtering of a 100 nm thick layer of Cr followed by a 1 μm thick

Au layer via electro-beam evaporation. The Cr layer acts as an adhesive layer while the Au acts as the main masking layer for the HF wet etching of the Pyrex. The surface of the Au layer is coated by a ~11 μm thick photoresist (AZ P4620) layer using a spinner. This photoresist layer is patterned via photolithography using a glass-Cr mask. This patterned photoresist is used as a masking layer for the wet etching of the Cr/Au layer. The Au and Cr layers are successively etched using standard Au and Cr etchants. Although the main role of the photoresist layer is masking the Cr/Au layer during the wet etching of the Cr/Au, it can act as extra protection, along with the Cr/Au masking layer, during the Pyrex aggressive HF wet etching. To encourage this, a hard baking of the thick photoresist is performed on a hotplate for 30 min at a temperature of 115 °C. Then, the backside of the Pyrex wafer is covered by a sputtering of Cr/copper (Cu; 100 nm / 1 μm) to protect the backside of the wafer during HF etching of the Pyrex wafer. The Pyrex wafer is etched in HF 49% to 100 μm. The etching rate is ~6 - 8 μm/min. After etching the Pyrex wafer, the photoresist layer is removed with acetone and the Cr/Au and Cr/Cu metal masks are removed with standard etchants.

Different masking materials can be used for wet etching of the Pyrex substrate depending on the height of etching inside the Pyrex substrate. Thick photoresist is a good masking layer which can resist aggressive HF solution up to 2 – 3 min before starting to peel off [123]. Silicon, which can be either bonded or deposited on the Pyrex surface, is another masking material used for deep Pyrex etching [122, 124- 126]. Using the bonded Si layer is not preferred due to the large undercutting of the etching and the difficulty in a second bonding process between the etched glass and the Si device layer [122].

Cr/Au is one of the most commonly used metal masks for HF etching of the Pyrex glass since Au is inert in HF [120, 122, 127-128]. However, the etch time is limited by the defect generation on the etching mask. The thickness of the Au mask has an influence on the etching time. While a 400 nm thick Au layer can resist HF solution for 15 min before HF penetrates the defects, by increasing the thickness of the Au mask to 1.2 μm, this time is increased to 45 min [127]. A hard baked thick photoresist on the Au surface also enhances the mask performance.

After etching the Pyrex wafer and removing the masking layers, the Pyrex and Si wafers are cleaned during the Piranha process and prepared for anodic bonding. For good quality of the bonding process, the two surfaces in contact must be clean. The anodic bonding between the Pyrex and Si is done at a temperature of 450 ºC by applying a bond voltage of 1000 volts. Anodic bonding between Si and Pyrex terminates in a strong connection between the two wafers.

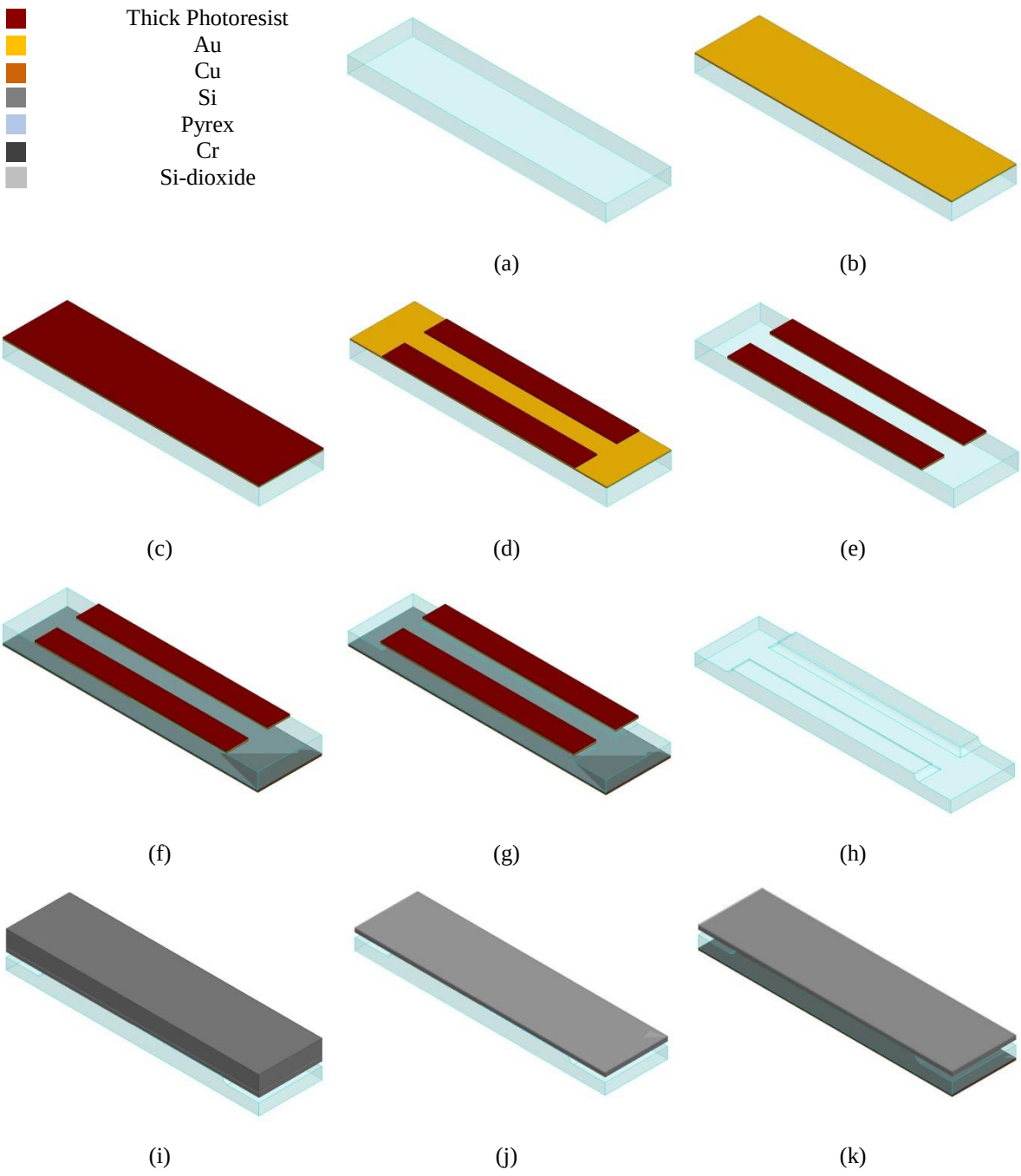
Thick Photoresist
Au
Cu
Si
Pyrex
Cr
Si-dioxide
(a)
(b)
(c)
(d)
(e)
(f)
(g)
(h)
(i)
(j)
(k)

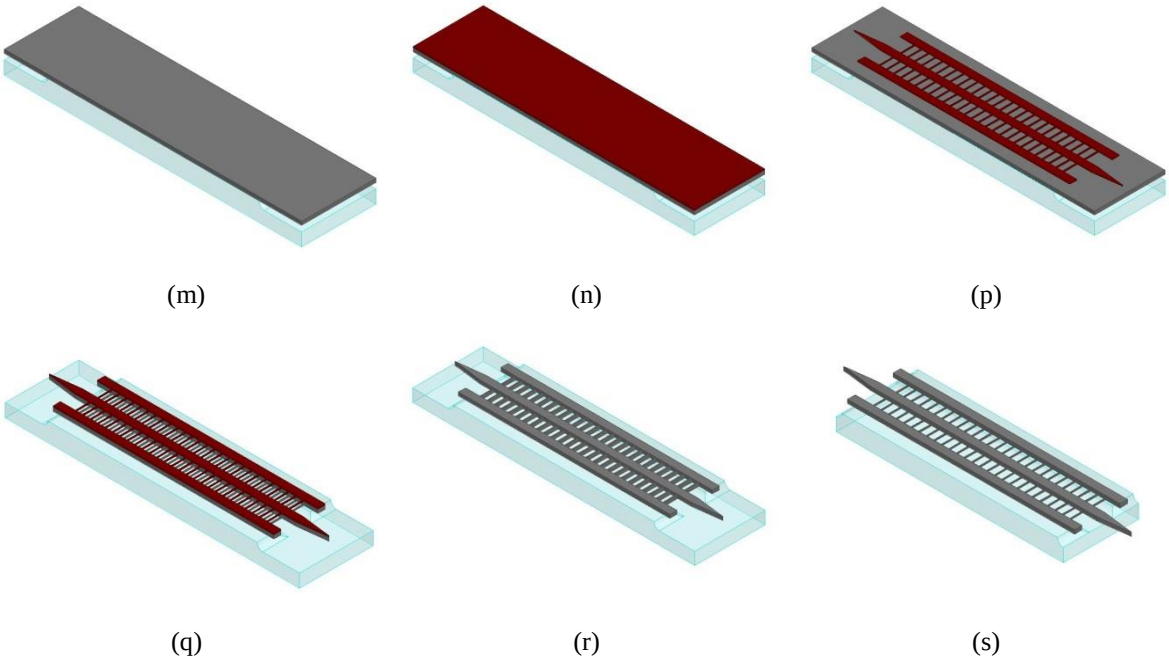

Fig. 4.7 Process flow of the fabrication of the suspended SOG waveguide:

(a) Cleaning the Pyrex wafer

(b) Sputtering of a Cr/Au layer on the surface of the Pyrex wafer

(c) Coating the Au surface with the thick photoresist

(d) Patterning the photoresist layer via optical lithography

(e) Etching the Cr/Au masking layer

(f) Sputtering of a Cr/Cu layer on the backside of the Pyrex wafer

(g) Wet etching of the Pyrex wafer in HF 49 %

(h) Removing the photoresist layer, Cr/Au and Cr/Cu masking layers in acetone and standard metal etchants, respectively

(i) Bonding the etched surface of Pyrex wafer to the SOI wafer

(j) Etching the Si handle layer in TMAH

(k) Covering the backside of the Pyrex wafer with thick photoresist

(m) Etching the oxide layer in HF and cleaning the backside photoresist with acetone

(n) Coating the Si device layer with the thick photoresist

(p) Patterning the photoresist via optical lithography

(q) DRIE of the Si layer using the photoresist mask

(r) Removing the photoresist in acetone

(s) Dicing the Pyrex wafer and removing the glass from below the tapered sections.

For the range of frequencies on interest in this research, the thickness of the high-resistivity Si wafer used is 100 μm. These wafers are extremely thin and fragile; in order to handle and work with them they are always carried on top of a thick handle layer in the form of a silicon-on-insulator (SOI) wafer. After bonding the high-resistivity device layer of the SOI wafer on top of the Pyrex wafer, the 500 μm thick Si handle and oxide layers are successively removed by wet etching.

There are two etchants used with Si: potassium hydroxide (KOH), and tetramethylammonium hydroxide (TMAH) [129, 130]. The etch rate of Si in KOH is higher than in TMAH [129]. The etching rates are dependent on the temperature, the solution concentration, and the Si crystalline orientation. The top Si handle layer is etched in TMAH which is a uniform etchant with an etch rate of 0.5 - 1 μm/min. This process takes about 8 hours. The dioxide layer has a negligible etching rate (~ 0.2 nm/min in 25 % solution at 80 °) in TMAH. As a result, the 1 - 2 μm thick oxide layer acts as an etch stop in TMAH and protects the main Si device layer against the TMAH. Although KOH provides a higher etch rate than TMAH, it is not the preferred etchant as it is not a uniform etching technique and it etches oxide with an etching rate of ~ 10 nm/min (20 % solution at 90 °).

Before etching the thin oxide layer in HF 49 %, a thick photoresist layer is coating the back side of the Pyrex wafer to protect the wafer against the HF solution. This process is completed in less than 2 min. A thick photoresist layer is strong enough to protect the backside of the wafer during the process [123]. Etching the oxide layer in an HF solution forms the SOG wafer. The thick photoresist layer is then removed from backside of the wafer in acetone.

A thick photoresist (AZ P4620) is used as a mask for the DRIE step of the Si. This photoresist is used to coat the Si surface with a thickness of ~ 11 μm, using a spinner. The second glass-Cr mask is used to pattern the thick photoresist mask by optical lithography, via the steps of UV exposure and development in AZ 400K. The photoresist layer is exposed to UV radiation passing through the glass-Cr mask to pattern the photoresist. Before exposing the photoresist to UV, mask alignment is required to align the pattern on the glass-Cr mask with the etched patterns on the Pyrex wafer. This is done using backside alignment with an accuracy of ~ 1 μm. The transparency of the Pyrex wafer is an advantage to look at the etched patterns on the Pyrex wafer from the backside.

In the proposed suspended SOG technology, the etched patterns on the Pyrex wafer are quite large when compared with the Si components' dimensions. In the suspended SOG waveguide structure, the Si supporting beams are quite long. In this case, misalignments up to ± 50 μm between the Si waveguide

and the etched region on the Pyrex wafer are tolerable. The accuracy provided by the mask aligner is much greater than this tolerable misalignment.

Finally, the Si parts of the waveguide, the Si guiding channel and supporting parts, are formed via DRIE through the Si layer using the thick photoresist mask. The remaining photoresist mask is removed in acetone. The wafer is then diced and each individual waveguide is ready for testing.

The waveguides, as shown in Fig. 4.7, are tapered on both sides. These tapered sections are designed to provide a low-loss coupling into the rectangular waveguide ports of the measurement setup. To facilitate insertion of the tapered section inside the rectangular waveguide, and to minimize the coupling loss, the Pyrex is removed from below the tapered sections. To do this, the Pyrex below the tapered sections is partly etched during the HF process and then removed by dicing.

DRIE is capable of providing high aspect ratios. This property is appropriate for the new suspended structure due to the small thickness of the supporting beams as compared to the guiding channel dimensions. Wet etching is the most common and economical method of etching Pyrex; Pyrex dry etching is slow and is used only when vertical sidewalls are desired [131, 132]. HF wet etching of Pyrex is a fully isotropic etching process leaving rounded sidewalls. In the proposed suspended SOG structure, the dimensions of the etched regions are selected such that the Pyrex substrate has minimal interaction with the modal fields confined inside the Si channel. Therefore, the fast and economical chemical etching of the Pyrex wafer provides the required performance. The proposed THz SOG technology, which relies on currently available Si-based fabrication techniques, provides high-precision at low-cost.

4.5 Suspended Silicon-on-Glass Waveguide

In the suspended SOG waveguide structure, wet etching of the Pyrex below the Si guiding channel is used to decrease the SOG waveguide attenuation due to the glass substrate. A periodic configuration of Si beams supports the Si guiding channel over the Pyrex substrate. The suspended SOG waveguide is studied in this Section.

4.5.1 Computational Simulations and Studies

In this section, to study the performance of the suspended SOG waveguide, the structure is simulated in HFSS. The simulated configuration consists of a length of L_1 = 9.7 mm of the waveguide, and two transitions from the suspended SOG dielectric waveguide to the measurement system rectangular waveguide ports. The suspended SOG waveguide dimensions are the same as those studied in Fig. 4.4

(W = 310 μm and H = 100 μm), while W_b and P (see Fig. 4.5) are different in the four simulated structures. The dimensions of the simulated structures are provided in Table 4.1. The simulation results are shown in Fig. 4.8.

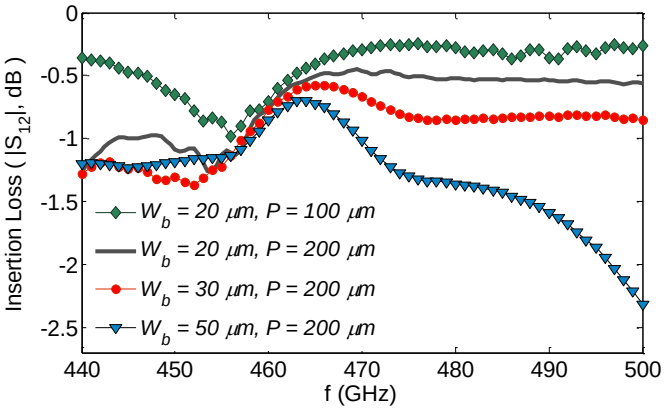

(a)

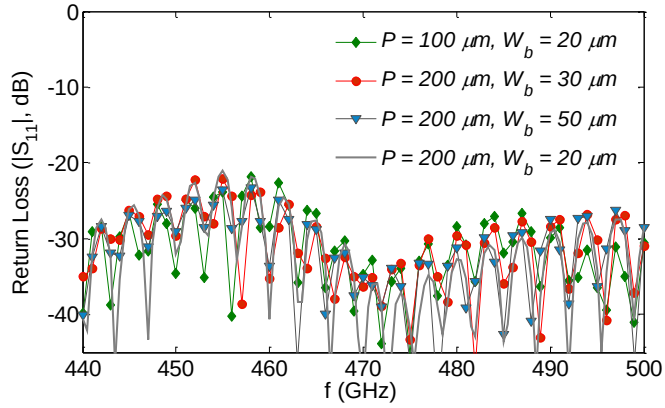

(b)

Fig. 4.8 Scattering parameters of the suspended SOG waveguide structures, including the back-to-back transitions to the rectangular waveguide ports, for different Si beam dimensions: a) insertion loss, and b) return loss [121].

As shown in Fig. 4.8, for a constant P, increasing the thickness of the beams increases the waveguide attenuation. When P = 200 μm, selecting W_b = 20 μm leads to an insertion loss of less than 1.2 dB over 440 - 500 GHz. This loss includes the attenuation of 9.7 mm length of the suspended SOG waveguide, and the transition losses from the rectangular waveguide port to the SOG waveguide and then back

again to the rectangular waveguide. The transition loss includes the radiation loss and the materials loss along the sections. The tapered segments have a length of L_t = 1.3 mm each.

The additional loss caused by the supporting beams is mainly due to the radiation. For a similar W_b = 20 μm, a lower period of P = 0.1 mm leads to an insertion loss of less than 1 dB over the entire band. In all of the simulated structures, the return loss is better than 20 dB, over the entire 440 - 500 GHz frequency band. Further investigations show that the dip in the insertion loss at ~ 455 GHz in all of the simulated structures is due to the transition and not due to the periodic characteristics of the structures. Simulation of the suspended Si guiding channel without supporting beams, show similar behavior at the same frequency of ~ 455 GHz.

For a choice of P = 200 μm and W_b = 50 μm, the attenuation increases as the frequency increases toward 500 GHz. The dip at ~ 500 GHz is due to the radiation. However, the effect is insignificant when W_b = 20 μm and 30 μm. The coupling of the propagating modal fields to the periodic supporting beams increases with the thickness of the beams and, consequently, the increase in the insertion loss due to the radiation becomes greater.

Table. 4.1. Dimensions of the suspended SOG waveguide structures studied in Fig. 4.8.

	W (μm)	H (μm)	a (μm)	b (μm)	W_b (μm)	P (μm)	l_b (μm)	T (μm)
# 1	310	100	100	3	20	100	820	500
# 2	310	100	100	3	20	200	820	500
# 3	310	100	100	3	30	200	820	500
# 4	310	100	100	3	50	200	820	500

Fig. 4.9 shows the magnitude of the electric field of the E_x^{11} dominant mode over a cross section passing through the middle of the beams for the structure with P = 200 μm and W_b = 20 μm. Other dimensions are the same as those mentioned in Table 4.1 (line # 2). As it is clearly observed in this figure, the interaction of the fields with the supporting beams is quite week.

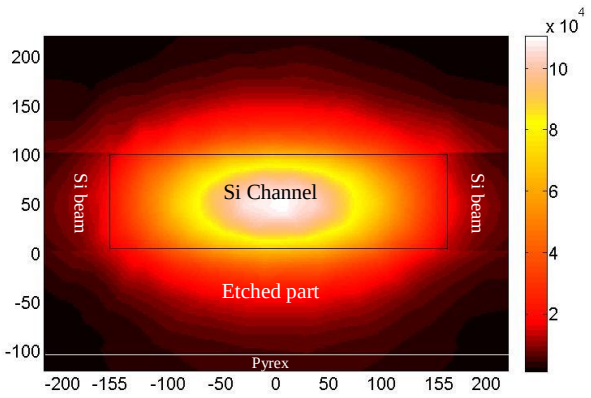

Fig. 4.9 Magnitude of the electric field at one time instant on a cross section of the suspended SOG waveguide passing through the middle of the supporting beams [121].

4.5.2 Experimental Results

A network analyzer PNA-X (Keysight Technologies Inc.) is used to test the proposed suspended SOG waveguide. The frequency extenders (OML Inc.) connecting to the PNA have standard rectangular waveguide ports. The fabricated sample is shown in Fig. 4.10. This waveguide, as shown in the figure, is tapered on both sides. Fig. 4.11 shows the test setup. The tapered segments of the Si guiding channel are inserted inside the WR 2.2 (0.56 × 0.28 mm) waveguides. The rectangular waveguides are rotated by 90 ° to provide a low-loss coupling into the dominant E_x^{11} mode of the suspended SOG waveguide.

As mentioned in Chapter 3, the glass substrate below the Si guiding channels is removed to improve the coupling characteristics of the transitions. The rectangular metallic ports get smaller at higher frequencies. In these conditions, etching and removing the glass substrates from below the tapered sections become essential for insertion of the tapered segments inside the metallic ports. The height of the ground planes in the aluminum holders are designed to center the tapered segments inside the metallic ports.

As frequency increases, the measurement results become extremely sensitive to misalignments and errors. As a result, the test setup shown in Fig. 3.16, where rectangular waveguides (connecting to rectangular metallic ports of the PNA) are parts of the aluminum holder, is not operational. Since the aluminum sample holders are made using standard machining techniques, they become extremely lossy at higher frequencies mainly due to fabrication inaccuracies.

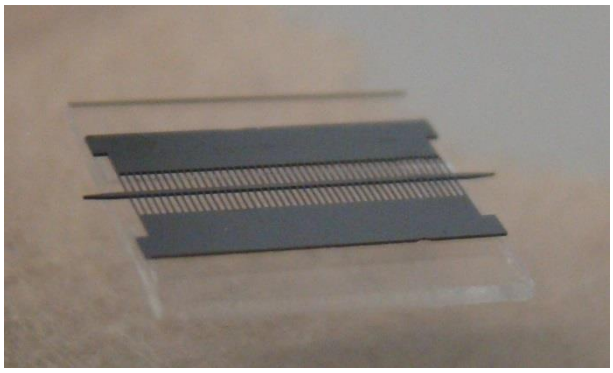

Fig. 4.10 Fabricated suspended SOG waveguide [121].

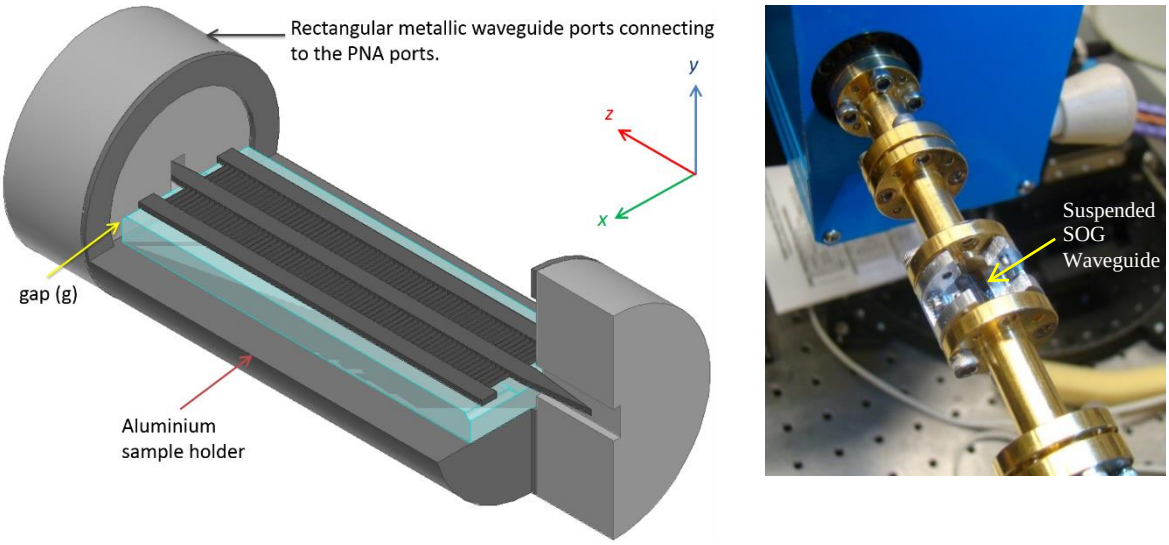

(a) (b)

Fig. 4.11 Modified test setup structure: a) in the modified test setup the aluminum sample holder connects to the rectangular metallic ports which are fabricated with the same high-precision as those of the PNA-X metallic ports. The height of the ground plane in the sample holder is adjusted to center the tapered segments inside the metallic waveguides. b) Actual setup picture.

To overcome the problem of high attenuations of the metallic waveguides, the test setup is refined for higher frequencies. In the modified test setup, as shown in Fig. 4.11, the aluminum holder is functioning as a simple sample holder, while the metallic waveguides connecting to them are made by OML with

high dimensional accuracies. These metallic waveguide segments are connected to the aluminum sample holder on one side and to the metallic ports of the OML frequency extenders on the other side.

4.5.2.1 Measurement Results

The simulated results and measured data are compared to validate the theoretical model and the experimental procedure. Fig. 4.12 shows the simulated and measured scattering parameters of the entire test structure including the transition from the rectangular waveguide to the suspended SOG waveguide, the SOG waveguide segment, and the transition back to the rectangular waveguide. The suspended SOG waveguide test sample has dimensions of W = 310 µm, H = 100 µm, a = 100 µm, b = 3 mm, W_b = 20 µm, P = 200 µm, and l_b = 820 µm. The length of the suspended SOG waveguide section between the two transitions is L_2 = 19.7 mm. The tapered sections have a length of 1.3 mm, each.

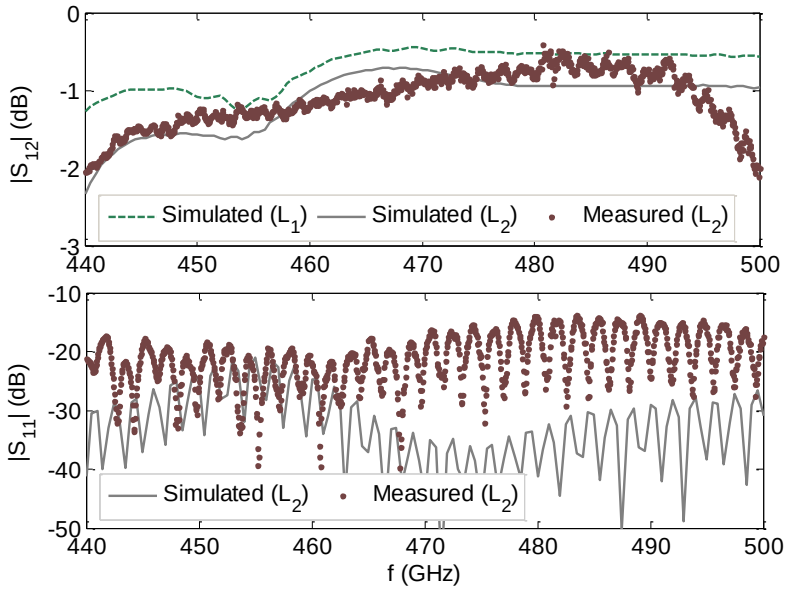

Fig. 4.12 Simulated and measured scattering parameters of the back-to-back transitions from rectangular waveguide (WR 2.2) ports to the proposed suspended SOG waveguide [121].

As shown in Fig. 4.12, the simulated insertion loss ($|S_{12}|$) of the test structure, including the two back-to-back transition losses from the rectangular waveguides to the proposed waveguide, varies between 0.72 dB and 2.33 dB with an average of 1.12 dB over 440 - 500 GHz. The return loss is always better

than 21 dB. As shown in Fig. 4.12, the measured insertion loss (S_{12}) varies between 0.42 dB and 2.11 dB over 440 - 500 GHz with an average of 1.11 dB. Over a large bandwidth of 469 - 489 GHz, the measured insertion loss is less than 1 dB, with an average of 0.76 dB. The measured return loss is always better than 13.8 dB.

In addition to the simulated and measured scattering parameters of the test sample, the simulated scattering parameters for a different length of L_1 = 9.7 mm of the waveguide are presented in Fig. 4.12. The simulated insertion loss ($|S_{12}|$) for this structure varies between 0.45 dB and 1.27 dB. The averaged difference between the simulated insertion losses of the two structures with L_2 = 19.7 mm and L_1 = 9.7 mm is 0.41 dB. An average attenuation constant of 0.04 dB/mm is estimated from this insertion loss difference.

There is good agreement between the simulated and measured scattering parameters for L_2 = 19.7 mm. The misalignment of the suspended SOG waveguide inside the test setup, and the network analyzer calibration error, are the two main sources responsible for the small discrepancies between the two results. Over this range of wavelengths, which demands very high precision alignment, small calibration errors are inevitable. The averaged calibration error over 440 - 500 GHz is 0.06 dB. This error is defined as the insertion loss of the two WR 2.2 ports directly connected ("through connection" of the two WR 2.2 ports) after the calibration. The maximum calibration error is 0.23 dB which occurs at 482 GHz.

To facilitate the insertion of the dielectric waveguide sample into the test setup, it was intended that a gap of g = 100 μm would exist between the glass substrate and the rectangular waveguide opening on each side (as shown in Fig. 4.11). There are several possibilities for the misalignment of the suspended SOG waveguide sample position inside the test setup, for example, the waveguide may be slightly shifted along the *x*- or *z*-axis, or the waveguide is not precisely parallel to the *z*-axis. The effect of the misalignment of the waveguide inside the test setup is discussed in Section 4.5.2.3.

Although a dip in the insertion loss is observed at 500 GHz for a period of P = 200 μm due to the radiation, according to the simulations the effect is not significant for W_b = 20 μm. The dimensions of the fabricated structure are measured under the microscope. These measurements show excellent agreement with the design parameters. The increase in the measured insertion loss around 500 GHz is therefore assumed to be related to the misalignment rather than to the radiation.

4.5.2.2 Extracting the Propagation Constant

In this section the simulated and measured scattering parameters of the test sample are analyzed to extract the suspended SOG waveguide complex propagation constant. First, the attenuations estimated from the simulated and measured scattering parameters for a length of L_2 = 19.7 mm of the waveguide are presented. Then, the attenuation constant, which is obtained based on the method in [119] from the simulated scattering parameters of the two different lengths of L_1 = 9.7 mm and L_2 = 19.7 mm of the waveguide, is presented. Finally, the patterns of maxima in the simulated and measured return losses are used to estimate the phase constant.

The measured scattering parameters for L_2 = 19.7 mm are studied to extract information about the suspended SOG waveguide propagation constant. In this regard, expression 4.1 can be used to derive an upper limit of the waveguide attenuation.

$$10 \times \log_{10}\left(\frac{|S_{12}|^2}{1-|S_{11}|^2}\right) \tag{4.1}$$

This expression, which expresses the ratio of the power exiting port 2 to the portion of the incident power which enters the structure from port 1, represents the total power dissipated within the structure. This ratio, which also includes the portion of attenuation along the transition sections, expresses an upper limit of the waveguide attenuation constant when it is divided by the length of the waveguide between the two transitions. The approximated attenuation constants obtained based on this method from the simulated and measured scattering parameters of the test structure (L_2 = 19.7 mm), are shown in Fig. 4.13.

The attenuation constant derived from the simulations varies between 0.036 dB/mm and 0.118 dB/mm over 440 - 500 GHz with an average of 0.057 dB/mm. As shown in Fig. 4.13, the measured attenuation constant varies between 0.018 dB/mm and 0.104 dB/mm, which occur at 481.5 GHz and 500 GHz, respectively. The average attenuation over the entire 440 - 550 GHz band is 0.054 dB/mm; equivalently, the average attenuation constant per wavelength is 0.0346 dB/λ. Since the losses belonging to the transition sections contribute to this attenuation, the actual attenuation constant of the waveguide is less than this value. The agreement between the attenuations obtained from the experiment and those obtained from the simulation is excellent. Table 4.2 summarizes the reported simulated and measured attenuations. The measured and simulated attenuations obtained based on expression 4.1 are represented in lines 4 and 5 in Table 4.2, respectively.

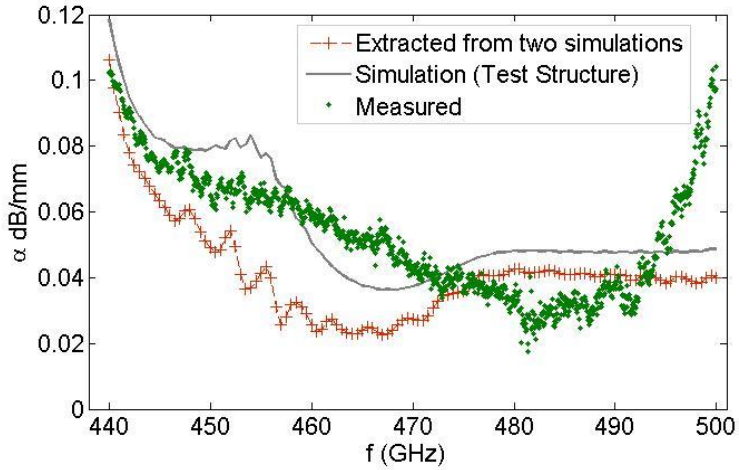

Fig. 4.13 Attenuation constant of the suspended SOG waveguide [121].

The calibration method in [119] can be used to extract the waveguide attenuation from the simulated scattering parameters of the two different lengths. The attenuation constant extracted from the two simulations is plotted in Fig. 4.13 and summarized in line 6 of Table 4.2.

Table. 4.2. Simulated and measured attenuation.

line	attenuation	minimum	maximum	average
1	$\|S_{12}\|$ (dB), measured (19.7 mm)*	0.42	2.11	1.11
2	$\|S_{12}\|$ (dB), simulated (19.7 mm)	0.72	2.33	1.12
3	$\|S_{12}\|$ (dB), simulated (9.7 mm)	0.45	1.27	0.71
4	α (dB/mm), measured (upper limit)	0.018	0.104	0.054
5	α (dB/mm), simulated (upper limit)	0.036	0.118	0.057
6	α (dB/mm), extracted from two length simulations	0.023	0.1064	0.042
7	α (dB/mm), measured (corrected)	-------	-------	0.039

*The scattering parameters are from the rectangular waveguide port to the rectangular waveguide port, including the transition loss and attenuation along the suspended SOG waveguide section with the mentioned length.

As expected, the attenuation based on expression (4.1) obtained from the simulation of the structure with L_2 = 19.7 mm, which is actually an upper limit, is higher than the extracted attenuation from the simulations of the two lengths over the entire band. The average difference between the two attenuation

curves is 0.015 dB/mm, which is related to the additional loss of the transition segments. The excellent agreement between the simulated and the measured scattering parameters of the structure with L_2 = 19.7 mm, verifies that the actual transition loss contribution to the total measured loss of the structure can be obtained from simulations with high accuracy. Subtracting the additional loss due to the transition segments obtained from the simulation, from the measured results, leaves an average measured attenuation of 0.039 dB/mm (Line 7 in Table 4.2) for the suspended SOG waveguide.

A comparison of the simulated and measured return losses presented in Fig. 4.12 indicates good agreement between the patterns of maxima and minima in the two graphs due to the Fabry-Perot reflections at the transitions. This pattern is used to estimate the phase constant. The two graphs for the derived dispersion diagrams from the simulated and measured return losses are shown in Fig. 4.14. Here again, there is good agreement between the two graphs.

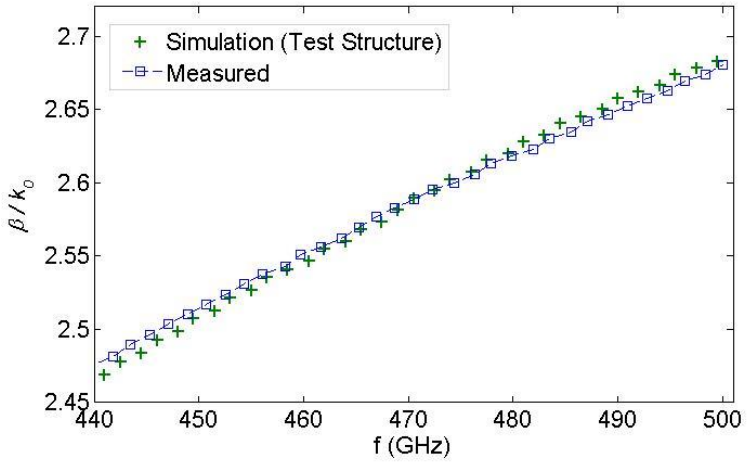

Fig. 4.14 Normalized propagation constant of the suspended SOG waveguide [121].

4.5.2.3 Analyzing the Misalignment Effect

To study the effect of structural misalignment, structures with different misalignments of the waveguide position are simulated in HFSS. As shown in Fig. 4.11, there is a gap (g) between the rectangular waveguide opening and the glass substrate sidewall. If the suspended SOG waveguide is perfectly centered inside the test setup, this gap is g = 100 μm on each side (the length of the Si channel between the two tapered sections is L = 9.7 mm, the length of the glass substrate is 10 mm and the distance between the two rectangular waveguide openings of the test setup is 10.2 mm).

There are several ways in which the waveguide sample's position inside the test setup can be misaligned. These possibilities are: the waveguide is not centered in the *x*- or *z*-direction, or is not parallel with the *z*-axis, or a combination of these. Four typical cases are studied. These cases are described in in Fig, 4.15 and Table 4.3. The simulation results for these cases are shown in Fig. 4.16 and compared with the results when the waveguide is fully aligned inside the test setup.

As the simulation results show, the misalignment causes discrepancies in the insertion loss results when compared to the case when the waveguide is precisely aligned. However, misalignment along the *z*-axis affects the scattering parameters significantly. Simulations show that misalignment along the *x*-axis, or a lack of parallelism with the *z*-axis (within the maximum possible ranges inside the test setup), does not change the scattering parameters significantly. A displacement of 14 μm along the *x*-axis for the suspended SOG waveguide with L = 9.7 mm increases the insertion loss by 0.03 dB, on average, over the entire frequency band of 440 - 500 GHz. A shift of 14 μm from the centered position is the maximum displacement; at that point the tapered section is touching the edges of the rectangular waveguide port of the test setup. A misalignment of 0.16 ° with respect to the *z*-axis degrades the insertion loss by 0.05 dB, on average.

Table. 4.3. Misalignment cases studied.

Misaligned 1	The suspended SOG waveguide is not parallel with respect to the *z*-axis and is misaligned by 0.16 ° *.
Misaligned 2	The suspended SOG waveguide is shifted in *z*-direction by 100 μm *.
Misaligned 3	The suspended SOG waveguide is shifted in *x*-direction by 14 μm *.
Misaligned 4	The suspended SOG waveguide is shifted in *z*-direction by 50 μm.

*The misalignment cases show the maximum possible displacement, where the tapered sections are touching the edges of the rectangular waveguide ports.

As shown in Fig. 4.12, for the two different lengths of L_1 and L_2, dips are observed in the simulated insertion loss diagrams at ~ 455 GHz. The dip at ~ 455 GHz is not observed in the measured insertion loss for L_2 = 19.7 mm, however, the measured results show a dip at 500 GHz which is not predicted in the simulation. The dip observed at ~ 455 GHz in the simulated insertion loss plots in Figs. 4.8, 12, is highly sensitive to the distance between the beginning of the tapered section and the rectangular waveguide opening on each side (*d* in Fig. 4.15(d)).

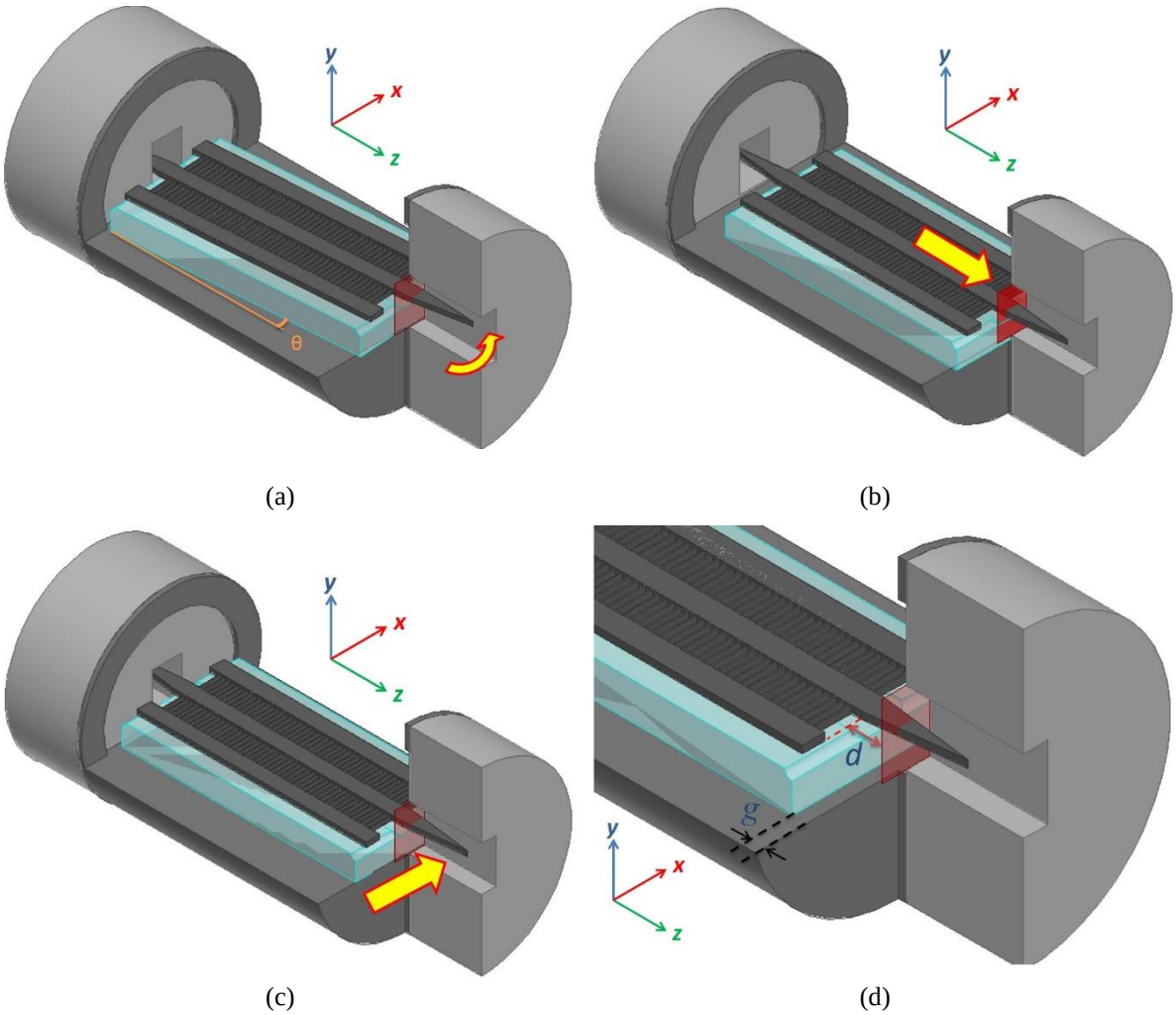

Fig. 4.15 Misalignment of the suspended SOG waveguide inside the test setup: a) the waveguide is not parallel with respect to the z-axis and is misaligned by angle θ, b) the waveguide is shifted in z-direction, c) the waveguide is shifted in x-direction, d) distances d and g between the metallic waveguide opening and different segments of the suspended SOG waveguide.

The displacement of the waveguide in z-direction is the reason for diminishing the dip, which is observed in the simulation results of the aligned structure at 455 GHz, in the measured results and the simulation results of the misaligned cases studied in Fig. 4.16. A displacement of 100 μm along the z - axis shifts the dip in the insertion loss to higher frequencies, ~ 500 GHz, and degrades the insertion loss by 0.3 dB, on average, for L = 9.7 mm. A displacement of 50 μm along the z-axis shifts the dip frequency to ~ 470 GHz, and degrades the insertion loss by 0.06 dB, on average over 440 - 500 GHz, for L = 9.7 mm.

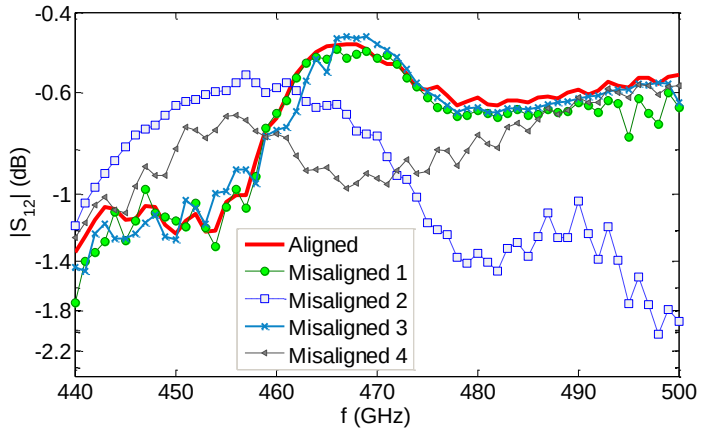

(a)

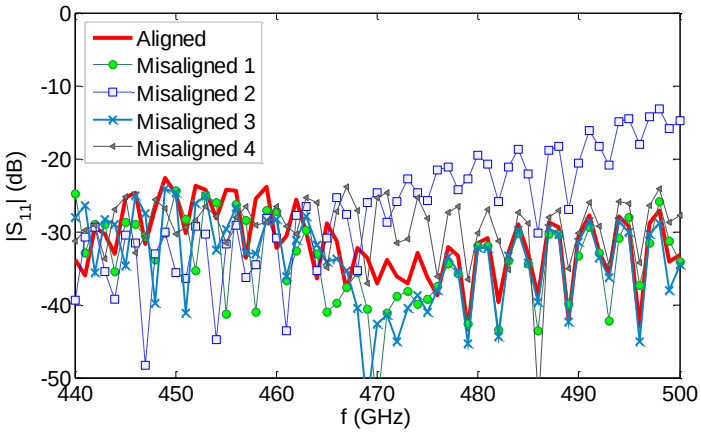

(b)

Fig. 4.16 Simulation results of the scattering parameters for different cases of misalignment mentioned in Table 4.3, compared with the aligned case.

To clarify the effect of the shift in z-direction, part of the test setup as shown in Fig. 4.15(d) is simulated in HFSS for different values of distance between the beginning of the tapered section and the rectangular waveguide opening (d). Two wave-ports are defined in the simulated structure, the first the rectangular waveguide port exciting the structure, and the second on the suspended SOG waveguide cross section. The length of the suspended SOG waveguide connected to the tapered section is $L' = 2.3$ mm. The simulation results for the generalized scattering parameters of this structure, which show the coupling to the dominant mode (the scattering parameter S_{12}:E_x^{11}), are shown in Fig. 4.17.

As the simulation results in Fig. 4.17 show, changing the distance d shifts the dip in the insertion loss over frequency. When d = 250 µm (g = 100 µm), the SOG waveguide is centered inside the test setup, and the dip frequency is 455 GHz. When the SOG is misaligned and shifted in z-direction, d is different on both sides (on one side the waveguide is shifted outward and on the other side it is shifted toward the rectangular waveguide port). For values of d = 150 µm and d = 200 µm, dips in the simulated insertion losses are observed at frequencies of 500 GHz and 480 GHz, respectively. For a value of d = 350 µm, there is no significant dip frequency over 440 - 500 GHz. The displacement of the suspended SOG waveguide along the z-direction is the main source of the dip observed at 500 GHz in the measured insertion loss.

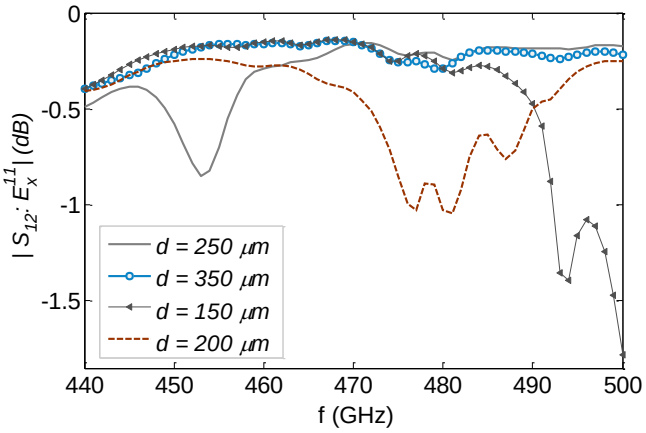

Fig. 4.17 Magnitude of the scattering parameter $|S_{12}: E_x^{11}|$ for different distances from the beginning of the tapered section to the rectangular waveguide opening.

Machining techniques has been used to make the aluminum sample holder of the test setup. The inaccuracies in the dimensions of the test holder are another source of disagreement between the simulated and measured results. These inaccuracies could displace the level of the ground plane or cause a lack of parallelism between the ground plane and the xz-plane. In this case, the tapered sections are shifted upward/downward along the y-direction with respect to their centered positions inside the rectangular metallic waveguides and/or the suspended SOG waveguide is not parallel to the xz-plane.

4.5.3 Bragg Effect and Design Modifications for Single-Mode Operation

4.5.3.1 Modal Analysis

Modal simulations on the SOG waveguide's cross section *B*, shown in Fig. 4.18, are performed in HFSS. All propagating modes are considered in these simulations. The waveguide dimensions are provided in Table 4.4. Three waveguides with three different widths of the Si guiding channel are studied while the thickness of the Si wafer is the same in all of the structures and equal to H = 100 μm. The modal analysis results for these three waveguides are shown in Figs. 4.19-21. As shown in these figures, the single mode operation bandwidths for the waveguides with W = 310 μm, 200 μm, and 160 μm, extend over frequency ranges of 330 - 490 GHz, 420 - 565 GHz, and 480 - 600 GHz, respectively.

To obtain the cutoff frequencies for the Si-confined modes, modal fields are observed inside the Pyrex substrate. The lowest frequencies where the field components are still exponentially decaying inside the Pyrex substrate ($\sim \beta / k_0 > n_{px}$, in which $n_{px} = 2.1$ is the refractive index of Pyrex) is defined as the cutoff. It is quite interesting that although the simulated propagation constants are obtained considering a ground plane below the 500 μm thick Pyrex substrate, the attenuation constants below the cutoff frequencies (where $\beta / k_0 < 2.1$) show strong attenuations due to the Pyrex material loss. In other words, the cutoff frequencies are accompanied by upward trends in the attenuation constants at lower frequencies. This is interesting, since unconfined modes are suppressed due to increased Pyrex material loss at higher frequencies.

The purpose of this section is to present a design for low-loss suspended SOG waveguide structures which cover the frequency range of 330 - 600 GHz with single mode operations.

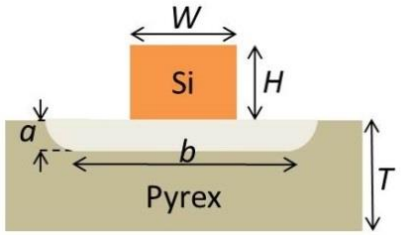

Fig. 4.18 Suspended SOG waveguide cross section.

Table. 4.4. Dimensions of the SOG structures (Fig. 4.18) studied in Figs. 4.19-21.

W (μm)	H (μm)	T (μm)	a (μm)	b (μm)
310	100	500	100	500
200	100	500	100	200
160	100	500	100	140

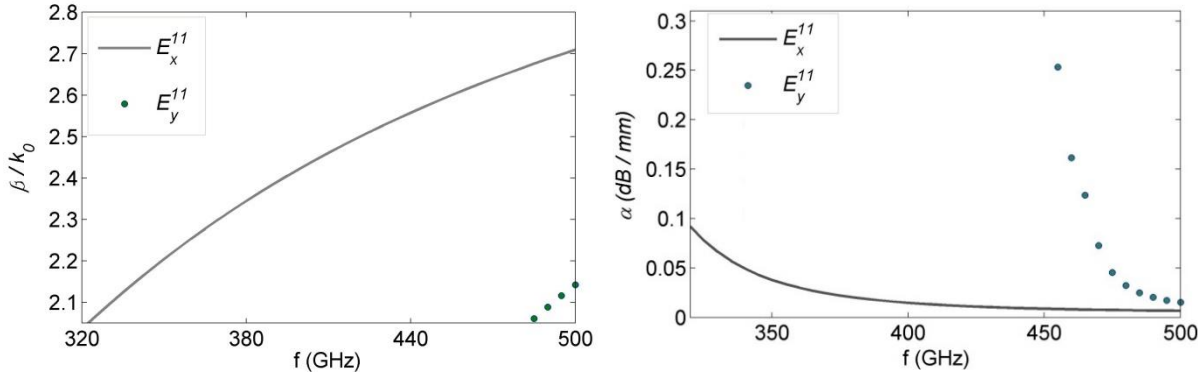

(a) (b)

Fig. 4.19 Propagation constant of the suspended SOG waveguide with W = 310 μm: a) normalized phase constant, and b) attenuation constant.

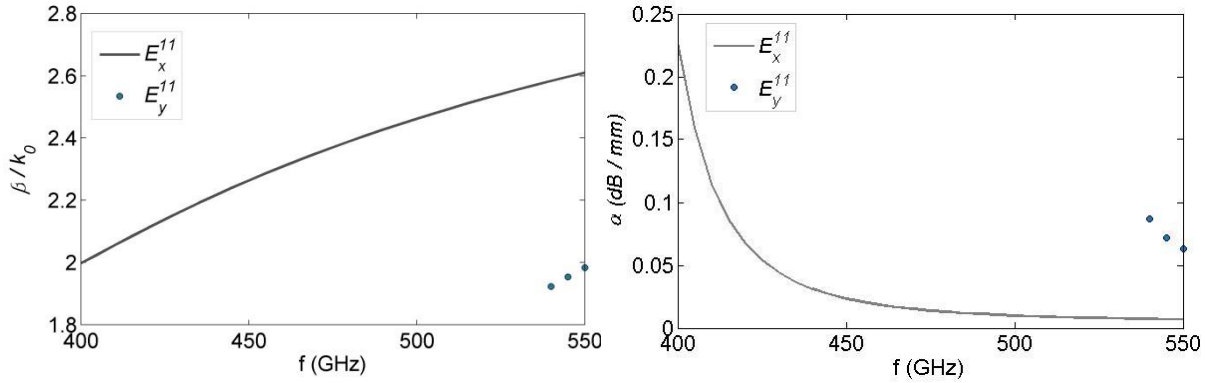

(a) (b)

Fig. 4.20 Propagation constant of the suspended SOG waveguide with W = 200 μm: a) normalized phase constant, and b) attenuation constant.

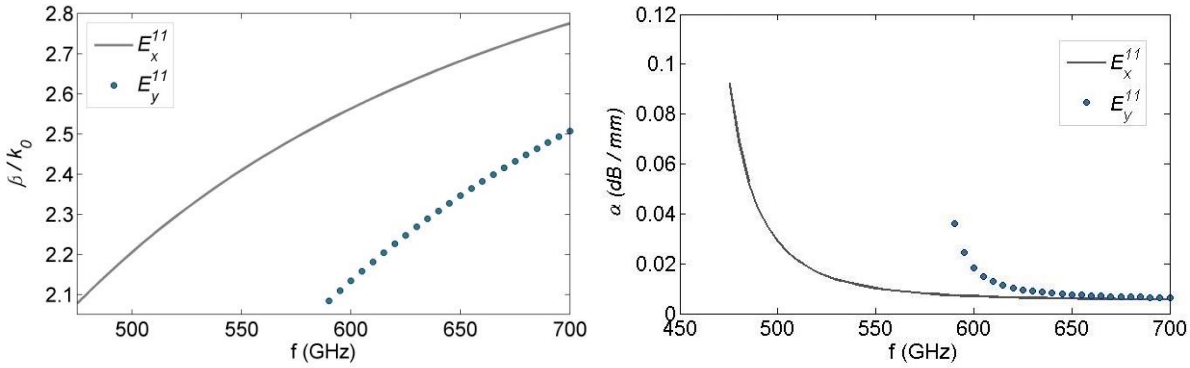

(a) (b)

Fig. 4.21 Propagation constant of the suspended SOG waveguide with W = 160 μm: a) normalized phase constant, and b) attenuation constant.

For the suspended SOG waveguide with W = 310 μm investigated theoretically and experimentally in the previous section, the simulation and measurement results over 440 - 500 GHz were in excellent agreement. The measurement results showed an average attenuation constant of 0.0346 dB/λ_0 (upper limit) over the frequency range of 440 - 500 GHz. Although the waveguide was not measured over its single mode operation bandwidth, the E_y^{11} mode was not excited due to the polarization of the electric field of the rectangular waveguide exciting the SOG waveguide. This is confirmed by simulating part of the test setup including the rectangular waveguide port, the transition to the suspended SOG waveguide, and a length L' = 2.3 mm of the suspended SOG waveguide. The simulation is performed for a number of guided modes of the suspended SOG waveguide. The results demonstrate that the coupling to the higher order mode is always below -20 dB, even in the misaligned cases studied in Fig. 4.16.

To gain a better understanding of the performance of the suspended SOG waveguide, simulation and measurement results of the structure, which were discussed in Section 4.5.2.1, are shown in Fig. 4.22 over the frequency range of 350 - 500 GHz. As shown in Fig. 4.22, there are dips at frequencies of ~ 344 GHz and ~ 421 GHz in the simulated and measured insertion loss results. Further investigation shows that the dip at ~ 345 is due to the Bragg Effect in the periodic structures, while the dip at ~ 421 GHz is due to the coupling to the leaky modes inside the Pyrex substrate. These effects, which limit the operation bandwidth of the suspended SOG waveguide, are studied in this Section.

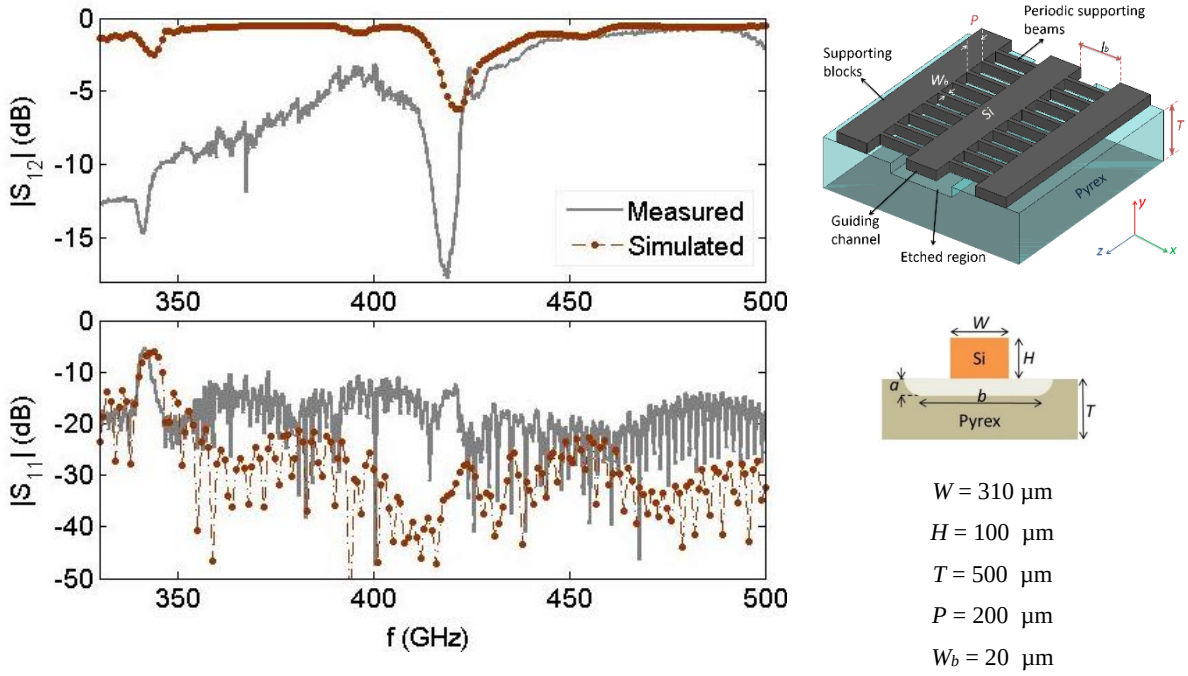

Fig. 4.22 Simulated and measured scattering parameters of the suspended SOG waveguide.

4.5.3.2 Bragg Effect

To understand the dips at ~ 344 GHz and 420 GHz in the suspended SOG waveguide structure more deeply, simulations are performed in HFSS for different beam dimensions over 330 - 500 GHz. The simulation results are shown in Fig. 4.23. For a choice of $P = 200$ μm, three dips are observed at frequencies of ~ 344 GHz, ~ 396 GHz, and ~ 421 GHz. Further studies show that at 344 GHz, the Bragg condition is satisfied which means $\beta \times P$ is an absolute coefficient of π. Observation of the electric field distributions at ~ 396 GHz and ~ 421 GHz confirms that the dips are related to the coupling to the leaky modes inside the Pyrex substrate.

Table 4.5 summaries the dip frequencies and the insertion loss at these frequencies for different thicknesses of the Si beams. By increasing the thickness of the beams, the frequencies of the dips are shifted downward. However, the variation in the dip frequencies with the thickness of the beams is not very clear. The insertion loss at the dip frequency of ~ 420 GHz increases from - 1.1 dB to - 15.6 dB when the thickness of the beams increases from $W_b = 10$ μm to $W_b = 50$ μm.

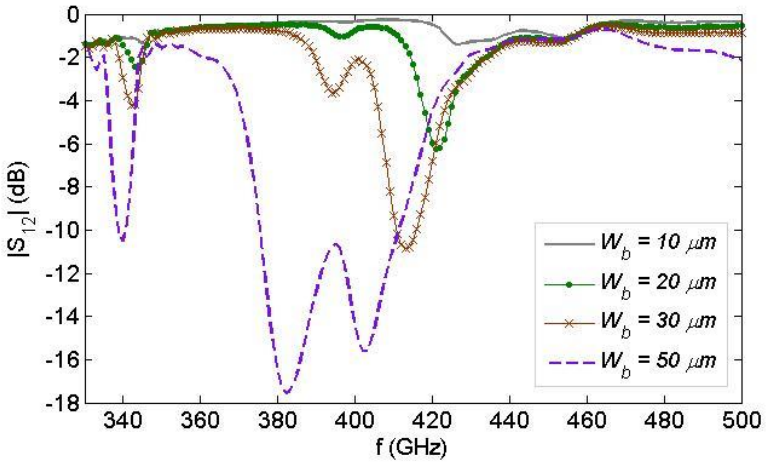

(a)

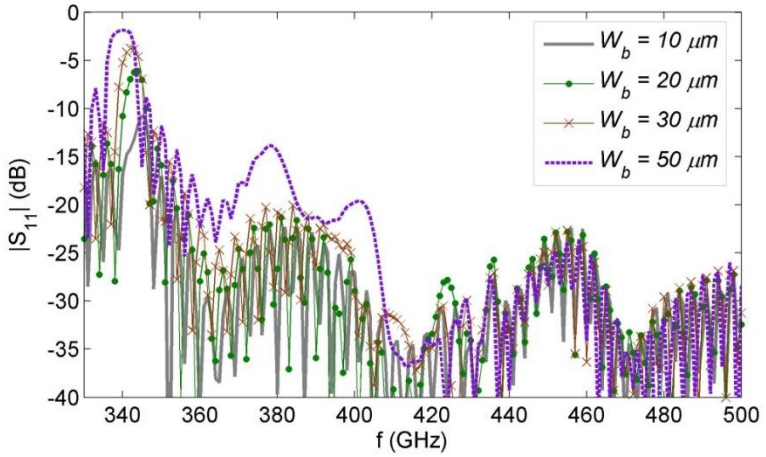

(b)

Fig. 4.23 Scattering parameters of the suspended SOG waveguide with $P = 200$ μm for different thicknesses of the Si beams: a) insertion loss, and b) return loss.

Table. 4.5. Dip frequencies in the insertion loss of the suspended SOG waveguide.

W_b (μm)	f_{dip1} (GHz)	$\|S_{12}\|$ (f_{dip1}, dB)	f_{dip2} (GHz)	$\|S_{12}\|$ (f_{dip2}, dB)	f_{dip3} (GHz)	$\|S_{12}\|$ (f_{dip3}, dB)
10	345	-1.4	397	-0.38	427	-1.4
20	344	-2.5	396	-1.0	421	-6.2
30	342	-4.2	394	-3.7	413	-10.9
50	340	-10.5	382	-17.5	403	-15.6

To overcome the problem of higher attenuation due the Bragg effect, two solutions are considered. The first approach investigated is to decrease the thickness of the beams (W_b) to make the effect of the supporting beams on the propagation constant weaker. However, decreasing the thickness of the beams sacrifices the mechanical stability of the Si guiding channel. To provide a strong mechanical support for the Si guiding channel over the etched region of the Pyrex substrate, the Si supporting beams cannot be made thinner than certain limit.

Decreasing the period of the structure is the preferred and more practical solution to avoid the appearance of the Bragg effect and leaky modes over the single-mode operational bandwidth of the waveguide. This solution also provides stronger mechanical support for the Si guiding channel by increasing the number of supporting beams.

4.5.3.3 Design Parameters and Simulation Results

Suspended SOG waveguides with three different widths of the guiding channel are designed to cover the frequency ranges of 350 - 490 GHz, 420 - 500 GHz, and 500 - 600 GHz with single mode operation. Fig. 4.24 shows the structure of the suspended SOG waveguide and its parameters. The dimensions of these waveguides are provided in Table 4.6. The simulation results for these structures are shown in Figs. 4.25-29. Each suspended SOG waveguide is simulated for two different widths of the etched region below the Si guiding channel (*b* in Fig. 4.24). Simulations are conducted to find the magnitudes of the scattering parameters for the transitions from the rectangular waveguide to the suspended SOG waveguide, a length of $L_1 \sim 10$ mm of the suspended SOG waveguide, and back again to the rectangular waveguide. For these new designs, the length of the aluminum holder (the distance between the two rectangular waveguide openings) is 10.4 mm. The length of the glass substrate is 10.2 mm. The length L_1, mentioned in Table 4.6, indicates the lengths of the Si guiding channels between the two Si tapered sections.

In all of the suspended SOG waveguide structures, the period of the waveguide is designed to prevent the appearance of the Bragg effect over the operation bandwidths. In the case of the waveguides with $W = 310$ μm and 200 μm, this is achieved with a choice of $P = 100$ μm. In the waveguide with $W = 160$ μm, which is designed for operation over 500 - 660 GHz, a period of $P = 100$ μm leads to the appearance of the Bragg effect at 584 GHz. However, a choice of $P = 80$ μm gives excellent performance without the appearance of the Bragg effect over the 500 - 660 GHz band. In these structures with a period of $P = 80$ μm, a Bragg band gap occurs at a frequency of 677 GHz where the insertion losses in suspended SOG waveguides 5 and 6 (Table 4.6) reaches 12 dB and 10.7 dB,

respectively. Fig. 4.28 shows the simulation results for the suspended SOG waveguide 8, which has dimensions similar to those of suspended SOG waveguide 6, with a different period of P = 100 µm. With a period of P = 100 µm, the waveguide shows a Bragg band gap at the center frequency of 584 GHz, with an insertion loss of 16 dB at the dip.

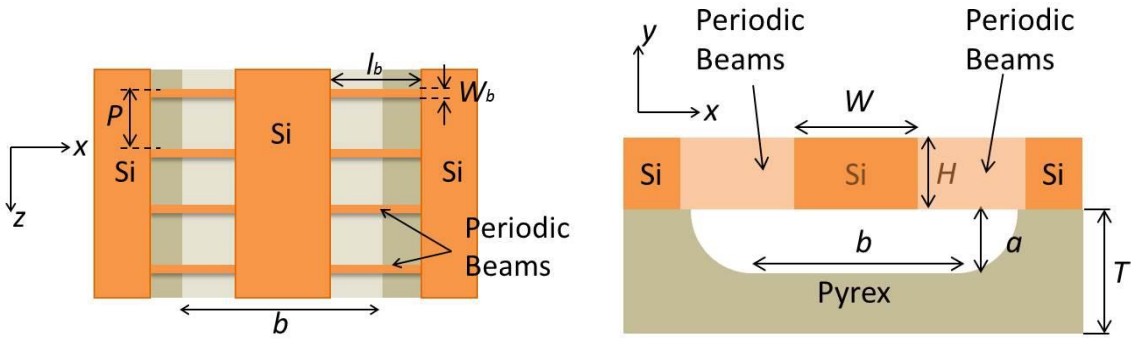

(a) (b)

Fig. 4.24 Suspended SOG waveguide structure and dimensions: a) top view, and b) side view.

Table. 4.6. Dimensions of the suspended SOG waveguides studied in Figs. 4.25-29.

Suspended SOG #	L_1 (mm)	L_2 (µm)	W (µm)	H (µm)	P (µm)	a (µm)	b (µm)	T (µm)	l_b (µm)	bandwidth (GHz)	fabricated
1	10.0	20.0	310	100	100	100	500	500	400	350-490	fabricated
1 (modified)	10.1	20.1	310	100	100	100	500	500	400	350-490	fabricated
2	10.2	20.2	310	100	100	100	700	500	400	350-490	---
3	10.2	20.2	200	100	100	100	200	500	300	420-500	fabricated
4	10.2	20.2	200	100	100	100	300	500	300	420-500	fabricated
5	10.2	20.2	160	100	80	100	140	500	300	500-660	fabricated
6	10.2	20.2	160	100	80	100	220	500	300	500-660	fabricated
7	10.2	20.2	160	100	80	100	320	500	300	500-660	fabricated
8	10.2	20.2	160	100	100	100	220	500	300	500-660	---

It is worth mentioning that while the single mode operation bandwidth extend over the frequency range of 500 - 600 GHz for the suspended SOG waveguide with W = 160 μm, it is designed for measurement over the wider frequency range of 500 - 660 GHz. For single mode operation up to 660 GHz, Si wafers with smaller thickness would be required. However, to test the high performance of the proposed suspended SOG waveguide at high frequencies up to 660 GHz, the single mode condition is neglected over 600 - 660 GHz. Since the simulations confirm that even in the case of misalignments of the suspended SOG waveguide inside the test setup, the higher order E_y^{11} mode is not excited, the dominant mode propagation constant derived from the measurements can be considered valid.

In the fabricated suspended SOG waveguide, for which the measurement results were presented in Section 4.5.2.1, the length of the beams was equal to l_b = 820 μm. Simulations show that with a length of l_b = 300 μm of the beams, the coupling between the main Si guiding channel and the two Si supporting blocks is negligible. In the modified designs, as shown in Table 4.4, the length of the supporting beams is reduced to l_b = 300 / 400 μm.

One effect which has been observed to destroy the fabrication accuracy of the suspended SOG process, is the rising temperature of the Si in the suspended regions during DRIE [91]. It is possible to cool the glass substrate during DRIE, but the heat induced on suspended Si structures needs to be transferred to the glass substrate through narrow Si beams. If the suspended beams are long, the heat cannot be quickly transferred to the glass substrate. Excessive heating of Si causes photoresist mask erosion, a reduction in the etch rate and mask selectivity, and a thinning of narrow features.

To make sure the shapes of the Si suspended beams are accurately maintained during DRIE, the width of the etched region on the glass substrate (b) is decreased in the modified designs. To see the effect of this parameter on the waveguide attenuation, simulations are performed for several values of the widths of the etched region on the Pyrex substrates. As the simulation results in Figs. 4.25-27 show, by increasing the widths of the etched regions on the Pyrex substrates, the insertion losses of the suspended SOG waveguides decrease. However, with the selected design parameters, as long as the interaction of the modal fields with the Pyrex substrate remains minimal, an increase in the insertion loss due to a decrease in the width of the etched region is not crucial. In the waveguide with W = 160 μm, three suspended SOG structures 5, 6, and 7 show average insertion losses of 0.54 dB, 0.47 dB, and 0.43 dB over 500 - 660 GHz, respectively.

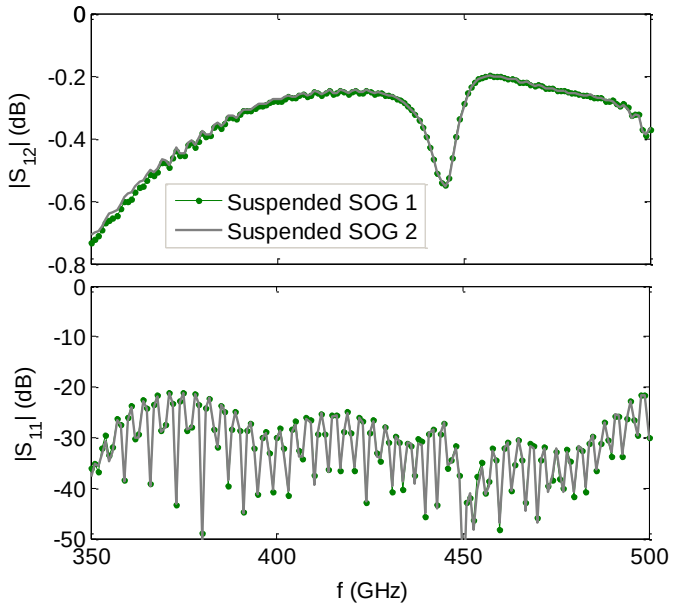

Fig. 4.25 Simulated scattering parameters of the suspended SOG waveguides (W = 310 μm, Table 4.6) for length L_1.

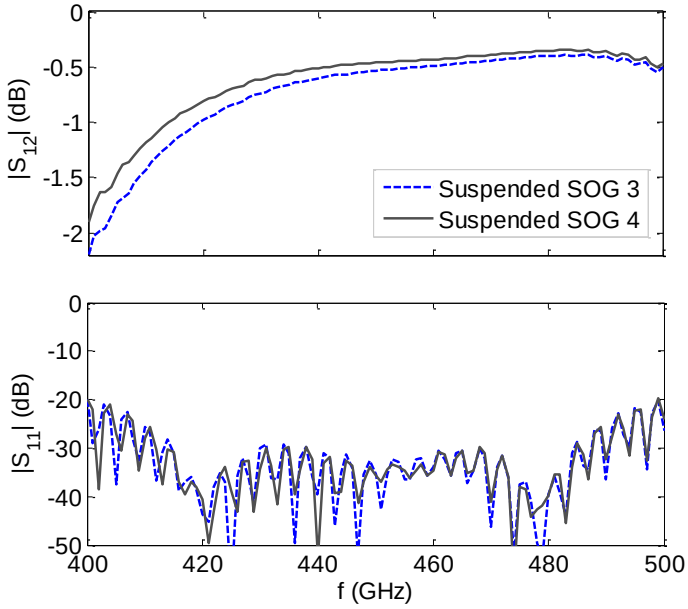

Fig. 4.26 Simulated scattering parameters of the suspended SOG waveguides (W = 200 μm, Table 4.6) for length L_1.

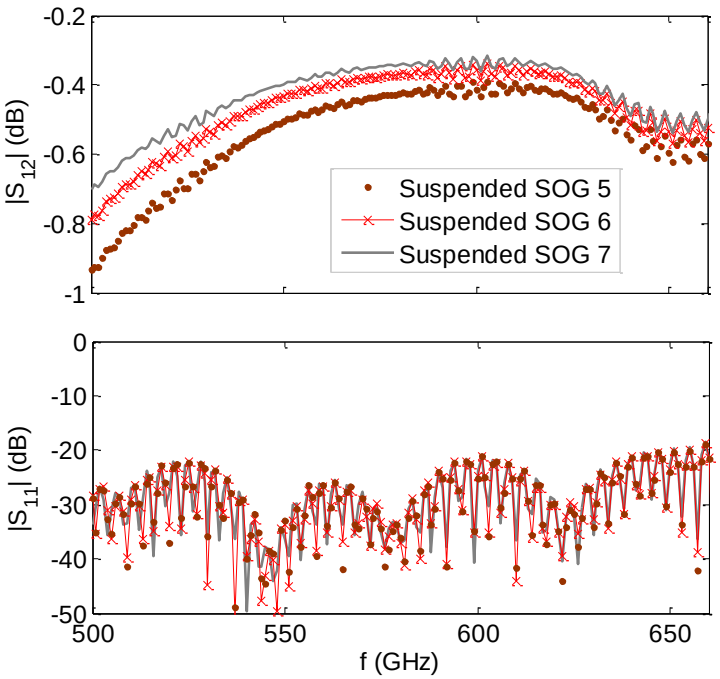

Fig. 4.27 Simulated scattering parameters of the suspended SOG waveguides (W = 160 µm, Table 4.6) for length L_1.

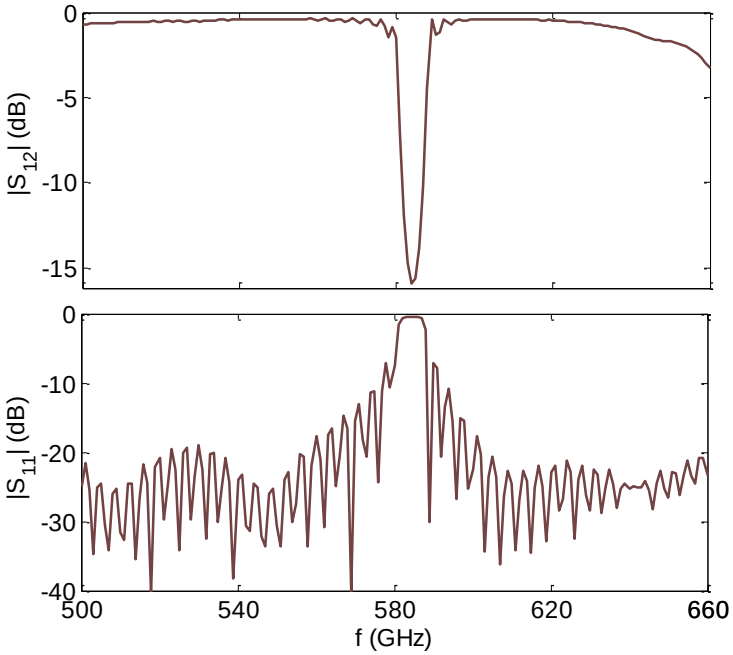

Fig. 4.28 Simulated scattering parameters of the suspended SOG waveguide 8 (W = 160 µm, Table 4.6) for length L_1.

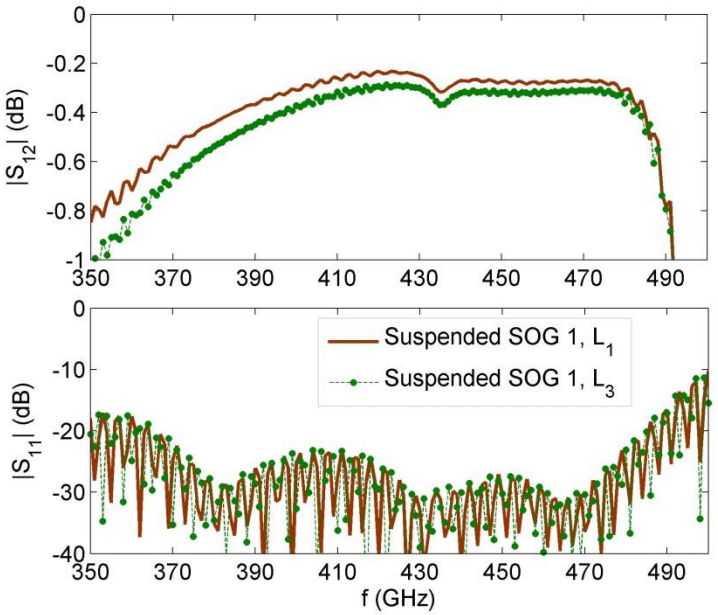

Fig. 4.29 Simulated scattering parameters of the suspended SOG waveguide (W = 310 µm, suspended SOG 1 (modified) in Table 4.6) for two lengths of L_1 = 10.1 mm and L_3 = 15.1 mm.

Due to the isotropic characteristic of HF wet etching, the etched sidewalls are not vertical [127]. This characteristic is represented in Fig. 4.24. As shown in this figure, the etched sidewalls are round. An isotropy of 1:1 was reported for Pyrex glass HF etching using a Cr/Au mask [127]. Considering an isotropy of 1:1, the etched region on the top is bigger than that at the bottom (b) by two times of the depth of etching into the glass substrate and equal to $W_c = 2 \times a + b$.

The simulation results presented in Fig. 4.17 confirmed that the dip at ~ 453 GHz in the insertion loss of the suspended SOG waveguide (W = 310 µm and P = 200 µm) is related to the transition. The dip frequency is dependent on the distance between the rectangular waveguide opening and the beginning of the tapered section. In the modified designs, this waveguide is designed in two different lengths of 10 mm and 10.1 mm (d = 200 µm and d = 150 µm, respectively), which shifts the dip frequency to 440 GHz and 500 GHz, respectively. The simulation results for these two structures are shown in Figs. 4.25, 29, respectively. This waveguide is fabricated for these two transitions. The fabricated suspended SOG waveguides are represented as "fabricated" in Table 4.6. All of the fabricated waveguides are made in two different lengths of L_1 ~ 10 mm and L_2 ~ 20 mm.

Fig. 4.29 shows the simulation results for the insertion losses of the two different lengths of L_1 = 10.1 mm and L_3 = 15.1 mm of the suspended SOG 1 waveguide. Since the simulation of a length of L_2 = 20.1 mm of the fabricated waveguide needs a large amount of memory and simulation time, the simulations are performed for a shorter length of L_3 = 15.1 mm. The insertion losses of the two lengths of L_1 = 10.1 mm and L_3 = 15.1 mm of the waveguide are respectively 0.49 dB and 0.56 dB, on average, over the frequency band of 350 - 500 GHz. An estimated attenuation constant of 0.14 dB/cm is obtained from the difference between the insertion losses of the two different lengths.

4.5.3.4 Fabricated Samples

Microscopic and SEM images of the samples at different stages of the fabrication are provided in Fig. 4.30. Fig. 4.30(a) shows the microscopic image of the etched surface of the Pyrex substrate. This figure shows the etched channel on the Pyrex surface for the suspended SOG 6 (W = 160 μm and b = 220 μm) design. The black regions show the etched sidewalls. The measured width of the etched region is b = 228 μm. The etched depth, which was measured under the dektak profilometer (a measuring instrument used to measure a surface's profile), is 86 μm. The measured width of the etched sidewalls at one point is 108 μm. As shown in this figure, the etched sidewalls do not have a regular shape. The light color shows the smooth surfaces, either etched or non-etched, on the glass substrate while the black regions show the sloped etched sidewalls.

Fig. 4.30(b, c) show the thick photoresist mask on the Si surface before DRIE for the suspended SOG 6 (W = 160 μm and P = 80 μm). Fig. 4.30(d) shows the microscopic image of the fabricated suspended SOG 1 with W = 310 μm, P = 100 μm, and W_b = 20 μm. The corresponding measured parameters are 314.3 μm, 100.2 μm, and 19.3 μm, respectively. The errors are mainly reading errors under the microscope and not fabrication errors. Fig. 4.30(e) shows the SEM image of the fabricated sample looking in the z-direction. The etched region inside the Pyrex substrate is shown in this figure. Fig. 4.30(f) shows the SEM image of the waveguide at the connection between the Si supporting block and Si supporting beams. Fig. 4.30(g) shows the fabricated samples in two different lengths.

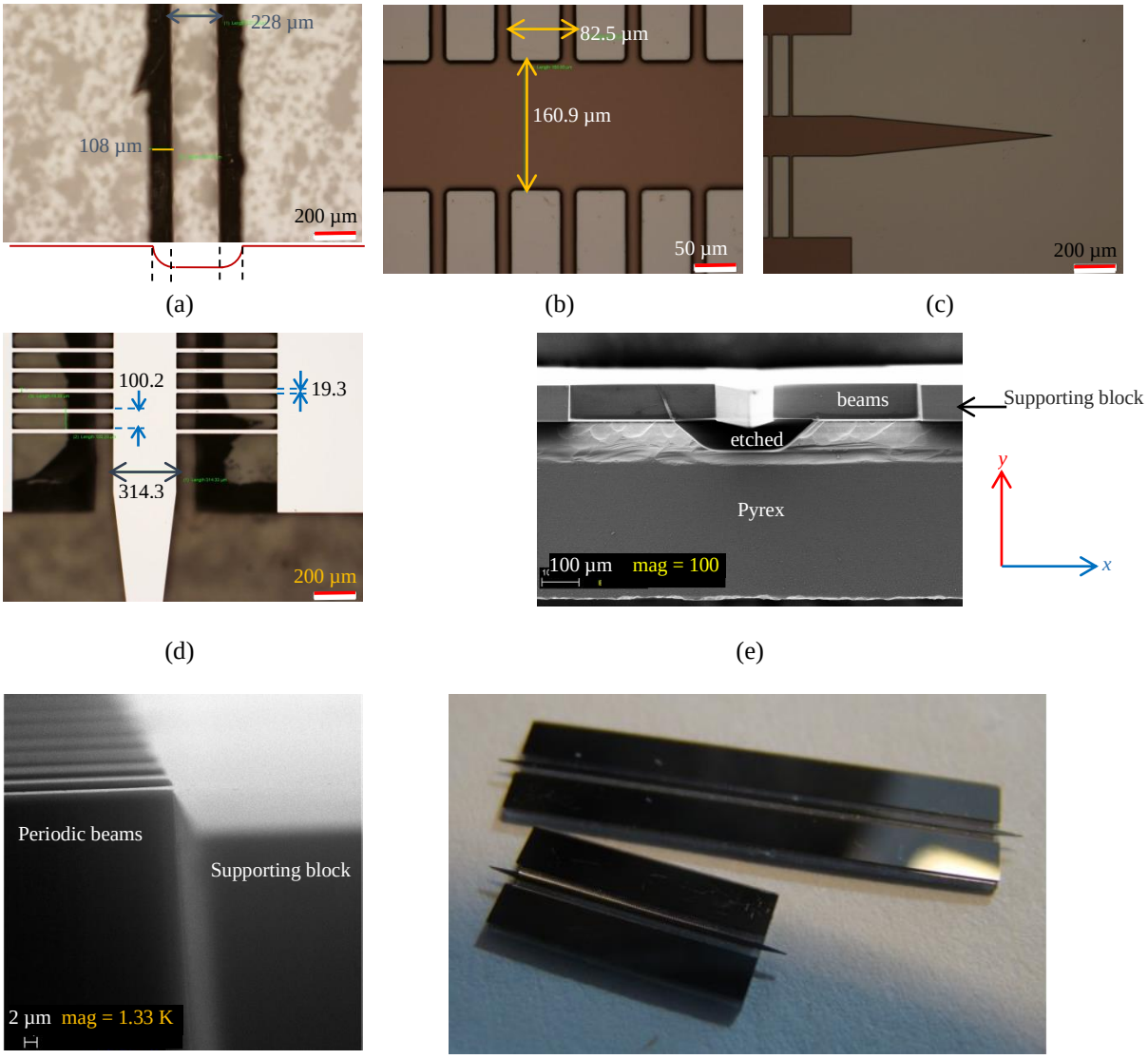

Fig. 4.30 Microscopic and SEM images of the suspended SOG waveguides: a) microscopic image of the etched region on the Pyrex surface, b) and c) microscopic images of the patterned photoresist mask on the Si surface at different locations, d) microscopic image of the fabricated sample after DRIE, e) SEM image of the waveguide looking in the *z*-direction, f) SEM image of the waveguide showing the supporting block and the Si beams connected to it, and g) fabricated suspended SOG waveguides for two different lengths of ~10 mm and ~20 mm.

4.5.3.5 Measurement Results

The fabricated suspended SOG waveguides with $W = 310$ μm, $W = 200$ μm, and $W = 160$ μm are measured over frequency ranges of 350 - 500 GHz, 400 - 500 GHz, and 500 - 660 GHz, respectively. For these measurements metallic rectangular waveguide ports WR 2.2 and WR 1.5 are used over frequency ranges of 325 - 500 GHz and 500 - 750 GHz, respectively.

Fig. 4.31 shows the measured scattering parameters of the suspended SOG waveguide 1 ($W = 310$ μm) for two different lengths of $L_1 = 10.1$ mm and $L_2 = 20.1$ mm. For a length of $L_1 = 10.1$ mm, the insertion loss varies between 0.56 dB and 2.35 dB with an average of 1.08 dB over the frequency band of 350 - 500 GHz. For a length of $L_2 = 20.1$ mm, the insertion loss varies between 0.92 dB and 3.3 dB dB with an average of 1.44 dB. In both structures, the return loss is always better than 15 dB. The average difference between the insertion losses of the two lengths of L_1 and L_2 is 0.36 dB over the frequency band of 350 - 500 GHz. An average attenuation constant of 0.36 dB/cm is estimated from this difference.

The calibration technique in [119] (explained in Chapter 3) is used to extract the waveguide attenuation constant from the measured scattering parameters. The measured attenuation constants obtained using this method are shown in Fig. 4.32. The attenuation constant obtained using the same method for the simulated scattering parameters of this waveguide, for two different lengths of $L_1 = 10.1$ mm and $L_3 = 15.1$ mm, are included in this figure for comparison. For this waveguide, the single mode operation extends up to 490 GHz. However, since the second E_y^{11} mode is not excited with the polarization of the electric field of the dominant mode of the rectangular waveguide in x-direction, the dominant mode propagation constant obtained from the simulations of the two different lengths is still valid up to 500 GHz.

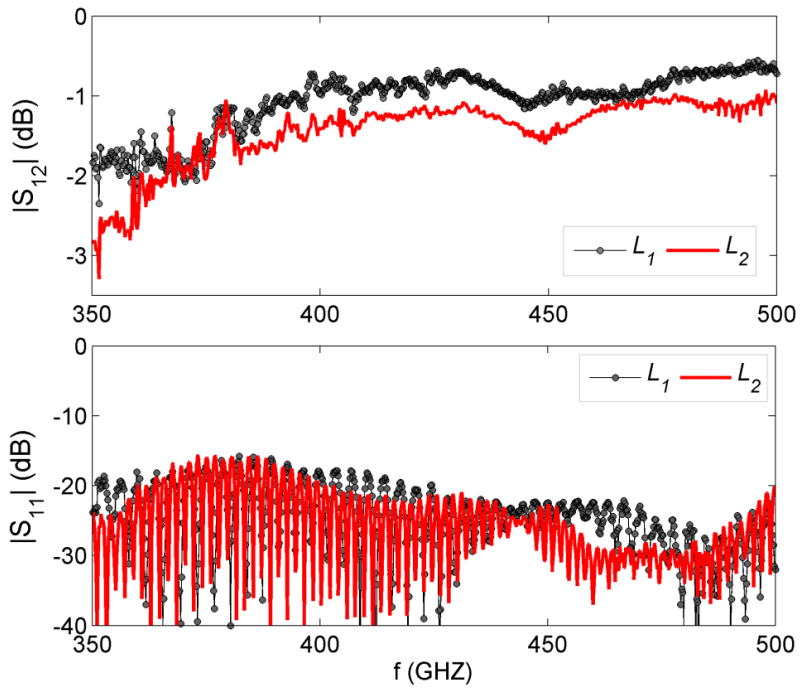

Fig. 4.31 Measured scattering parameters of the suspended SOG 1 waveguides of lengths L_1 = 10.1 mm and L_2 = 20.1 mm between the transitions.

The simulations show an attenuation constant varying over 0.002 - 0.042 dB/mm across the entire band. Measurements show an average attenuation constant of 0.043 dB/mm, or equivalently 0.031 dB/λ_0, over the entire band. The agreement between the attenuation constants obtained from the simulation and measurement is excellent. The small discrepancies between the two attenuation constants are due to the misalignments of the SOG waveguides inside the test setups and to the network analyzer calibration errors. Although precise alignments are performed during the calibration steps (Thru, Reflect, Line), small calibration errors are still inevitable at these high frequencies.

Fig. 4.32(b) shows the network analyzer calibration error, which is defined as the insertion loss of the thru connection of the two metallic ports after the calibration. The maximum calibration error is $|S_{12}|$ = 0.6 dB at 367 GHz. The average calibration error over the entire band of 325 - 500 GHz, is 0.08 dB. Due to the low-loss characteristics of the SOG waveguides under test, the differences between the insertion losses of the two lengths (0.36 dB on average) falls under PNA-X calibration error. In this situation, even small calibration errors will affect the test results. Over the frequency range of 360 -

380 GHz, the obtained attenuation constants are not valid due to the calibration error which reaches to its maximum value at ~ 367 GHz.

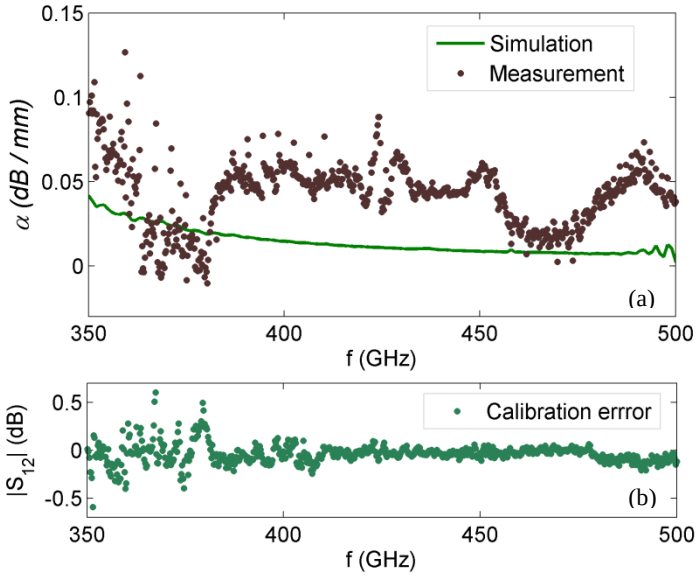

Fig. 4.32 a) Attenuation constant of the suspended SOG 1 obtained based on simulations and measurements of the two lengths and b) the calibration error of the PNA-X.

The measured scattering parameters for a length of L_1 = 10.2 mm of the suspended SOG waveguides 3 and 4, which have dimensions W = 200 μm with two different widths of the etched regions on the Pyrex substrates of b = 200 and 300 μm, are shown in Fig. 4.33. As this figure shows, the differences between the insertion losses of the two waveguides are not significant. The two waveguides with b = 300 μm and b = 200 μm show insertion losses of 1.6 dB and 1.7 dB (on average over 400 - 500 GHz), respectively. As the frequency decreases to 400 GHz, the difference between the measured scattering parameters of the two waveguides becomes more expressed. The confinement of the modal fields inside the Si decreases with frequency; therefore, the effects of the dimensions of the etched regions on the scattering parameters become more significant.

Fig. 4.34 shows the measured scattering parameters of the suspended SOG waveguide 4 (W = 200 μm and b = 300 μm) for two different lengths: L_1 = 10.2 mm and L_2 = 20.2 mm. For a length of L_1 = 10.2 mm, the insertion loss varies between 0.9 dB and 5.03 dB with an average of 1.70 dB over the frequency

band of 400 - 500 GHz. For a length of L_2 = 20.2 mm, the insertion loss varies between 1.17 dB and 7.60 dB with an average of 2.29 dB. For both structures the return loss is always better than 12.5 dB. The average difference between the insertion losses of the two lengths, L_1 and L_2, is 0.59 dB over the entire frequency band of 400 - 500 GHz. An average attenuation constant of 0.59 dB/cm is estimated from this difference. The attenuation constant obtained from the measurements of the two lengths of this waveguide, based on the calibration technique in [119], is shown in Fig. 4.35.

The attenuation constant obtained from the measurements is quite small, varying between 0.009 dB/mm and 0.3 dB/mm with an average of 0.061 dB/mm, or equivalently 0.042 dB/λ_0, over the entire frequency band of 400 - 500 GHz. Table 4.7 summarizes the measurement results of the suspended SOG waveguides.

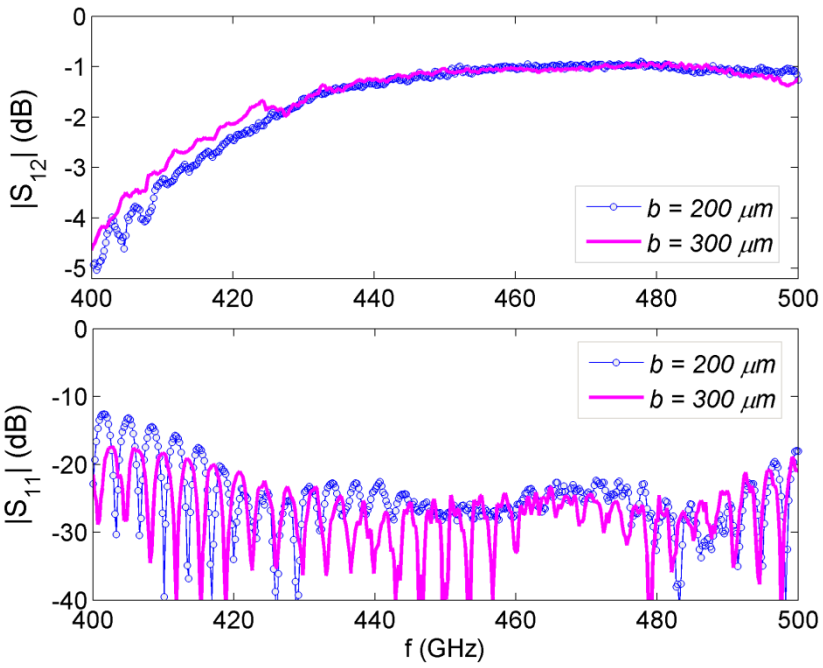

Fig. 4.33 Measured scattering parameters of the suspended SOG 3 and 4 waveguides with W = 200 μm, for a length of L_1 = 10.2 mm between the transitions.

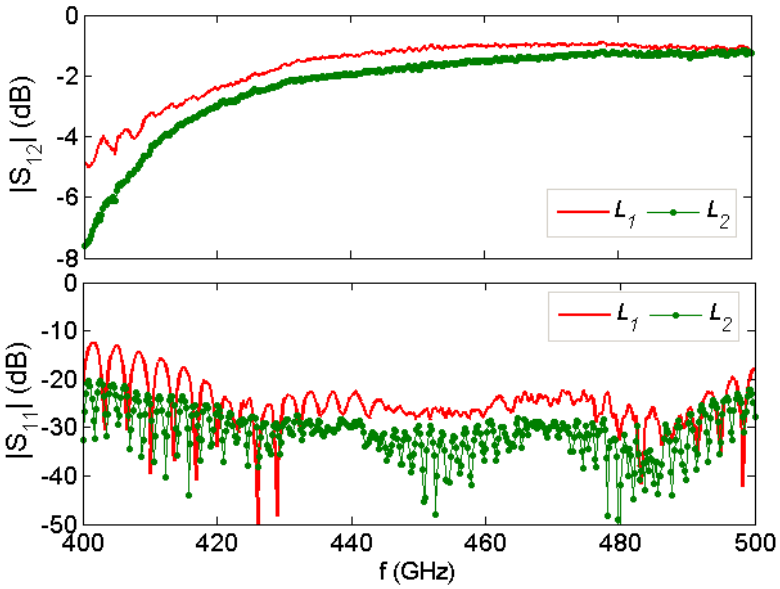

Fig. 4.34 Measured scattering parameters of the suspended SOG 4 waveguides of lengths L_1 = 10.2 mm and L_2 = 20.2 mm between the transitions.

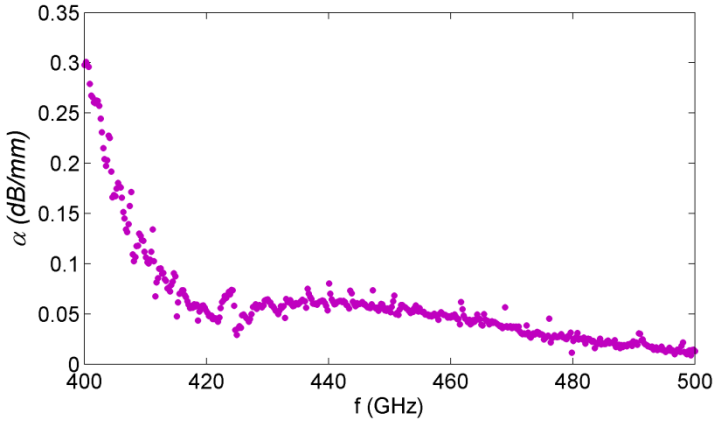

Fig. 4.35 Attenuation constant of the suspended SOG 4 obtained from measurements.

Table. 4.7. Measured attenuation constants (α) of the suspended SOG waveguides.

W (μm)	f (GHz)	dB/mm	dB/mm (average)	dB/λ_0 (average)
310	350 - 500	0.002 - 0.042	0.043	0.031
200	400 - 500	0.009 - 0.3	0.061	0.042

4.6 Corrugated SOG Integrated Technology Platform

For applications requiring high density circuits, a new and more convenient SOG structure is proposed. In the proposed structure, which is called the *corrugated SOG platform*, parts of the glass substrate below the high-quality Si channels and passive components are etched in periodic patterns [109, 114]. In the first part of this section, measurement results of the corrugated SOG waveguides are provided and compared to those of the simple SOG waveguides over a frequency range of 85 - 110 GHz. These findings demonstrate how etching the Pyrex substrate improves the SOG waveguide's loss characteristics. In the second part, simulation results are presented to investigate the application of the corrugated SOG platform at higher frequencies, up to 500 GHz. For higher frequency applications, two techniques of etching the Pyrex substrate are investigated by computational simulations. These two techniques are: Pyrex dry etching technique, and wet etching in HF 49 %.

4.6.1 Performance Verification

In this section, SOG waveguides are experimentally investigated in two different configurations: SOG waveguide (in which the Pyrex substrate is not etched) and corrugated SOG waveguide. The corrugated SOG waveguide structure is shown in Fig. 4.36. In the two SOG waveguide configurations, the width of the Si channels is W = 1.1 mm, their height is H = 500 µm, and the thickness of the glass substrates is T = 500 µm. In the SOG waveguide structures, the glass substrates are not etched, while in the corrugated SOG waveguide structures, as shown in Fig. 4.36, the glass substrates are etched in a periodic manner. In the corrugated structures, the period of the etched patterns is P = 500 µm, the depth of etching is a = 100 µm, and the other dimensions are selected as b = 1 cm and d = 60 µm. The SOG waveguides are excited with their dominant E_x^{11} modes.

The measured insertion losses for two different lengths of these waveguides, L_1 = 1 cm and L_2 = 2 cm, which fall between the two transitions to the rectangular waveguide ports of the test setup (WR 10), are shown in Fig. 4.37.

The estimated waveguide attenuations obtained from the differences between the averaged measured insertion losses of the two lengths of these waveguides are 0.25 dB/cm and 0.21 dB/cm for the SOG waveguide and corrugated SOG waveguide, respectively. Using the corrugation technique, the attenuation constant of the corrugated SOG waveguide is decreased by 0.04 dB/cm (average over 95 - 110 GHz). At higher frequencies above 200 GHz, the material loss in the Pyrex substrate increases rapidly and etching the glass substrate reduces the waveguide attenuation more significantly.

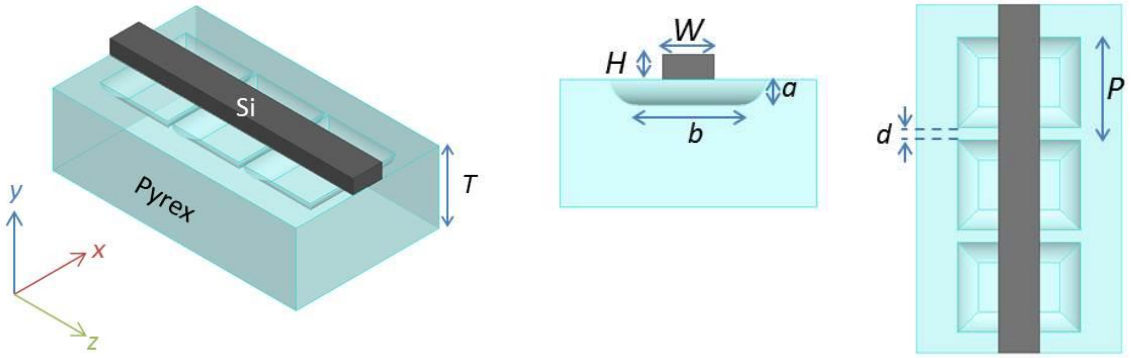

(a) (b) (c)

Fig. 4.36 Corrugated SOG waveguide structure and dimensions: a) 3D view, b) side view, and c) top view. The Pyrex patterns have been created by wet etching.

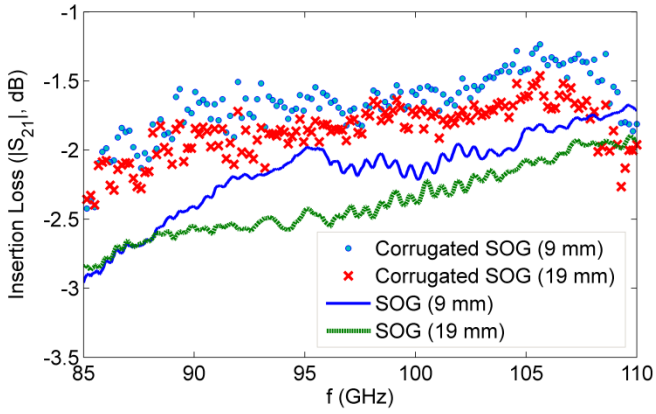

Fig. 4.37 Measured insertion losses of different SOG waveguide structures.

Fig. 4.38 shows the simulated scattering parameters of the SOG and corrugated SOG waveguides over the frequency band of 250 - 300 GHz. This figure shows the scattering parameters for a length of L = 10.2 mm of these waveguides between the two transitions to the metallic waveguides (WR 3). In these two waveguides, the Si channels have dimensions of H = 200 μm and W = 350 μm, and the thickness of the glass substrate is T = 500 μm. The corrugation patterns have a period of P = 500 μm. The other dimensions are provided in Fig. 4.38. As the simulation results show, with a thickness of d = 50 μm between the two etched regions, the corrugated SOG serves as a low-loss waveguide over this range of

frequencies. The SOG and corrugated SOG waveguide structures show average insertion losses of 1.36 dB and 0.87 dB over 250 - 300 GHz, respectively.

Table. 4.8. Measured insertion loss.

	min	max	average
$\|S_{12}\|$ (dB), SOG (1 cm)	1.67	2.21	1.97
$\|S_{12}\|$ (dB), SOG (2 cm)	1.90	2.55	2.22
SOG - α (dB/cm)	-------	-------	0.25
$\|S_{12}\|$ (dB), *corrugated* SOG (1 cm)	1.23	1.86	1.59
$\|S_{12}\|$ (dB), *corrugated* SOG (2 cm)	1.46	2.27	1.80
corrugated SOG - α (dB/cm)	-------	-------	0.21

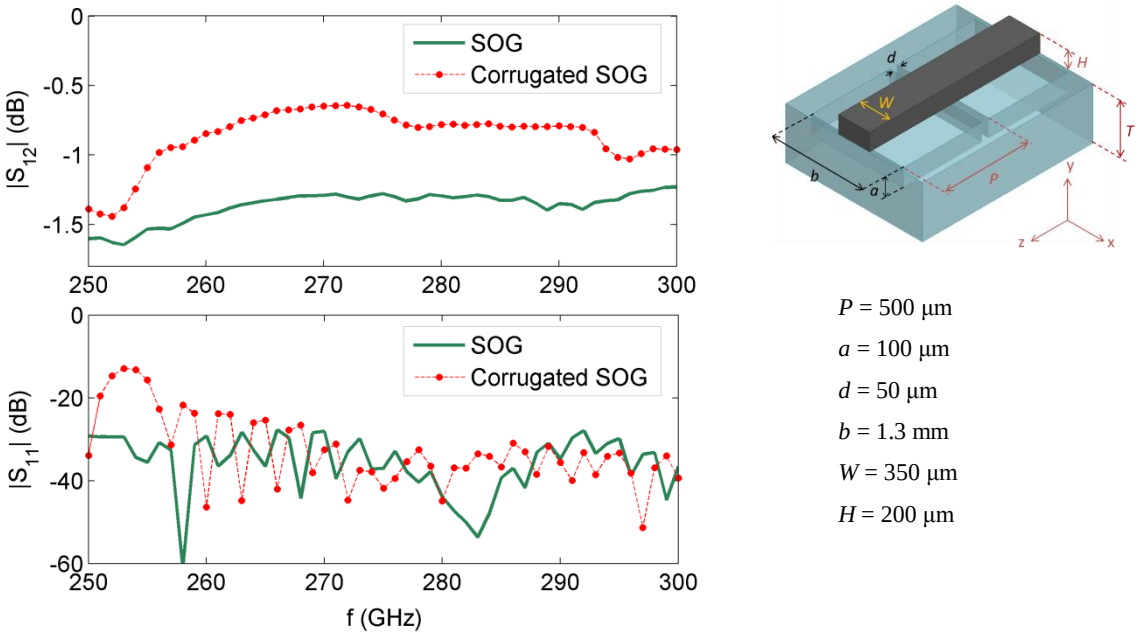

Fig. 4.38 Simulated scattering parameters of the SOG waveguide and corrugated SOG waveguide.

For the E_y^{11} mode which has weaker confinement inside the Si channel, the corrugation has a more significant effect in decreasing the insertion loss at frequencies below 200 GHz, as compared to the

E_x^{11} mode. Several integrated passive components based on the corrugated SOG technology, including bends and a power divider with E_y^{11} mode operation, are being designed for operation over the W-band by other colleagues at CIARS (Centre for Intelligent Antenna and Radio Systems) [109].

4.6.2 Investigation of Higher-Frequency Performance

To investigate the performance of the proposed corrugated SOG waveguide at higher frequencies up to 500 GHz, simulations are performed in HFSS for different dimensions of the corrugated pattern on the Pyrex substrate. In all of the simulations, the Si guiding channel dimensions are W = 200 μm and H = 100 μm, and the thickness of the Pyrex substrate is T = 500 μm (Fig. 4.36). The dimensions of the periodic corrugated patterns in all of the simulated structures are provided in Table 4.9.

The simulation results for these structures over 440 - 500 GHz are presented in Figs. 4.39-41, 43. The waveguides are simulated over their single mode operation bandwidths. The simulation results show the magnitudes of the scattering parameters for the back-to-back transitions from the rectangular waveguide to the corrugated SOG waveguide, a length of L = 10.2 mm of the corrugated SOG waveguide, and back again to the rectangular waveguide. The transition dimensions are similar to those of the suspended SOG waveguides with W = 200 μm (L_t = 1 mm).

4.6.2.1 Corrugating the Pyrex Substrate Using Hydrofluoric Acid Wet Etching Technique

Wet chemical etching using HF is the lowest cost and most commonly used technique for etching glass. Cr/Au is a commonly used mask for glass wet etching. Wet HF etching of the glass is an aggressive process. For defect-free deep channel etching into the glass substrate, masking layers which remain robust against the aggressive etchant are required. For better quality in the etched regions, a higher concentration of HF is preferred. The etch rate is determined by the concentration of HF enchant, while the defect generation rate remains the same [133]. With a highly concentrated solution (HF 49%), an etch rate ranging over 6 – 8 μm/min is achieved [133].

Due to the isotropic nature of the HF wet etching, the etched sidewalls, as shown in Fig. 4.36, are round [133]. The isotropy of the etching process is dependent on the masking material. For Cr/Au, an isotropy of 1:1 was reported [133]. As a result, the openings of the etched regions are bigger on the top of each side by the two times of the depth of etching into the Pyrex substrate. In this case, the dimensions of the periodic patterns are dependent on the depth of etching into the Pyrex substrate. The opening of the etched region should be bigger than two times the depth of etching into the Pyrex substrate. These limitations have been considered in the simulated corrugated dimensions provided in Table 4.9.

To overcome the problem of high attenuations over the Bragg band, one solution is to decrease the effect of the Bragg band. This can be done by decreasing the thickness of the Pyrex wall between the two adjacent etched regions (*d* in Fig. 4.36), and increasing the period of the corrugated SOG structure to a larger value as this minimizes the interaction of the modal fields with the Pyrex substrate. A large value for the period is also advantageous in terms of increasing the etch depth into the Pyrex substrate (e.g., to a value of a = 100 μm), which further limits the interaction of the modal fields with the Pyrex substrate. For the simulated structures with these conditions, the set of parameters are provided in Table 4.9 as corrugated SOGs 1-3.

A second solution is to prevent the appearance of the Bragg band and leaky modes over the operation bandwidth by decreasing the period of the structure. If the corrugated pattern is made by HF wet etching of the Pyrex substrate, a decrease in the period of the structure is accompanied by a decrease in the depth of the etching into the Pyrex substrate. In these structures, considering the round pattern of the etched sidewalls, the condition $P > (2 \times a + d)$ should be satisfied. Figs. 4.40, 41 show the simulated scattering parameters for the corrugated SOG waveguides with periods of P = 150 μm and P = 100 μm, respectively.

Table. 4.9. Dimensions of the corrugated SOG waveguides studied in Figs. 4.39-41, 43. The dimensions are defined in Fig. 4.36.

Corrugated SOG #	W (μm)	H (μm)	P (μm)	a (μm)	d (μm)	b (μm)	L_1 (mm)	bandwidth (GHz)	Etching technique
# 1	200	100	500	100	30	400	10.2	440 - 500	wet
# 2	200	100	500	100	20	400	10.2	440 - 500	wet
# 3	200	100	500	100	10	400	10.2	440 - 500	wet
# 4	200	100	150	50	20	400	10.2	440 - 500	wet
# 5	200	100	150	50	30	400	10.2	440 - 500	wet
# 6	200	100	150	50	10	400	10.2	440 - 500	wet
# 7	200	100	100	30	20	400	10.2	440 - 500	wet
# 8	200	100	100	30	10	400	10.2	440 - 500	dry
# 9	200	100	500	30	10	400	10.2	440 - 500	dry

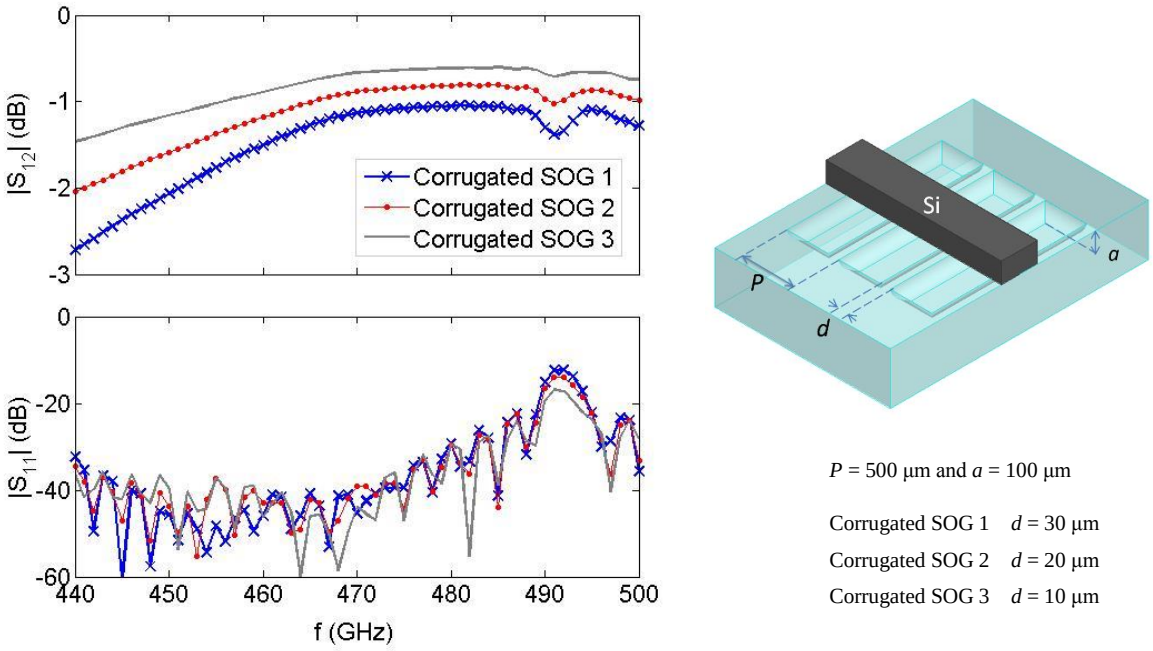

Fig. 4.39 Simulated scattering parameters of the corrugated SOG waveguides 1-3 (Table 4.9) for length L_1.

The simulation results for the corrugated SOG structures 1 - 3 show that with larger values for the period of the structure and the depth of the etching (P = 500 μm and a = 100 μm), lower insertion losses are obtained as compared to those of corrugated SOGs 4 - 7. Corrugated SOGs 1, 2, and 3 show insertion losses of 1.48 dB, 1.14 dB, and 0.85 dB, on average, over 440 - 500 GHz, respectively. As expected, in these structures the attenuation constant decreases when the thickness of the Pyrex wall between the two adjacent etched regions (d) is decreased. Table 4.10 summarizes the performances of the simulated corrugated SOG structures 1 - 7 over their operation bandwidths.

Corrugated SOG waveguides with periods of P = 100 and 150 μm are simulated in HFSS (corrugated SOGs 4 - 7). The simulation results show that for a period of P = 150 μm, the Bragg band is observed at the frequency of ~ 440 GHz. However, if the operation bandwidths of these waveguides are limited to the frequency range of 450 - 500 GHz, the corrugated SOGs 4, 5, and 6 show average insertion losses of 2.18 dB, 2.63 dB, and 1.77 dB, respectively. With a period of P = 100 μm in the corrugated SOG 3, the appearance of the Bragg effect is prevented over 440 - 500 GHz. However, this structure shows an insertion loss of 2.93 dB, on average, over 440 - 500 GHz. This amount of insertion loss is high as compared to those of corrugated SOGs 4-6 (P = 150 μm). The main reason for this difference is the

stronger interaction of the modal fields with the Pyrex substrate in the corrugated SOG 7, due to the smaller etch depth into the Pyrex substrate and smaller period.

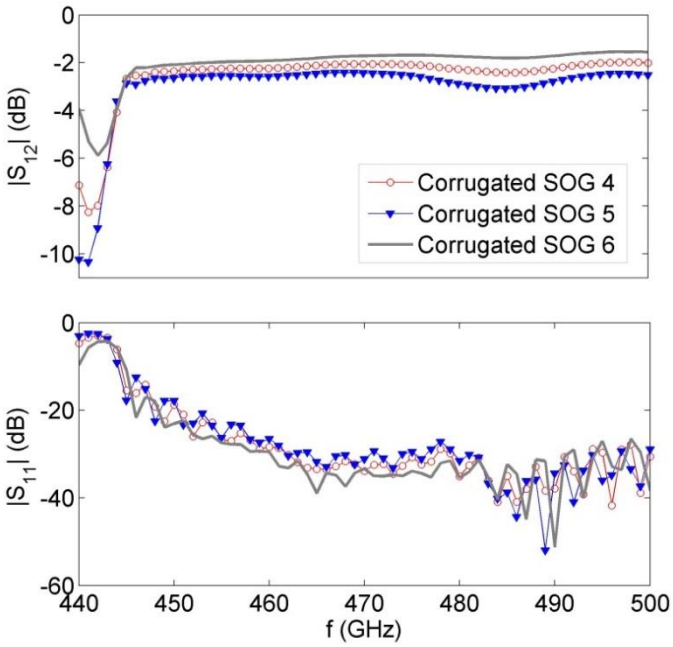

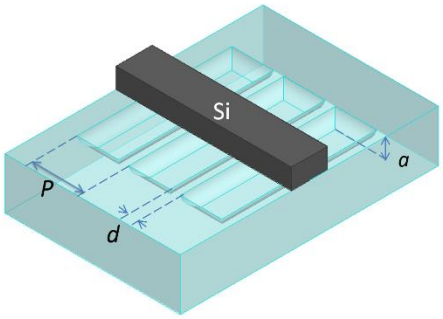

P = 150 μm and *a* = 50 μm
Corrugated SOG 4 *d* = 20 μm
Corrugated SOG 5 *d = 30 μm*
Corrugated SOG 6 *d = 10 μm*

Fig. 4.40 Scattering parameters of the corrugated SOG waveguides (Table 4. 9) for length L_1.

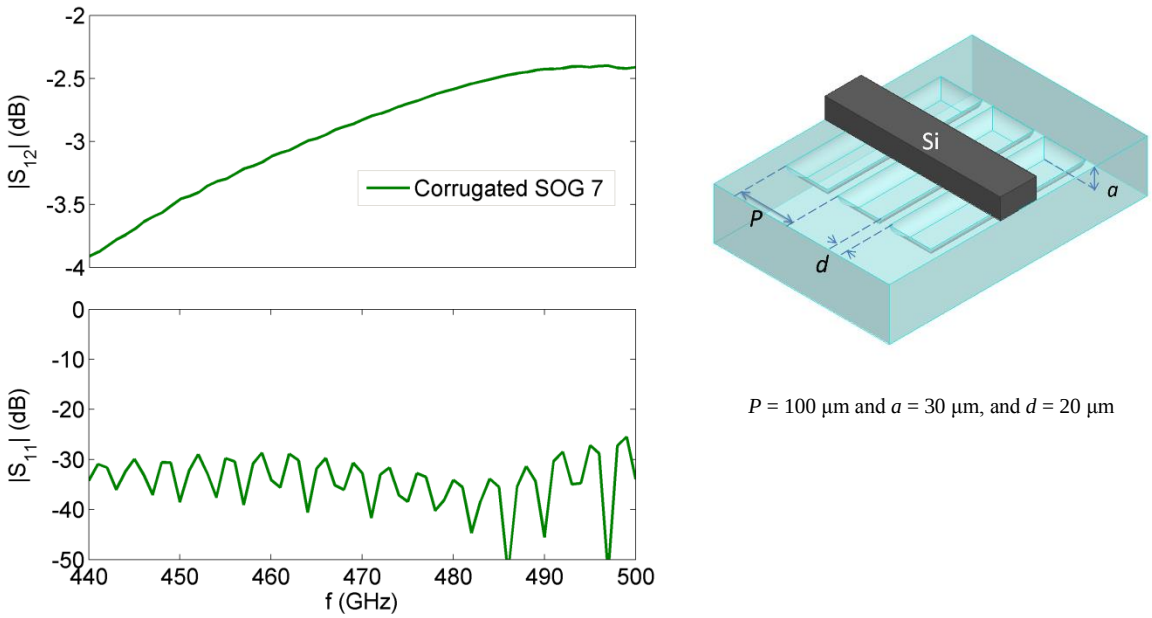

P = 100 μm and a = 30 μm, and d = 20 μm

Fig. 4.41 Scattering parameters of the corrugated SOG waveguides (Table 4. 9) for length L_1.

Table. 4.10. Performance comparison of the simulated corrugated SOGs 1 - 9. The reported values show the simulated insertion loss of the test setup.

Corrugated SOG #	f (GHz)	$\|S_{12}\|$ (average, dB)	$\|S_{12}\|_{min}$	$\|S_{12}\|_{max}$	P/d (μm)	Etching technique
1	440 - 500	1.48	1.05	2.72	500/30	wet
2	440 - 500	1.14	0.81	2.04	500/20	wet
3	440 - 500	0.85	0.60	1.47	500/10	wet
4	450 - 500	2.18	1.98	2.42	150/20	wet
5	450 - 500	2.63	2.42	3.08	150/30	wet
6	450 - 500	1.77	1.54	2.08	150/10	wet
7	440 - 500	2.93	2.40	3.91	100/20	wet
8	440 - 500	2.18	1.71	3.12	100/10	dry
9	440 - 500	2.00	1.54	2.94	500/10	dry

Several corrugated SOG structures with corrugation dimensions of P = 500 μm, a = 100 μm, and values of d = 5, 10, and 20 μm were designed for fabrication. These corrugated SOG waveguides were designed with different widths of the Si guiding channels for measurements over different frequency

ranges from 330 GHz up to 500 GHz. However, in practice, etching periodic patterns with small dimensions between cavities is quite challenging using HF wet etching. The main reason is related to the mask defects which can occur during the etching process. Wet etching of Pyrex glass is an aggressive process. Although an isotropy of 1:1 is reported for a Cr/Au/photoresist mask, the isotropy of the process is still highly dependent on the quality of the mask. An Au mask is peeled off along the edges during the process. Due to the isotropic and aggressive nature of HF etching, a tiny defect in the masking layer can be the source of a wide hole on the glass surface. Pinholes and notches along the edges are two typical defects of the mask layer. Pinholes are generated during the metal deposition [133].

The notch defects on the edges are due to the tensile stress in the Cr/Au masking layer. The creation of notch defects is shown in Fig. 4.42. The bending of the mask due to under etching generates tensile stress. As this figure shows, as the etchants penetrates below the etching mask, the mask becomes a freestanding structure along the edges. Consequently, the etching mask starts to break down during the process and uncover some areas along the edges.

Fig. 4.42 Defects formed during the Pyrex wet etching process: a) a notch defect on the masking layer, b) the target etched pattern on the surface of the Pyrex, and c) typical resultant etched pattern on the Pyrex surface due to the mask defects along the edges.

As shown in Fig. 4.42(b), the patterns on the etching mask should be designed with consideration for the Pyrex wet etching isotropic nature (isotropy of 1:1), for which the etched region extends beyond the etching mask by the depth of etching. Fig. 4.42(b) shows the target etched pattern on the Pyrex

surface. However, due to the notch defects along the edges, the thin Pyrex walls separating the periodic etched regions are cut in the resultant etched pattern.

Strategies have been reported to strengthen the Cr/Au etching mask for deep etchings into the Pyrex substrate [122, 133]. Specifically, a low stress masking layer was formed with multiple depositions of Au. The process of Cr/Au (100 nm/1 μm) deposition was performed in four 250 nm thick layers with relaxation times of 30 minutes between successive depositions for cooling [122, 133]. This helped prevent the formation of pinhole defects. Pinholes formed during each relaxation time were covered during the next deposition while new defects formed in different locations. Retaining the patterned thick photoresist, which was initially used as an etching mask for the Cr/Au etching, and baking it on a hot plate at 120 °C for 30 min, acts as extra protection during the etching process.

The abovementioned techniques are used in this research to prevent the formation of defects in the masking layer of the corrugated glass substrate. Nevertheless, even after applying these techniques, the creation of periodic patterns with small thicknesses of $d = 5 – 20$ μm between etched regions do not succeed. Aperiodic patterns on the corrugated Pyrex substrate were simulated in HFSS. The simulation results for a typical aperiodic structure shows higher attenuation as compared to the periodic structures. Although it is possible to optimize the aperiodic pattern for minimal attenuation, since it requires large amount of memory and simulation time, it is not tried in this research.

4.6.2.2 Corrugating the Pyrex Substrate Using Dry Etching Technique

DRIE of Pyrex enables the fabrication of high aspect ratio microstructures with high precision. This is an expensive and slow process which is used only when precisely etched patterns and vertical sidewalls are desired. This technique can be optimized to form closely vertical etched sidewalls up to 85 ° and 88 ° [131- 135]. However, the technique has limitations and difficulties that restrict its application for deep etching of Pyrex.

The main disadvantage of using DRIE on Pyrex is the low etch rate (~ 90 nm/min) [136]. Another drawback is the low selectivity of the etching mask due to the high energies used to increase the etch rate. The low selectivity of the etching mask limits the etch depth. Furthermore, due to contamination of the chamber during the process, it is necessary to clean the equipment during long etching sessions after each 10 μm depth etch [137]. The most commonly used etching masks are Si, photoresist, and nickel (Ni). The etch rate and the selectivity of the etching mask are dependent on the etching gas

mixture and the equipment power setting [136, 138]. With appropriate selection of these parameters, etch rates of 0.5 - 0.6 μm/min have been reported [138].

A selectivity of ~ 2 with an etch rate of ~ 350 nm/min was reported using the SU8 photoresist mask. An etched depth of 47 μm with a verticality of about 85° was reported for this process [135].

Two different corrugated patterns on the Pyrex substrate are simulated in HFSS. The dimensions of the simulated structures are provided in Table 4.9. The magnitudes of the scattering parameters for the simulated structures are provided in Fig. 4.43.

Using the dry etching technique, there is no limitation on the corrugation dimensions P and d (the period of the structure and the thickness of the Pyrex wall between the two etched regions) since the etched sidewalls are close to the vertical (~ 85 ° - 88 °). In these simulations, the etched sidewalls are considered vertical. Two different periods of P = 100 μm and P = 500 μm are simulated with a small thickness d = 10 μm. In these two structures the depth of etching is considered a = 30 μm. These two structures, respectively, have average insertion losses of 2.18 dB and 2 dB over 440 - 500 GHz. These two structures show higher insertion losses than the corrugated SOGs 1-3, for which the corrugations were based on the wet etching technique with P = 500 μm. The main reason is due to the smaller etch depth into the Pyrex substrate. To overcome this problem, solutions should be applied to increase the depth of etching.

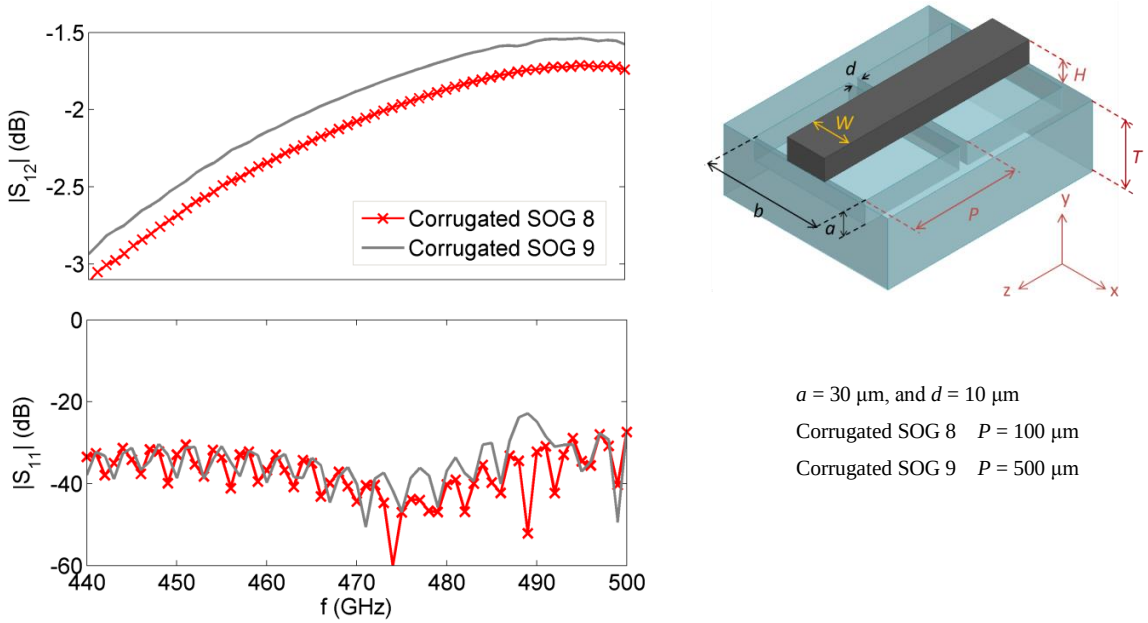

Fig. 4.43 Scattering parameters of the corrugated SOG waveguides (Table 4.9) for length L_1.

To increase the etch depth, other masking materials such as Ni and Si have been used. With a 20 μm thick Ni electroplated mask, an etch depth of 200 μm with an etch profile angle of 88 ° was reported [131]. However, using metallic masks for Pyrex etching causes significant contamination of the chamber and therefore not used in most facilities.

Using Si film as the etching mask, the selectivity was improved to ~ 20 [135]. To increase the etch depth to higher than 40 μm, a thickness of at least 2 μm of Si is required. As in the case of poly-Si, the deposition of a thick Si mask film without fractures is a critical fabrication step during which the stress has to be controlled [135]. An etch depth of 430 μm in the Pyrex substrate was reported using a thick bonded Si masking layer [138]. The main drawback to using this technique in the proposed SOG technology, is the fact that after removing the Si masking layer which was bonded to the Pyrex surface, the Pyrex surface is no longer appropriate for the secondary anodic bonding to the main high-resistivity Si layer [122]. Due to the abovementioned problems, Pyrex dry etching is not tried in this research.

4.7 Concluding Remarks and Discussion

Two new low-loss SOG waveguide structures were proposed for sub-mmW/THz applications. The proposed waveguides use the SOG wafer as their platforms, in which the glass substrate below the Si

guiding channels is etched to overcome the problem of high glass material loss in the THz range. These two structures are called the suspended SOG waveguide and the corrugated SOG waveguide.

- In the suspended SOG waveguide structure, Si beams and supporting blocks are used to hold the Si guiding channel over the etched part of the glass substrate. To fabricate this waveguide, the high-resistivity Si guiding channel, along with its supporting beams and blocks, is realized via DRIE through the Si layer of the SOG platform.
- The application of the suspended SOG waveguide for THz integrated wave-guiding was theoretically and experimentally investigated up to 500 GHz. With an appropriate choice of the Si supporting beam dimensions that avoids the appearance of the Bragg effect over the waveguide operation bandwidth, the attenuation constant of the suspended SOG waveguide is quite small. Experiments showed average attenuation constants of 0.031 dB/λ_0 and 0.042 dB/λ_0 over the frequency ranges of 350 - 500 GHz and 400 - 500 GHz, respectively. Table 4.11 compares the performance of the proposed suspended SOG waveguide with other mmW/THz waveguide structures reported in the literature. As this Table shows the proposed suspended SOG waveguide shows a significant reduction in the insertion loss as compared to the other mmW/THz techniques reported in the literature.

Table. 4.11. Performance comparisons.

Structure	α	frequency
Metallic waveguide [43]	0.12 dB/λ	3 THz
Metallic waveguide [37]	0.07 dB/λ	600 GHz
Metallic waveguide [33]	1.1 - 1.6 dB/λ	220 - 325 GHz
Metallic waveguide [139]	0.027 - 0.032 dB/λ	325 - 360 GHz
Planar Goubau Line [73]	1.8 dB/λ	300 GHz
Suspended SOG waveguide	0.031 dB/λ (average)	350 - 500 GHz
Suspended SOG waveguide	0.042 dB/λ (average)	400 - 500 GHz

- In the SOG technology, the thick glass substrate acts as a strong mechanical support for the integrated Si components attached to it. The requirement for a supporting substrate becomes essential as the frequency increases and the Si slab becomes thinner and consequently more fragile.

- An alternative approach for the realization of mmW planar dielectric waveguides is based on the image guide. However, the performance of these waveguides is affected by the additional loss due to the conduction loss and surface roughness at the ground plane. As the frequency increases, the skin depth decreases by a factor of $1/\sqrt{f}$ and the waveguide performance degrades rapidly at higher frequencies.

  Fig. 4.44 shows the attenuation constant of the SOG waveguide compared to that of a high-resistivity Si image guide with similar guiding channel dimensions (W = 310 μm and H = 100 μm). In these simulations, surface roughness on the ground plane is not included. Based on these simulations, due to the increasing material loss in the Pyrex substrate with frequency, the SOG waveguide attenuation constant is higher than that of the Si image guide over 350 - 500 GHz. The Si image guide and SOG waveguide show attenuation constants ranging over 0.19 - 0.20 dB/mm and 0.30 - 0.37 dB/mm, respectively. However, as discussed in this chapter, the compatibility of Pyrex with Si microfabrication and other well-developed techniques enables us to overcome Pyrex's material loss with the proposed fabrication technique, wherein the Pyrex substrate below the Si is etched.

  The attenuation constant of the suspended SOG waveguide is also included in Fig. 4.44 for comparison. The plots show the attenuation constants of the suspended SOG waveguide with supporting beams (W = 310 μm, H = 100 μm, and P = 100 μm, and W_b = 20 μm), which is extracted from the simulated and measured scattering parameters of the two different lengths of the suspended SOG waveguides based on the calibration technique explained in Chapter 3. The simulated attenuation constant of the suspended SOG waveguide varies over 0.007 - 0.038 dB/mm. The average measured attenuation constant is 0.043 dB/mm (0.031 dB/λ_0) over the entire frequency band of 440 - 500 GHz. This low attenuation constant shows the excellent performance of the proposed suspended SOG waveguide as compared to the Si image guide at THz frequencies.

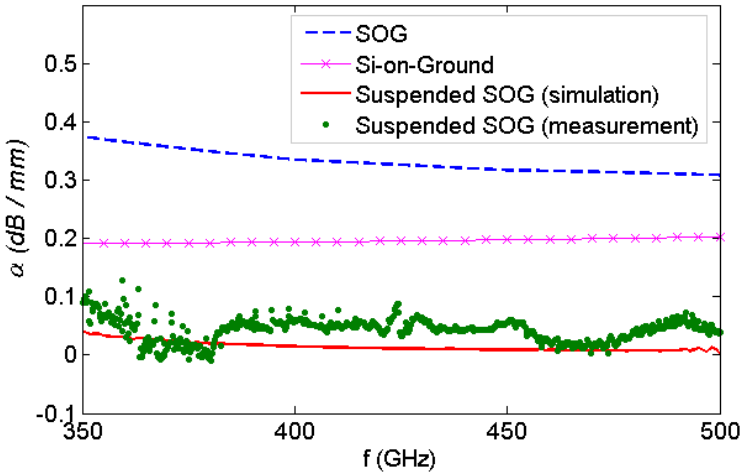

Fig. 4.44 Attenuation performance of the suspended SOG waveguide as compared to the conventional image guide.

- As mentioned in Chapter 3, only Si-confined modes for which field components are exponentially decaying in the outer region, are considered *guiding* modes in this research. However, due to the finite thickness of the Pyrex substrate, modes with sinusoidal variations inside the Pyrex substrate are also supported due to the total reflection at the Pyrex boundaries. The main advantage of the suspended SOG waveguide proposed for higher frequencies, is that the unconfined modes are suppressed due to increased Pyrex material loss with frequency. Etching the Pyrex substrate decreases the attenuation constants of the Si-confined modes significantly, while higher order unconfined modes are strongly attenuated due to the material loss in the Pyrex.

- In the corrugated SOG waveguide, parts of the Pyrex substrate below the Si guiding channel and other components are etched in a periodic manner. Corrugation offers a more convenient SOG structure as compared to the suspended SOG waveguide for applications in which high-density integrated circuits are required. Although the simulations and fabrication limitations show restrictions in application of this technique at higher frequencies, still it can serve as a low-loss platform for high-density mmW integrated circuits up to 300 GHz.

- The other important advantage of the proposed SOG technique is that the requirement to align the substructures is eliminated due to the excellent bonding characteristics of the Pyrex-Si. In this technique, the alignment between the substructures is automatically achieved during the

DRIE process when the Si components are made out of the Si slab. The Pyrex substrate acts as an etch stop during the process and at the same time supporting substrate for the Si components.

Chapter 5 Rib Silicon-on-Glass and U-Silicon-on-Glass Dielectric Waveguides for THz Integrated Circuits

5.1 Introduction

In Chapter 3, a silicon-on-glass (SOG) platform was proposed, fabricated, and demonstrated for millimeter-wave (mmW) integrated circuits. Chapter 4 discussed the extension of the proposed SOG platform into higher sub-mmW/terahertz (THz) frequencies (up to 660 GHz). It was shown that Pyrex's material loss increases rapidly at higher frequencies above 200 GHz. To overcome the problem of high material loss of the Pyrex substrate, the idea of etching the Pyrex substrate below the Si was proposed and demonstrated. Two periodic SOG waveguide structures, named the *suspended* SOG waveguide and the *corrugated* SOG waveguide, were developed to support the silicon (Si) guiding channel over the etched region of the Pyrex substrate. The low-loss performance of the suspended SOG waveguide was theoretically and experimentally demonstrated up to 500 GHz. The potential application of the corrugated SOG platform for mmW low-loss and high-density integrated circuits was theoretically demonstrated up to 300 GHz.

In this Chapter, the application of the proposed SOG technology into higher THz frequencies (up to 1.1 THz) is investigated. First, the suspended SOG waveguide is studied as a potential candidate. Simulations of the suspended SOG waveguide over 0.9 - 1.1 THz confirm the waveguide's high-performance in regards to the attenuation constant. However, when considering THz high-density integrated circuits, more convenient SOG waveguide structures with more compact supporting configurations will outperform the suspended SOG platform. To this end, and to avoid design concerns about the appearance of the Bragg band, new configurations of the SOG waveguide are studied. Two new SOG waveguide structures called *rib* SOG waveguide and *U*-SOG waveguide are proposed and their fabrication techniques are discussed. These two new structures can provide low attenuation constants for THz frequencies with strong mechanical support. Furthermore, they can serve as potential platforms for THz high-density integrated circuits. The effects of different parameters are studied on the propagation characteristics of these waveguides. Rib SOG and U-SOG waveguides are designed for fabrication over the frequency ranges of 0.8 – 0.9 THz and 0.9 – 1.1 THz. The fabrication of the U-SOG waveguide is underway.

5.2 Investigation of Suspended SOG Waveguide Performance at Terahertz

In this Section, extending the suspended SOG waveguide's application into higher THz frequencies (~ 1.1 THz) is investigated; its limitations and advantages are studied. A suspended SOG waveguide with dimensions of W = 100 μm, H = 50 μm, a = 100 μm, b = 20 μm (on the top W_c = 220 μm, $b + 2 \times a$), P = 50 μm, W_b = 20 μm, and l_b = 250 μm is simulated in high frequency structure simulator (HFSS). In all of the simulations reported in this Chapter, Si has a conductivity of 0.02 σ/m and Pyrex's conductivity follows the graph in Fig. 4.2. Fig. 5.1 shows the suspended SOG waveguide structure and its dimensions. Fig. 5.2 shows the simulation results over the frequency range of 0.9 - 1.1 THz. This figure shows the scattering parameters for a length of 5.2 mm of the suspended SOG waveguide plus two transitions to the WR-1 (0.254 × 0.127 mm) rectangular metallic ports of the test setup. The tapered segments of the transitions have a length of L_t = 0.8mm each. Over a wide bandwidth of 0.9 – 1.08 THz, the insertion loss of the suspended SOG waveguide including the two transition losses is only 0.81 – 1.78 dB. Lower waveguide attenuation can be achieved by a smaller thickness of the periodic supporting beams (W_b). However, to maintain a strong mechanical support it is more desirable to keep the thickness of the supporting beams at W_b = 20 μm. As the frequency increases toward 1.1 THz, the insertion loss reaches to 4.58 dB due to the radiation. To avoid this at 1.1 THz, one needs to change the periodic beam dimensions.

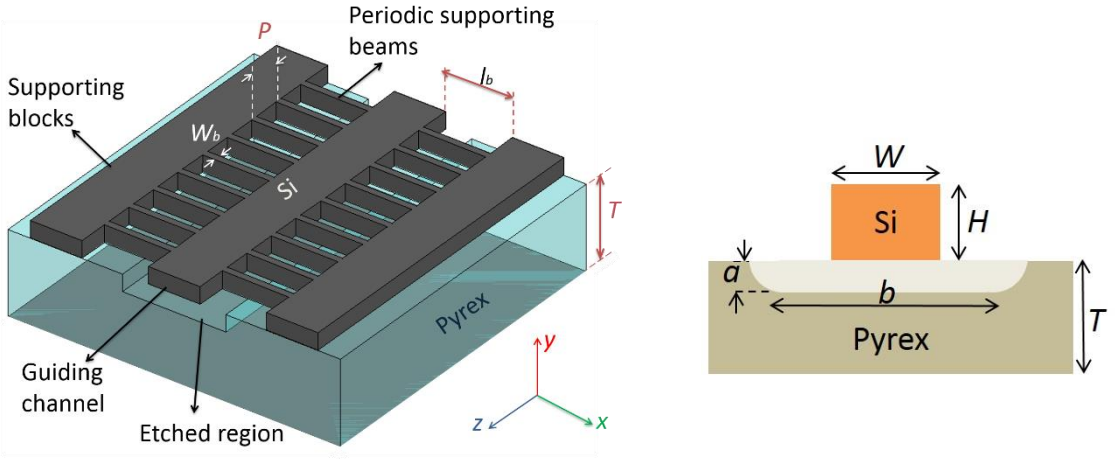

(a) (b)

Fig. 5.1 Suspended SOG waveguide: a) waveguide structure, and b) waveguide cross-section (cross-section *B*).

One main drawback to using dielectric waveguides for planar integrated circuits is their high scattering and radiation loss at bends and discontinuities. However, this is the main barrier for waveguide structures where the index contrast between the guiding channel and its surrounding media is low. In the proposed SOG technology platform, strong field confinement within the Si guiding channel is achieved due to the large index contrast between the Si and its surrounding media. This is a big advantage in terms of minimizing the scattering loss at the bends and minimizing the coupling between the adjacent Si components in integrated circuits. The low coupling between Si guiding channels in the SOG platform was studied in Chapter 3. Different mmW bend structures on the Si image guide platform with low insertion losses were designed and tested by the other colleagues at CIARS (Centre for Intelligent Antenna and Radio Systems) [109]. Achieving low coupling and leakage, as well as small scattering loss at bends and discontinuities, guide the work toward the realization of high-density integrated circuits.

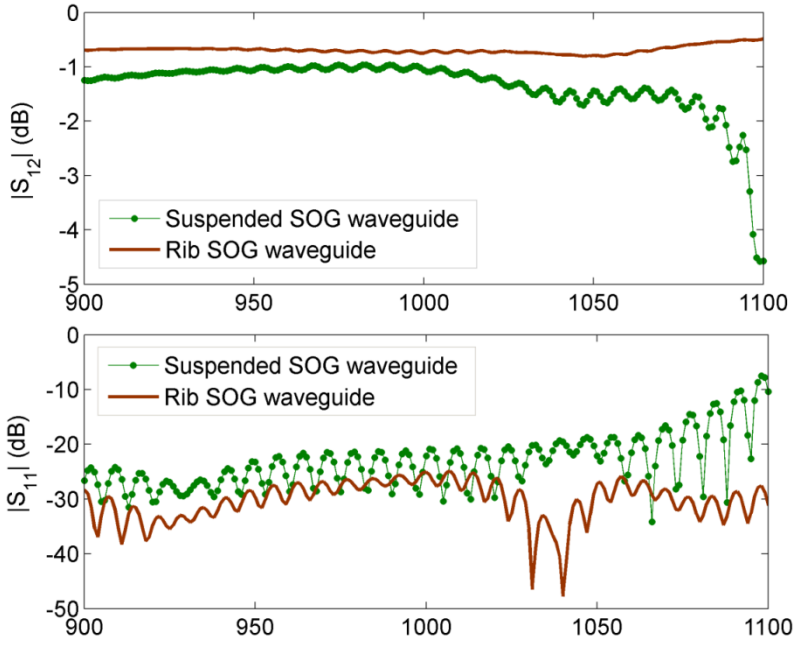

Fig. 5.2 Scattering parameters of the SOG waveguides with W = 100 µm for a length of 5.2 mm between the two transitions.

As a proof of concept, a suspended Si guiding channel bend structure over the etched Pyrex substrate is simulated in HFSS. Fig. 5.3(a) shows the bend structure. The dimensions are selected as follows: W = 100 µm, H = 50 µm, a = 100 µm, W_c = 200 µm, R_b = 1 mm, θ_b = 30º, L_{pI} = 0.5 mm, and L_{pII} = 0.25 mm. The simulated scattering parameters for this bend structure are provided in Fig. 5.4. Simulations show a return loss better than 40 dB, and an insertion loss less than 0.08 dB, over the entire frequency band of 0.9 - 1.1 THz. However, the addition of Si supporting beams, which play the role of mechanical support in the suspended SOG platform, to the Si bend structure will degrade the bend low-loss performance due to the huge scattering at the discontinuity of beams along the bend segment. The implementation of the same bend structure in the suspended SOG platform is shown in Fig. 5.3(b) and its simulated scattering parameters are shown in Fig. 5.4. In this bend structure, along the straight segments with lengths L_{tI} and L_{tII} the supporting beams are oriented with a period of P = 50 µm. Along the bend segment, three parallel beams at a distance of d = 60 µm are supporting the structure. All supporting beams have a length of L_b = 150 µm and a thickness of W_b = 20µm.

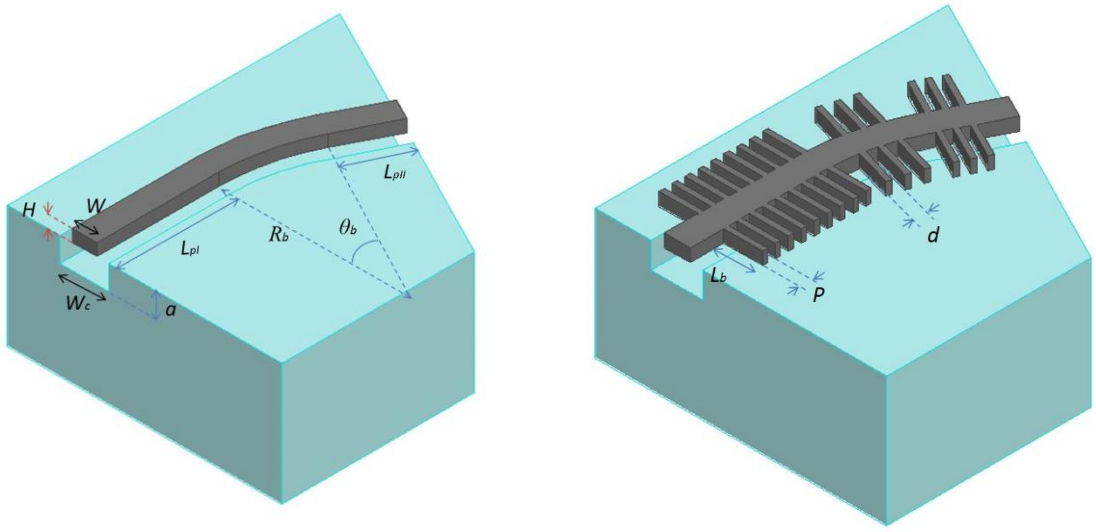

(a) (b)

Fig. 5.3 Structures of the simulated bends in different SOG platforms: a) suspended Si channel on top of the etched Pyrex substrate, and b) suspended SOG bend structure.

The suspended SOG bend structure shows a return loss of better than 10 dB and an insertion loss of 1.5 – 3.7 dB over the frequency band of 0.9 - 1.1 THz. Although lower insertion loss can be achieved for the suspended SOG bend structure by optimizing the orientation of supporting beams along the bend,

the implementation of bends and different passive components on the suspended SOG platform still suffers from additional scattering loss. Furthermore, these optimizations, which need to be performed for each single passive component implemented on the suspended SOG platform, require additional simulation time and memory. To overcome the abovementioned problems at higher THz frequencies, two new high-performance SOG waveguide configurations are introduced and demonstrated in the following Sections. These two novel structures can serve as potential candidates for THz high-performance and high-density integrated circuits.

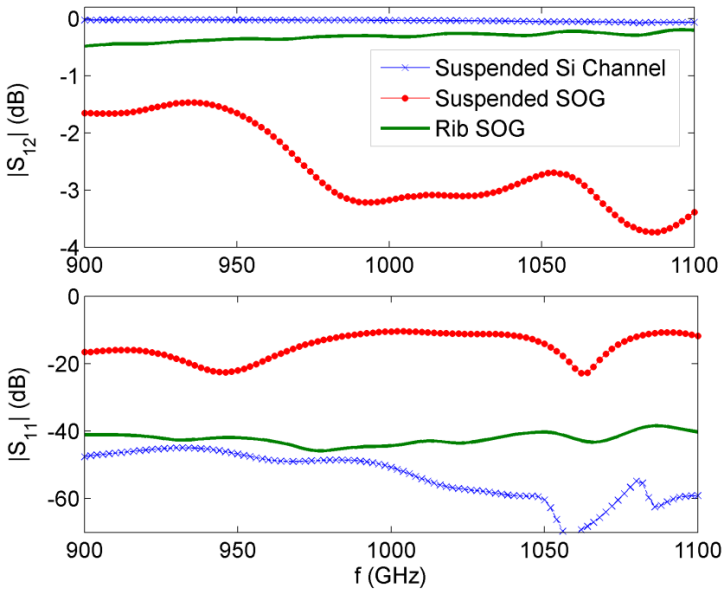

Fig. 5.4 Simulated scattering parameters of the bend structures shown in Fig. 5.3.

5.3 Rib SOG Waveguide for Terahertz Applications

When increasing the frequency, smaller periods in a periodic structure are needed to prevent the occurrence of the Bragg effect over the waveguide operation bandwidth. To avoid intrinsic characteristics of the periodic structures and to provide a more convenient platform for THz integrated circuits, a new SOG waveguide structure, called the rib SOG waveguide, is proposed in this Section. In the proposed structure, non-periodic mechanical supports are provided for the Si guiding channel over the etched region of the Pyrex substrate.

5.3.1 Waveguide Structure

The waveguide structure is shown in Fig. 5.5. The waveguide consists of a rib Si waveguide which is supported on the etched part of the Pyrex substrate. This structure provides a strong mechanical support for the waveguide channel in a non-periodic form.

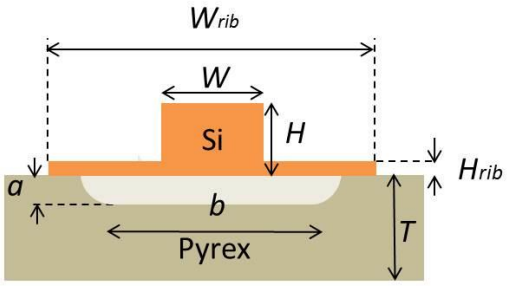

Fig. 5.5 Structure of the rib SOG waveguide.

5.3.2 Performance Comparison

In this Section, simulation results are provided to demonstrate high-performance of the proposed rib SOG waveguide. In order to compare the performance of the rib SOG waveguide with other Si waveguide structures, modal analysis is conducted on different Si waveguide structures. These structures are: a Si image guide (Si channel on the ground plane made of aluminum with a conductivity of $\sigma = 3.744\times10^7$ S/m), a SOG waveguide, a SOG waveguide with cross-section B (Fig. 5.1(b)) in which the Pyrex substrate is etched below the Si guiding channel (suspended SOG waveguide without Si supporting beams), and a rib SOG waveguide. In all of the waveguide structures, the Si channel has dimensions $W = 310$ μm and $H = 100$ μm. In the rib SOG waveguide, and SOG waveguide with cross-section B, the etched region has dimensions of $a = 100$ μm and $b = 500$ μm. In the rib SOG waveguide, $H_{rib} = 40$ μm.

As shown in Fig. 5.6, while the SOG waveguide attenuation constant is higher than that of the Si image guide at higher frequencies due to the increased Pyrex material loss, the SOG waveguide attenuation constant is significantly decreased by etching the Pyrex substrate. The rib SOG waveguide attenuation constant is quite low and varies between 0.007 - 0.06 dB/mm over the frequency range of 320 – 500

GHz. This confirms excellent performance of the rib SOG waveguide in terms of a low attenuation constant as compared to the other Si waveguide structures.

To have a better comparison of the performances of the suspended SOG and rib SOG waveguides at the THz range, a length of 5.2 mm of the rib SOG waveguide between the two transitions to the WR-1 (0.254 × 0.127 mm) rectangular metallic ports of the test setup is simulated in HFSS. The simulated scattering parameters of the rib SOG waveguide are shown in Fig. 5.2 and compared with those of the suspended SOG waveguide. The rib SOG's Si guiding channel has dimensions similar to those of the suspended SOG waveguide. In this structure, W = 100 µm, H = 50 µm, and H_{rib} = 20 µm. All other dimensions, including the dimensions of the etched region on the Pyrex substrate, are also similar to those of the suspended SOG waveguide. As shown in Fig. 5.2, the rib SOG waveguide shows even lower attenuation than the suspended SOG waveguide. For the rib SOG waveguide, the simulated insertion loss varies between 0.49 dB and 0.81 dB over the wide frequency range of 0.9 – 1.1 THz.

To investigate the high performance of the rib SOG platform for THz integrated circuits, a bend structure similar to those shown in Fig. 5.3 is simulated in the rib SOG configuration. The simulated rib SOG bend is shown in Fig. 5.7. All bend structure dimensions, and the dimensions of the etched region on the Pyrex substrate, are similar to those of the bend structures shown in Fig. 5.3. These dimensions are W = 100 µm, H = 50 µm, H_{rib} = 20 µm, a = 100 µm, W_c = 200 µm, R_b = 1 mm, θ_b = 30°, L_{pI} = 0.5 mm, and L_{pII} = 0.25 mm.

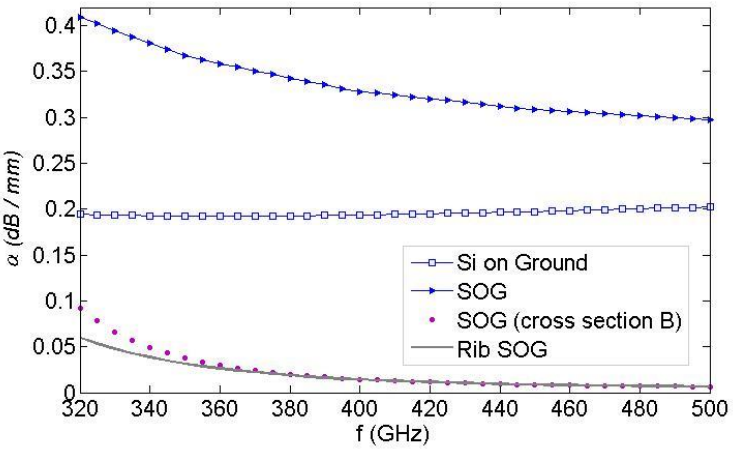

Fig. 5.6 Attenuation constants of different Si waveguide structures.

The simulated scattering parameters are added to Fig. 5.4 and compared to those of bend structures in Fig. 5.3. As the simulation results show, the rib SOG waveguide significantly outperforms the suspended SOG waveguide in terms of the low scattering and radiation loss at the bends. The insertion loss of the rib SOG bend varies between 0.2 dB and 0.5 dB over the frequency range of 0.9 – 1.1 THz. The return loss is better than 38 dB over the entire band. The average insertion loss of the rib SOG bend structure is 0.32 dB over the entire frequency band of 0.9 – 1.1 THz. This low insertion loss confirms the potential application of the rib SOG platform for THz high-density and low-loss integrated circuits.

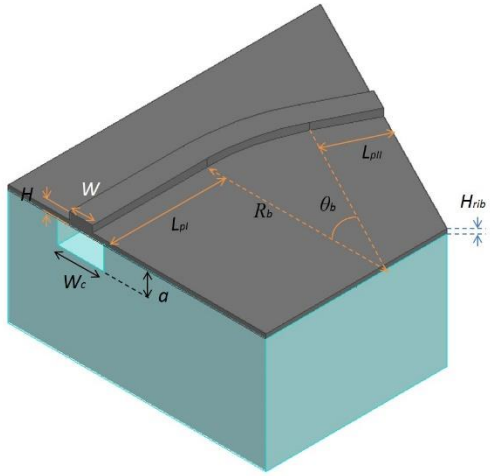

Fig. 5.7 Structure of the simulated rib SOG waveguide bend.

5.3.3 Modal Analysis

Modal analysis of the proposed rib SOG dielectric waveguide is conducted in HFSS. Fig. 5.8 shows the propagation constants of the Si-confined guided modes of the rib SOG waveguide with dimensions of W = 140 µm, H = 50 µm, H_{rib} = 20 µm, W_{rib} = 800 µm, a = 50 µm, b = 80 µm, and T = 500 µm (Fig. 5.5). Over the frequency band of 0.58 – 1.1 THz, the two E_x^{11} and E_y^{11} modes are confined within the Si. These two modes have cutoff frequencies of 580 GHz and 745 GHz, respectively. The attenuation constant of the dominant E_x^{11} mode decreases from 2 dB/mm to 0.04 dB/mm as the frequency rises from 580 GHz to 1.1 THz. This is due to better field confinement within the Si as the frequency rises.

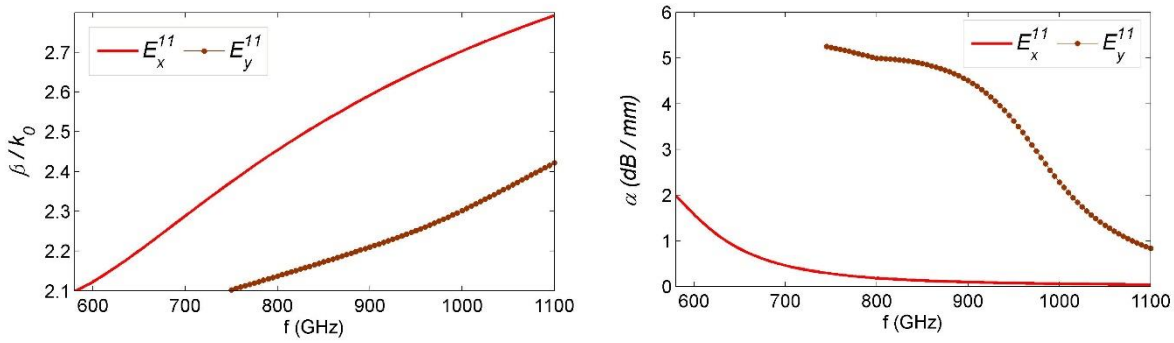

(a) (b)

Fig. 5.8 Propagation constants of the rib SOG waveguide with $W = 140$ µm: a) normalized phase constant (β/k_0), and b) attenuation constant (α, dB/mm).

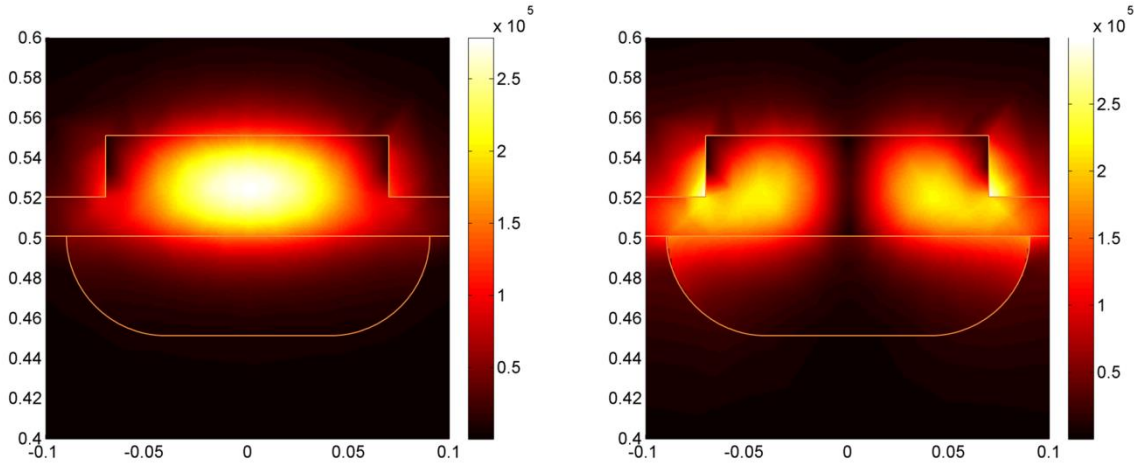

(a) (b)

Fig. 5.9 Distribution of the magnitude of the electric field in the rib SOG with $W = 140$ µm at 1 THz: a) E_x^{11} mode, and b) E_y^{11} mode.

Fig. 5.9 shows the distribution of the magnitude of the electric field of these two modes over the rib SOG waveguide cross-section at 1 THz. This figure shows significantly stronger confinement within the Si for the E_x^{11} mode than for the E_y^{11} mode. This is the main reason for the significantly smaller attenuation constant of the E_x^{11} mode as compared to that of the E_y^{11} mode.

5.3.4 Parametric Studies

Several rib SOG waveguide structures are simulated in HFSS to study the effect of different parameters on the waveguide propagation constant. Rib SOG waveguides with Si guiding channel dimensions of W = 100 μm and H = 50 μm are simulated over the frequency range of 0.85 – 1.1 THz. To provide a strong mechanical support for the proposed rib SOG waveguide, it is more advantageous to choose smaller values for the width of the etched region inside the Pyrex substrate ($W_c = 2 \times a + b$) and choose larger values for the thickness of the Si supporting the Si guiding channel (H_{rib}). However, decreasing W_c and increasing H_{rib} increases the waveguide attenuation due to the higher interactions of the modal fields with the Pyrex substrate.

Fig. 5.10 shows the attenuation constants and phase constants of the rib SOG waveguide with dimensions W = 100 μm, H = 50 μm, T = 500 μm, W_{rib} = 800 μm, and H_{rib} = 20 μm for different values of the etched region on the Pyrex substrate. As expected, by increasing W_c ($2 \times a + b$) the waveguide attenuation and its normalized phase constant (β / k_0) decreases due to lower contractions of the modal fields with the glass substrate. Selecting pair dimensions W_c / a equal to 220/100, 180/90, and 160/80 μm, low attenuation constants of 0.017 – 0.084 dB/mm, 0.036 – 0.18 dB/mm, and 0.054 – 0.26 dB/mm are achieved over the frequency range of 0.85 – 1.1 THz, respectively. To study the effect of H_{rib} on the rib SOG waveguide performance, simulated attenuation constants of the waveguides are provided in Figs. 5.11-13 for different values of H_{rib} equal to 10 μm, 20 μm, and 30 μm. These figures show that while a change of H_{rib} from 20 μm to 30 μm significantly increases the attenuation constant, the increase in the attenuation constant due to the increase in H_{rib} from 10 μm to 20 μm is tolerable. A ratio of H_{rib}/H equal to 3/5 can provide strong mechanical support for the proposed rib SOG waveguide.

5.3.5 Simulation Results of the Designed Test Devices

Several rib SOG waveguide test devices are designed to experimentally verify the waveguide high performance. Two waveguides cover the frequency range of 0.75 – 1.1 THz. It is worth mentioning that there is no limitation on extending the proposed waveguide operation bandwidth to higher THz frequencies above 1.1 THz. However, the PNA-X operation frequency is currently limited to 1.1 THz. The dimensions of the designed test devices are provided in Table 5.1. Fig. 5.14 shows part of the designed test setup for these waveguides. The tapered segment of the rib SOG waveguide inside the metallic port is shown in this figure. As shown in this figure, the Si is etched through the whole layer along the tapered segments. The simulation results for the scattering parameters of three of these devices, which are being fabricated for two different lengths of ~ 10 mm and ~ 20 mm between the two

transitions, are provided in Figs. 5.15-17 for the lengths of ~ 10 mm. The lengths of the tapered segments in all of these structures is L_t = 0.8 mm. Fig. 5.15 shows the simulated scattering parameters for the rib SOG waveguide with W = 160 µm (line 2 in Table 5.1) over the frequency range of 0.75 – 0.9 THz. The insertion loss of a length of L_1 = 10 mm of this waveguide, plus two transitions to the metallic ports, is only 0.53 – 0.74 dB over the entire frequency band of 0.75 – 0.9 THz. The return loss is always better than 17 dB.

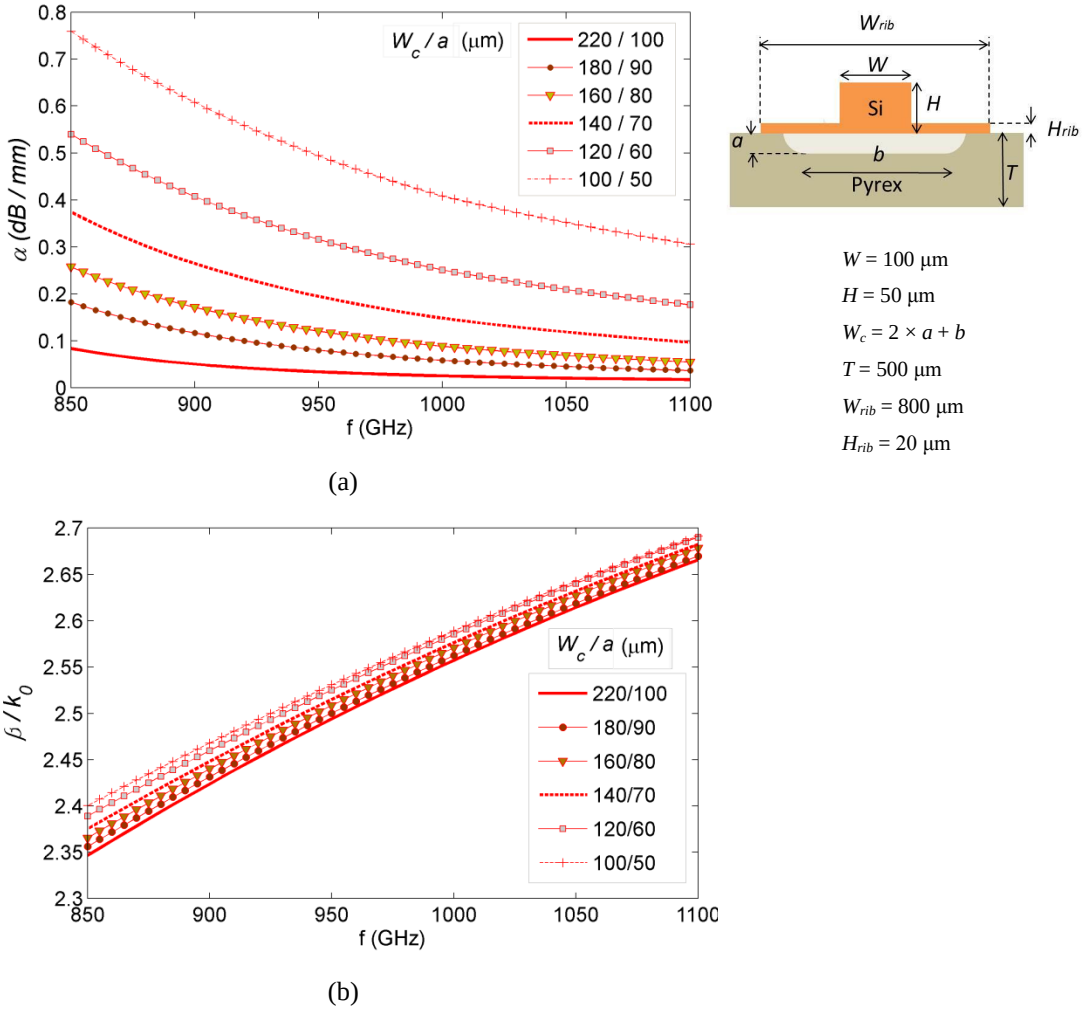

Fig. 5.10 Simulation results of the rib SOG waveguide, the variation of the propagation constant with dimensions of the etched cavity inside the Pyrex substrate: a) attenuation constant, and b) phase constant.

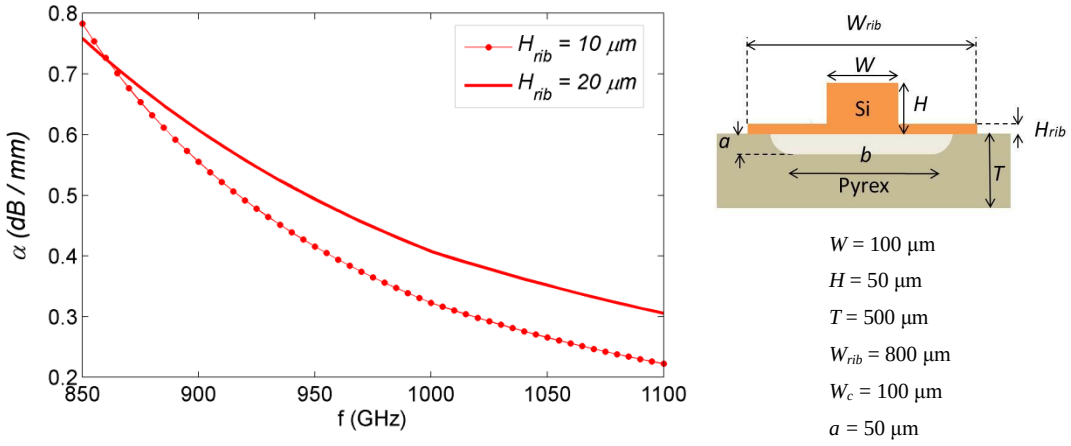

Fig. 5.11 Variation of the attenuation constant of the rib SOG waveguide with H_{rib}.

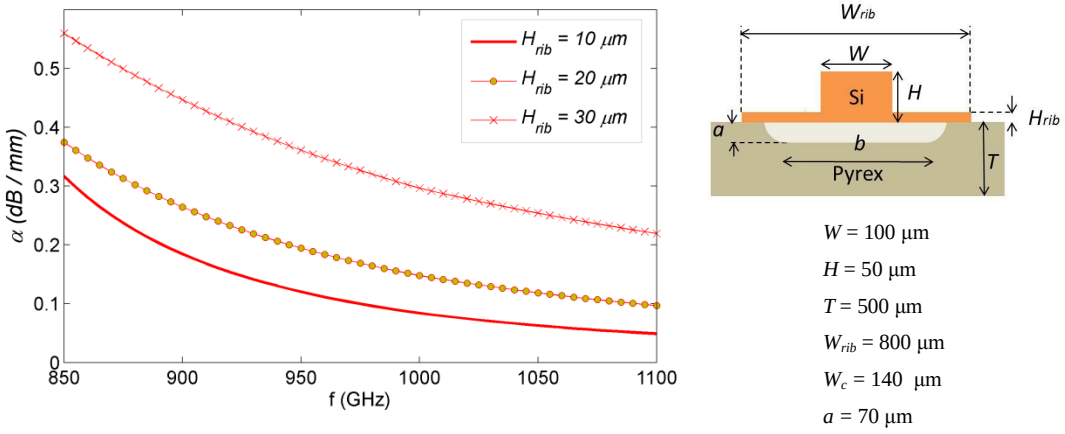

Fig. 5.12 Variation of the attenuation constant of the rib SOG waveguide with H_{rib}.

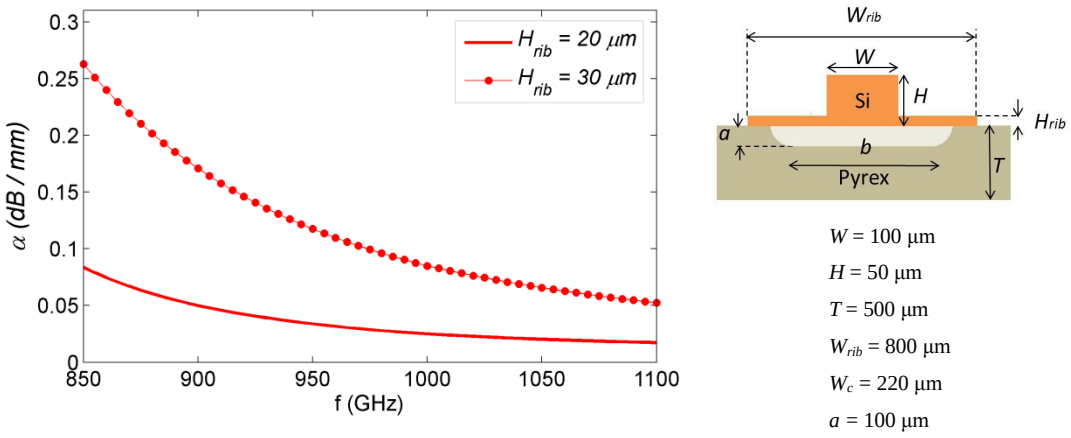

Fig. 5.13 Variation of the attenuation constant of the rib SOG waveguide with H_{rib}.

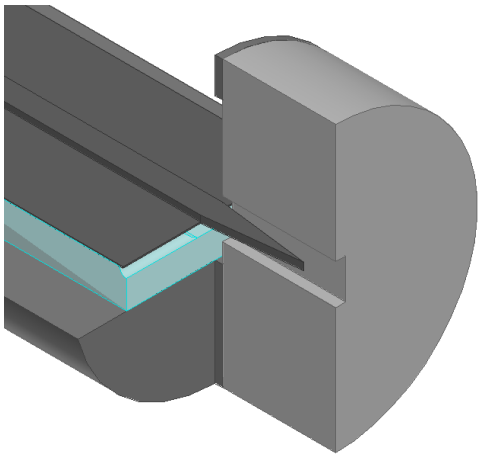

Fig. 5.14 Test setup structure for the rib SOG waveguide.

Table. 5.1. Dimensions of the rib SOG waveguides studied in Figs. 5.15–17.

Rib SOG #	W	H	H_{rib}	W_c*	a	W_{rib}	L_1	L_2	L_t
1	160	50	20	260	100	800	10	20	0.8
2	160	50	20	280	100	800	10	20	0.8
3	120	50	20	200	100	800	10.1	20.1	0.8
4	120	50	20	220	100	800	10.1	20.1	0.8
5	100	50	20	200	100	800	10.2	20.2	0.8
6	100	50	20	220	100	800	10.2	20.2	0.8

*$W_c = a + 2 \times b$ shows the width of the etched region on the top surface of the Pyrex substrate considering an isotropy of 1:1 for the HF wet etching.

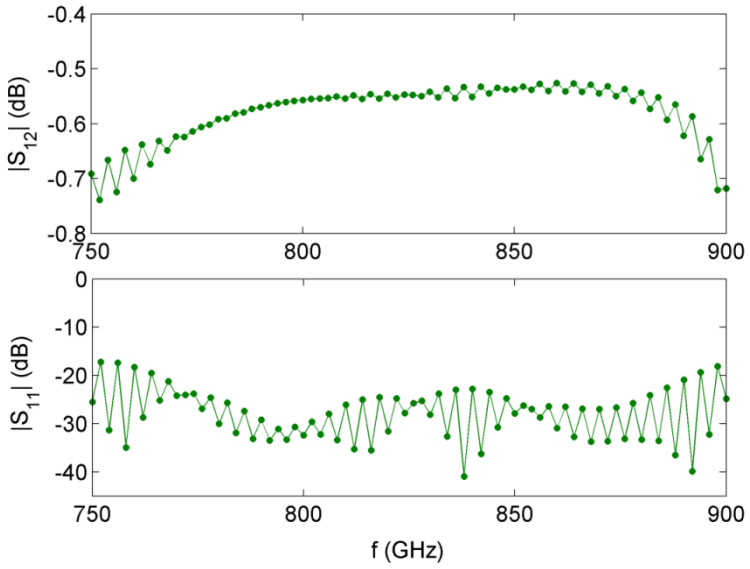

Fig. 5.15 Scattering parameters of the rib SOG waveguide with W = 160 μm (line 2 in Table 5.1) for a length of 10 mm between the two transitions.

Fig. 5.16 shows the results for the rib SOG waveguide with W = 120 μm (line 4 in Table 5.1) for a length of L_1 = 10.1 mm plus transition loss. For this structure, the insertion loss is 0.62 – 0.75 dB over the entire frequency band of 0.9 – 1.1 THz. The return loss is always better than 25 dB. Fig. 5.17 shows the similar results for the rib SOG waveguide with W = 100 μm (line 6 in Table 5.1) for a length of L_1 = 10.2 mm. For this structure, the insertion loss is 0.58 – 0.9 dB over the entire frequency band of 0.9 – 1.1 THz. The return loss is always better than 25 dB.

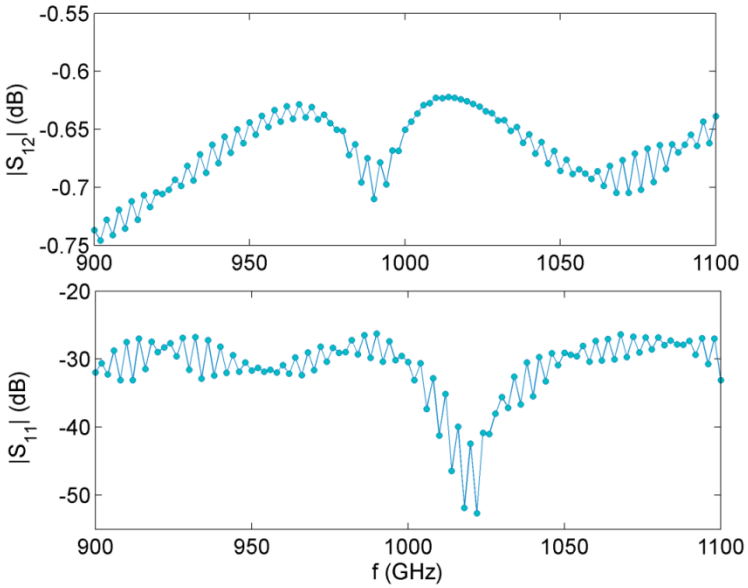

Fig. 5.16 Scattering parameters of the rib SOG waveguide with W = 120 μm (line 4 in Table 5.1) for a length of 10.1 mm between the two transitions.

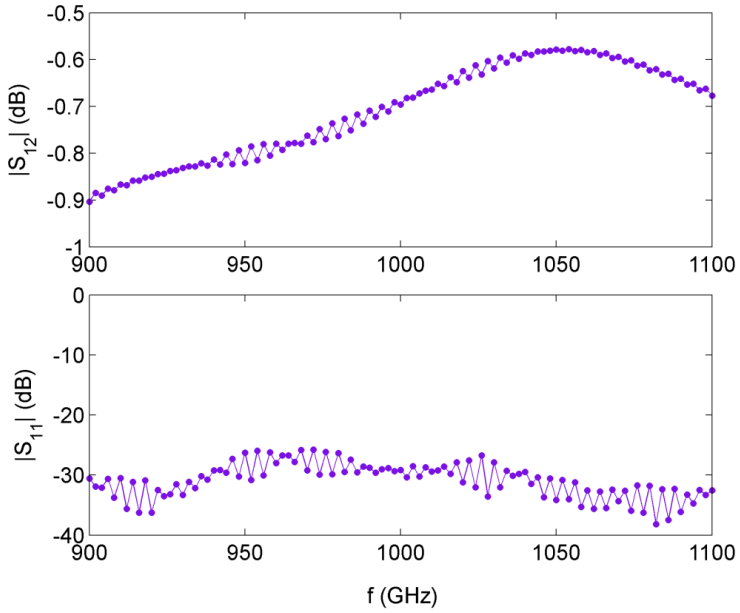

Fig. 5.17 Scattering parameters of the rib SOG waveguides with W = 100 μm (line 6 in Table 5.1) for a length of 10.2 mm between the two transitions.

5.3.6 Fabrication Technique

The fabrication technique of the new rib SOG waveguide mainly consists of the same processes used in the fabrication of the previously proposed SOG waveguide structures (corrugated/suspended SOG waveguides). The main difference is that deep reactive ion etching (DRIE) of the Si layer is not performed through the whole Si layer. Control of the etching depth needs to be done during the DRIE process. In the ultimate SOG integrated circuit, all components, including the coupling to the active devices, are implemented in the same platform without any transition to the metallic waveguides. The fabrication of the ultimate rib SOG integrated circuit is a two-mask process. However, in the designed test devices, the Si needs to be etched through the whole layer around the tapered segments to form low transitions to the metallic ports of the test setup. To make the rib SOG waveguide test devices, DRIE of the Si layer is performed in two subsequent steps with two different masks. As a result, the fabrication of the test devices is actually a three-mask process. Fig. 5.18 shows the steps of the fabrication of the rib SOG waveguide after bonding the etched surface of the Pyrex substrate to the Si device layer of the silicon-on-insulator (SOI) wafer. The steps for etching the Pyrex substrate are the same as those followed for the suspended SOG waveguide.

Oxide and thick photoresist are used as the two masking layers for the subsequent DRIE steps of the Si layer. After anodic bonding and wet etching of the Si handle layer, the surface of the insulator oxide layer, which is now used as an etching mask, is coated with a 1 - 2 μm thick Shipley 1811 photoresist layer using a spinner. A second glass-chromium mask (the first mask is used for the Pyrex glass etching) is used to pattern the photoresist via ultraviolet (UV) exposure. The exposed photoresist is developed in MF 319. The etched patterns on the etched Pyrex layer, and the patterns on the second mask, are aligned in the mask aligner before the exposure.

After pattering the photoresist layer, this layer is used as an etching mask for pattering the oxide masking layer via the reactive ion etching (RIE) of the oxide. Then, the photoresist mask is washed out in acetone. A ~ 11 μm thick photoresist (AZ 4620) is coating the Si surface, which is now covered by a patterned oxide layer, using a spinner. Due to the small thickness of the oxide mask (2 μm) as compared to that of the thick photoresist mask, the patterned oxide mask below the thick photoresist has no significant effect on the quality of the coating thick photoresist layer.

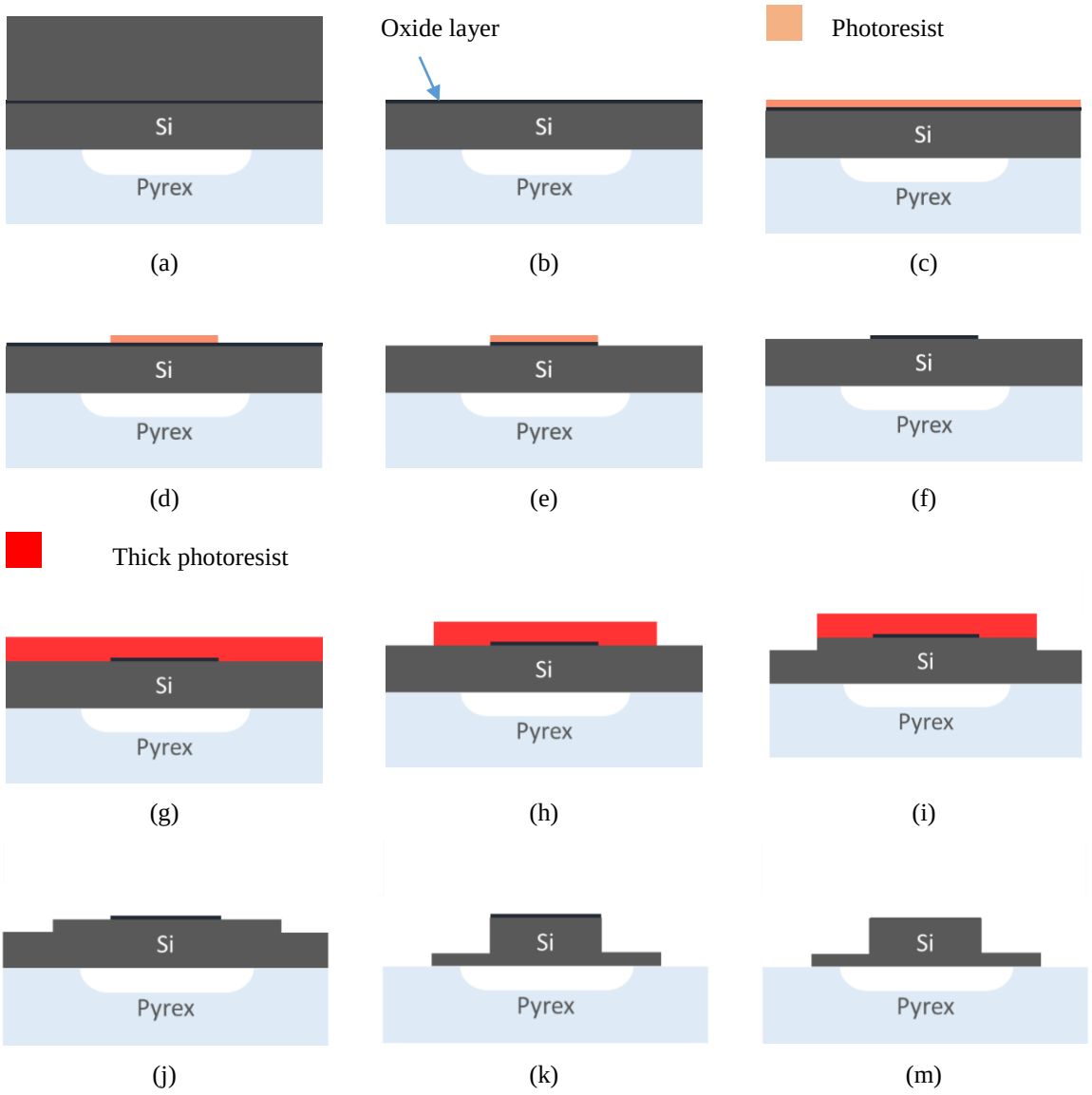

Fig. 5.18 Process flow of the fabrication of the rib SOG waveguide.

a) The structure after anodic bonding of the SOI wafer on the etched Pyrex wafer, b) etching the Si handle layer, c) coating the oxide surface with photoresist, d) pattering the photoresist via optical lithography, e) etching the oxide via RIE, f) washing out the photoresist mask, g) coating the Si surface with thick photoresist, h) patterning the thick photoresist layer via optical lithography, i) DRIE of the Si layer using the photoresist mask, j) washing out the photoresist mask, k) DRIE of Si using the oxide mask, m) etching the oxide mask via RIE.

The coating thick photoresist layer is patterned via UV exposure using the third glass-chromium mask. The pattern on this mask is aligned with the patterned oxide mask using the mask aligner machine. The exposed photoresist is developed in AZ 400 K. Now the masking layers for the subsequent etchings of the Si layer are formed [Fig. 5.18(h)].

Using the thick photoresist mask, the Si layer is etched up to a depth of H_{rib} and higher. The height of the etching is controlled during the DRIE process. After this step, the thick photoresist mask is washed out in acetone. The DRIE of the remaining Si layer continues for a depth of $H - H_{rib}$ with the second oxide mask. Precise control of the etching depth is needed during this second DRIE process. After the DRIE process, the masking layer is etched via RIE of the oxide.

5.4 U-SOG Waveguide for Terahertz Integrated Circuits

The second SOG waveguide structure, proposed for THz integrated circuits, consists of a U-shaped Si guiding channel attached to the glass substrate. In this waveguide, which is called the U-SOG waveguide, the Si guiding channel is etched in the form of a cavity from the bottom to reduce the waveguide attenuation due to the Pyrex material loss. This waveguide is studied in this section. Using this structure, the requirement of etching the Pyrex substrate is eliminated. The fabrication of this waveguide is a two-mask process which can be performed at a lower cost compared to the fabrication of the suspended SOG, corrugated SOG, and rib SOG waveguides. The elimination of etching the Pyrex glass results in significant cost reduction sine gold sputtering was used as the masking layer for etching the Pyrex glass.

5.4.1 Waveguide Structure

The structure of the U-SOG waveguide is shown in Fig. 5.19. As shown in this figure, the Si guiding channel is etched from below the guiding channel to reduce the contraction of the modal fields with the Pyrex substrate. The U-SOG waveguide can serve as a potential candidate for THz high-density integrated circuits.

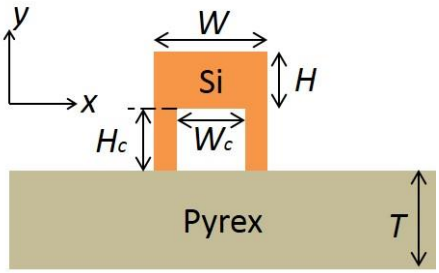

Fig. 5.19 U-SOG waveguide structure.

As a proof of concept, the bend structure shown in Fig. 5.20 is simulated in the U-SOG platform. The simulated scattering parameters of the U-SOG bend structure are shown in Fig. 5.21. The bend dimensions are the same as those simulated for the rib SOG bend and suspended SOG bend structures. These dimensions are R_b = 1 mm, θ_b = 30 °, L_{pI} = 0.5 mm, and L_{pII} = 0.25 mm. The U-SOG waveguide dimensions are W = 100 µm, H = 50 µm, W_c = 60 µm, and H_c = 50 µm. A low insertion loss of 0.07 – 0.48 dB is obtained for this bend structure over the entire frequency band of 0.9 – 1.1 THz and the return loss is always better than 25 dB.

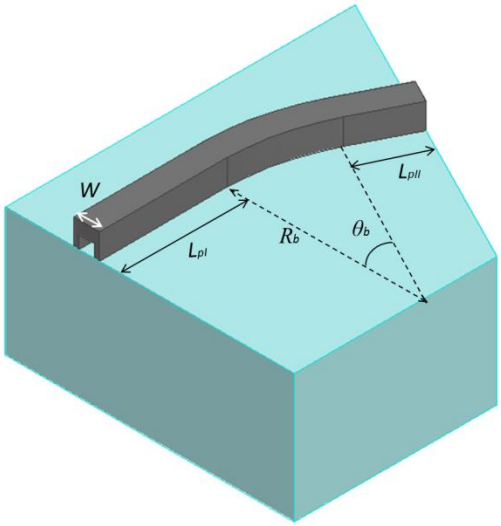

Fig. 5.20 Structure of the U-SOG waveguide bend.

5.4.2 Modal Analysis

Modal analysis of the U-SOG waveguide is performed in HFSS. Two U-SOG waveguides with two different widths of the Si guiding channels equal to W = 100 μm and W = 150 μm are simulated and their results are shown in Figs. 5.22 and 23, respectively. In these two waveguides, the etched cavities below the Si guiding channels have widths of W_c = 60 μm and W_c = 110 μm, respectively. The other dimensions in these two structures are selected as H = 40 μm, H_c = 60 μm, and T = 500 μm (see Fig. 5.19).

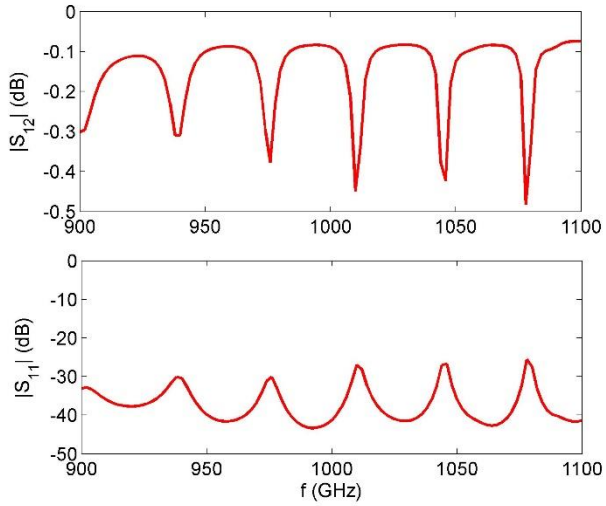

Fig. 5.21 Simulated scattering parameters of the U-SOG bend structure shown in Fig. 5.20.

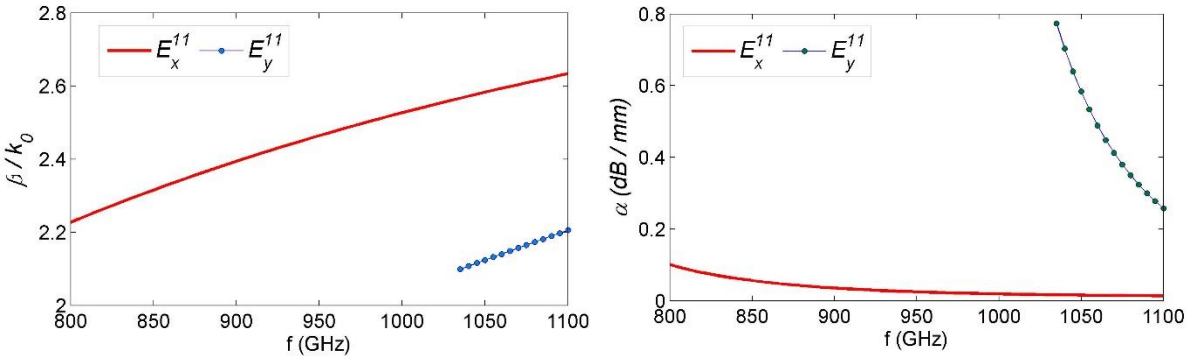

(a) (b)

Fig. 5.22 Modal analysis results of the U-SOG waveguide with W = 150 μm: a) normalized phase constant (β/k_0), and b) attenuation constant (α, dB/mm).

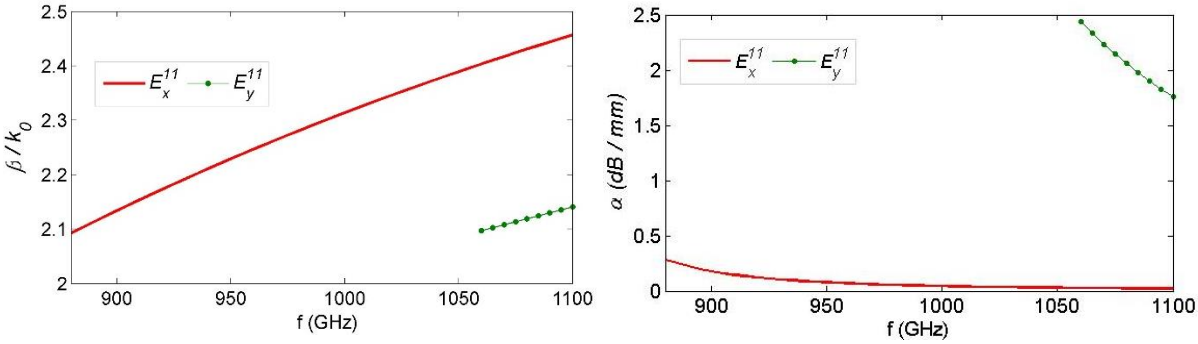

(a) (b)

Fig. 5.23 Modal analysis results of the U-SOG waveguide with $W = 100$ µm: a) normalized phase constant (β/k_0), and b) attenuation constant (α, dB/mm).

The single mode operation bandwidths in these two structures with $W = 150$ µm and $W = 100$ µm, extend over the frequency ranges of 0.8 – 1.035 THz and 0.88 – 1.06 THz, respectively. The two guided modes in these two structures are the E_x^{11} and E_y^{11} modes, respectively. In the waveguide with $W = 150$ µm, the attenuation constant is quite small and varies between 0.014 – 0.1 dB/mm over 0.8 – 1.035 THz.

In the waveguide with $W = 100$ µm, the attenuation constant is between 0.021 – 0.28 dB/mm over 0.88 – 1.1 THz. Fig. 5.24 shows the distributions of the magnitudes of the electric field of the two E_x^{11} and E_y^{11} modes for the U-SOG waveguide with $W = 100$ µm, $H = 50$ µm, $W_c = 60$ µm, and $H_c = 50$ µm, at 1 THz. As shown in this figure, the dominant E_x^{11} mode is highly confined within the top region of the Si guiding channel.

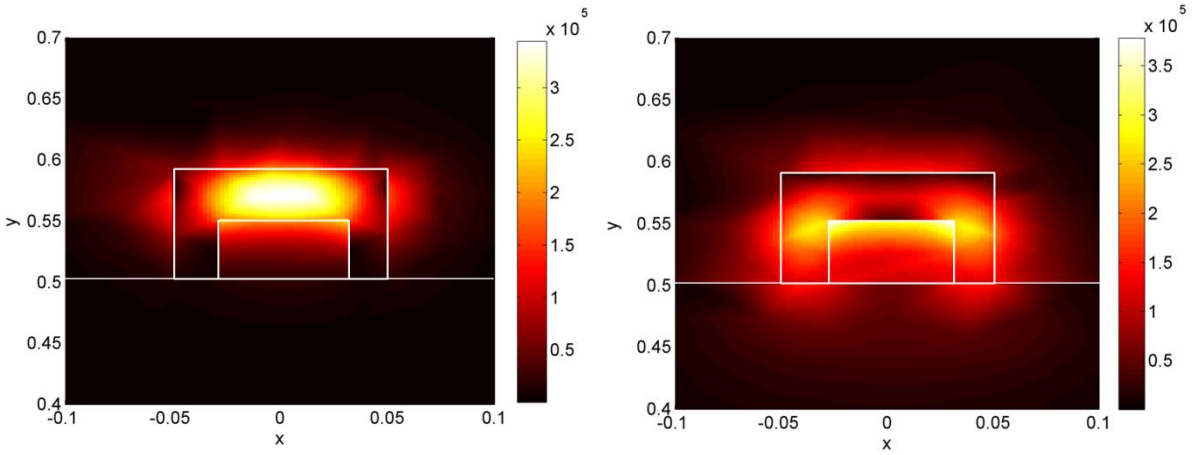

(a) (b)

Fig. 5.24 Distribution of the magnitude of the electric field in the U-SOG waveguide with W = 100 µm and H = 50 µm: a) E_x^{11} mode, and b) E_y^{11} mode.

5.4.3 Parametric Studies

Simulations are conducted to study the effect of different parameters on the propagation constant of the U-SOG waveguide. Fig. 5.25 shows the propagation constants of the waveguides with W = 100 µm, W_c = 60 µm, and T = 500 µm, for different values H and H_c, while $H + H_c$ is constant and equal to 100 µm (the thickness of the Si device layer is 100 µm). As expected, by decreasing H, the operation bandwidth of the waveguide is shifted to higher frequencies. Fig. 5.26 shows the attenuation constant of the U-SOG waveguide for different values of H_c when all other parameters are kept constant and equal to W = 100 µm, H = 50 µm, W_c = 60 µm, and T = 500 µm. By increasing H_c, the waveguide attenuation decreases. With an H_c = 50 µm, the waveguide attenuation is 0.038 – 0.32 dB/mm over the frequency band of 0.9 – 1.1 THz.

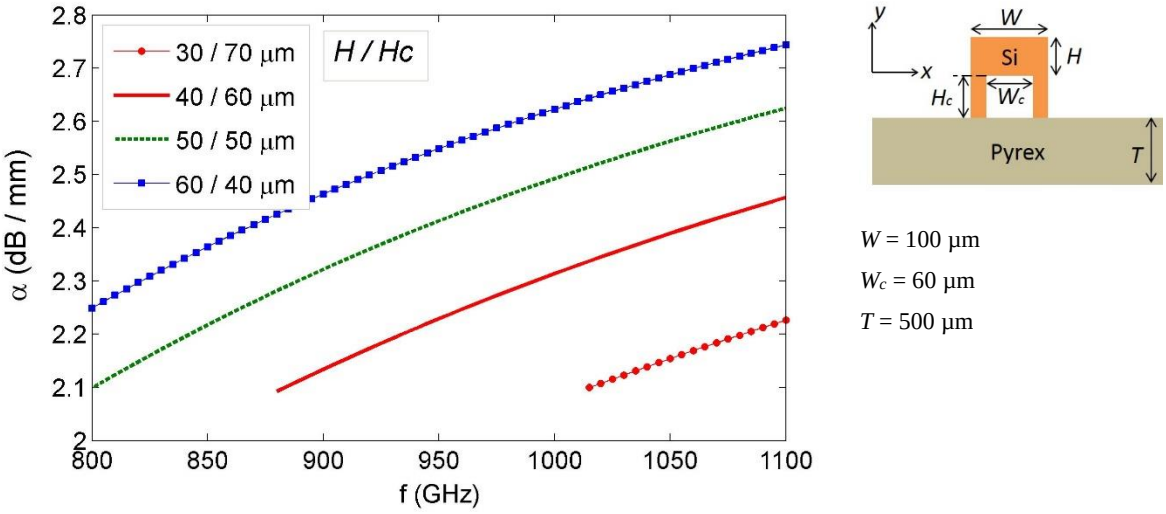

(a)

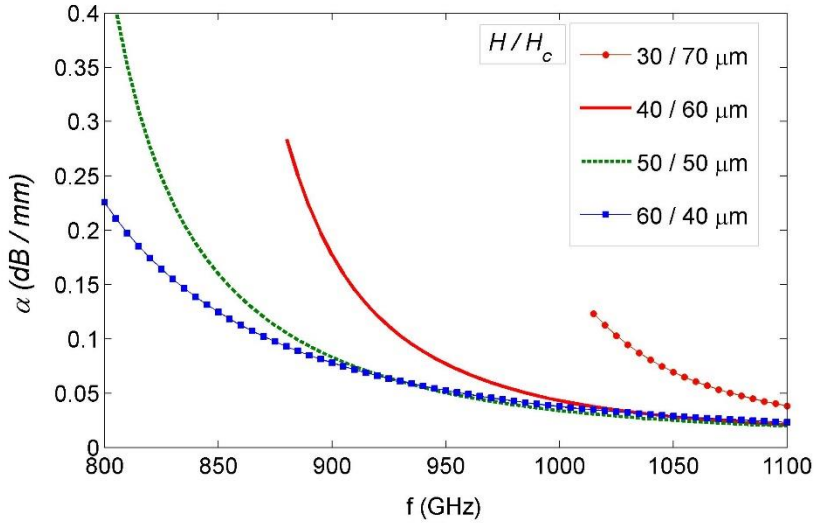

(b)

Fig. 5.25 Simulation results of the U-SOG waveguide: a) attenuation constant, and b) phase constant.

5.4.4 Simulation Results of the Designed Test Devices

Several U-SOG waveguide test devices are designed for fabrication and measurement. These waveguides completely cover the frequency range of 0.8 – 1.1 THz. The dimensions of the designed test devices are provided in Table 5.2. Fig. 5.27 shows part of test setup where the top region of the Si guiding channel is tapered inside the metallic ports. The simulation results for the scattering parameters

of two of these devices are provided in Figs. 5.28, 29 for lengths of ~ 10 mm. The length of the tapered segments in all of these structures is L_t = 0.7 mm. Fig. 5.28 shows the simulated scattering parameters for the U-SOG waveguide with W = 150 µm (line 1 in Table 5.2) over the frequency range of 0.8 – 0.9 THz. The insertion loss of a length of L_1 = 9.8 mm of this waveguide, plus two transitions to the metallic ports, is only 0.61 – 1.4 dB over the entire frequency band of 0.8 – 0.9 THz. The return loss is always better than 25 dB. Fig. 5.29 shows the simulated scattering parameters for the U-SOG waveguide with W = 100 µm (line 5 in Table 5.2) over the frequency range of 0.9 – 1.1 THz. The insertion loss of a length of L_1 = 10 mm of this waveguide is only 0.48 – 1.93 over the entire frequency band of 0.9 – 1.1 THz. The return loss is always better than 30 dB.

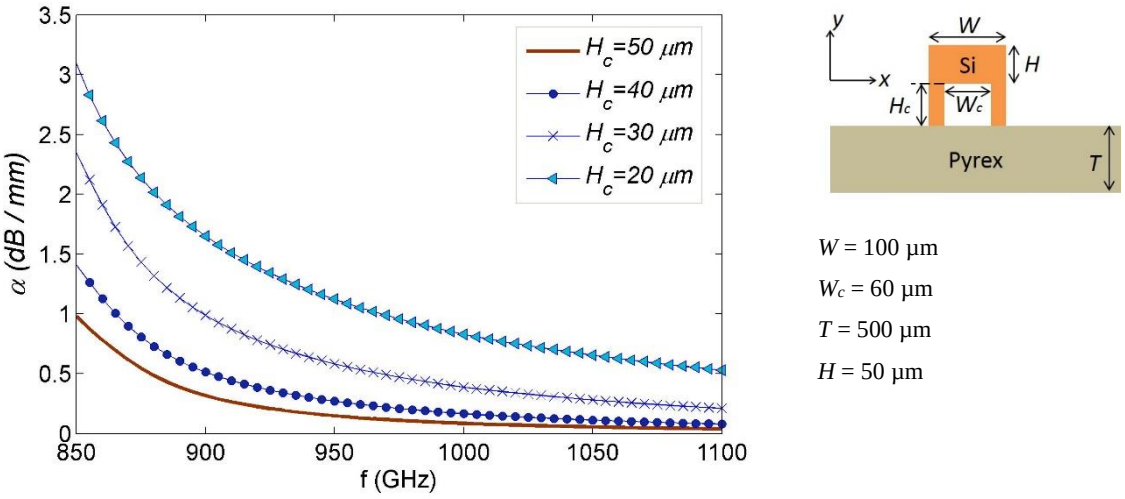

Fig. 5.26 Attenuation constants of the U-SOG waveguides for different values of H_c.

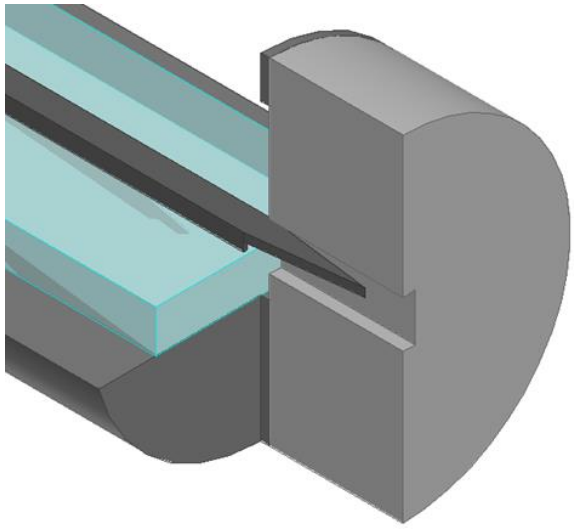

Fig. 5.27 Test setup structure for the U-SOG waveguide.

Table. 5.2. Dimensions of the U-SOG waveguides studied in Figs. 5.28, 29.

Rib SOG #	W (μm)	H (μm)	H_c (μm)	W_c (μm)	T (μm)	L_1 (mm)	L_2 (mm)	L_t (mm)
1	150	40	60	110	500	9.8	19.8	0.7
2	150	40	60	90	500	9.8	19.8	0.7
3	110	40	60	70	500	10	20	0.7
4	110	40	60	50	500	10	20	0.7
5	100	40	60	60	500	10	20	0.7
6	100	40	60	40	500	10	20	0.7

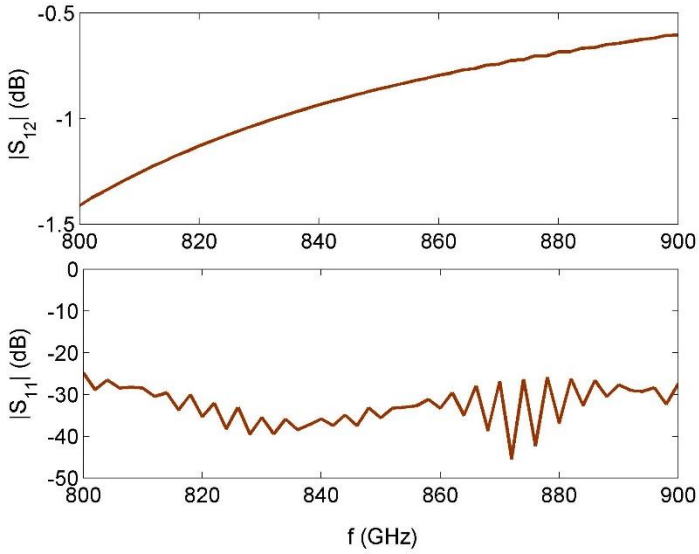

Fig. 5.28 Scattering parameters of the U-SOG waveguide with W = 150 μm (line 1 in Table 5.2) for a length of 9.8 mm between the two transitions.

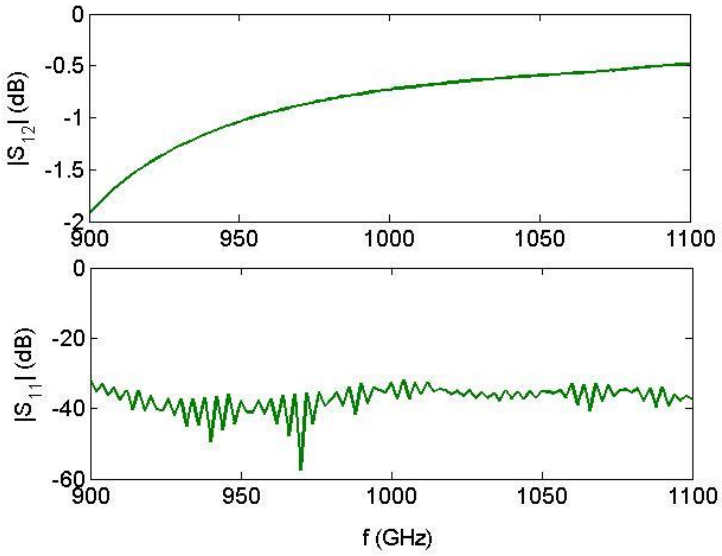

Fig. 5.1 Scattering parameters of the U-SOG waveguide with W = 100 μm (line 5 in Table 5.2) for a length of 10 mm between the two transitions.

5.4.5 Fabrication Technique

The fabrication of the U-SOG waveguide is a two-mask process. To fabricate the proposed U-SOG waveguide, the device layer of the SOI wafer is etched up to a depth of H_c before bonding to the Pyrex wafer. The entire process flow is shown in Fig. 5.30.

First the SOI wafer is cleaned using the Piranha process. The Si surface of the device layer of the SOI is coated with an 11 μm-thick photoresist using a spinner. The photoresist layer is patterned via optical lithography using the first glass-chromium mask. The DRIE technique is used to etch the Si device layer with the thick photoresist mask. The etch depth (H_c) is precisely controlled during the process. The two SOI and Pyrex wafers are cleaned using the Piranha process before bonding. The etched surface of the Si device layer is bonded to the Pyrex wafer via the anodic bonding technique. After successive wet etching of the Si handle and oxide layers, the Si device layer is etched. A thick photoresist mask, which is patterned via optical lithography using the second glass-chromium mask, is used as the etching mask. The Si guiding channel is formed via DRIE through the Si layer. The fabrication of the U-SOG waveguide test devices is currently underway at the time of writing.

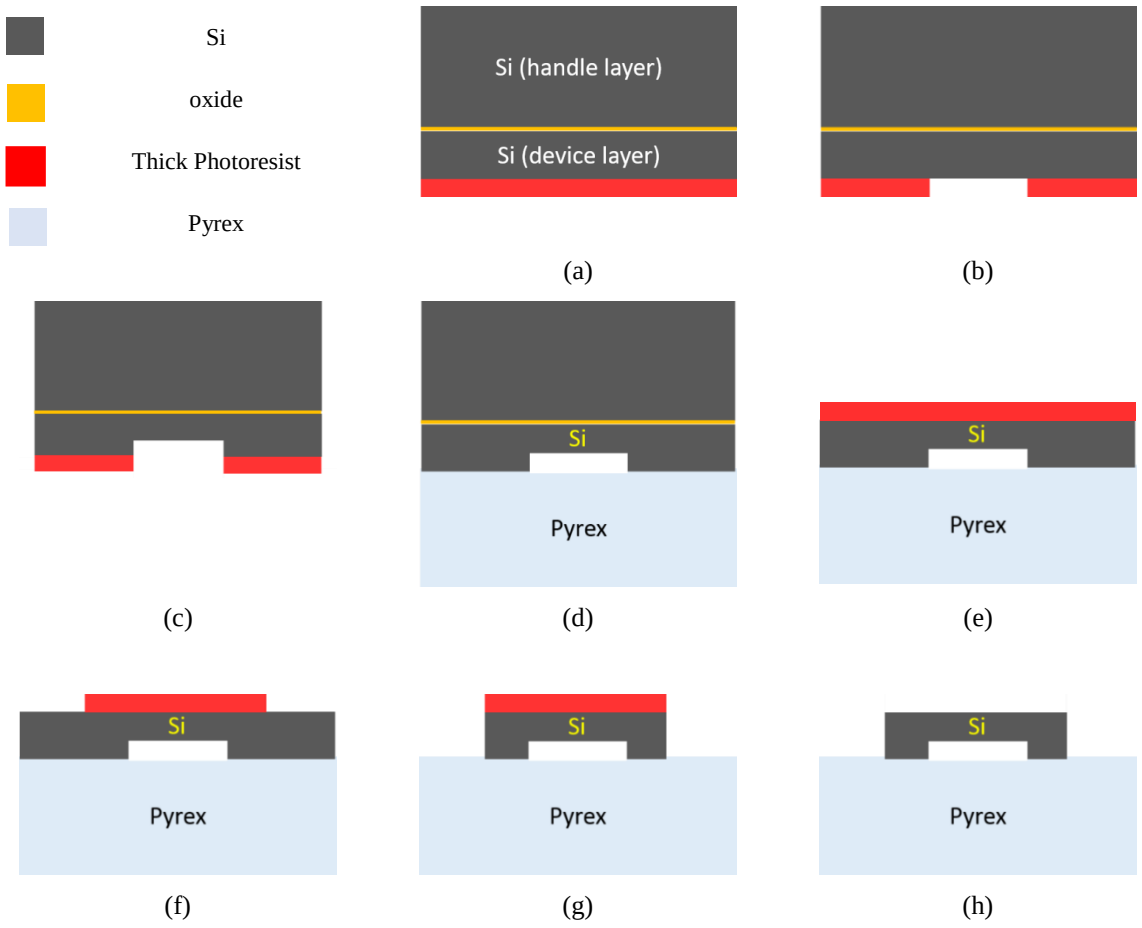

Fig. 5.2 Process flow of the fabrication of the U-SOG waveguide:

a) coating the Si device layer with thick photoresist, b) optical lithography to pattern the mask, c) DRIE to etch below the Si guiding channel, washing out the photoresist mask in acetone, and piranha cleaning of the SOI and Pyrex wafers, d) anodic bonding of the etched Si surface to the Pyrex wafer, e) wet etching the Si handle and oxide layers, and coating the Si surface with photoresist, f) optical lithography to form the thick photoresist mask for the DRIE of Si, g) DRIE of the Si device layer to form the Si guiding channel, and h) washing out the photoresist mask in acetone.

5.5 Conclusion and Discussion

This Chapter discussed the extension of the SOG platform into THz frequencies with the emphasis on high-density integrated circuits application. It was theoretically shown up to 1.1 THz that although suspended SOG waveguide has low-loss at THz frequencies, still it has drawbacks in terms of high-

density passive-circuit integration. To overcome these drawbacks and to achieve a more convenient structure, which does not show the intrinsic design limitations of a periodic structure, two new SOG waveguide structures, called the rib SOG and U-SOG waveguides, were proposed.

It was demonstrated that these two SOG waveguides outperformed the suspended SOG waveguide at higher frequencies ~ 1.1 THz. These two novel SOG structures can serve as low-loss platforms for THz high-density integrated circuits. The fabrication techniques of these two new SOG structures were developed. The effect of different parameters on the proposed waveguides' performances was studied. Rib SOG and U-SOG waveguides were designed for fabrication and measurement over the frequency ranges of 0.75–1.1 THz and 0.8–1.1 THz, respectively. Simulated results of the designed rib SOG waveguides showed attenuation constants of 0.01 – 0.03 dB/mm and 0.02 – 0.05 dB/mm over the frequency ranges of 0.75–0.9 THz and 0.9–1.1 THz, respectively. Simulations of the designed U-SOG waveguides demonstrated low attenuation constants of 0.02 – 0.1 dB/mm and 0.02 – 0.18 dB/mm over the frequency ranges of 0.8–1 THz and 0.9–1.1 THz, respectively. The fabrication of the U-SOG waveguides is underway.

Chapter 6 Integrated Passive Components Implemented on the Silicon-on-Glass Platform

In Chapters 3, 4, and 5, silicon-on-glass (SOG) waveguides were proposed for millimeter-wave (mmW) and terahertz (THz) integrated circuits and their low-loss properties were demonstrated theoretically up to 0.5 THz and experimentally up to 1.1 THz. The fabrication technique of the SOG technology uses photolithography and deep reactive ion etching (DRIE) to define the features with sub-micron accuracy. The high-precision and compact features that are achievable in this technology make it an attractive candidate for use in mmW/THz compact passive components.

In this Chapter, mmW passive components implemented on the SOG technology are discussed. Dielectric SOG tapered antennas and fully-dielectric tunable SOG phase shifters are designed, fabricated, and measured. Other mmW SOG passive components, including bend, power divider, dielectric resonator, and phase shifter, have been studied in [109].

6.1 Millimeter-Wave Tunable Dielectric Phase Shifters

Low-loss phase shifters at mmW/THz ranges of frequencies are the key elements for phased array systems which are vital for fifth generation mobile networks (5G), mmW/sub-mmW radar, and mmW/THz imagers. At mmW/THz frequency ranges, dielectric phase shifters offer lower insertion loss than those based on resistive perturbation, due to the increasing skin effect as the frequency rises.

The idea of dielectric phase shifters, by varying the distance between the waveguide and a block of dielectric, was first introduced for microwave frequencies in [140, 141]. In [141], researchers developed a theoretical model based on the effective permittivity method to study dielectric phase shifters consisting of asymmetrical slabs coupled to the rectangular rod dielectric waveguides, and simulation and measurement results were compared up to 30 GHz. In this Section, mmW dielectric phase shifters implemented on the SOG platform are discussed. Two kinds of dielectric phase shifters, the first one consisting of a symmetric silicon (Si) slab coupled to the SOG waveguide and the second one using asymmetric BLT (barium lanthanide tetratitanates) slab-loaded on the SOG waveguide, are designed, fabricated, and measured. Their low-loss characteristics are then compared with those of state-of-the-art mmW phase shifters.

6.1.1 Symmetric Si-Coupled SOG Phase Shifter

6.1.1.1 Phase Shifter Structure

The proposed phase shifter along with its test setup is shown in Fig. 6.1. The phase shifter consists of a symmetric Si slab which is coupled to the Si channel of the corrugated SOG waveguide studied in Chapter 4. The Si slab and the Si guiding channel have similar dimensions: H = 0.5 mm and W = 1.1 mm. The thickness of the glass substrate is T = 0.5 mm. The etched pattern has dimensions P = 0.5 mm, a = 100 µm, b = 1 cm, and d = 60 µm. The tapered sections of the Si channel each have lengths of L_t = 6 mm and the Si channel between these two tapered sections has a length of L = 19 mm. In addition to decreasing the insertion loss, the corrugation provides a highly symmetric medium surrounding the Si channels since the glass substrate is etched in most of the regions below the Si guiding channel. Along the coupled section, two orthogonal *odd* and *even* modes are propagating. The length of the coupling slab is designed to couple back most of the energy to the Si waveguide at the end of the coupling region with minimal insertion loss. The operation principle is discussed in the following Section in more details. The coupling length is l_s = 5 mm. The phase shifting is achieved by changing the coupling distance between the Si waveguide and the Si slab.

This is the first time that a phase shifter based on the coupling of a dielectric object to the dielectric waveguide is implemented in the mmW range. As a proof-of-concept, a micro-positioner is used to move the Si slab. In the next step, a micro-electromechanical systems (MEMS) based technology which is fully compatible with the SOG technology platform, will be introduced for moving the top dielectric slab.

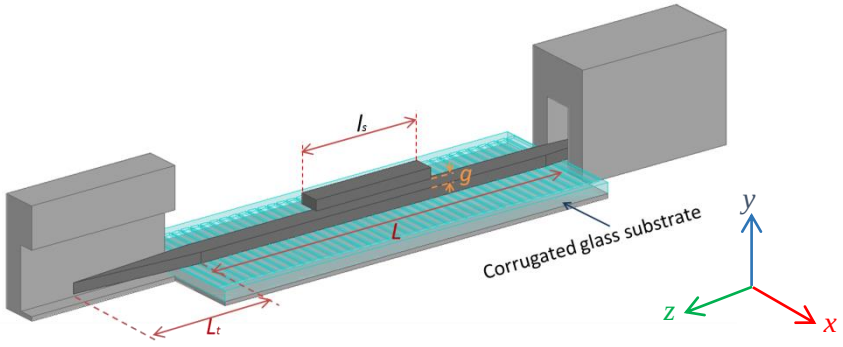

Fig. 6.1 Symmetric coupled SOG phase shifter and its test setup [114].

6.1.1.2 Operation Principle

The operation principle of the proposed phase shifter is based on the coupling. Dominant E_x^{11} mode is excited in the SOG waveguide. This mode propagates along the waveguide and at the beginning section of the coupling segment two even and odd modes are excited. These two modes propagate along the coupling segment. At the end of this section, if the difference in the phase variation of these two modes is π (this is a quantitative explanation to obtain an initial design parameter), then E_x^{11} mode, after experiencing a certain amount of phase shift controlled by the coupling distance g, is coupled back to the SOG waveguide with minimal insertion loss. By varying the coupling distance g, the propagation constants and the coupling amplitudes of the two *even* and *odd* modes change. Consequently, the total output phase of the wave exiting the coupled segment changes. The operation principle of this phase shifter should be differentiated from those based on perturbing the dielectric waveguide [109, 142-143].

To confirm the fact that only even and odd modes are excited along the coupling segment, the following simulations are conducted in high frequency structure simulator (HFSS). In the simulated structure, which is shown in Fig. 6.2, cross sections *A* and *B* are defined as wave-ports with the dominant E_x^{11} mode and quite enough number of modes, respectively. Fig. 6.3 shows the simulation results of the coupling to the even and odd modes for different values of g. The simulation of this structure for different values of the coupling distances (g) shows how the amplitude of couplings to the two even and odd modes vary with g.

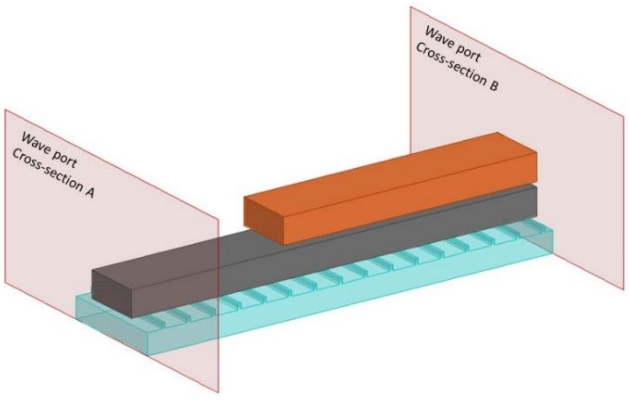

Fig. 6.2 Simulated structure in HFSS.

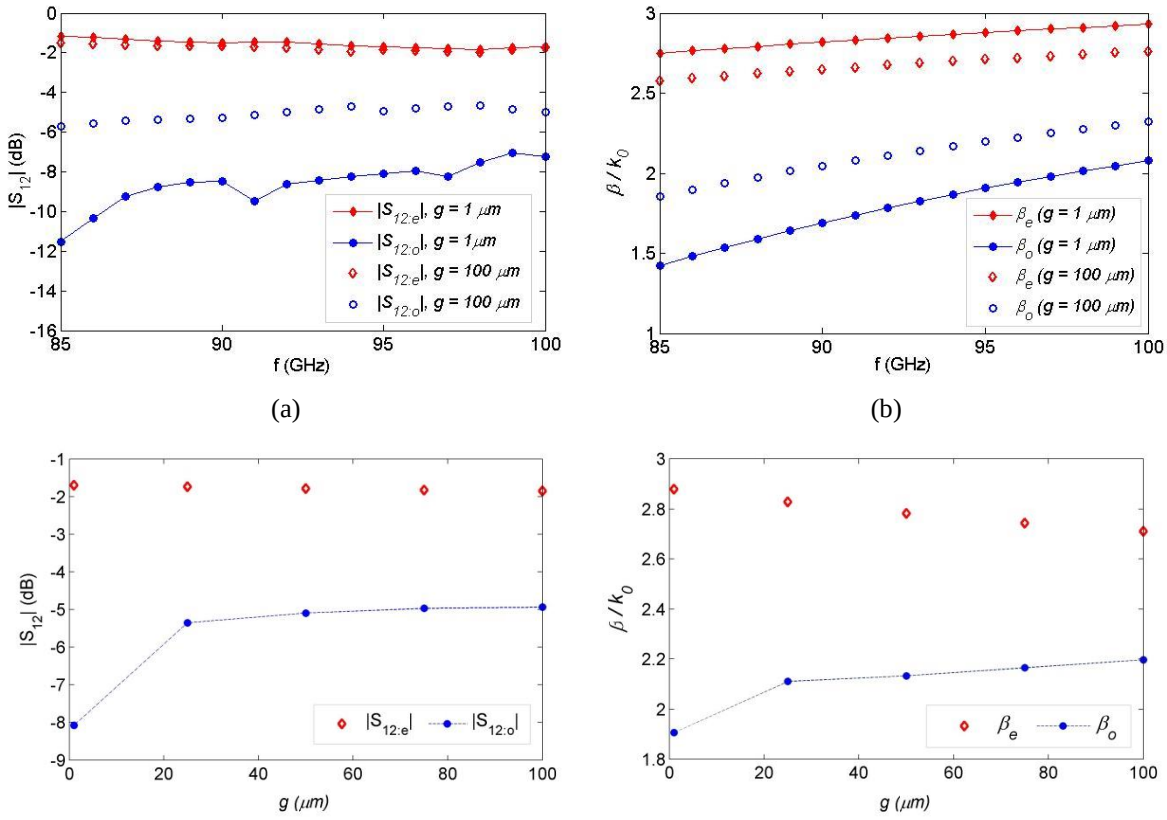

Fig. 6.3 Simulation results of the structure shown in Fig. 6.2: a) variation of the coupling amplitude to the two even and odd modes ($|S_{12:e}|$ and $|S_{12:o}|$ respectively) versus frequency for two different values of the coupling distance g = 1 and 100 μm, b) variation of the normalized phase constants (β/k_0) of the two even and odd modes versus frequency for two different values of g = 1 and 100 μm, c) variations of the $|S_{12:e}|$ and $|S_{12:o}|$ versus g at f = 95 GHz, and d) variation of β/k_0 of the even and odd modes versus g at f = 95 GHz.

As the simulation results show, two main modes are propagating along the coupling segment. The simulation results confirm that the coupling to the higher order modes is negligible and below -20 dB. Figs. 6.3(b, d) show the simulation results how the phase constants of the two modes (β_e and β_o) vary with the coupling distance (g). The total phase variation is a combination of these two effects. As the simulation results show the generalized scattering parameters $|S_{12:e}|$ and $|S_{12:o}|$, which respectively show the coupling amplitudes to the two even and odd modes, tend to each other by increasing the coupling distance g. This is quite reasonable given that by increasing g, the coupling between the two Si blocks (Si guiding channel of the SOG waveguide and the coupled Si slab) is decreased, and consequently the

two even and odd modes tend to have similar characteristics.

6.1.1.3 Experimental Verification

Fig. 6.4 shows the measured output phase over 95-110 GHz as the coupling distance (g) varies by steps of 12.5 µm. The plots show the relative phase shifts with respect to when g = 0. Phase shifts of 111° and 129° are achieved at frequencies of 85 GHz and 100 GHz, respectively. Fig. 6.5 shows the measured scattering parameters of the phase shifter test setup (Fig. 6.1) for four different values of g. As this figure shows, the return loss is always better than 15 dB.

Fig. 6.6 shows the frequency variation of the maximum measured insertion loss for nine different values of g. The measured scattering parameters belong to a length of 19 mm of the structure (a length of l_s = 5 mm of the phase shifter plus 14 mm length of the waveguide), plus two transitions between the dielectric waveguide and the rectangular waveguide ports. The measured insertion loss of the transitions for a length of 19 mm of the corrugated SOG waveguide has been added to Fig. 6.6. The small difference between the two graphs confirms the low-loss characteristics of the proposed phase shifter.

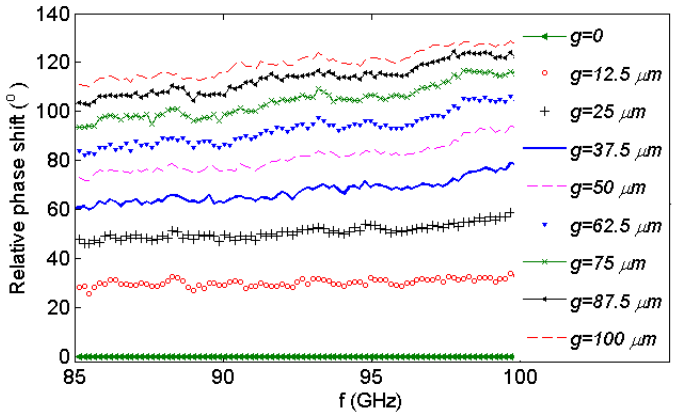

Fig. 6.4 Measured relative phase shifts of the SOG phase shifter [114].

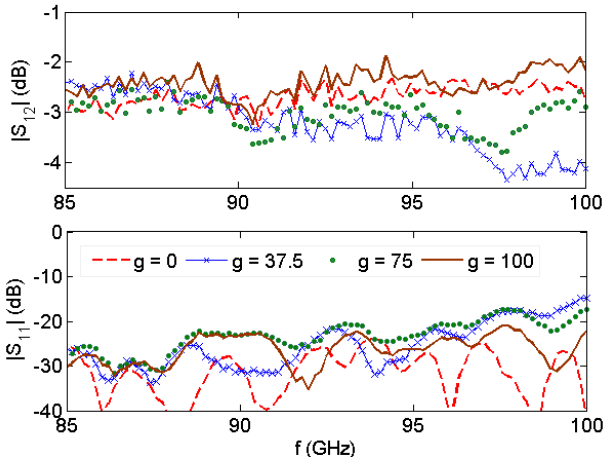

Fig. 6.5 Measured scattering parameters of the phase shifter test setup [114].

To extract the phase shifter insertion loss, the measured insertion loss of the waveguide is subtracted from that of the phase shifter test setup to de-embed the effect of transitions and the SOG waveguide segments. The maximum insertion loss of the phase shifter, extracted based on this technique, is shown in Fig. 6.6. The phase shifter insertion loss is quite small (< 2.8 dB) over the entire band. At 88 GHz, the maximum insertion loss is only 0.6 dB for a phase shift of 114° achieved at this frequency. Fig. 6.7 displays the phase shifter's figure of merit which is defined as the ratio of the maximum achievable phase shift over the maximum insertion loss ($\Delta\varphi / |S_{12}|_{max}$), versus frequency. A maximum figure of merit of 187 is achieved at the frequency of f = 88 GHz.

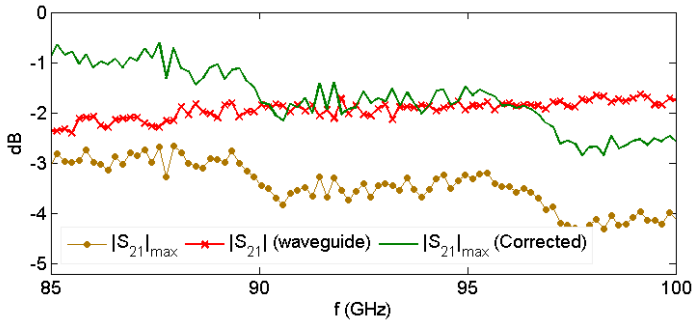

Fig. 6.6 Maximum insertion loss of the phase shifter extracted from the measured scattering parameters ($|S_{21}|_{max}$ (corrected)). $|S_{21}|_{max}$ shows the maximum insertion loss of the test setup (Fig. 6.1) [114].

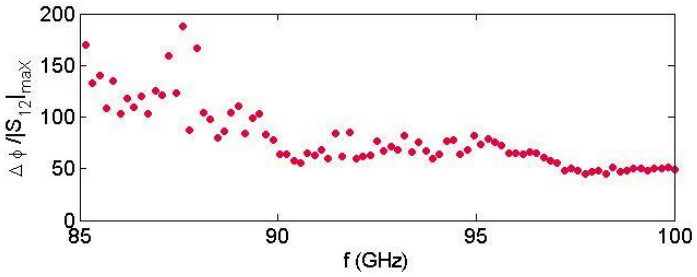

Fig. 6.7 Figure of merit of the phase shifter ($\Delta\varphi/|S_{12}|_{max}$).

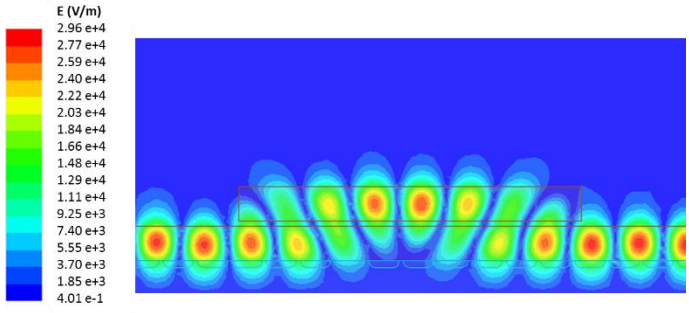

(a)

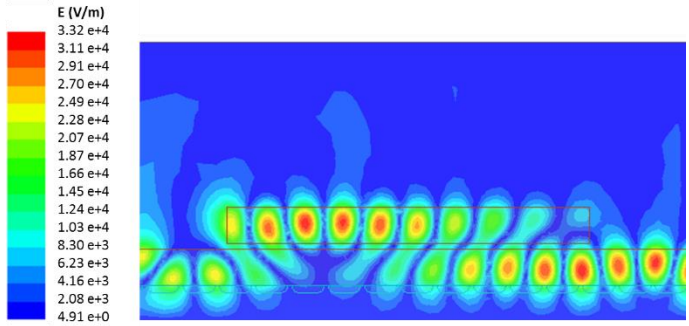

(b)

Fig. 6.8 Electric field distribution over the *y-z* plane bisecting the structure: a) at 90 GHz and b) at 110 GHz.

Fig 6.8 shows the distribution of the magnitude of the electric field over the *y-z* plane bisecting the structure at frequencies of 90 GHz and 110 GHz (the phase shifter operational bandwidth is over 85 – 100 GHz). As shown in this figure, at 90 GHz, the electric field couples to the Si slab and couples back to the SOG waveguide with low scattering loss. However, at 110 GHz, the length of the coupled slab is too long. As a result, there is scattering and radiation loss at the discontinuity of the coupled slab.

6.1.2 BLT-Loaded SOG Phase Shifter

A fully-dielectric phase shifter based on loading of the SOG waveguide with a BLT slab is demonstrated in this Section. This technique was previously implemented on a coplanar waveguide and a Si image guide [144-146]. The main advantage of the phase shifting technique reported in [144-146] is that the variation in the insertion loss is quite small over a large phase change. The new SOG implementation of the BLT-loaded phase shifter structure is shown in Fig. 6.9.

The phase shift is achieved by changing the propagation mode of the SOG waveguide using a high dielectric constant material placed over the top of the waveguide. In the BLT-loaded phase shifter, due to the high permittivity of the BLT material, the field is highly confined within the air region between the Si channel and the BLT slab. The phase shifting is achieved by changing the air gap, which can be considered as a new waveguide (BLT-air-Si). The Si channel of the corrugated SOG waveguide has dimensions W = 1.1 mm and H = 500 µm. The BLT dielectric slab has a dielectric constant of ε_r = 60, a thickness of T_s = 280 µm, a width of W_s = 5.6 mm, and a length of L_s = 4.2 mm.

Figs. 6.10, 11 show the measured phase shift and the measured scattering parameters of the SOG phase shifter test setup (Fig. 6.9) as the distance g between the BLT slab and the Si channel of the SOG waveguide is changed by steps of 12.5 µm, respectively. A large phase variation was measured when the dielectric slab moved over a distance of g = 62.5 µm. In Fig. 6.10, the plots show the relative phase shifts with respect to when g = 0. Large total phase shifts of 138° and 82° are observed at frequencies of 95 GHz and 110 GHz, respectively. At 110 GHz, over a large phase variation of 82°, the change in the insertion loss is only 0.7 dB. When g = 62.5 µm, the insertion loss of the whole system, consisting of a length of 19 mm of the SOG waveguide and the two transitions to the rectangular waveguide ports, varies between 1.38 dB and 2.19 dB over 95-110 GHz. The return loss is always better than 16 dB.

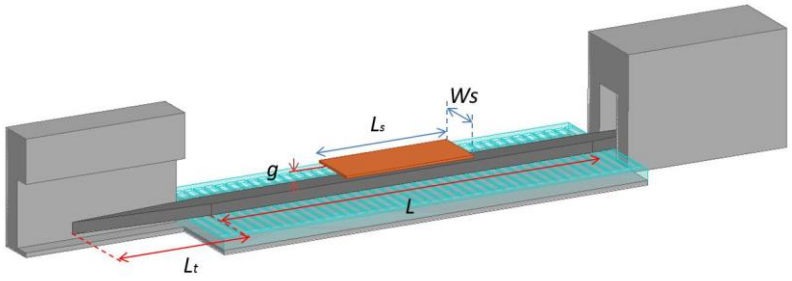

Fig. 6.9 BLT-loaded SOG phase shifter and its test setup.

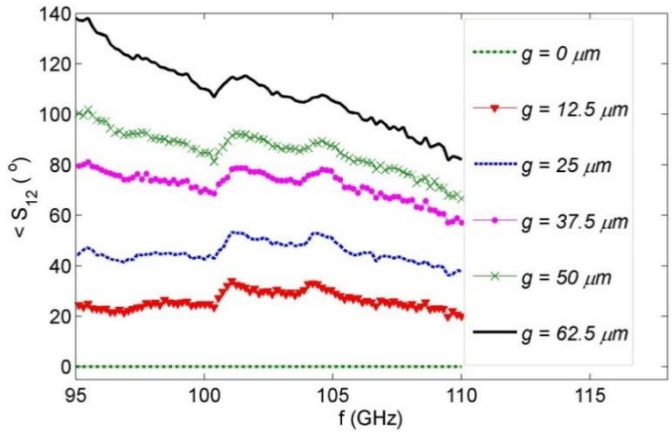

Fig. 6.10 Measured relative phase shift of the BLT-loaded SOG phase shifter.

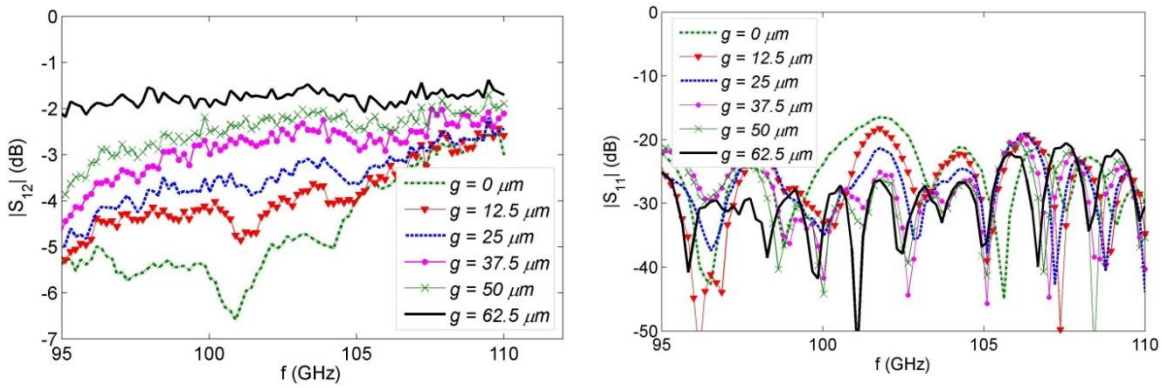

(a) (b)

Fig. 6.11 Measured scattering parameters of the BLT-loaded SOG phase shifter test setup: a) insertion loss and b) return loss.

Fig. 6.12 shows the frequency variation of the maximum measured insertion loss for six different values of g. The measured scattering parameters belong to a length of 19 mm of the structure plus two transitions to the rectangular waveguide ports. The measured insertion loss of the transitions for a length of 19 mm of the corrugated SOG waveguide has been added to Fig. 6.12. To extract the phase shifter insertion loss, the measured insertion loss of the waveguide is subtracted from that of the phase shifter test setup. The maximum insertion loss of the phase shifter, extracted based on this technique, is shown in Fig. 6.12. The phase shifter insertion loss is 0.4 - 4.9 over the frequency range of 95 - 110 GHz.

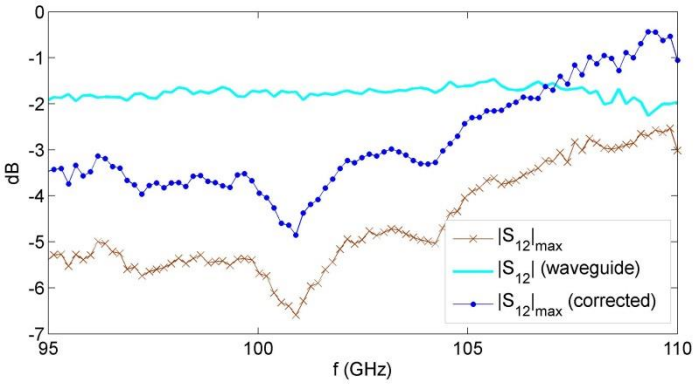

Fig. 6.12 Maximum insertion loss of the phase shifter extracted from the measured scattering parameters ($|S_{21}|_{max}$ (corrected)). $|S_{21}|_{max}$ shows the maximum insertion loss of the test setup (Fig. 6.9).

6.1.3 Performance Comparison

Table 6.1 compares the performance of the proposed phase shifters with other mmW techniques in the literature. The Si-coupled SOG phase shifter shows measured phase shifts of 111° and 129° at frequencies of 85 GHz and 100 GHz, with maximum insertion losses of 0.65 dB and 2.5 dB, respectively. This table confirms the significant reduction in both the insertion loss and the size of the symmetric Si-coupled SOG phase shifter as compared to other techniques.

Table. 6.1. Phase shifter performance comparisons.

f (GHz)	$\Delta\phi$	$\Delta\phi$ / l_s (°/cm)	$\lvert S_{21}\rvert_{max}$	$\Delta\phi$ /$\lvert S_{21}\rvert_{max}$ (°/dB)	
110	200	125	-6	33	[142]
110	200	300	-4.6	43	[147]
110	400	715	-4	98	[148]
105	318	221	-2.7	148	[149]
94	331	770	-3.4	97	[150]
76.5	360	1028	-5.7	63	[151]
109	87	21	-0.4	217	BLTloaded phase shifter
101	113	27	-4.9	23	BLTloaded phase shifter
100	129	258	-2.5	52	Si coupled phase shifter
85	111	222	-0.65	170	Si coupled phase shifter

The Si-coupled SOG phase shifter and BLT-loaded phase shifter show measured insertion losses of 0.65 - 2.5 dB over 85 - 110 GHz and 0.4 - 4.9 over 95 - 110 GHz, respectively.

6.2 Millimeter-Wave Integrated Tapered Antennas

One essential component in the realization of any imaging and wireless communication system is a high-performance antenna which can be integrated into a low-cost planar circuit technology. A dielectric tapered antenna with advantages including broad-bandwidth, high-efficiency, and compatiblity with mmW integrated circuits based on dielectric waveguides, is a promising candidate for high-speed communications, mmW phased array systems, and mmW/THz imagers.

In [152- 154], tapered dielectric rod antennas excited by horn transitions from rectangular waveguides were reported for mmW applications. Although the reported antenna structures were based on dielectric waveguides, the metallic feeding structures were incompatible with integrated planar technologies. In [63], a tapered dielectric antenna made of alumina was realized in a substrate integrated image guide (SIIG, also known as a perforated image guide) platform. Using this technique, the tapered dielectric antenna was an integrated part of a planar circuit structure, in which low-permittivity regions surrounding the guiding channel were synthesized by dielectric slab perforation, at the cost of losing simplicity and lowering the circuit density [63]. A measured gain of 12.8 dB and a simulated efficiency of 74 % at 94 GHz were reported for this tapered antenna. For prototyping, a laser was used to cut the antenna structure out of the alumina substrate.

A high-resistivity gallium arsenide (GaAs) dielectric tapered rod antenna was designed, fabricated, and measured in [155]. A gain of ~ 10 dB was reported for this antenna over 75-325 GHz. The antenna gain was limited by fabrication constraints which prevented a long tapering since cutting sharp tapered tips using a diamond blade makes the tips too fragile. Although the antenna was reported for mmW integrated circuits, no supporting substrate was introduced for the designed high-permittivity dielectric elements [155, 156].

A two-stepped pyramidal tapered rectangular rod antenna fabricated by controlled wet chemical etching of high-resistivity Si was fabricated and measured in [157]. A gain of 8–10 dB at W-band frequencies was reported for this antenna. Unfortunately, wet chemical etching of Si does not provide sufficient dimensional accuracy, which is highly critical at mmW/THz frequencies. A lateral dimension control of 5 μm was reported using this technique [157].

This Section presents mmW high-efficiency tapered dielectric antennas, which are designed and fabricated in the SOG platform. The fabrication process makes the tapered antennas with DRIE of the Si layer of the SOG platform. Two SOG tapered antenna configurations are investigated. In the first configuration, the glass substrate below the Si tapered antenna is laser-cut around the tapered segments. This antenna is designed for high-gain/efficiency over the frequency range of 50-75 GHz. In the second configuration, to further improve the radiation characteristics of the SOG tapered antenna in terms of gain/efficiency, the glass substrate below the Si tapered antenna is etched with hydrophilic acid (HF, 49 %). This antenna can operate under either E_x^{11}-mode or E_y^{11}-mode excitations with highly linear polarizations, over the frequency band of 110 - 130 GHz. Numerical and experimental results are presented to validate the proposed antennas' high-performance. These two SOG tapered antennas feature additional advantages including integrability and low-cost fabrication.

6.2.1 Silicon-on-Glass Tapered Antenna

The antenna structure, the measurement setup, and the near-field measurement system are shown in Fig. 6.13. The radiation measurements have been performed in the *Electromagnetic Radiation Lab* at the *Centre for Intelligent Antennas and Radio Systems* (*CIARS*), University of Waterloo. The radiation measurements are performed using near-field measurement systems from NSI, a PNA-X (Agilent Technologies Inc.), and OML extension modules with standard rectangular waveguide ports.

The proposed SOG antennas is simulated and optimized in HFSS. The antenna is supported on an aluminum test setup with a conductivity of $\sigma = 3.744\times10^7$ S/m. The ground plane is set to be advantageous so as to increase the antenna directivity due to the image effect. The proposed SOG waveguide is tapered inside the rectangular waveguide to couple the TE_z^{01} mode of the rectangular waveguide to the E_y^{11} mode of the SOG waveguide. The tapered section of the transition has a length of L_c = 4 mm. This transition is optimized for maximum coupling to the dielectric waveguide modes with minimal return loss and spurious radiation from the transition. A length of L_w = 2 mm of the SOG waveguide, which connects this transition to the antenna, excites the antenna with the E_y^{11} mode of the SOG waveguide. The Si channel of the SOG waveguide has a width of W = 0.8 mm and a height of H = 0.4 mm, and the thickness of the Pyrex is T = 0.5 mm.

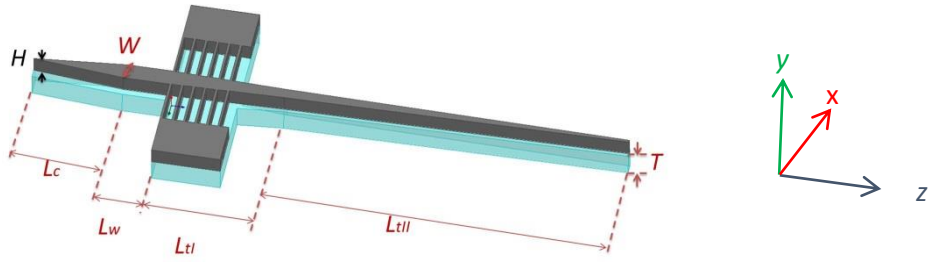

(a)

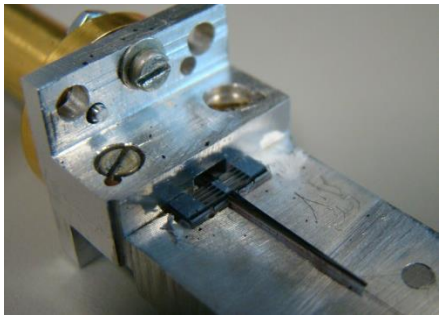

(b)

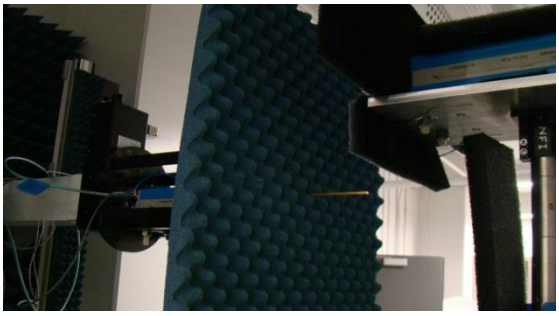

(c)

Fig. 6.13 Tapered SOG antenna measurement, (a) antenna structure, (b) measurement setup and the fabricated sample, and (c) near-field measurement system in CIARS [111].

The tapered antenna has two segments: 1) a feeding segment; and 2) a radiating segment [158]. Along the feeding segment, the width of the Si channel gradually decreases to make the normalized phase constant close to that of the air, or $\beta/k_0 \sim 1$. The radiation is mainly coming from the radiating segment, whose length and taper angle are optimized to obtain uniform radiation along the segment. The antenna design is based on previously published work in the literature [158]. The antenna's radiating tapered segment has a length of a few λ_0. After the initial design values were obtained, the antenna is optimized in the HFSS to find the optimal shape of the antenna in terms of high directivity and low side-lobe level (SLL). For the optimized structure, the feeding and terminal tapers have lengths of L_{tI} = 5 mm and L_{tII} = 15 mm, respectively. At the end of the feeding taper, the width of the Si antenna reaches to 0.5 mm and the antenna tip is 0.1 mm.

Two Si blocks are connected to the feeding tapered segment from both sides using a periodic configuration of Si beams. Simulations show that this configuration has an insignificant effect on the radiation characteristics of the antenna. These Si blocks are used for the alignment of the antenna inside the aluminum test setup. To fabricate the antenna, a pre-bonded SOG wafer with thicknesses of 400/500 μm (Si/Pyrex) is used. After photolithography and DRIE through the Si layer, a laser machine is used

to cut the Pyrex substrate around the antenna's feeding and radiating tapered segments and the transition tapered segment.

The radiation measurements are performed using the planar near-field measurement technique. This technique operates by sampling the amplitude and phase of the orthogonal components of the near-field over a planar surface (the antenna aperture). A metallic rectangular waveguide probe samples the *x*/*y*-components of the electric field over a well-defined surface a few wavelengths in front of the antenna under test (AUT). The far-field vector patterns are obtained by combining the two sampled orthogonal tangential field components [159].

6.2.1.1 Simulation and Measurement Results

Computational simulations and experimental studies are conducted to verify the proposed antenna performance over the wide bandwidth of 50-75 GHz. Fig. 6.14 shows the simulated and measured return losses of the antenna. The simulated and measured return losses of the antenna are better than 13.7 dB and 15.5 dB, respectively, over the entire 50-75 GHz band. There is good agreement between the simulated and measured return losses over the entire band.

Fig. 6.15 shows the simulated and measured *E*-plane and *H*-plane radiation patterns of the antenna at 50 GHz. It can be seen that there is good agreement between the simulated and measured radiation patterns. Due to the presence of the ground plane, the main lobe has an elevation relative to the ground plane. Simulation and measurement results show the maximum radiation at elevation angles of $\theta = 16^{\circ}$ and $\theta = 17^{\circ}$, respectively.

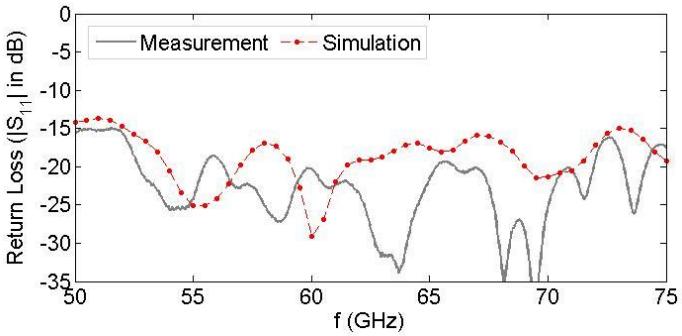

Fig. 6.14 Simulated and measured return losses of the antenna [111].

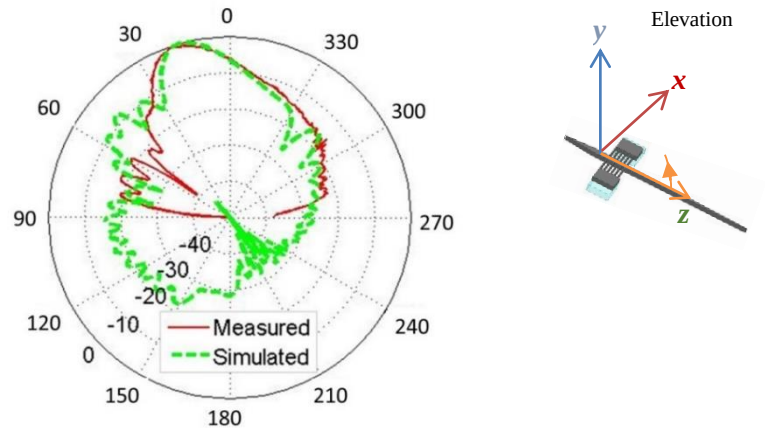

(a)

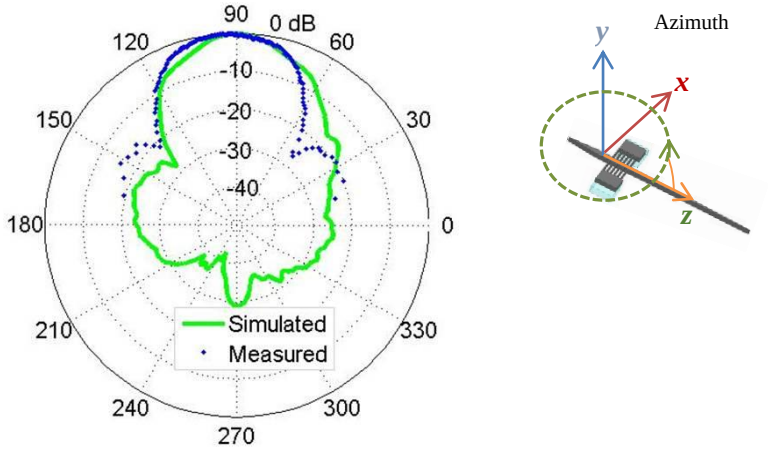

(b)

Fig. 6.15 Simulated and measured radiation patterns of the antenna at 50 GHz: (a) *E*-plane radiation patterns and (b) *H*-plane radiation patterns at θ = 16°/17° (simulation/measurement) [111].

The simulated and measured *E*-plane SLLs are -9 dB and -13 dB, respectively. The simulated and measured *H*-plane SLLs are -16 dB and -15.9 dB, respectively. Simulation and measurement results reveale half-power beam-widths of 16° and 22° for the *E*-plane radiation pattern and 26° and 36° for the *H*-plane radiation pattern, respectively. Both simulation and measurement data indicate that the beam squint as frequency changes is not significant. Beam squint varies by only 6°, namely from 19° to 13° (less than 30% of the beam width), as the frequency changes over 50-75 GHz according to the simulations.

Fig. 6.16 shows the simulated and measured directivities and gains of the antenna over its wide

operation bandwidth. As shown in Fig. 6.16(a), there is good agreement between the simulated and measured directivities of the antenna. At 50 GHz, the simulated and measured directivities are 16.6 dB and 16.4 dB, respectively. Simulations show maximum and minimum directivities of 17.1 dB at 55 GHz and 14.5 dB at 74 GHz, respectively. A maximum measured directivity of 17.5 dB occurs at 67 GHz and the minimum directivity of 14.6 dB occurs at 59 GHz.

As mentioned before, a planar near-field measurement system is used to obtain the far-field radiation pattern. Using this method, the field radiated to the back of the antenna is not measured and therefore it is assumed that the radiating aperture is completely unidirectional (no back radiation). Thus the directivity measured by this method is always greater than the true directivity of the antenna and depends on the intensity of the back radiation (back-lobe) and the size of the scanned area. Large back-lobe can cause large error (overestimation) in measured directivity. This is the main source of the small observed discrepancies between the two simulated and measured directivities**.** Simulations and measurements results show average directivities of 16 dB and 16.7 dB over 50-75 GHz, respectively.

In the actual test structure, made of aluminum, the ground plane is finite. This adds conduction loss and wedge-diffracted field to the measurements. To study these effects, simulations are performed in HFSS, taking into consideration the actual geometry and material properties of the test setup structure. As shown in Fig. 6.16(b), the calculated gain, which is obtained by simulating the actual antenna test setup, is in good agreement with the measured gain. The difference between the averaged gain obtained from the simulation and that obtained from the measurement is 0.19 dB. However, as shown in Fig. 6.16(a), the gain obtained from simulation of the antenna on a large perfect electric conductor (PEC) ground plane (touching the radiation boundaries) shows very high radiation efficiency for the SOG antenna. In this case, the simulated gain and directivity have insignificant differences which results in an average efficiency of 0.98 % over 50 - 75 GHz. This high radiation efficiency demonstrates that the material losses in Pyrex and Si (the internal loss of the antenna) are quite small and that the reduction in the actual structure's radiation efficiency is mainly due to test setup imperfections.

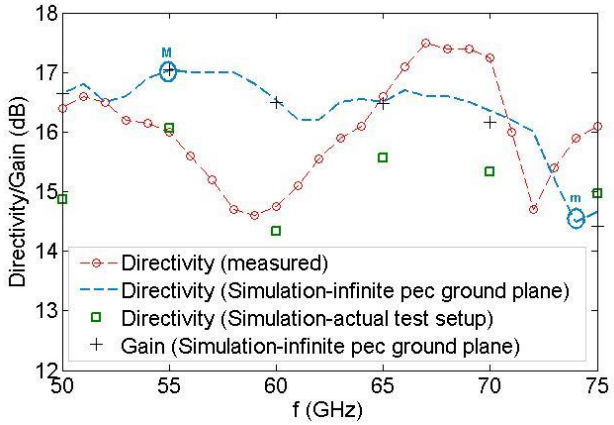

(a)

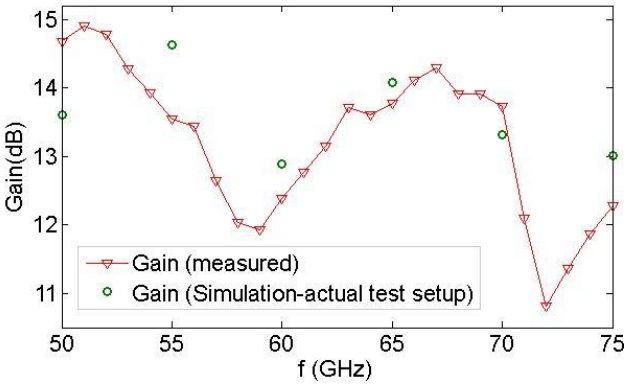

(b)

Fig. 6.16 Simulated and measured directivities and gains (a, b) [111].

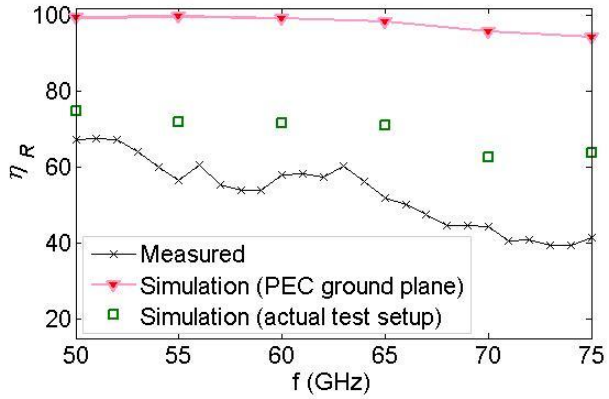

Fig. 6.17 Radiation efficiency [111].

Fig. 6.17 shows the efficiencies derived from simulations and measurements. The average measured efficiency over the entire band is 53 %. A maximum radiation efficiency of 67 % at f = 50 GHz is achieved by the measurement. As mentioned before, planar near-field measurement leads to an overestimation of the antenna directivity and consequently an underestimation of the efficiency. Therefore, the planar near-field measured efficiency is less than the true efficiency, which should be close to the simulated 70 % efficiency of the antenna, taking into account all the surrounding structures including the finite ground plane. The other source of discrepancies between the simulated and measured efficiencies is due to power leakage at the discontinuity between the rectangular waveguide segment of the test setup and that of the PNAX port (Fig. 6.13(b)). The leakage is suppressed in the modified test setup structure presented in Section 6.2.2.2.

6.2.2 Suspended SOG Tapered Antenna with Dual-Mode Operation

One of the unique advantages of the proposed SOG technology is the possibility of etching parts of the Pyrex substrate from below the devices to enhance their performances. This technique was used in Chapters 4 and 5 to reduce the waveguide loss at mmW/THz frequencies above 200 GHz. Even at lower frequencies, where the Pyrex is a high-quality low-loss substrate, etching the Pyrex provides better confinement within the Si structure. This property is used in designing the devices for which the lower interaction of the modal fields with the Pyrex substrate is highly advantageous to enhance their performances. In this Section, this property is used to significantly enhance the radiation performance of the SOG tapered antenna. The Pyrex substrate is removed from below the antenna tapered section in order to achieve a better radiation performance in terms of antenna directivity, gain, and efficiency as compared to SOG tapered antenna in Section 6.2.1. Although the antenna is tapered only in the *x*-direction, it can support both E_x^{11}- and E_y^{11}- mode excitations with high-directivities, high-efficiencies, and low cross-polarization levels. This is due to the fact that the absence of the glass substrate below the Si tapered antenna provides better confinement within the Si and a higher degree of symmetry in the antenna structure.

6.2.2.1 Design Specifications and Simulation Results

The antenna is made of two Si and Pyrex wafers with thicknesses of 500 μm. The antenna structure is shown in Fig. 6.18. The same mask used for the fabrication of the SOG tapered antenna in Section 6.2.1, is used to fabricate this antenna. All design parameters are similar between the two antennas. The

design parameters for the suspended tapered antenna are W = 800 μm, H = 500 μm, T = 500 μm, W_{tI} = 500 μm, W_{tip} = 100 μm, L_c = 4 mm, L_w = 2 mm, L_{tI} = 5 mm, L_{tII} = 15 mm, P = 500 μm.

To fabricate the antenna, the Pyrex wafer is first etched in HF 49 % using a Cr/Au mask. After anodic bonding of the etched surface of the Pyrex wafer to the Si wafer, the antenna is formed by DRIE through the Si layer. Dicing of the wafer is performed from the Pyrex side in such a way as to totally remove the Pyrex substrate from below the transition and antenna tapered segments (Fig. 3.17 in Chapter 3). The suspended SOG tapered antenna has a more convenient fabrication technique than the SOG tapered antenna (Section 6.2.1) due to difficulties inherent in laser cutting the glass substrate.

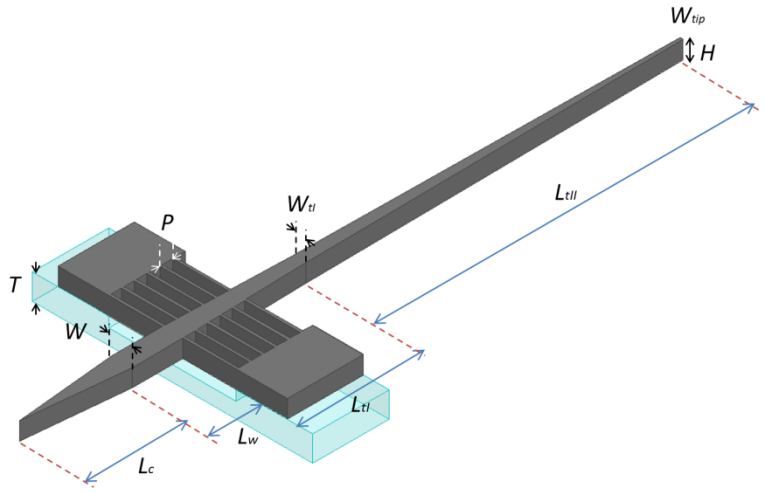

Fig. 6.18 Structure of the suspended SOG tapered antenna.

Over the frequency band of 110 - 130 GHz, the proposed suspended SOG antenna demonstrates good radiation characteristics for both E_x^{11}- and E_y^{11}- mode excitations in terms of directivity, gain, and SLL. Since the antenna is fabricated with the same mask as the one used for the fabrication of the SOG tapered antenna, it is not optimized for short length. There are a range of variables for which the antenna shows good radiation performance. Simulation confirms that similar radiation characteristics could be obtained with shorter lengths of the antenna radiating segment.

Fig. 6.19 shows the electric field distribution and the far-field radiation patterns in the suspended SOG tapered antenna for the two mode excitations. This figure shows the field distribution over the *yz*-plane bisecting the antenna structure, and over the *xz*-plane on the top face of the glass substrate at 130 GHz.

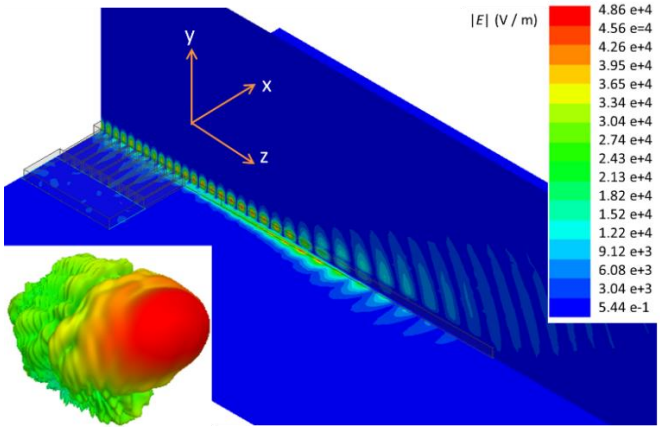

(a)

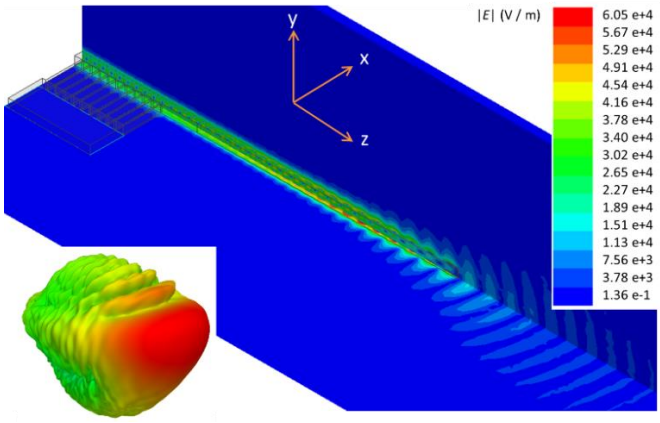

(b)

Fig. 6.19 Electric field distributions and far-field radiation patterns of the suspended SOG tapered antenna configuration of structure *I* at 130 GHz: a) Ex^{11}-mode excitation and b) E_y^{11}-mode excitation.

It is worth mentioning that the antenna is designed for an SOG integrated circuit, the ultimate goal being to have fully integrated circuits (including the source) in the SOG platform. However, since the measurement system has metallic ports, the SOG waveguide connected to the antenna is tapered. In the simulation results presented in this Section, the antenna structures shown in Fig. 6.20 are simulated in HFSS with wave-port excitations on the cross sections of the SOG waveguides to mimic their operation in the ultimate SOG integrated circuit.

Fig. 6.21 shows the simulated radiation gains of the suspended SOG antenna structures *I* and *II* (Fig. 6.20) for two different guided E_x^{11}-mode and E_y^{11}- mode excitations. For E_x^{11}- mode and E_y^{11}- mode excitations, structure *I* shows gains of 16 - 17.7 dB, and 17 - 17.6 dB, respectively, over the entire frequency band of 110 - 130 GHz.

As shown in Fig. 6.20, the suspended SOG tapered antenna of structure *I* is excited with the suspended SOG waveguide proposed in Chapter 4. In other words, the Si guiding channel exciting the antenna is supported using periodic Si beams over the etched region on the Pyrex substrate. This configuration is highly recommended at mmW/THz frequencies above 200 GHz, where the significant material loss of the Pyrex substrate should be minimized. However, over the operation frequency range of this research, there is no requirement to etch the Pyrex below the Si guiding channel. Alternatively, the antenna configuration shown in Fig. 6.20(b) as structure *II*, can be used based on the application. From the point of view of antenna performance and fabrication simplicity, these two structures are the same. However, they are excited with two different SOG and suspended SOG waveguide connections. Simulation results of the suspended SOG tapered antenna of structure *II* show gains of 16.4 - 17.4 dB and 16.2 - 17.5 dB for E_x^{11}-mode and E_y^{11}-mode excitations, respectively. In the suspended SOG tapered antenna of structure *II*, a transition from the SOG waveguide (Si channel is attached to the Pyrex substrate) to the suspended Si waveguide is required.

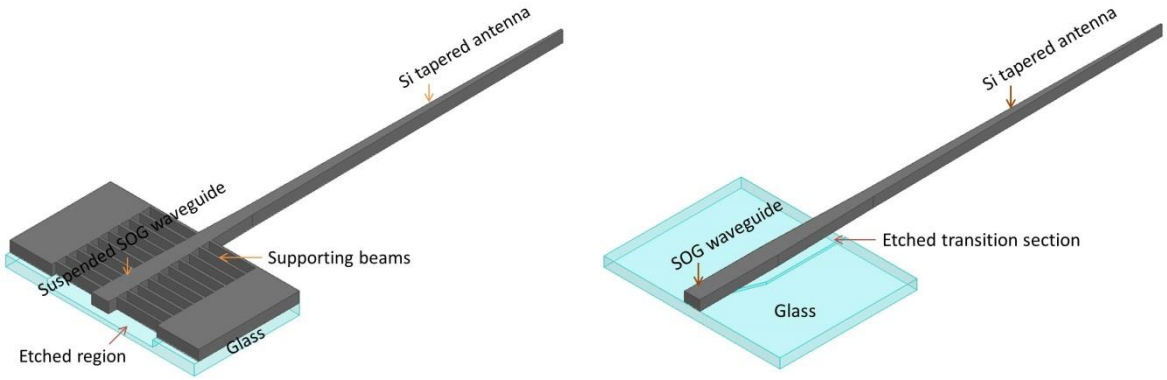

(a) (b)

Fig. 6.20 Structures of the two studied SOG tapered antenna configurations: a) structure *I*: suspended tapered Si antenna connected to the suspended SOG waveguide and b) structure *II*: suspended tapered Si antenna connected to the SOG waveguide.

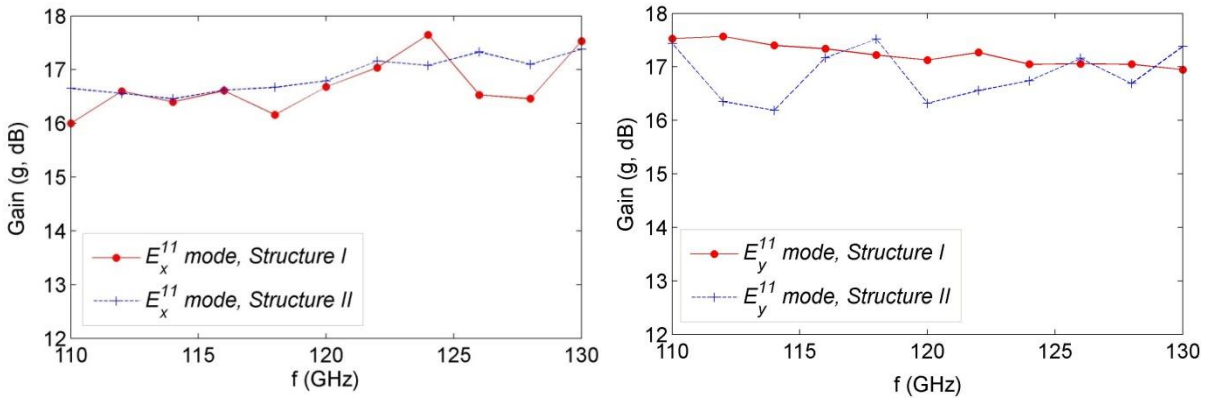

(a) (b)

Fig. 6.21 Simulated antenna gain: a) E_x^{11}- mode excitation and b) E_y^{11}- mode excitation.

Simulations demonstrate that for a confined mode within the Si channel, a sharp transition from the simple SOG waveguide to the suspended Si channel results in quite low transition loss. Fig. 6.22(a) shows the structure of this transition. The Si channel of the SOG waveguide has a width of W = 800 µm, a height of H = 500 µm, and the thickness of the glass substrate is T = 500 µm. Fig. 6.23 shows the scattering parameters of this transition structure for the two E_x^{11} and E_y^{11} modes excitations. For the E_x^{11} mode, the insertion loss of the transition varies between 0.05 dB and 0.18 dB over 110-150 GHz. However, for the E_y^{11} mode, which has weaker confinement within the Si guiding channel, the insertion loss variation ranges from 0.14 to 2.4 dB.

To reduce the transition loss in the suspended SOG tapered antenna configuration of structure *II*, the glass substrate of the SOG waveguide connected to the antenna is etched in a tapered configuration to form a smooth transition between the two waveguides. This structure is shown in Fig. 6.22(b). The length of the tapered etched section is L_{tg} = 2 mm and at the end of this section, the width of the etched section reaches to W_t = 1.6 mm. Fig. 6.24 shows the scattering parameters of this transition structure, when the structure is excited with E_x^{11} and E_y^{11} modes. For the E_x^{11} mode, the insertion loss of the transition varies between 0.04 dB and 0.11 dB over 110-150 GHz. For the E_y^{11} mode, this variation ranged between 0.1 - 0.49 dB. The return loss is better than 20 dB for both modes. This transition structure is used in the suspended SOG tapered antenna of structure *II*.

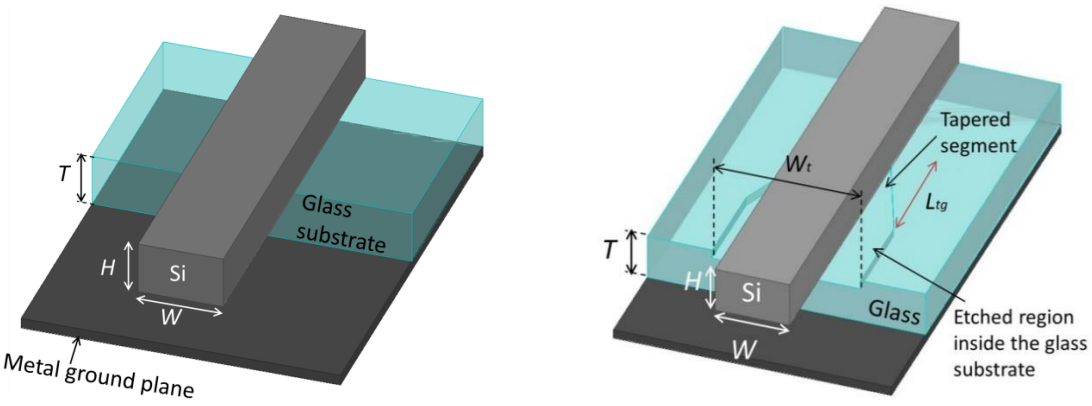

(a) (b)

Fig. 6.22 Structures of the transitions from the SOG waveguide to the suspended Si channel: a) sharp transition and b) tapered transition.

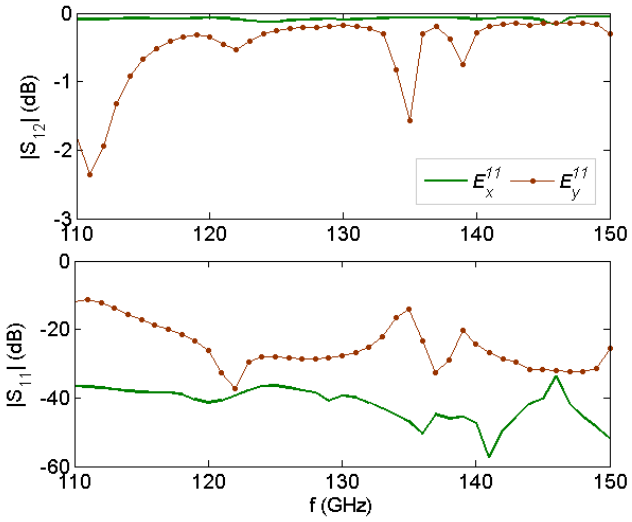

Fig. 6.23 Scattering parameters of the transition from the SOG waveguide to the suspended Si channel (structure in Fig. 6.22(a)).

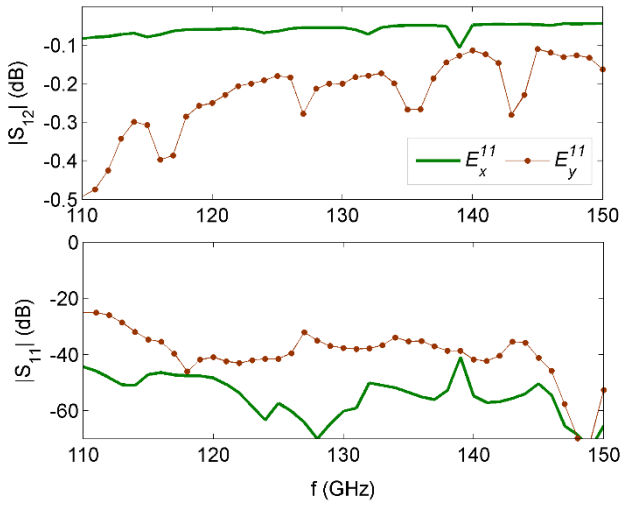

Fig. 6.24 Scattering parameters of the transition from the SOG waveguide to the suspended Si channel (structure in Fig. 6.22(b)).

6.2.2.2 Experimental Results

The suspended SOG tapered antenna of structure *I* is fabricated and measured. The fabricated antenna sample and the measurement setup are shown in Fig. 6.25. The tapered section of the Si channel of the SOG waveguide is inserted inside the rectangular waveguide with dimensions 1.65 mm × 0.825 mm (WR 6). For the E_x^{11}- mode excitation, the rectangular waveguide port is rotated by 90°. In order to decrease the effect of the measurement setup edge diffracted fields on the radiation pattern characteristics, the ground plane of the test setup is made larger than that used in Section 6.2.1 and the critical parts were covered by mmW absorbers during the measurements. To suppress the power leakage at the discontinuity of the connection between the metallic waveguides of the PNA-X port and that of the test setup (Fig. 6.13), in the modified test setup the metallic waveguide segment is omitted from the aluminum holder, which now works only as the ground plane (Fig. 6.25). Instead, the metallic waveguide segments made by OML Inc. with high dimensional accuracies are used to excite the antenna.

For the two different E_x^{11}-mode and E_y^{11}-mode excitations of the tapered antenna, the antenna is designed to radiate in azimuth and elevation polarizations, respectively. The azimuth and elevation directions are defined in Fig. 6.25. Figs. 6.26, 27 show the simulated and measured *E*-plane and *H*-plane radiation patterns of the antenna at 130 GHz for the two orthogonal E_x^{11}-mode and E_y^{11}-mode

excitations, respectively. For each excitation, the azimuth and elevation patterns of the co-polarization and the elevation pattern of the cross-polarization are provided.

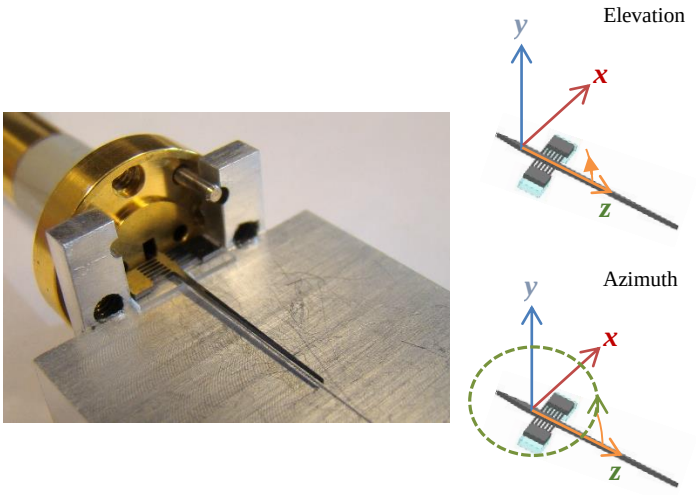

Fig. 6.25 Fabricated suspended SOG tapered antenna sample and the metallic test setup. The plots in the sub-figures show the definitions of elevation and azimuth directions (angles).

There is good agreement between the corresponding simulated and measured radiation patterns. Simulations result in maximum co-polarization radiation elevation angles of 25° and 16° for E_x^{11}-mode and E_y^{11}-mode excitations, respectively. The corresponding measured maximum radiation angles for these two excitations are 19 ° and 13.5 °, respectively. The simulated *E*-plane and *H*-plane SLLs for the E_x polarization are -17.7 dB and -14.9 dB, respectively and the measured corresponding SLLs are -18.1 dB and -13.5 dB, respectively. The simulated *E*-plane and *H*-plane SLLs for the E_y polarization are -20 dB and -18 dB, respectively and the measured corresponding SLLs are -12 dB and -21 dB, respectively.

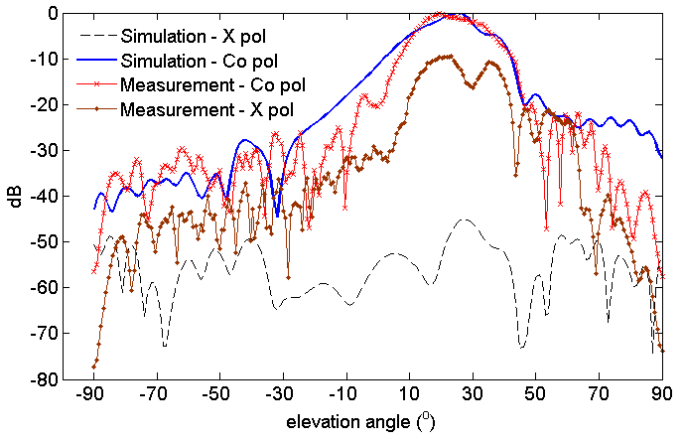

(a)

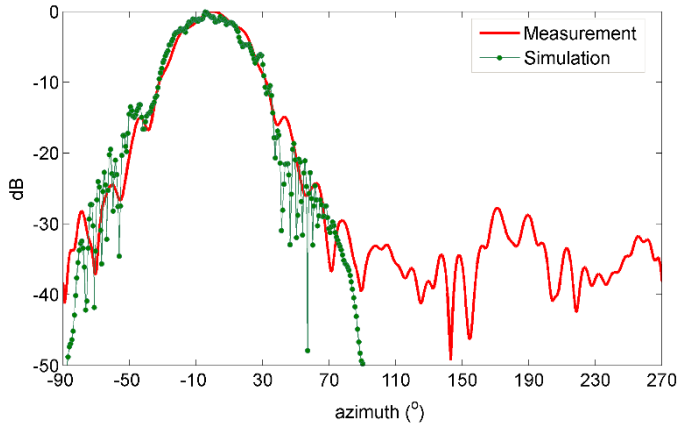

(b)

Fig. 6.26 Simulated and measured radiation patterns for the E_x^{11}-mode excitation: a) *H*-plane radiation patterns of the co-polarization (Co pol) and cross-polarization (X pol) components and b) *E*-plane radiation patterns at the maximum radiation elevation angle.

The simulated radiation patterns at 130 GHz show half-power beam-widths of 38 ° and 17 ° under E_x excitation for the *E*-plane and *H*-plane radiation patterns, respectively. For the E_y excitation, the *E*-plane and *H*-plane half-power beam-widths are 33 ° and 38 °, respectively. For the E_x and E_y polarizations, the simulations show cross-polarization levels of -45 dB and -50 dB at the maximum radiation directions, respectively. The measured corresponding cross-polarization levels are -9.7 dB and - 18 dB, respectively.

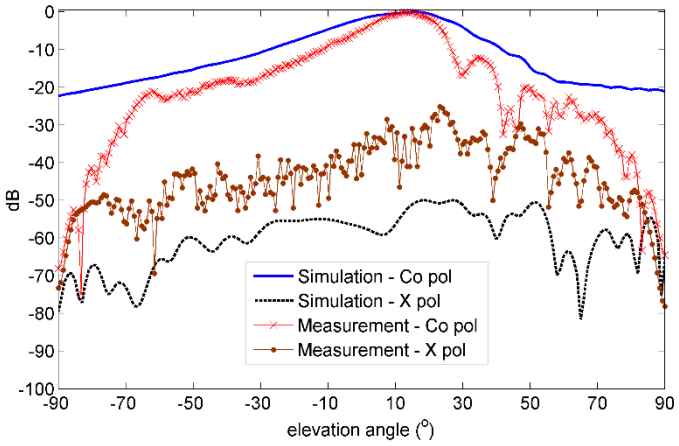

(a)

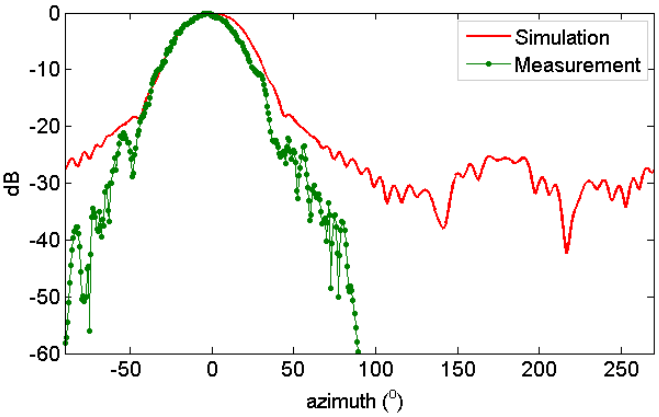

(b)

Fig. 6.27 Simulated and measured radiation patterns for the E_y^{11}-mode excitation: a) *E*-plane radiation patterns of the Co pol and X pol components and b) *H*-plane radiation patterns at the maximum radiation elevation angle.

Fig. 6.28 shows the measured return loss of the antenna for the two modes. The plots show the return loss measured from the rectangular waveguide ports. For the E_x and E_y modes, the return losses are better than 9.2 dB and 10.1 dB, respectively, over the entire band. The measured return losses are affected by the misalignment of the antenna tapered section inside the rectangular waveguide ports.

Simulations confirm that the beam squint as a function of frequency is insignificant. Fig. 6. 29 shows the simulation results for the co-polarization maximum radiation elevation angles for the two excitation modes. The beam squint is only 6°, namely from 19° to 25° (35% of the beam width), for the E_x

polarization as the frequency changed over 110-130 GHz. For the E_y polarization, this variation is only 3°, the beam squint being from 12° to 15° (10% of the beam width).

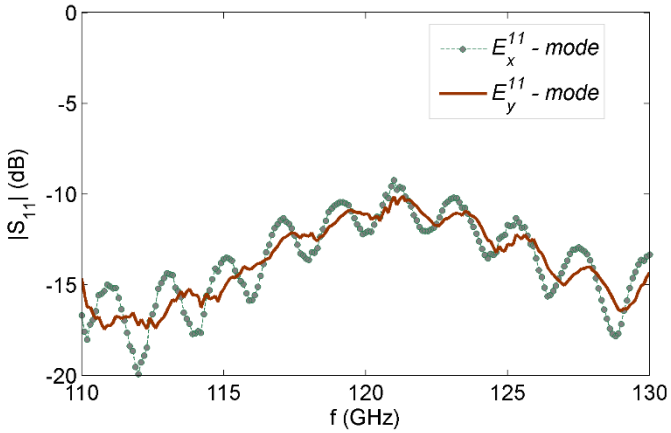

Fig. 6.28 Measured return losses of the antenna.

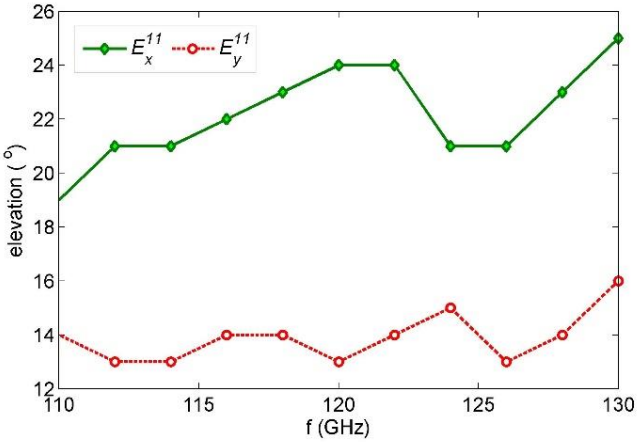

Fig. 6.29 Simulated elevation angles of the maximum radiation for the two mode excitations.

Standard gain horns (SGH) are used to measure the antenna's gain. In order to assess the gain, the measured far-field of the AUT is compared to that of an SGH with a known gain. The difference in signal level is the difference in gain between the AUT and SGH. The measured gain is accurate within ±0.3 dB.

Fig. 6.30 shows the simulated and measured directivities and the measured gains of the antenna over its wide operation bandwidth. There is reasonable agreement between the simulated and measured

directivities of the antenna. To obtain the simulated directivities in Fig. 6.30 the actual test setup including the rectangular waveguide port and tapered segment of the transition is simulated in HFSS. This is the main source of the small discrepancies observed between the simulated directivities presented in this figure and those presented in Fig. 6.21 for structure *I*.

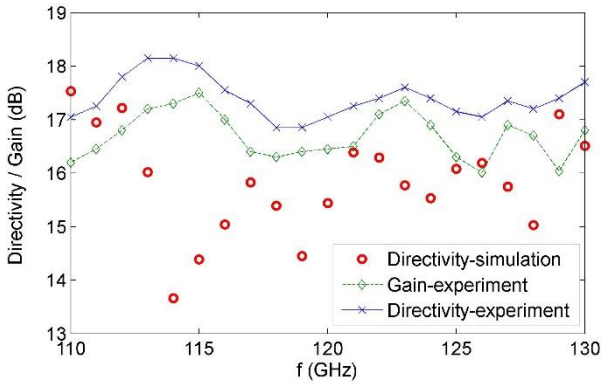

(a)

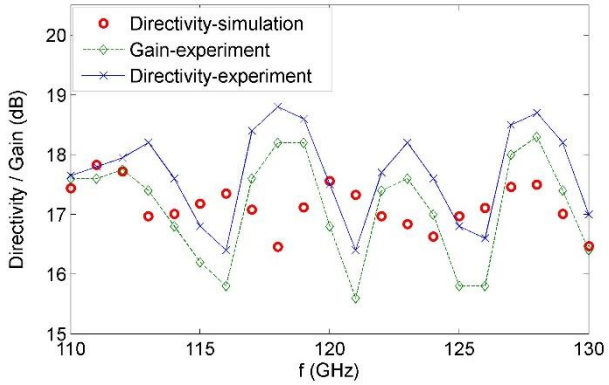

(b)

Fig. 6.30 Measured and simulated radiation directivities and gains: a) E_x polarization and b) E_y polarization.

As mentioned before, the far-field radiation patterns are obtained using a planar near-field measurement system, in which the field radiated to the back of the antenna is not measured. Thus, depending on the directivity of the AUT, the directivity measured by this method will be somewhat larger than the true directivity of the antenna. This is the main source of the small discrepancies seen between the simulated

and measured directivities. Misalignment of the antenna structure inside the test setup is the second source of the discrepancies.

Fig. 6.31 shows the radiation efficiencies derived from measurements for the two polarizations. Very high radiation efficiencies of 94 % at 123 GHz and 99 % at 110 GHz are measured for the E_x and E_y polarizations, respectively. The two polarizations show efficiencies of 85 % and 88 % (in average over 110 - 130 GHz), respectively. Table 6.2 summarizes these results. As mentioned before, the planar near-field setup overestimates the antenna directivity and consequently underestimates the efficiency. It is expected, therefore, that the actual efficiency of the antenna over the entire band is higher and closer to the maximum measured efficiencies.

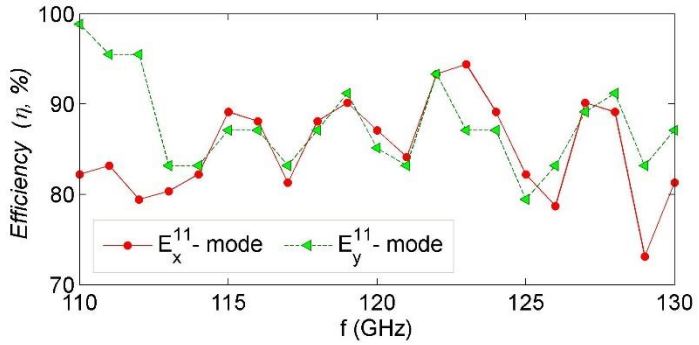

Fig. 6.31 Antenna measured radiation efficiency (η).

6.2.3 Performance Comparison

Table 6.3 compares the performance of the novel SOG tapered antenna and the suspended SOG tapered antenna with other mmW tapered dielectric antennas reported in the literature. The suspended SOG tapered antenna, which can be excited by either E_x or E_y modes (dual-mode operation), shows significantly better performance in terms of gain and efficiency as compared to the state-of-the-art techniques. In addition to dual-mode radiation, the proposed design can be integrated with the rest of the radio front end in high-precision SOG technology platform at low cost.

6.3 Concluding Remarks and Discussion

Two low-loss and compact fully-dielectric integrated phase shifters were designed, fabricated, and measured on the SOG platform. A high dielectric constant BLT-loaded SOG phase shifter was

presented with an operation bandwidth of 95-110 GHz. A phase shift of 138 ° at 95 GHz was demonstrated using a device length of 4.18 mm. At 110 GHz, a large measured phase shift of 82 ° was obtained, while the variation in the insertion loss was only 0.7 dB.

Table. 6.2. Antenna directivity, gain, and efficiency.

	min	f_{min}	max	f_{max}
gain (dB, test, E_x)	16	126	17.5	115
directivity (dB, test, E_x)	16.9	119	18.2	113
directivity (dB, simulation, E_x)	13.7	114	17.5	110
η (%, E_x, test)	73	129	94	123
gain (dB, test, E_y)	15.6	121	18.2	119
directivity (dB, test, E_y)	16.4	121	18.8	118
directivity (dB, simulation, E_y)	16.5	130	17.8	111
η (%, E_y, test)	79	125	99	110

Table. 6.3. Antenna performance comparison.

Structure	f (GHz)	Gain	η
Dielectric image tapered antenna [63]	94	12.8	74
Dielectric tapered rod antenna [155]	75 - 325	10	---
stepped pyramidal tapered rod antenna [157]	75 - 110	8 - 10	---
SOG tapered antenna	50 - 75	10.8 - 14.9	39 - 67
Suspended SOG tapered antenna (E_x)	110 - 130	16 - 17	73 - 94
Suspended SOG tapered antenna (E_y)	110 - 130	16 - 18	79 - 99

A phase shifter based on the coupling of a symmetric Si slab to the corrugated SOG waveguide was proposed. The operating principle of this phase shifter is based on the coupling. Along the coupling region, the coupling amplitude and propagation characteristics of the two even and odd modes are changed by changing the coupling distance between the two coupled Si channels. The fabricated sample showed measured phase shifts of 111 ° and 129 ° at frequencies of 85 GHz and 100 GHz, with maximum insertion losses of 0.65 dB and 2.5 dB, respectively.

A wideband tapered SOG dielectric antenna was proposed for mmW applications. The measured return loss of the antenna over a wide bandwidth of 50-75 GHz was better than 15.5 dB. The simulated and

measured radiation patterns were in good agreement. The measured directivity and gain of the antenna varied between 14.6 – 17.5 dB and 10.8 – 14.9 dB, respectively, over the entire frequency band of 50-75 GHz.

To improve the radiation efficiency and gain of the SOG tapered antenna at the mmW range of frequency, the idea of the suspended SOG tapered antenna was introduced. Based on this idea, a wideband suspended SOG tapered antenna was fabricated, and measured. The suspended SOG tapered antenna, which can be excited by either E_x^{11}-mode or E_y^{11}-mode, showed high-directivity, high-gain, and high-efficiency for both excitations. Using this technique, high efficiencies of 94 % for E_x polarization and 99 % for E_y polarization were achieved in the experiment. This is the first time that such high radiation efficiencies have been reported over the high frequency range of 110-130 GHz.

Chapter 7 Concluding Remarks and Recommendations for Future Work

7.1 Summary and Contributions

In this thesis, a new silicon-on-glass (SOG) platform was proposed for millimeter-wave (mmW)/terahertz (THz) low-loss integrated circuits. A high-precision technique was developed for the SOG fabrication where the alignment between the sub-structures in the integrated circuit is automatically achieved during the fabrication process without any manual intervention. In order to extend the operational frequency of the SOG platform toward the THz range, new SOG waveguide structures were proposed to overcome the problem of the increasing material loss of Pyrex glass as the frequency rises. The SOG waveguide low-attenuation constant was demonstrated theoretically up to 1.1 THz and experimentally up to 0.5 THz. Theoretically and practically, there is no limitation to extending the operating frequency of the SOG platform to higher THz frequencies (i.e., > 1.1 THz).

In Chapter 3, SOG dielectric waveguides were demonstrated for mmW low-loss propagation. The fabrication technique of the SOG platform was expounded. It was shown that how SOG technology overcomes the main drawbacks of the state-of-the-art mmW integrated-circuit technologies. Silicon (Si)-confined modes were explored in the SOG dielectric ridge waveguide structure, and their cutoff conditions were studied. A test setup was designed to measure the propagation characteristics of the SOG waveguide. To improve the coupling characteristics of the transitions from the metallic waveguides of the network analyzer to the SOG dielectric waveguides, the idea of removing parts of the glass substrate below the tapered segments of the transitions was developed. Measured dispersion diagrams of the SOG dielectric waveguide showed average attenuation constants of 0.63 dB/cm, 0.28 dB/cm, and 0.53 dB/cm over the frequency ranges of 55 – 65 GHz, 90 – 110 GHz, and 140 – 170 GHz, respectively.

In Chapter 4, the extension of the SOG platform to higher frequencies (i.e., > 200 GHz) was investigated. Highly resistive Si and Pyrex glass material loss characteristics were discussed over the mmW/THz range. The increasing material loss of Pyrex glass as the frequency rises, and the consequent increase in the SOG waveguide attenuation constant, were discussed at the THz frequencies. In order to overcome the problem of greater material loss in the Pyrex substrate at frequencies above 200 GHz, the idea of etching parts of the Pyrex substrate below the Si guiding channel was developed. Two new

SOG waveguide structures, called the *suspended* SOG waveguide and the *corrugated* SOG waveguide, were proposed.

It was shown that by proper design of the periodic supporting beams dimensions – the beams being used to provide strong mechanical support for the suspended SOG waveguide – the Bragg band gap is avoided over the waveguide operation bandwidth. Suspended SOG waveguides were designed for single mode operations. Low measured attenuation constants of 0.31 dB/λ_0 (average) and 0.42 dB/λ_0 (average) were achieved for the fabricated suspended SOG waveguides over the frequency ranges of 350 – 500 GHz and 400 – 500 GHz, respectively. These measured attenuation constants confirmed that the low-loss characteristics of the suspended SOG waveguide significantly outperformed state-of-the-art techniques. Two techniques, dry etching and wet etching, were considered for corrugating the Pyrex substrate in the corrugated SOG waveguide. It was shown that corrugated SOG, despite its performance limitations at higher frequencies, can still serve as a potential platform for mmW high-density integrated circuits up to ~ 300 GHz.

In Chapter 5, two new SOG waveguide structures, called the rib SOG and U-SOG waveguides, were proposed for THz high-performance integrated circuits. It was demonstrated that these two SOG waveguides outperformed the suspended SOG waveguide at higher frequencies ~ 1.1 THz. These two novel SOG structures can serve as low-loss platforms for THz high-density hybrid/integrated circuits. The fabrication techniques of these two new SOG structures were developed. The effect of different parameters on the proposed waveguides' performance was studied. Rib SOG and U-SOG waveguides were designed for fabrication and measurement over the frequency ranges of 0.75 – 0.9 THz and 0.9 – 1.1 THz. Simulated results of the designed Rib SOG waveguides showed attenuation constants of 0.01 – 0.03 dB/mm and 0.02 – 0.05 dB/mm over the frequency ranges of 0.75–0.9 THz and 0.9–1.1 THz, respectively. Simulations of the designed U-SOG waveguides demonstrated low attenuation constants of 0.02 – 0.1 dB/mm and 0.02 – 0.18 dB/mm over the frequency ranges of 0.8–1 THz and 0.9–1.1 THz, respectively. The fabrication of the U-SOG waveguides is underway.

In Chapter 6, new fully dielectric phase shifters and tapered dielectric antennas, implemented in the SOG platform, were discussed. A new SOG implementation of the BLT-loaded phase shifter was implemented and measured over the frequency range of 95 - 110 GHz. A symmetric Si-coupled SOG phase shifter was proposed, fabricated, and measured over the frequency range of 85- 100 GHz, where low-loss characteristics of the phase shifter were demonstrated. Two wideband SOG tapered antenna structures were developed for mmW applications. In the first configuration, the glass substrate below

the Si tapered antenna was diced around the antenna in a tapered manner. Simulations and measurements of this antenna structure showed high directivities of 14.5–17.1 dB and 14.6–17.5 dB over the frequency range of 50–75 GHz, respectively. In the second configuration, the idea of etching the Pyrex substrate below the Si tapered antenna was used to improve the radiation characteristics of the antenna in terms of efficiency and gain. This configuration, which is called a *suspended* SOG tapered antenna, can work either in E_x or E_y mode. Measurements of the suspended SOG tapered antenna over the frequency range of 110–130 GHz showed high gains of 16–17.5 dB and 15.6–18.2 dB for E_x and E_y polarizations, respectively. These two polarizations showed high measured efficiencies of 94% and 99%, respectively, which are great achievements when compared to state-of-the-art mmW techniques.

7.2 Future Work

1. **Packaging of the SOG technology platform**

   Packaging of the SOG platform, to ensure complete protection against any impact from the environment, is the next step for enabling the SOG platform to be used in application-specific products. In this regard, several integrated circuit packaging (IC) and micro-electromechanical systems (MEMS) packaging techniques can be adapted to the SOG platform. In particular, using soft materials inside the package as a part of the SOG holding structure will help absorb mechanical shock.

2. **Active integration into the SOG technology platform**

   SOG is a platform for hybrid integrated circuits for which a transition from planar off-chip waveguide to planar on-chip transmission line is required for active integration. To achieve this, two approaches are suggested. The first approach, which is mostly practical at lower mmW frequencies, is based on a transition from the SOG dielectric waveguide to the coplanar waveguide (CPW) and then a connection to the chip is achieved by the conventional flip-chip technique [160]. For the transition segment, a metallic layer is deposited and patterned on the top Si surface of the SOG waveguide [161]. The second approach uses an on-chip dipole antenna for coupling to the E_x^{11} mode of the SOG waveguide [65].

3. **Integration of MEMS technology into the SOG platform**

   MEMS technology is fully compatible with the SOG technology platform. SOG (with low-resistivity Si) is a well-developed technology platform for MEMS technology. To integrate

MEMS technology into the proposed SOG platform, one solution would be to implement metallic MEMS structures on the Si surface. Another solution could be to add a low resistivity Si layer to the SOG platform (in addition to the high-resistivity layer which is used for the passive component) for MEMS applications. A comprehensive fabrication technique needs to be developed for the integrated platform which consists of low-resistivity Si, high-resistivity Si, and the glass layers.

4. **Design and implementation of the Rib SOG and U-SOG passive components**

   Dielectric phase shifters and tapered antennas based on the SOG technology were designed, fabricated, and measured in this thesis. Other passive components, including bend, phase shifter, dielectric resonator, and power divider have been developed on the corrugated SOG platform over the W-band by the other colleagues at CIARS [109]. The rib SOG and U-SOG waveguides, whose low-loss transmissions were demonstrated up to 1.1 THz, can serve as promising candidates for THz low-loss and high-density integrated circuits. Different passive components such as power dividers, phase shifters, filters, and bends can be implemented in these two SOG platforms based on similar ideas already developed in optical/microwave integrated circuits.

5. **U-SOG waveguide fabrication and measurement**

   U-SOG waveguides with operation bandwidths over 0.75 – 0.9 THz and 0.9 – 1.1 THz were designed in Chapter 5. This new SOG waveguide configuration, whose fabrication is underway, should be further verified by experimental testing.

6. **Rib SOG waveguide fabrication and measurement**

   Rib SOG waveguides with operation bandwidths over 0.75–0.9 THz and 0.9–1.1 THz were designed and their fabrication technique was discussed in Chapter 5. This new SOG waveguide configuration should be fabricated and further verified by experimental testing.

7. **Potential application of quartz glass in SOG technology**

   The main drawback of using quartz, which has low propagation loss at THz, in place of the Pyrex substrate in SOG technology is the difficulty in directly bonding it to the Si due to their different thermal expansion coefficients. However, the potential application of quartz glass in SOG platform using adhesive material for the bonding to Si should be investigated. This will require that the bonding energies and THz material loss of the adhesive material be studied.

References

[1] Yun-Shik Lee, "Principles of Terahertz Science and Technology," Springer, first edition, 2009.

[2] Peter Smulders, "Exploiting the 60 GHz Band for Local Wireless Multimedia Access: Prospects and Future Directions," *IEEE Communications Magazine*, pp. 140-147, Jan. 2002.

[3] H. J. Song and T. Nagatsuma, "Present and Future of Terahertz Communications," *IEEE Trans. THz Sci. Technol.*, vol. 1, no. 1, pp. 256-263, Sep. 2011.

[4] H.-J. Song, K. Ajito, A. Wakatsuki, Y. Muramoto, N. Kukutsu, Y. Kado, and T. Nagatsuma, "Terahertz Wireless Communication Link at 300 GHz," *Proc. Int. Topical Meeting Microw. Photon*. (*MWP*), pp. 42-45, 2010.

[5] D. Steer, G. Dolman, and P. Row, "Radio System Design for Broadband Residential Access," *in IEEE Radio and Wireless Conference*, pp. 31-34, Aug. 1999.

[6] A. Hirata, R. Yamaguchi, H. Takahashi, T. Kosugi, K. Murata, N. Kukutsu, and Y. Kado, "Effect of Rain Attenuation for a 10-Gb/s 120-GHz-band Millimeter-wave Wireless Link," *IEEE Trans. Microw. Theory Techn.*, vol. 57, no. 12, pp. 3099-3105, Dec. 2009.

[7] J. Federici and L. Moeller, "Review of Terahertz and Subterahertz Wireless Communications," *J. Appl.Phys.*, vol. 107, p. 111101, 2010.

[8] T. Schneider, A. Wiatrek, S. Preussler, M. Grigat, R. Braun, "Link Budget Analysis for Terahertz Fixed Wireless Links," *IEEE Trans. THz Sci. Technol.*, vol. 2, no. 2, pp. 250-256, Mar. 2012.

[9] H. B. Liu, H. Zhong, N. Karpowicz, Y. Chen, and X. C. Zhang, "Terahertz Spectroscopy and Imaging for Defense and Security Applications," *Proc. IEEE*, vol. 95, no. 8, pp. 1514-1527, Aug. 2007.

[10] S. Schecklman, L. M. Zurk, S. Henry, and G. P. Kniffin, "Terahertz Material Detection from Diffuse Surface Scattering," J. Appl. Phys., vol. 109, no. 9, pp. 094902-1, 2011.

[11] R. Appleby and R. N. Anderton, "Millimeter-wave and Submillimeter-wave Imaging for Security and Surveillance," *Proc. IEEE*, vol. 95, no. 8, pp. 1683–1690, Aug. 2007.

[12] K. Humphreys, J. P. Loughran, M. Gradziel, W. Lanigan, T. Ward, J.A. Murphy, C. O'Sullivan, "Medical Applications of Terahertz Imaging: a Review of Current Technology and Potential Applications in Biomedical Engineering," *Conf Proc IEEE Eng Med Biol Soc.*, 2004, pp. 1302-5.

[13] E. Pickwell and V.Wallace, "Biomedical Applications of Terahertz Technology," *J. Phys. D: Appl. Phys.*, 2006, vol. 39, p. R301.

[14] K. Humphreys, J. P. Loughran, M. Gradziel, W. Lanigan, T. Ward, J. A. Murphy, and C. O. Sullivan, "Medical Applications of Terahertz Imaging: A review of Current Technology and Potential Applications in Biomedical Engineering," *Proc. 26th Annu. Int. Conf. IEEE Eng.*, 2004, pp. 1302-5.

[15] K. Ajitoand and Y. UenoTHz, "Chemical Imaging for Biological Applications," *IEEE Trans. THz Sci. Technol.*, vol. 1, no. 1, pp. 293-300, Sep. 2011.

[16] S. M. Kim, F. Hatami, and J. S. Harris, "Biomedical Terahertz Imaging with a Quantum Cascade Laser," *Appl. Phys. Lett.*, vol. 88, 153903, Apr. 2006.

[17] E. Pickwell-MacPherson, "Practical Considerations for in Vivo THz Imaging," *Terahertz Science and Technology,"* vol. 3, no. 4, pp. 163-171, Dec. 2010.

[18] B. M. Fischer, M. Walther, and P. Uhd Jepsen, "Far-infrared Vibrational Modes of DNA Components Studied by Terahertz Time-domain Spectroscopy," *Phys. Med. Biol.*, 47, pp. 3807-3814, 2002.

[19] W. R. Deal, K. Leong, X. B. Mei, S. Sarkozy, V. Radisic, J. Lee, P. H. Liu, W. Yoshida, J. Zhou, and M. Lange, "Scaling of InP HEMT Cascade Integrated Circuits to THz Frequencies," *Proc. IEEE Compound Semicond. IC Symp.*, pp. 1-4, Oct. 2010.

[20] L.A. Samoska, 'An Overview of Solid-State Integrated Circuit Amplifiers in the Submillimeter-Wave and THz Regime', *IEEE Trans. THz Sci. Technol.*, vol. 1, pp. 9-24, Sep. 2011.

[21] W. R. Deal, X. B.Mei, K. Leong, V. Radisic, S. Sarkozy, B.Gorospe, J. Lee, P. H. Liu, W. Yoshida, J. Zhou, M. Lange, and R. Lai, "Terahertz Monolithic Integrated Circuits Using InP High Electron Mobility Transistors," *IEEE Trans. THz Sci. Technol.*, vol. 1, no. 1, pp. 25-32, Sep. 2011.

[22] V. Jain, J. C. Rode, H. W. Chiang, A. Baraskar, E. Lobisser, B. J. Thibeault, M. Rodwell, M. Urteaga, D. Loubychev, A. Snyder, Y. Wu, J. M. Fastenau, and W. K. Liu, "1.0 THz f_{max} InP DHBTs in a Refractory Emitter and Self-Aligned Base Process for Reduced Base Access Resistance," *Proc. Device Res. Conf.*, Santa Barbara, pp. 271-272, Jun. 2011.

[23] M. R. Nezhad-Ahmadi, M. Fakharzadeh, B. Biglarbegian, and S. Safavi-Naeini, "High-Efficiency On-Chip Dielectric Resonator Antenna for mm-Wave Transceivers," *IEEE Trans. Antennas. Propag.*, vol. 58, no. 10, pp. 3388-3392, Oct. 2010.

[24] S. Sun, J. Shi, L. Zhu, S. C. Rustagi, and K. Mouthaan, "Millimeter-Wave Bandpass Filters by Standard 0.18-μm CMOS Technology," *Electron. Lett.*, vol. 28, no. 3, pp. 220-222, Mar. 2007.

[25] H. R. Lin, Ch. Y. Hsu, L. K. Yeh, H. R. Chuang, and Ch. Y. Chen, "A 77-GHz CMOS On-Chip Bandpass Filter Using Slow-Wave Stepped-Impedance Resonators," *APMC, Yokohama*, pp. 826- 828, Dec. 2010.

[26] Hirokawa, J. and M. Ando, "Single-Layer Feed Waveguide Consisting of Posts for Plane TEM Wave Excitation in Parallel Plates," *IEEE Trans. Antennas Propagat*., vol. 46, no. 5, pp. 625-630, May 1998.

[27] Ke Wu, "Towards the Development of Terahertz Substrate Integrated Circuit Technology," *SiRF* 2010, pp. 116-119, Jan. 2010.

[28] N. Ranjkesh and M. Shahabadi, "Reduction of Dielectric Losses in Substrate Integrated Waveguide," *Electron. Lett.*, vol. 42, no. 21, pp. 1230-1231, 2006.

[29] J. J. Simpson, A. Taflove, J. A. Mix, and H. Heck, "Substrate Integrated Waveguides Optimized for Ultrahigh-Speed Digital Interconnects," *IEEE Trans. Microw. Theory Tech*., vol. 54, no. 5, pp. 1983-1990, May 2006.

[30] Y. J. Cheng, W. Hong, and K. Wu, "94 GHz Substrate Integrated Monopulse Antenna Array," *IEEE Trans. Antennas Propagat*., vol. 60, no. 1, pp. 664 - 667, Jan. 2012.

[31] J. Xu, Z. N. Chen, X. Qing, and W. Hong, "140-GHz Planar Broadband LTC SIW Slot Antenna Array," *IEEE Trans. Antennas Propag.*, vol. 60, no. 6, pp. 3025–3028, Jun. 2012.

[32] J. Xu, Z. N. Chen, X. Qing, and W. Hong, "140-GHz TE_{20}-Mode Dielectric-Loaded SIW Slot Antenna Array in LTCC," *IEEE Trans. Antennas Propag.*, vol. 61, no. 4, pp. 1784–1793, Apr. 2013.

[33] W. H. Chow, A. Champion, and D. P. Steenson, "Measurements to 320 GHz of Millimeter-Wave Waveguide Components Made by High Precision and Economic Micro-Machining Techniques," *Proc. High Freq. Postgraduate Student Colloq.*, pp. 90-93, Sep. 2003.

[34] W. R. McGrath, C. Walker, M. Yap, and Y. Tai, "Silicon Micromachined Waveguides for Millimeter-Wave and Submillimeter-Wave Frequencies," *IEEE Microw. Guided Wave Lett.*, vol. 3, no. 3, pp. 61-63, Mar. 1993.

[35] J. P. Becker, J. R. East, and L. P. B. Katehi, "Performance of Silicon Micromachined Waveguide at W-band," *Electron. Lett.*, vol. 38, no. 13, pp. 638-639, Jun. 2002.

[36] P. L. Kirby, D. Pukala, H. Manohara, I. Mehdi, and J. Papapolymerou, "Characterization of Micromachined Silicon Rectangular Waveguide at 400 GHz," *IEEE Microw. Wireless Compon. Lett.*, vol. 16, no. 6, pp. 366-368, Jun. 2006.

[37] M. K. H. Leong, K. Hennig, Ch. Zhang, R. N. Elmadjian, Z. Zhou, B. S. Gorospe, P. P. Chang-Chien, V. Radisic, W. R. Deal, "WR 1.5 Silicon Micromachined Waveguide Components and Active Circuit Integration Methodology," *IEEE Trans. Microw. Theory Tech.*, vol. 60, no. 4, pp. 998-1005, Apr. 2012.

[38] J. Hu, Sh. Xie, and Y. Zhang, "Micromachined Terahertz Rectangular Waveguide Bandpass Filter on Silicon-Substrate," *IEEE Microw. Wireless Compon. Lett.*, vol. 22, no. 12, pp. 636-638, Dec. 2012.

[39] M. Vahidpor and K. Sarabandi, "2.5D Micromachined 240 GHz Cavity-Backed Coplanar Waveguide to Rectangular Waveguide Transition," *IEEE Trans. THz Sci. Technol.*, vol. 2, no. 3, pp. 315-322, May 2012.

[40] T. J. Reck, C. Jung-Kubiak, J. Gill, and G. Chattopadhyay, "Measurement of Silicon Micromachined Waveguide Components at 500–750 GHz," *IEEE Trans. THz Sci. Technol.*, vol. 4, no. 1, pp. 33-38, Jan. 2014.

[41] J. V. Siles, C. Lee, R. Lin, G. Chattopadhyay, T. Reck, C. Jung-Kubiak, I. Mehdi, and K. B. Cooper, "A high-power 105–120 GHz broadband on-chip power-combined frequency tripler," *IEEE Microw. Wireless Compon. Lett.*, vol. 25, no. 3, pp. 157-159, March 2005.

[42] N. Lombart, G. Chattopadhyay, A. Skalare, and I. Mehdi, "Novel Terahertz Antenna Based on a Silicon Lens Fed by a Leaky Wave Enhanced Waveguide," *IEEE Trans. Antennas Propag.*, vol. 59, no. 8, pp. 2834–2843, vol. 59, no. 6, pp. 2160-2168, Jun. 2011.

[43] Ch. D. Nordquist, M. C. Wanke, A. M. Rowen, Ch. L. Arrington, A. D. Grine, and Ch. T. Fuller, "Properties of Surface Metal Micromachined Rectangular Waveguide Operating Near 3 THz," *IEEE J. Sel. Topics Quantum Electron.*, vol. 17, no. 1, pp. 130-137, Jan. 2011.

[44] A. Rowen, A. E. Hollowell, M. Wanke, C. D. Nordquist, C. Arrington, R. Gillen and J. J. Coleman, "Multi-layer Metal Micromachining for THz Waveguide Fabrication," *SPIE Micromachining and Microfabrication*, San Jose, CA, Jan. 2010.

[45] M. C.Wanke, C. D. Nordquist,M. J. Cich, A.M. Rowen, C. L. Arrington, M. Lee, A. D. Grine, C. T. Fuller, J. L. Reno, and E. W. Young, "Terahertz Quantum Cascade Laser Integration with on-Chip Micromachined Rectangular Waveguides," *Proc. SPIE*, San Jose, vol. 7215, pp. 721504-1-721504-11, 2009.

[46] G. Gentile, R. Dekker, P. Graaf, M. Spirito, M. J. Pelk, L. C. N. de Vreede, and B. Rejaei Salmassi, "Silicon Filled Integrated Waveguides," *IEEE Microw. Wireless Compon. Lett.*, vol. 20, no. 10, pp. 536-538, Oct. 2010.

[47] G. Gentile, R. Dekker, P. de Graaf, M. Spirito, L. C. N. de Vreede, and B. Rejaei, "Millimeter-Wave Integrated Waveguides on Silicon," *Proc. IEEE 11th Topical Meet. Silicon Monolithic Integrated Circuits in RF Systems* (*SiRF*), pp. 37-40, Jan. 2011.

[48] G. Gentile, V. Jovanović, M. J. Pelk, L. Jiang, R. Dekker, P. de Graaf, B. Rejaei, L. C. N. de Vreede, L. K. Nanver, and M. Spirito, "Silicon-Filled Rectangular Waveguides and Frequency Scanning Antennas for mm-Wave Integrated Systems," *IEEE Trans. Antennas. Propag.*, vol. 61, no. 12, pp. 5893-5901, Dec. 2013.

[49] S. Shindo and T. Itanami, "Low-Loss Rectangular Dielectric Image Line for Millimeter-Wave Integrated Circuits," *IEEE Trans. Microw. Theory Tech.*, vol. 26, no. 10, pp. 747-751, Oct. 1978.

[50] K. Ogusu, "Numerical Analysis of the Rectangular Dielectric Waveguide and Its Modifications," *IEEE Trans. Microw. Theory Tech.*, vol. 25, no. 11, pp. 874-885, Nov. 1977.

[51] T. Itoh and B. Adelseck, "Trapped Image Guide for Millimeter-Wave Circuits," *IEEE Trans. Microw. Theory Tech.*, vol. 28, no. 12, pp. 1433-1436, Dec. 1980.

[52] R. M. Knox, "Dielectric Waveguide Microwave Integrated Circuits - An Overview," *IEEE Trans. Microw. Theory Tech.*, vol. 24, no. 11, pp. 806-814, Nov. 1976.

[53] T. Wang and S. E. Schwarz, "Design of Dielectric Ridge Waveguides for Millimeter-Wave Integrated Circuits," *IEEE Trans. Microwave Theory Tech.*, vol. 31, no. 2, pp. 128-134, Feb. 1983.

[54] W. McLevige, T. Itoh, and R. Mittra, "New Waveguide Structures for Millimeter-Wave and Optical Integrated Circuits," *IEEE Trans. Microw. Theory Techn.*, vol. MTT-23, no. 10, pp. 788–794, Oct. 1975.

[55] N. Dib and L. P. B. Katehi, "Characterization of Three-Dimensional Open Dielectric Structures Using the Finite-Difference Time-Domain Method," *IEEE Trans. Microw. Theory Tech.*, vol. 44, no. 4, pp. 513–518, Apr. 1996

[56] A. Engel, Jr. and L. P. B. Katehi, "Low-loss Monolithic Transmission Lines for Submillimeter and Terahertz Frequency Applications," *IEEE Trans. Microwave Theory Tech.*, vol. 36, no. 11, pp. 1847-1854, Nov. 1991.

[57] J. Patrik Pousi, D. V. Lioubtchenko, S. N. Dudorov, and A. V. Räisänen, "High Permittivity Dielectric Rod Waveguide as an Antenna Array Element for Millimeter Waves," *IEEE Trans. Antennas. Propag.*, vol. 58, no. 3, pp. 714-719, March 2010.

[58] J. Richter, Y. Yazici, Ch. Ziegler and L. P. Schmidt, "A Broadband Transition Between Dielectric and Planar Waveguides at Millimeterwave Frequencies," *EUMC 2003*, pp. 947-950, Oct. 2003.

[59] A. Patrovski and Ke Wu, "Substrate Integrated Image Guide (SIIG)-A Low-Loss Waveguide for Millimetre-Wave Applications," *Proc. 35th Eur. Microw. Conf.*, Paris, France, pp. 897-900, Oct. 2005.

[60] A. Patrovski and Ke Wu, "94-GHz Broadband Transition from Coplanar Waveguide to Substrate Integrated Image Guide (SIIG)," *Proc. IEEE MTT-S Int. Microwave*, pp. 1551-1554, Jun. 2007.

[61] A. Patrovski and Ke Wu, "Substrate Integrated Image Guide Array Antenna for the Upper Millimeter-Wave Spectrum," *IEEE Trans. Antennas Propag.*, vo. 55, no. 11, pp. 2994-3001, Nov. 2007.

[62] A. Patrovskyand Ke Wu., "94-GHz Planar Dielectric Rod Antenna with Substrate Integrated Image Guide (SIIG) Feeding," *IEEE Antennas Wireless Propag. Lett.*, vol. 5, no. 1, pp. 435-437, 2006.

[63] A. Patrovski and Ke Wu, "Substrate Integrated Image Guide (SIIG)-A Planar Dielectric Waveguide Technology for Millimeter-Wave Applications," *IEEE Trans. Microw. Theory Tech.*, vol. 54, no. 6, pp. 2872-2879, Jun. 2006.

[64] N. Dolatsha and J. Hesselbarth, "Low-Loss Millimeter-Wave Propagation of the E_x^{11} Mode in Insulated Image Guide," in *Proc. Int. Microw. Symp. (IMS'12)*, pp. 1-3, Jun. 2012.

[65] N. Dolatsha and J. Hesselbarth, "Millimeter-wave Chip-to-Chip Transmission Using an Insulated Image Guide Excited by an on-Chip Dipole Antenna at 90 GHz," *IEEE Microw. Wirel. Compon. Lett.*, vol. 22, no. 5, pp. 266-268, May 2012.

[66] Y. J. Cheng, X. Y. Bao, and Y. X. Guo, "LTCC-Based Substrate Integrated Image Guide and Its Transition to Conductor-Backed Coplanar Waveguide," *IEEE Microw. Wireless Compon. Lett.*, vol. 23, no. 9, pp. 450-452, Sep. 2013.

[67] Y. J. Cheng, Y. X. Guo, X. Y. Bao, and K. B. Ng, "Millimeter-Wave Low Temperature Co-Fired Ceramic Leaky-Wave Antenna and Array Based on the Substrate Integrated Image Guide Technology," *IEEE Trans. Antennas Propag.*, vol. 62, no. 2, pp. 669-676, Feb. 2014.

[68] Y. J. Cheng and Y. X. Guo, "60-GHz Substrate Integrated Imaging Guide Leaky-Wave Antenna on LTCC," *Int. IEEE AP-S Symp. Dig.*, pp. 2141-2142, July 2013.

[69] A. Malekabadi, S. A. Charlebois, D. Deslandes,and F. Boone, "High-Resistivity Silicon Dielectric Ribbon Waveguide for Single-Mode Low-Loss Propagation at F/G-Bands," *IEEE Trans. THz Sci. Technol.*, vol. 4, no. 4, pp. 447-453, July. 2014.

[70] W.J. Otter, S. M. Hanham, E. Episkopou, Y. Zhou, N. Klein, A. S. Holmes, and S. Lucyszyn, "Photoconductive Photonic Crystal Switch", *Int. Conf. on Infrared, Millim., and THz Waves* (*IRMMW-THz*), pp. 1 - 2, 2013.

[71] W.J. Otter, S. M. Hanham, N. M. Ridler, G. Marino, N. Klein, and S. Lucyszyn, "100 GHz Ultra-High Q-Factor Photonic Crystal Resonators", *Sens. Actuators A: Phys.*, vol. 217, pp. 151 - 159, 2014.

[72] Y. Xu and R. G. Bosisio, "A Comprehensive Study on the Planar Type of Goubau Line for Millimetre and Submillimetre Wave Integrated Circuits," *IET Microw. Antennas Propag.*, pp. 681-687, 2007.

[73] J. Emond, M. Grzeskowiak, G. Lissorgues, S. Protat, F. Deshours, E. Richalot, and O. Picon, "Low Loss Goubau Line on High-Resitivity Silicon in the 57-64 GHz Band," *EUMC 2011*, pp. 1459- 1462, Apr. 2011.

[74] T. Akalin, E. Peytavit, G. Ducournau, S. Lepilliet, D. Ducatteau, and J. F. Lampin, J.F., "J-Band On Wafer Measurements of Planar Goubau Sommerfeld Lines and Coplanar Waveguides," *IRMMW-THz*, pp. 1-2, Sep. 2009.

[75] G. Goubau, "Open Wire Lines", *IRE Trans. On Microwav. Theor.And Tech.*, vol. MTT-4, pp. 197-200, Oct. 1956.

[76] M. N. Afsar, "Dielectric Measurements of Millimeter- Wave Materials," *IEEE Trans. Microw. Theory Tech.*, vol. 32, no. 12, pp. 1598–1609, Dec. 1984.

[77] J. M. Dutta, C. R. Jones, and H. Dave, "Complex Dielectric Constants for Selected Near-Millimeter-Wave Materials at 245 GHz," *IEEE Trans. Microw. Theory Tech.*, vol. 34, no. 9, pp. 932-936, Sept. 1986.

[78] M.N. Afsar and K.J. Button, "Millimeter-Wave Dielectric Measurement of Materials", *Proc. IEEE*, vo1.73, no.1, pp.131-153, Jan. 1985.

[79] J. W. Lamb, "Miscellaneous Data on Materials for Millimeter and submillimeter and Optics," *Int. J. Infrared Millimeterwaves*, vol. 17, no. 19, pp. 1997-2034, Sep. 1996.

[80] D. Grischkowsky, S. Keiding, M. V. Exter, and Ch. Fattinger "Far-Infrared Time-Domain Spectroscopy with Terahertz Beams of Dielectrics and Semiconductors." *J. Opt. Soc. Am. B*, vol. 7, no. 10, pp. 2006-2015, Oct. 1990.

[81] J. Dai, J. Zhang, W. Zhang, and D. Grischkowsky, "Terahertz Time-Domain Spectroscopy Characterization of the Far-Infrared Absorption and Index of Refraction of High-Resistivity, Float-Zone Silicon," *J. Opt. Soc. Am. B*, vol. 21, no. 7, pp. 1379-1386, July 2004.

[82] M. N. Afsar, H. Chi, X. Li, "Millimeter Wave Complex Refractive Index, Complex Dielectric Permittivity and Loss Tangent of High Purity and Compensated Silicon", Conference on Precision Electromagnetic Measurements, *CPEM '90 Digest*, pp. 238-239, 1990.

[83] P. H. Bolivar, M. Brucherseifer, J. G. Rivas, R. Gonzalo, I. Ederra, A. L. Reynolds. M. Holkcr and P. de Maagt, "Measurement of the Dielectric Constant and Lass Tangent of High Dielectric-Constant Materials at Trrahrrtz Frequencies", *IEEE Trans. Microw. Theory Tech*., vol. 51, no. 4, pp. 1062-1066, Apr 2003.

[84] M. Naftaly, R.E. Miles, "Terahertz time-domain spectroscopy for material characterization," *Proc-IEEE*, vol. *95*, no. 8, pp. 1658-1665, Aug. 2007.

[85] M. Naftaly, R.E. Miles, "Terahertz Time-Domain Spectroscopy of Silicate Glasses and the Relationship to Material Properties," *J. Appl. Phys.*, vol. 102, p. 043517, 2007.

[86] S. Atakaramians, S. Afshar V., H. Rasmussen, O. Bang, T. M. Monro, and D. Abbott, "Direct Probing of Evanescent Field for Characterization of Porous Terahertz Fibers," *Appl. Phys. Lett.*, vol. 98, p. 121104, 2011.

[87] A. Hassani, A. Dupuis, and M. Skorobogatiy, "Low Loss Porous Terahertz Fibers Containing Multiple Subwavelength Holes," *Appl. Phys. Lett.*, vol. 92, no. 7, p. 071101, 2008.

[88] T. Hidaka, H. Minamide, H. Ito, J.-I. Nishizawa, K. Tamura, and S. Ichikawa, "Ferroelectric PVDF Cladding Terahertz Waveguide," *J. Lightw. Technol.*, vol. 23, no. 8, pp. 2469–2473, Aug. 2005.

[89] M. A. Basha, A Abdellatif, S Safavi-Naeini, "Low-Cost Fabrication of Millimeter-Wave All-Silicon High Efficiency Antenna," *Proc. IEEE AP-S Int.*, pp. 1-2, July 2012.

[90] J. Yeom, Y. Wu, J. C. Selby, M. A. Shannon, "Maximum Achievable Aspect Ratio in Deep Reactive Ion Etching of Silicon Due to Aspect Ratio Dependent Transport and the Microloading Effect," *J. Vac. Sci. Technol. B*, vol. 23, pp. 2319-2329, 2005.

[91] S. E. Alper, Y. Temiz, T.Akin, "A Compact Angular Rate Sensor System Using a Fully Decoupled Silicon-on-Glass MEMS Gyroscope," *J. Microelectromech. Syst.*, vol. 17, no. 6, pp. 1418–1429, 2008.

[92] N. P. Mahalik, "Micromanufacturing and Nanotechnology," Springer, ISBN 3-540-25377-7.

[93] Tung, R. T., J. M. Gibson, and J. M. Poate. "Formation of Ultrathin Single-Crystal Silicide Films on Si: Surface and Interfacial Stabilization of Si-Ni Si 2 Epitaxial Structures." Physical review letters 50.6 (1983): 429.

[94] Abe, Takao, Ken Sunagawa, Atsuo Uchiyama, Katsuo Yoshizawa, and Yasuyuki Nakazato. "Fabrication and bonding strength of bonded silicon-quartz wafers." Japanese journal of applied physics 32, no. 1S (1993): 334.

[95] Belford, R. E., and Sumant Sood. "Surface activation using remote plasma for silicon to quartz wafer bonding." Microsystem Technologies 15.3 (2009): 407-412.

[96] M. Despont, H. Gross, F. Arrouy, C. Stebler, and U. Staufer, "Fabrication of a Silicon-Pyrex-Silicon Stack by a.c. Anodic Bonding," *Sens. Actuators A: Phys.*, vol. 55, pp. 219-224, 1996.

[97] C. W. Lin, C. P. Hsu, H. A. Yang, W. Ch. Wang, and W. Fang, "Implementation of SOG devices with embedded through-wafer silicon vias using a glass reflow process for wafer-level 3D MEMS integration," *Micro. Electro. Mechanical Systems, MEMS 2008. IEEE 21st International Conference on*, pp. 802-805, 2008.

[98]] E. Tatar, S.E. Alper, and T. Akin, "Quadrature error compensation and corresponding effects on the performance of fully decoupled MEMS gyroscopes," *J. Microelectromech. Syst*., vol. 21, no. 3, pp. 656-667, June 2012.

[99] E. Tatar, M.M. Torunbalci, S.E. Alper, and T. Akin, "A Method and Electrical Model for the Anodic Bonding of SOI and Glass Wafers," *IEEE MEMS 2012*, Paris, France, pp. 68-71, Jan. 2012.

[100] G. Wallis, "Field Assisted Glass Sealing," *Active and Passive Electronic Components*, vol. 2, no. 1, pp. 45-53, 1975.

[101] A. Cozma and B. Puers, "Characterization of the Electrostatic Bonding of Silicon and Pyrex Glass," *J. Micromech. Microeng*., vol. 5, pp. 98-102, 1995.

[102] K. Albaugh, P. Cade, and D. Rasmussen, "Mechanisms of Anodic Bonding of Silicon to Pyrex Glass," *Dig. IEEE Solid-State Sensor and Actuator Workshop* (*Hilton Head, NC*), pp. 109-110, June 1988.

[103] Rogers, T., and J. Kowal. "Selection of glass, anodic bonding conditions and material compatibility for silicon-glass capacitive sensors." *Sensors and Actuators A: Physical* 46.1 (1995): 113-120.

[104] N. Ranjkesh, M. Basha, A. Taeb, A. Zandieh, S. Gigoyan, and S. Safavi-Naeini, "Silicon-on-glass dielectric waveguide—Part I: For millimeter-wave integrated circuits," *IEEE Trans. THz Sci. Technol.*, vol. 5, no. 2, pp. 268 – 279, Mar. 2015.

[105] J. Yang1, L. Guangbo, S. Xiao1, L. Yubo, J. Xiaoqing, W. Minghua, , and Y. Wang, "Fabrication of Silicon-on-Glass Waveguides," *in Proc. IEEE Int. Conf. Group IV Photon*., pp. 65–67, Sep. 2005.

[106] E. A. J. Marcatili, "Dielectric Rectangular Waveguide and Directional Coupler for Integrated Optics," *Bell Syst. Tech. J*., vol. 48, no. 9, pp. 2071–2102, Sep. 1969.

[107] D. Marcuse, "Theory of Dielectric Optical Waveguides," New York: Academic, 1991.

[108] K. Ogusu, "Numerical Analysis of the Rectangular Dielectric Waveguide and Its Modifications," *IEEE Trans. Microw. Theory Tech.*, vol. 25, no. 11, pp. 874-885, Nov. 1977.

[109] A. Taeb, "A New Silicon-Based Dielectric Waveguide Technology for Millimeter-Wave/Terahertz Devices and Integrated Systems," Ph.D. dissertation, University of Waterloo, 2015.

[110] W. T. Anderson and P. F. Glodis, "Design Diagrams for Depressed Cladding Single-Mode Fibers," *AT&T Bell Laboratories Tech. J.*, vol. 63, no. 3, pp. 425-430, March 1984.

[111] N. Ranjkesh, A. Taeb, S. Gigoyan, M. Basha, and S. Safavi-Naeini "Millimeter-Wave Silicon-on-Glass Integrated Tapered Antenna," *IEEE Antennas Wireless Propag. Lett.*, vol. 13, pp. 1425-1428, July 2014.

[112] N. Ranjkesh, A. Taeb, S. Gigoyan, M. Basha, and S. Safavi-Naeini, "Millimeter-Wave Suspended Silicon-On-Glass Tapered Antenna with Dual-Mode Operation," to be published on *IEEE Trans. Antennas. Propag.*

[113] N. Ranjkesh, A. Taeb, A. Abdellatif, S. Gigoyan, M. Basha, and S. Safavi-Naeini, "Millimeter-Wave Silicon-On-Glass Integrated Technology," in *IEEE MTT-s IMaRC 2014*, India, Dec. 2014, pp. 233–236.

[114] N. Ranjkesh, M. Basha, A. Abdellatif, S. Gigoyan, and S. Safavi-Naeini, "Millimeter-Wave Tunable Phase Shifter on Silicon-On-Glass Technology," *IEEE Microw. Wireless Compon. Lett*., no. 99, June 2015.

[115] A. A. Ayón, X. Zhang, and R. Khanna. "Anisotropic Silicon Trenches 300–500 μm Deep Employing Time Multiplexed Deep Etching (TMDE)," *Sens. Actuators A: Phys.*, vol. 91, no. 3, pp. 381-385, 2001.

[116] Hwang, Gyeong S., and Konstantinos P. Giapis. "On the origin of the notching effect during etching in uniform high density plasmas." Journal of Vacuum Science & Technology B 15.1 (1997): 70-87.

[117] Li, J., et al. "Technique for preventing stiction and notching effect on silicon-on-insulator microstructure." Journal of Vacuum Science & Technology B 21.6 (2003): 2530-2539.

[118] G. E. Ponchak and N. I. Dib, "Design and Analysis of Transitions from Rectangular Waveguide to Layered Ridge Dielectric Waveguide*," IEEE Trans. Microw. Theory Tech.*, vol. 44, no. 7, pp. 1032-1040, July 1996.

[119] M. D. Janezic and J. A. Jargon, "Complex Permittivity Determination from Propagation Constant Measurements," *IEEE Microwave and Guided Wave Lett*., vol. 9, no. 2, pp.76-78, Feb. 1999.

[120] C. Iliescu, B. Chen, and J. Miao, "On the Wet Etching of Pyrex Glass," *Sens. Actuators A: Phys.*, vol. 143, no. 1, pp. 154–161, May 2008.

[121] N. Ranjkesh, M. Basha, A. Taeb, and S. Safavi-Naeini, "Silicon-on-Glass Dielectric Waveguide, Part II: for THz Applications." *IEEE Trans. THz Sci. Technol.*, vol. 5, no. 2, pp. 280 – 287, Mar. 2015.

[122] C. Iliescu, J. Miao, F. E.H. Tay, "Stress Control in Masking Layers for Deep Wet Micromachining of Pyrex Glass," *Sens. Actuators A*, vol. 117, pp. 286–292, 2005.

[123] C. Iliescu, J. Jing, F. E.H. Tay, J. Miao, and T. Sun, "Characterization of Masking Layers for Deep Wet Etching of Glass in an Improved HF/HCl Solution," *Surface and Coatings Technology*, vol. 198, pp. 314– 318, 2005.

[124] D.C.S. Bien, P.V. Rainey, S.J.N. Mitchell, H.S. Gamble, "Characterization of Mask Materials for Deep Glass Micromachining," *J. Micromech. Microeng.*, vol. 13, pp. 34–40, 2003.

[125] T. Corman, P. Enokson, G. Stemme, "Deep Wet Etching of Borosilicate Glass using Anodically Bonded Silicon Substrate as Mask," *J. Micromech. Microeng.*, vol. 8, pp. 84–87, 1998.

[126] M.A. Grettilat, F. Paoletti, P. Thiebaud, S. Roth, M. Kondelka-Hep, N.F. de Rooij, "A New Fabrication Method for Borosilicate Glass Capillary Tubes with Lateral Inlets and Outlets," *Sens. Actuators A*, vol. 60, pp. 219–222, 1997.

[127] F. E. H. Tay, C. Iliescu, J. Jing, and J. Miao "Defect-free Wet Etching Through Pyrex Glass Using Cr/Au Mask," *Microsystem Tech.*, vol. 12, no. 10-11, pp. 935-939, Sep. 2006.

[128] C. Iliescu, K. L. Tan, F. EH Tay, and J. Miao, "Deep Wet and Dry Etching of Pyrex Glass: A Review," *ICMAT 2005*, July 2005.

[129] K. R. Williams and K. Gupta, "Etch Rates For Micromachining Processing," *J. MEMS*, vol. 5, no. 4, pp. 256-269, Dec. 1996.

[130] P. B. Sullivan, W. Offord, and M. E. Aklufi, "Tetra-Methyl Ammonium Hydroxide (TMAH) Preferential Etching for Infrared Pixel Arrays," no. TD-3097. *Space and Naval Warfare Systems Center San Diego CA*, 2000.

[131] X. Li, T. Abe, and M. Esashi, "Deep Reactive Ion Etching of Pyrex Glass Using SF6 Plasma," *Sens. Actuators A*, vol. 87, pp. 139-145, 2001.

[132] B. Adi and M. Naftali. "Dry Etching of Deep Cavities in Pyrex for MEMS Applications Using Standard Lithography," *J. Micromech. Microeng.*, vol. 16, pp. 2287–2291, 2006.

[133] C. Iliescu, F. E.H. Tay, and J. Miao, "Strategies in Deep Wet Etching of Pyrex Glass," *Sens. Actuators A*, vol. 133, pp. 395-400, 2007.

[134] M. Bu, T. Melvin, G. J. Ensell, J. S. Wilkinson, and A. G. R. Evans, "A New Masking Technology for Deep Glass Etching and its Microfluidic Application," *Sens. Actuators A*, vol. 115, pp. 476–482, 2004.

[135] T. Akashi, and Y. Yoshimura, "Profile Control of a Borosilicate-Glass Groove formed by Deep Reactive Ion Etching," *J. Micromech. Microeng.*, vol. *18*, no. 10, p. 105004, 2008.

[136] D. A. Zeze, R. D. Forrest, J. D. Carey, D. C. Cox, , I. D. Robertson, B. L. Weiss, and S. R. P. Silva, "Reactive Ion Etching of Quartz and Pyrex for Microelectronic Applications," *J. Appl. Phys*., vol. 92, no. 7, pp. 3624-3629, 2002.

[137] C. Iliescu and F. E. H. Tay "Wet Etching of Glass," *Semiconductor Conference, CAS 2005 Proceedings*, vol. 1, pp. 35-44, 2005.

[138] T. Akashi, Y. Yoshimura, and S. Higashiyama, "Deep Reactive Ion Etching of Pyrex Glass Using a Bonded Silicon Wafer as an Etching Mask," *Micro. Electro. Mechanical Systems, MEMS 2008. IEEE 18th International Conference on*, pp. 520-523, 2005.

[139] T. Reck, C. Jung-kubiak, J. V. Siles, C. Lee, R. Lin, G. Chattopadhyay, I. Mehdi, and K. Cooper, "A Silicon Micromachined Eight-Pixel Transceiver Array for Submillimeter-Wave Radar," *IEEE Trans. THz Sci. Technol.*, vol. 5, no. 2, pp. 197 – 206, Mar. 2015.

[140] P. R. Young, R. J. Collier, and P.G.G. Bianconi, "A Low Loss Phase Shifter for Dielectric Waveguide using Asymmetrical Guides," *European Microwave Conference* 1997, Jerusalem, Israel, vol. 1, pp. 631–635, Sep. 1997.

[141] Young, Paul R., and Richard J. Collier. "Low loss phase shifter for dielectric waveguide." *High Frequency Postgraduate Student Colloquium, 2nd*. *IEEE*, 1996.

[142] D. Chicherin1, M. Sterner, J. Oberhammer, S. Dudorov, and D. Lioubtchenko, "MEMS Based High-Impedance Surface for Millimetre Wave Dielectric Rod Waveguide Phase Shifter," *European Microwave Conference 2010*, Paris, France, pp. 950-953, Sep. 2010.

[143] M. Y. Li and K. Chang, "New Tunable Phase Shifters Using Perturbed Dielectric Image Lines," *IEEE Trans. Microw. Theory Tech.*, vol. 46, no. 10, pp. 1520-1523, Oct. 1998.

[144] A. Abdellatif, A. Taeb, N. Ranjkesh, S. Gigoyan and S. Safavi-Naeini, "W-band Piezoelectric Transducer-Controlled Low Insertion Loss Variable Phase Shifter," *Electron. Lett.*, vol. 50, no. 21, pp. 1537-1538, Oct. 2014.

[145] A. Abdellatif, A. Taeb, N. Ranjkesh, S. Gigoyan and S. Safavi-Naeini "Low Insertion Loss Phase Shifter for Millimeter-Wave Phased Array Antennas", *International Journal of Microwave and Wireless Technologies*, 2014, pp. 1-7.

[146] A. Abdellatif, M. S. Faraji-Dana, N. Ranjkesh, A. Taeb, M. Fahimnia, S. Gigoyan, and S. Safavi-Naeini, "Low Loss, Wideband, and Compact CPW-Based Phase Shifter for Millimeter-Wave Applications," *IEEE Trans. Microw. Theory Techn.*, vol. 62, no. 12, Dec. 2014, pp. 3403-3413.

[147] Y. Garbovskiy, V. Zagorodnii, P. Krivosik, J. Lovejoy, R. E. Camley, Z. Celinski, A. Glushchenko, J. Dziaduszek, and R. Dąbrowski, "Liquid Crystal Phase Shifters at Millimeter Wave Frequencies," Appl. Phys. Lett. 111, 054504 (2012).

[148] N. Somjit, G. Stemme, and J. Oberhammer, "Binary-Coded 4.25 bit W-band Monocrystalline–Silicon MEMS Multistage Dielectric-Block Phase Shifters', IEEE Trans. Microw. Theory Tech., vol. 57, no. 11, pp. 2834–2840, 2009.

[149] M. Jost, C. Weickhmann, S. Strunck, A. Gäbler, C. Fritzsch, O.H. Karabey and R. Jakoby, "Liquid Crystal Based Low-Loss Phase Shifter for W-band Frequencies," *Elec. Lett.*, vol. 49, no. 23, pp. 1460–1462, Nov. 2013.

[150] J. Hung, Juo-Jung, L. Dussopt, and G. M. Rebeiz, "Distributed 2- and 3-bit W-band MEMS phase shifters on glass substrates," *IEEE Trans. Microw. Theory Tech*., vol.52, no.2, pp.600 - 606, Feb. 2004.

[151] A. Stehle, G. Georgiev, V. Ziegler, B. Schoenlinner, U. Prechtel, H. Seidel, U. Schmid, "RF-MEMS Switch and Phase Shifter Optimized for W-Band," *European Microwave Conference* 2008, pp. 104-107, Oct. 2008.

[152] S.A. Yahaya, M. Yamamoto, K. Itoh, and T. Nojima, “Dielectric Rod Antenna Based on Image NRD Guide Coupled to Rectangular Waveguide,” *Electron. Lett.,* vol. 39, no. 15, pp. 1099-1101, July 2003.

[153] Kobayashi, R. Mittra, and R. Lampe, “Dielectric Tapered Rod Antennas for Millimeter-Wave Applications,” *IEEE Trans. Antennas Propagat*., vol. AP-30, no. 1, Jan. 1982.

[154] J. Patrik Pousi, D. V. Lioubtchenko, S. N. Dudorov, and A. V. Räisänen, “High Permittivity Dielectric Rod Waveguide as an Antenna Array Element for Millimeter Waves,” *IEEE Trans. Antennas. Propag*., vol. 58, no. 3, pp. 714-719, March 2010.

[155] A. A. Generalov, J. A. Haimakainen, D. V. Lioubtchenko, and A. V. Räisänen, “Wide band mm- and sub-mm-wave dielectric rod waveguide antenna,” *IEEE Trans. THz Sci. Technol*., vol. 4, no. 5, pp. 568-574, Sep. 2014.

[156] D. V. Lioubtchenko , J. P. Pousi , S. N. Dudorov and A. V. Räisänen, "Millimetre-wave phase shifterbased on dielectric rod waveguide", *Proc. 38thEur. Microw. Conf.*, pp.1204 -1206, 2008.

[157] A. M. Marconnet, M. M. He, S. Sengele, Sung-Jin Ho, H. Jiang, N. J. Ferrier, J. Nicola, V. D. Weide, V. Madhavan, N. Nelson, J. H. Booske, “Microfabricated Silicon High-Frequency Waveguide Couplers and Antennas,” *IEEE trans. On Elctron. Devices*, vol. 56, no. 5, pp. 721-729, May. 2009.

[158] S. Kobayashi, R. Mittra, and R. Lampe, “Dielectric tapered rod antennas for millimeter-wave applications,” IEEE Trans. Antennas Propagat., vol. AP-30, pp. 5&58, Jan. 1982.

[159] S. Gregson, J. McCormick, and C. Parini, “Principles of Planar Near-Field Antenna Measurements,” IET Electromagnetic Waves Series; v. 53, Institution of Eng. And Technol., 2007.

[160] H.-C. Lu, C.-C. Kuo, P.-A. Lin, C.-F. Tai, Y.-L. Chang, Y.-S. Jiang, et al., “Flip-chip-assembled W-band CMOS chip modules on ceramic integrated passive device with transition compensation for millimeter-wave system-in-package integration,” *IEEE Trans. Microw. Theory Tech*., vol. 60, no. 3, pp. 766–777, Mar. 2012.

[161] A. Zandieh, N. Ranjkesh, S. Safavi-Naeini, and M. Basha. "A low-loss CPW to dielectric waveguide transition for millimeter-wave hybrid integration." *In Antennas and Propagation Society International Symposium* (APSURSI), pp. 1-2, July 2012.